Development and Testing of Augmentations of Continuously-Operating GPS Networks to Improve Their Spatial and Temporal Resolution

By

Linlin Ge

M.Sc., Institute of Seismology, State Seismological Bureau, P.R. China, 1988.
B.Eng. (1st Hons), Wuhan Technical University of Surveying and Mapping, P.R. China, 1985.

A thesis submitted to The University of New South Wales
in partial fulfillment of the requirements for the degree of
Doctor of Philosophy

School of Geomatic Engineering
The University of New South Wales
Sydney NSW 2052, Australia

November 2000

ABSTRACT

Continuously-operating networks of GPS receivers (CGPS) are not capable of determining the characteristics of crustal deformation at the fine temporal or spatial scales required. Four ‘temporal densification schemes’ and two 'spatial densification schemes' to augment the CGPS networks have been developed and tested.

The four ‘temporal densification schemes’ are based on the high rate Real-Time Kinematic (RTK) GPS technique, GPS multipath effects, Very Long Baseline Interferometry (VLBI) and Satellite Laser Ranging (SLR).

The 'serial scheme' based on using GPS as a seismometer has been proposed. Simulated seismic signals have been extracted from the very noisy high rate RTK-GPS results using an adaptive filter based on the least-mean-square algorithm. They are in very good agreement with those of the collocated seismometers. This scheme can improve the CGPS temporal resolution to 0.1 second.

The 'retro-active scheme' takes advantage of the fact that the GPS multipath disturbance is repeated between consecutive days. It can therefore provide a means of correcting multipath errors in the observation data themselves. A reduction of the standard deviations of the pseudo-range and carrier phase multipath time series to about one fourth and one half the original values respectively, has been demonstrated.

The 'all-GPS parallel scheme' uses the multipath effects as a signal to monitor the antenna environment. Models relating the changes of multipath and antenna environment have been derived.

The 'cross-technique parallel scheme' integrates the collocated CGPS, VLBI and SLR results, taking advantage of the decorrelation among their biases and errors. Crustal

displacement signature has been extracted as a common-mode signal using data from two stations: Matera in Italy and Wettzell in Germany.

Two 'spatial densification schemes' which can verify with each other have been developed and tested. The 'soft' scheme integrates CGPS with radar interferometry (InSAR). The Double Interpolation and Double Prediction (DIDP) approach combines the strengths of the high temporal resolution of CGPS and the high spatial resolution possible with the InSAR technique. This scheme can improve the spatial resolution to about 25m.

The 'hard' scheme requires the deployment of single-frequency receivers to in-fill the present CGPS arrays. Alternatively some receivers may be installed at some geophysically strategic sites outside existing CGPS arrays. The former has been tested within Japan's GEONET, while the latter has been tested using a five-station array.

TABLE OF CONTENTS

LIST OF FIGURES

LIST OF TABLES

ACKNOWLEDGEMENTS

This research was conducted from March 1998 through to November 2000 under the supervision of Professor Chris Rizos and Dr Shaowei Han. I am truly grateful to them for their encouragement, invaluable advice, and patient guidance during this work.

I would like to warmly thank all the members of the Satellite Navigation And Positioning (SNAP) Group, at The University of New South Wales, for numerous discussions and valuable assistance in undertaking relevant experiments.

I would also like to express my gratitude to Drs Yuzo Ishikawa, Mitsuyuki Hoshiba, and Yasuhiro Yoshida of the Meteorological Research Institute, Japan; Dr Yuki Hatanaka of the Geographical Survey Institute, Ministry of Construction, Japan; Professor Makoto Omura of the Kochi Women's University, Japan; Dr D. Massonnet of CNES, the French space agency; Dr J. T. Freymueller of the University of Alaska (U.S.A.), and Professor Howard Zebker of Stanford University (U.S.A.) for their collaboration in many different ways.

I am very grateful to the sponsorship provided to me by an International Postgraduate Scholarship of The University of New South Wales, and later a SNAP Scholarship.

Last, but far from least, I thank my family right from the bottom of my heart, especially my father Xinpu and mother the late Huanxian, my wife Xiaojing, my daughter Bei and my son George, for their love and understanding during my PhD studies.

1 INTRODUCTION

1.1 The Global Positioning System (GPS)

The NAVSTAR Global Positioning System (GPS) is a space-based radio-positioning system of unprecedented versatility and utility. It provides 24 hour, three-dimensional position, velocity and time (PVT) information to all suitably equipped users anywhere on or near the surface of the Earth. The Global Navigation Satellite System (GNSS) is a generic term for a space-based radio-positioning system that can provide users with sufficient accuracy and integrity information for critical navigation applications. At present it comprises GPS and the Russian Federation's GLONASS system, but in the future it will also include the European Union's Galileo system.

The nominal GPS constellation consists of 24 satellites orbiting around the Earth at an altitude of approximately 20200km, in six orbital planes with an inclination of 55° (with four satellites per plane, as depicted in Fig. 1.1). At that altitude the satellites complete two orbits around the Earth in just under 24 hours (approximately the length of the sidereal day: 23 hours 56 minutes). The orbital groundtracks of these satellites traverse the Earth in swaths between 55° North and South latitudes, which enables the satellite signals to be received anywhere on Earth. One of the biggest benefits over previous land-based navigation systems is that GPS works in all weather conditions.

Each satellite weighs approximately 908kg and is about 5.2m across with the solar panels extended. Transmitter power is only 50 watts! Each satellite transmits two navigation signals: L1 (1575.42 MHz) and L2 (1227.60 MHz). Most civilian GPS receivers track and process the 'L1' frequency signal only. The GPS signal contains a 'pseudo-random code', ephemeris and almanac data. The pseudo-random (PRN) code identifies which satellite is

transmitting - in other words, it is an I.D. code. Satellites are referred to by their PRN code, numbered from 1 through 32.

'Navigation Message' data is constantly transmitted by each satellite and contains important information such as the position of the satellite (at a certain time, in the WGS84 reference frame), status of the satellite (healthy or unhealthy), current date and time, as well as other data. The PRN modulations on the carrier wave permit the tramsit time to be determined. Without this data a GPS receiver would have no idea what the distance to the tracked satellite(s) would be, and hence would not be able to compute the PVT information. As part of the ‘GPS Control Segment’, the GPS Ground Stations monitor the satellites, checking both their operational health, and determining their satellite clock time and their orbit. The Master Control Station performs the necessary computations to determine each satellite's ephemeris and clock offsets (in relation to the master GPS Time scale). This data is uploaded to the satellites, which then transmit this information as modulations on the broadcast signals. There are five Ground Stations: Hawaii, Ascension Island, Diego Garcia, Kwajalein, and Colorado Springs (Fig. 1.5). (For details on the GPS system architecture, signal specifications, and basic operations the reader is referred to such excellent engineering texts as Parkinson & Spilker, 1996.)

To determine position the receiver compares the time a signal was transmitted by a satellite with the time it was received by the GPS receiver. The time difference so determined is a measure of the distance or 'range'. **With a minimum of four satellites, a GPS receiver can determine its 3D position, as well as solve for the correct receiver time by a process analogous to classical trilateration.** One factor affecting GPS accuracy is satellite geometry, that is, where the satellites are located relative to each other (from the perspective of the GPS receiver). Satellite geometry becomes an issue when using a GPS receiver in a vehicle, near tall buildings, or in mountainous or canyon areas. In the case of volcano deformation monitoring, because most of the receivers will be located either on the slope or at the foot of the mountain, the GPS signals from several satellites may be blocked.

A significant source of error for GPS positioning is multipath. Multipath is the result of the interference between a radio signal and its reflections from objects near the GPS antenna. Chapters 4 and 5 discuss GPS multipath in more detail. Another major source of GPS error is the propagation delay due to the atmosphere. The dual-frequency signal (L1 and L2) is designed to permit the compensation of the ionospheric delay. However, the tropospheric effects are not frequency-dependent and must therefore be modelled some how. It is the spatial correlation of the atmospheric effects (troposphere and ionosphere) that affects the efficiency of network-based techniques, as discussed in Chapter 8.

Figure 1.1 The 24 NAVSTAR GPS satellites (not to scale).

The GLONASS (*Glo*bal *Na*vigation *S*atellite *S*ystem) is similar in design and operation, and may be considered complimentary, to the NAVSTAR GPS system (GLONASS, 1995). GLONASS is a system which has since 1970s been developed and deployed by the former Soviet Union. There are currently more than ten operational satellites in orbit (well down on the number in 1996 when the system was first declared operational). Both the navigation and scientific communities have an interest in maximizing the benefits of a 36 or more satellite constellation. Integrated GPS and GLONASS receivers are especially useful for deformation monitoring for volcanoes, and positioning in opencut mines, or anywhere the

number of visible satellites is limited by blockages. Another application is atmospheric monitoring and satellite geodesy research.

In addition to GPS and GLONASS, in February 1999 the Commission of the European Union made a strong recommendation for a European-led development of Galileo, a constellation of new civil navigation satellites (COM, 1999). The European approach for the design of the next generation GNSS is based on an open system architecture comprising the two sub-constellations GPS IIF and Galileo. (No mention is made of GLONASS.) The system will provide an Open Access Service (OAS) and a Controlled Access Service (CAS). The OAS will be compatible with the GPS IIF public service. As a design goal for the CAS service the joint sub-constellations, i.e. GPS and Galileo, are expected to be able to fulfil the stringent requirements for sole means navigation for aviation.

In order to provide users worldwide with navigation capabilities well into the next decade that are both accurate and reliable, the *modernization* of NAVSTAR GPS is underway.

1.2 The NAVSTAR GPS Modernization

As shown in Fig. 1.2, there are several components to the GPS modernization that have been proposed, but *which are mostly targeting navigation applications*. However, precise applications such as deformation monitoring may benefit from one of the main components of this modernization effort, that is, the two new navigation signals that will be available for civil use (Fig. 1.3). The first of these new signals will be modulated on the L2 (effectively ending the Anti-Spoofing policy currently implemented), and will be available for general use in non-safety critical applications. This will be available beginning with the initial GPS Block IIF satellite scheduled for launch in 2003. The other signal, located at 1176.45 MHz (L5), will be available on GPS Block IIF satellites scheduled for launch beginning around 2005. This new L5 signal falls in a band which is reserved worldwide for aeronautical radionavigation, and therefore will be protected for safety-of-life applications.

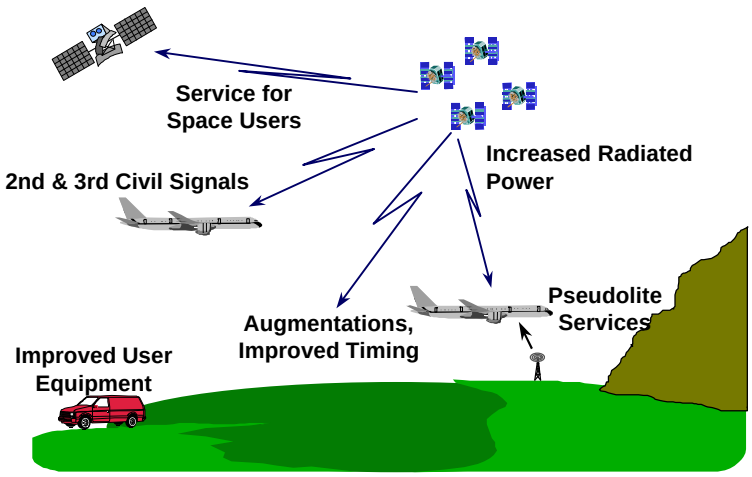

Figure 1.2 GPS Modernization (McDonald, 1999).

At the current GPS satellite replenishment rate, all three civil frequencies (L1, L2, and L5) will be available for initial operational capability by 2010, and for full operational capability by approximately 2013. Some of the benefits of three frequencies are:

- Improve the ability of GPS to provide aviation and other transportation applications with continuous, accurate, three-dimensional position information.
- Increased availability of precision navigation services around the world, and provide redundancy in the event of intentional or unintentional electromagnetic interference or jamming.
- Speed up the resolution of the cycle ambiguities of the carrier phase measurements, mainly benefiting the surveying and precise navigation user communities.

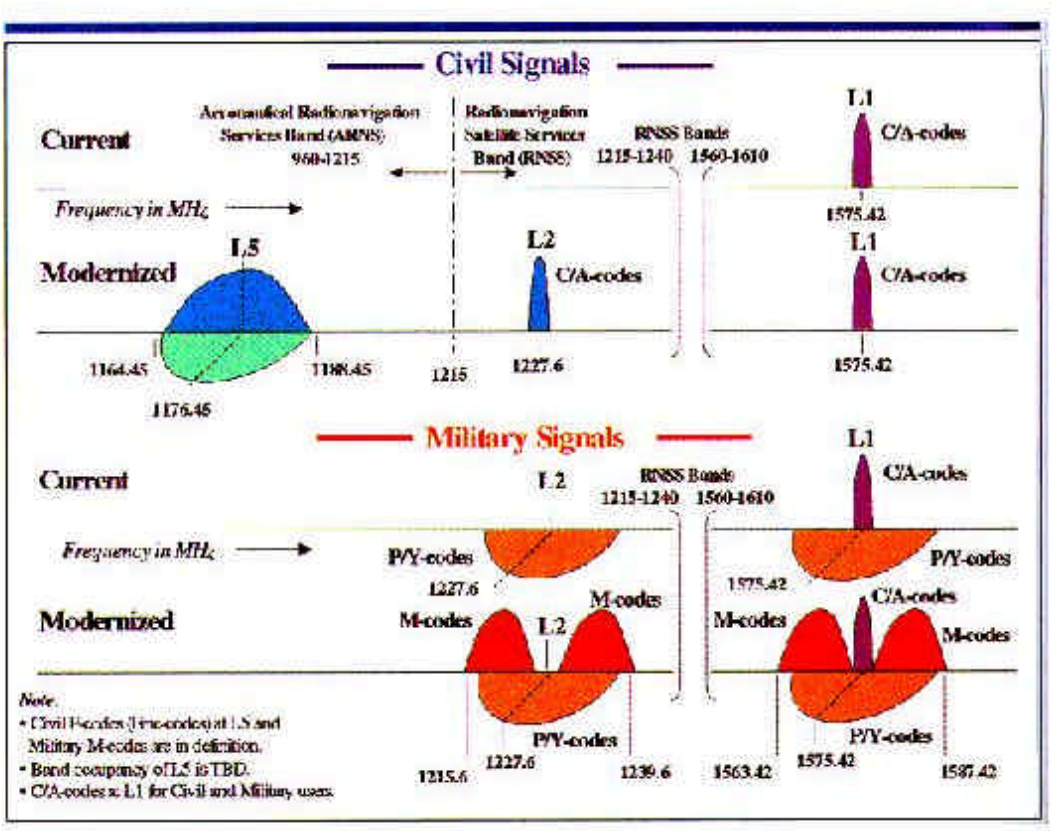

Figure 1.3 Current and Proposed GPS Signal Spectrum (McDonald, 1999).

The new civilian F-codes (Fine codes) at L5, and the military M-codes on both L1 and L2, are in addition to the standard C/A-codes currently modulated on the L1 signal (and which will be added to the L2 signal), as shown in Fig. 1.4.

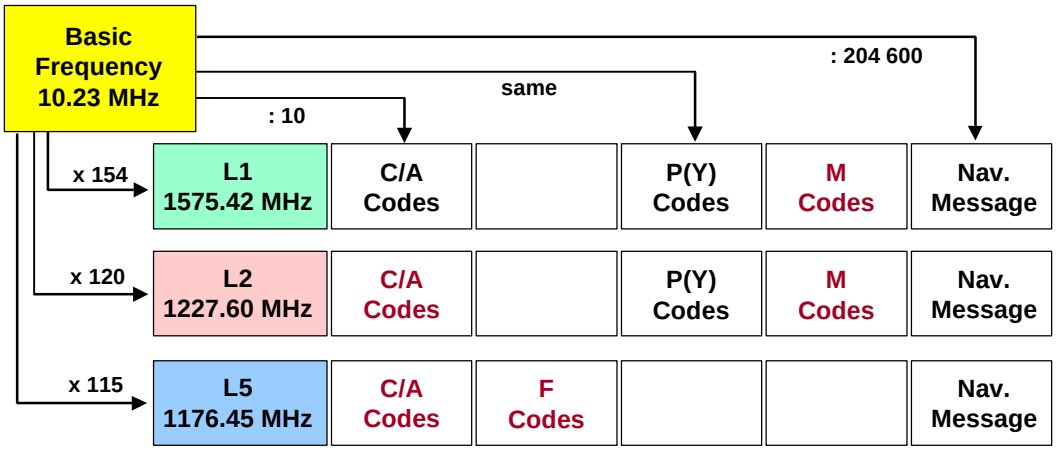

Figure 1.4 Future GPS Signal Structure (McDonald, 1999).

No matter how the GNSS evolves, continuously-operating GPS (CGPS) receiver networks will continue to play important roles for many applications such as precise orbit determination and crustal deformation monitoring.

1.3 Continuously-operating Networks of GPS Receivers (CGPS)

CGPS is a methodology based on using a network of permanently installed GPS receivers, though several different terms have been used in recent years, including:

- Continuous GPS arrays
- Continuously operating GPS networks
- Continuously-operating reference receivers (CORS)
- Permanent GPS networks
- Fixed-point GPS network

In this thesis all of these are simply referred to as CGPS or continuous GPS.

The genesis of CGPS is usually "... a tool for geodynamic studies that emerged in the 1980s". However, geodynamics is only one of the applications addressed by CGPS. CGPS can be considered to have first been associated with the GPS Control Segment. Hence, CGPS is as old as GPS itself! As already mentioned, the Ground Stations (Fig. 1.5) track the GPS signals. The Master Control Station uses this tracking data to determine the satellite ephemerides, clock offsets, and other parameters. These ae uploaded to the satellites, and broadcast to users as part of the 'Navigation Message'.

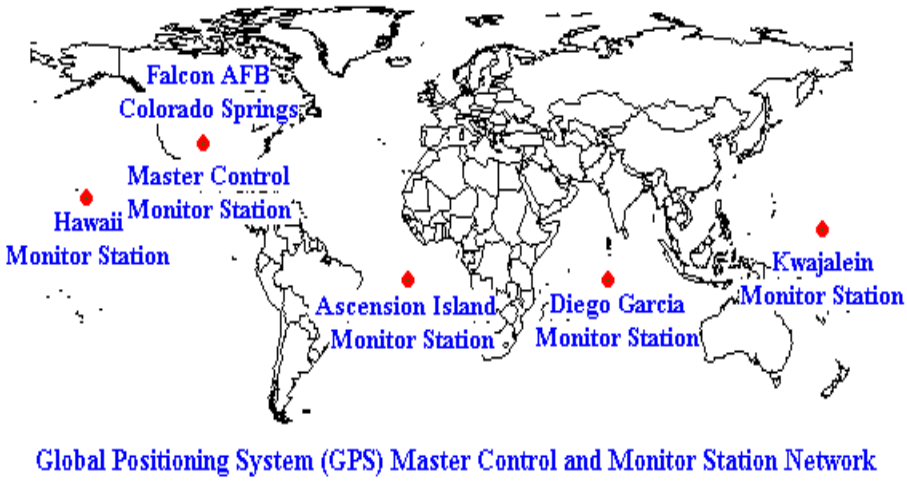

Figure 1.5 The first CGPS network.

1.4 CGPS Achievements

During the last decade of the 20th century, the Global Positioning System has increasingly become an important part of the worldwide geospatial information infrastructure. Continuously-operated GPS networks consisting of state-of-the-art, dual-frequency receivers have been established in many parts of the world (e.g. Bock et al., 1993; Miyazaki et al., 1996) to address geodynamic applications, on a range of spatial scales. These include tracking surface crustal deformation on local and regional scales associated with active seismic faults and volcanoes, local monitoring of slope stability (caused by open pit mining operations, unstable natural features, etc.), and measuring ground subsidence over small areal extents (due to underground mining, extraction of fluids, etc.). Current GPS capabilities permit the determination of inter-receiver distances at the sub-cm accuracy level (typically on a daily basis) for receiver separations of tens to hundreds of kilometres, from which can be inferred the rate-of-change of distance between precisely monumented groundmarks. This is the basic geodetic measure from which can be inferred the ground deformation. The pattern of ground deformation determined from the analysis of such measures across a CGPS network is an important input to models that seek to explain the

mechanisms for such deformation, and hopefully to mitigate the damage to society caused by such (slow or fast) ground movements.

Table 1-1 gives a brief overview of the early CGPS networks. Among them, the GEONET (GPS Earth Observation Network) operated by the Geographical Survey Institute (GSI) of Japan, has evolved into the world's densest GPS network (denoted by grey (red) dots), with an average spatial resolution of 25km and temporal resolution of 30 seconds (data sampling rate) (Fig. 1.6; GSI, 2000).

Table 1-1 Early CGPS networks.

Network	GRAPES COSMOS-G2 GEONET	PGGA SCIGN	NIED CGPS
Organization	GSI, Japan	SCEC/USGS/JPL /SIO, USA	NIED, Japan
Time, No. stations, and instrument of first permanent installation	1989, 3 stations	1990, 4 stations Rogue SNR-8 dual-freq.	1988, 10 stations, Mini-Mac 2816AT dual-freq.
Location of first permanent installation	Izu Peninsula	Southern California	Kanto-Tokai region
Sampling	30sec, 1sec	30sec	30sec
Mainstream receivers	Trimble 4000SSE	Ashtech Z-12	Ashtech Z-12
Current station No.	947	47	17

Remarks:

COSMOS-G2: COntinous Strain MOnitoring System with GPS by GSI

PGGA: the southern California Permanent GPS Geodetic Array, now a regional component of SCIGN;

SCIGN: Southern California Integrated GPS Network

GSI: Geographical Survey Institute, Japan

SCEC: Southern California Earthquake Center, USA

USGS: United States Geological Survey, USA

JPL: Jet Propulsion Laboratory, USA

SIO: Scripps Institution of Oceanography, Institute of Geophysics and Planetary Physics, USA

NIED: National Institute for Earth Science and Disaster Prevention, Japan

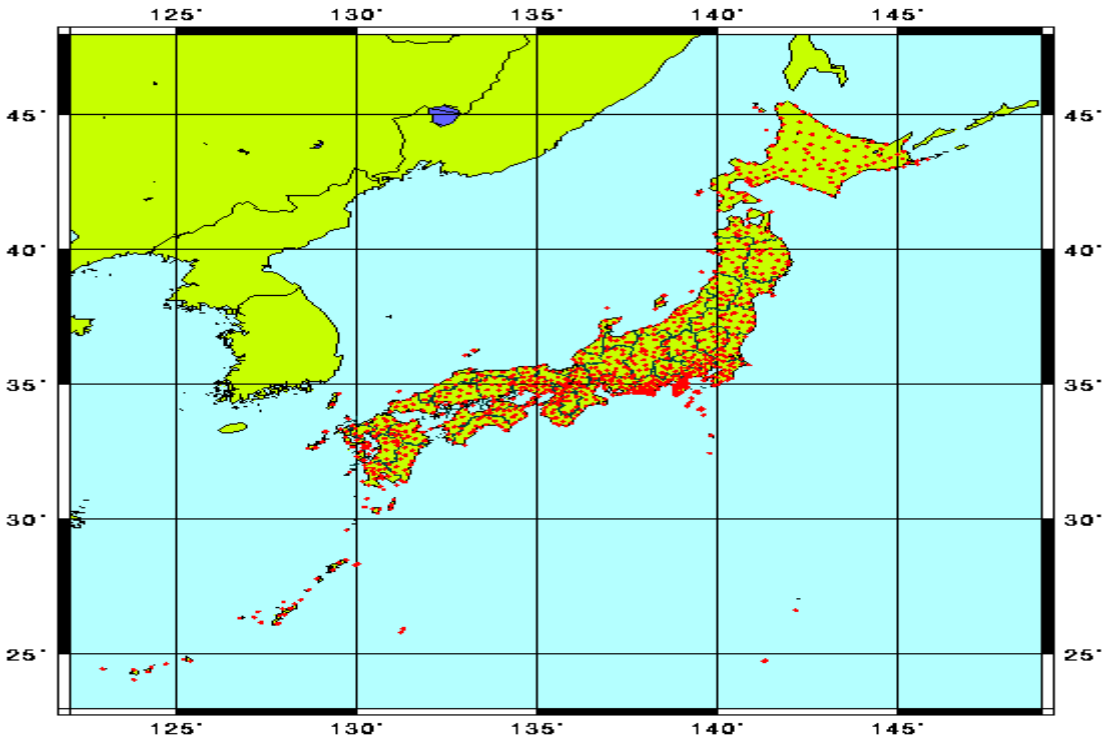

Figure 1.6 The GEONET operated by the Geographical Survey Institute of Japan.

1.5 Temporal and Spatial Resolution Requirements on CGPS From Some Geodynamic and Engineering Applications

As mentioned earlier, CGPS networks are capable of determining changes in relative positions of the receivers to very high accuracies, on a continuous basis, and have made significant contributions to the measurement of the Earth's surface dynamics in support of local earthquake and volcano mechanism investigations. However, **for many geodynamic applications these CGPS arrays of receivers are not capable, on their own, of determining the characteristics of crustal motion at the fine temporal or spatial scales required (Ge et al., 2000a).** For example, although the spatial resolution of Japan's GEONET, **the largest and best instrumented of the CGPS networks, consisting of almost 1000 stations,** is now as high as about 30km, due to the high cost of dual-frequency GPS receivers they may not be established in a dense enough configuration to address all of

the geodetic applications. One of these applications, the monitoring of pre-seismic or post-seismic faulting, requires sub-km resolution, as indicated by the faulting lengths of some past earthquakes in Table 1-2.

Table 1-2. Earthquake surface faulting (compiled from various sources).

Locality	Date (dd/mm/yy)	Magnitude (M)	Length (km)	Maximum displacement (m)	
				Horizontal	Vertical
Chedrang Fault, India	12/06/1897	8.7	19		11.0
Formosa	16/03/1906	7.1	48	2.5	1.3
California, USA	18/04/1906	8.3	434	6.4	1.0
Nevada, USA	03/10/1915	7.8	32		4.5
Murchison, New Zealand	16/06/1929	7.6	4		4.6
Chile	22/05/1960	8.3	1600		
Alaska, USA	28/03/1964	8.5	900	6.0	6.0
Iran	31/08/1968	7.4	27	4.0	

In fact, if one inspects the resolution requirements for some geophysical and geological applications (as shown in Fig. 1.7, where the coverage of the current CGPS is indicated by the dashed-line rectangle), **the requirements for a majority of the applications remain unsatisfied.** If the rectangle is extended in the negative direction of the vertical axis, this represents a 'temporal densification of the GPS measurements' (Ge et al., 1999b). If the rectangle is extended in the negative direction of the horizontal axis, this is a 'spatial densification of the GPS measurements'. While it is straightforward to realize these temporal and spatial densifications by increasing the data sampling rate on the one hand, and by deploying many more GPS receivers on the other hand, it is not generally economically feasible to do so.

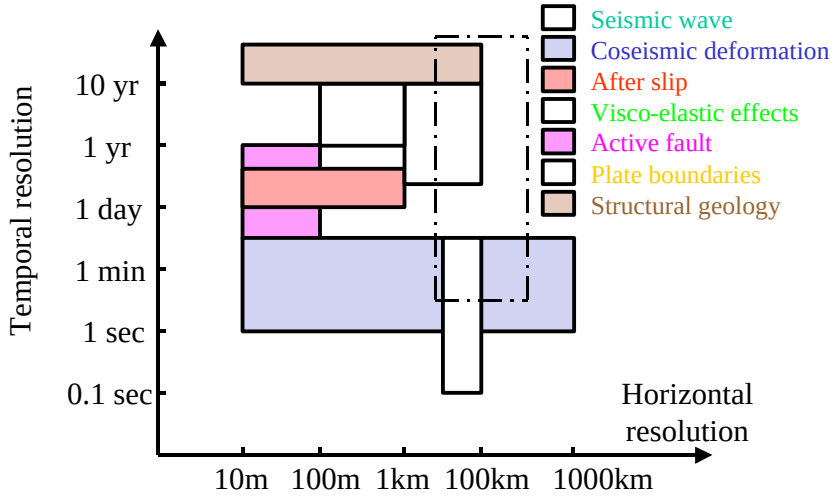

Figure 1.7 Resolution requirements of some geophysical and geological applications (various sources).

Moreover, although extreme care has always been taken in the selection of the site and the construction of the CGPS station, it is inevitable that some stations simply have to be deployed in harsh or non-ideal environments. For example, the strongly multipath-affected stations within the German CGPS network comprise about 20% of the total stations (Wanninger & Wildt, 1997). In the case of volcano monitoring, all the GPS receivers have to be placed on the slope or at the foot of the mountain. The only antenna site which may be free of multipath is the one on the summit, where there is often a great reluctance to install a receiver! Even for stations with a good antenna environment, multipath errors can become significant due to, for example, the accumulation of snow in winter (Hatanaka and Fujisaku, 1999) or ash during a volcanic eruption. For many geodynamic applications seeking mm-level accuracy, it is crucial to monitor this subtle change in the antenna environment, and try to mitigate its effects. Failure to correct for the multipath environment and to account for its change at a GPS site produces time-varying systematic errors in the CGPS data, which in turn degrades the accuracy of the results, and hence could lead to a misinterpretation of the results.

Therefore, this research is **not** just about pushing the temporal and spatial limits of Fig. 1.7. Techniques to improve and strengthen the CGPS results and to take advantage of GPS noises have been investigated as well.

1.6 Methodology

A possible solution to these problems is to **augment** the CGPS networks by exploiting the dual-frequency CGPS measurements themselves, or by integrating measurements from other geodetic techniques such as radar interferometry (InSAR) and, where available, Very Long Baseline Interferometry (VLBI) and Satellite Laser Ranging (SLR). **The current crustal deformation monitoring applications cannot benefit from the proposed GNSS modernizations to the same extent as many navigation applications. Therefore, augmentations specific to CGPS will have to be developed and tested. These augmentations, which are the focus of this thesis, have been developed and tested in several densification schemes.**

The first augmentation scheme is the 'serial temporal densification of CGPS'. As illustrated in Fig. 1.8, the sampling interval between the two successive measurements A1 and A2 at a current CGPS Station S would typically be:

T2 – T1 = 30 second

In this scheme, the measurements are temporally densified by adding extra measurements D1, D2, ... in a serial manner in order to address applications designed to resolve the high-frequency features of the crustal deformation, such as using GPS as a **seismometer**. The development and testing of this densification scheme based on the standard Real-Time Kinematic (RTK) GPS technique is described in Chapter 3.

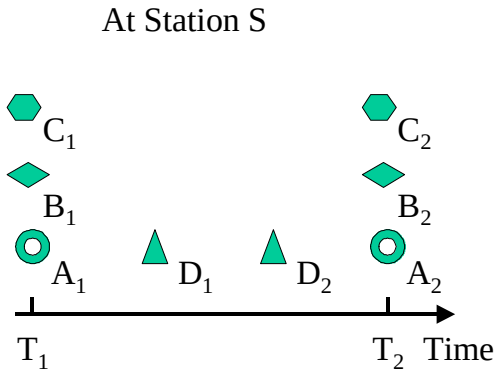

Figure 1.8 Temporal densification schemes.

The second augmentation scheme is the 'retro-active temporal densification'. Now consider Fig. 1.8, T2 stands for 'today' and T1 for 'yesterday'. A1 and A2 are the GPS measurement sequences (either pseudo-range or carrier phase) collected on the two days respectively. One of the biggest advantages of the CGPS technique is that the GPS receivers are operating 24 hours a day, 7 days a week. However, when the CGPS data is processed for deformation monitoring one always focuses on the *current* data (e.g. A2), and compares the *current* result with the *past* results in order to trace the evolution of the deformation. On the other hand, because the GPS antenna is not unidirectional it is often difficult to identify antenna sites which are not vulnerable to multipath. In other words, the GPS antenna, unlike the VLBI antenna, is very multipath "friendly". Since the geometry relating the GPS satellites and a specific receiver-reflector location repeats every sidereal day (because the CGPS antenna environment is constant), the multipath disturbance has a periodic characteristic and is repeated between consecutive days. Therefore, it is advisable to estimate the multipath effects in the **current** CGPS data (A2) from the **past** CGPS data (A1), and remove them from the current day's data (A2) before they are used in the GPS solution. This is, in fact, a 'retro-active temporal densification' to the current CGPS data (A1), that is

A2' = A2 - (A2@A1)

Where A2' is the corrected measurement sequence for Day T2; and @ is the operator that extracts the multipath component from the A1 and A2 measurements.

This densification scheme would provide a mechanism for the correction of multipath errors from the observation data (the RINEX files) themselves. Hence there is no need to change the operational mode of CGPS arrays. Using the data from the immediate past, the algorithms developed should be flexible enough to ensure the correction of multipath errors that vary seasonally as well. The development and testing of this densification scheme is discussed in Chapter 4.

The third augmentation scheme is referred to as 'all-GPS parallel temporal densification'. As mentioned earlier, measurements from at least four GPS satellites have to be used in order to solve for the three-dimensional position of the GPS antenna and the receiver clock offset. When using multipath effects as a *signal* to, for example, monitor the change of antenna environment, each GPS satellite can produce independent monitoring information concerning the antenna environment because multipath errors detected by the receiver is actually an interferometry between the direct and indirect GPS signals. Referring to Fig. 1.8 again, with this densification scheme at epoch T1, for example, there will be independent results A1, B1, C1, ... (as many as 9 or more for the GPS consetllation, each produced by an individual satellite). Chapter 5 describes the concept of the 'all-GPS parallel temporal densification'.

The fourth augmentation scheme is the referred to as 'cross-technique parallel temporal densification'. In recent years, space geodetic techniques such as GPS, VLBI, and SLR have been collocated to address many applications in geoscience. 'Cross-technique parallel temporal densification' requires the integration of the CGPS results with VLBI and SLR data. In other words, an appropriate fusion of these multi-technique space geodetic results must be developed. Whilst results from all these techniques are contaminated by various biases and errors, when GPS, VLBI and SLR instruments are installed at the same site, the same crustal displacement signature will be present as a common-mode signal, which can be extracted by an appropriate filter. Again, referring to Fig. 1.8, this scheme can be

understood by assuming that A1, A2, ... are the GPS results, whilst B1, B2, ... the VLBI results, and C1, C2, ... the SLR results. This scheme is discussed in Chapter 6.

So far all the augmentation schemes fall into the 'temporal densification' category. The next two augmentation schemes, however, are 'spatial densification' techniques. Spatial densification will augment CGPS's capability in resolving spatially high frequency features of crustal deformation. Moreover, even when the CGPS networks are densified in order to recover the signature of the deformation, the station configuration design may not be ideal. As shown in Fig. 1.9, suppose that all the measurements are taken at epoch T.

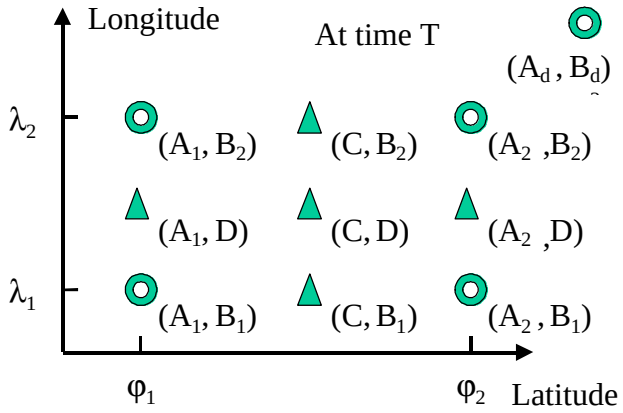

Figure 1.9 Spatial densification schemes.

The fifth augmentation scheme is 'soft spatial densification'. In this scheme CGPS is integrated with techniques such as differential Synthetic Aperture Radar Interferometry (InSAR) (the word "soft" is used because no additional GPS hardware installation is needed). Since data from CGPS arrays (GPS measurements collected at sites denoted by (Ai, Bj), where i, j = 1, 2 in Fig. 1.9) can be used to map tropospheric water vapour and ionospheric disturbances, these results can be used to remove atmospheric biases in InSAR. With the support of SLR and VLBI, GPS coordinates can be considered as being 'absolute' in the sense that they are tied to a well-defined terrestrial reference system. By assuming that there are no displacements at a few points (reference points) in a radar image, InSAR results are essentially relative measurements. GPS measurements on the reference points

(Ai, Bj) in a SAR image can also be used as constraints to mitigate the influence of SAR satellite orbit errors. On the other hand, InSAR, with its high spatial resolution (25m in the case of ERS-2), can be used to **densify** GPS results in a spatial sense. The densified measurements are (Ai, D), (C, Bj), and (C, D) in Fig. 1.9. Therefore, the CGPS and InSAR techniques are very complimentary. The integration of CGPS with InSAR is discussed in Chapter 7.

The sixth and last augmentation scheme is concerned with 'hard spatial densification' (the word "hard" is used because in this scheme additional GPS hardware has to be installed). 'Hard spatial densification' can be achieved either by deploying a sub-network of low-cost GPS receivers (located at (Ai, D), (C, Bj), and (C, D)), to in-fill the present CGPS arrays (located at (Ai, Bj) where i, j = 1, 2 in Fig. 1.9). This typically involves the integration of single-frequency and dual-frequency GPS receivers in a so-called '**inward hard spatial densification**'. Alternatively, by deploying receivers at some geophysically 'strategic' sites located at (Ad, Bd) outside the existing CGPS array located at (Ai, Bj), so that combinations of different baselines can be used to, for example, separate plate tectonic and seismic fault movements, in a so-called '**outward hard spatial densification**'. The development and testing of hard densification schemes is described in Chapter 8.

These augmentations can be used either independently or collectively, depending on the resources available in a CGPS array, and at a specific site. For example, the retro-densification and the all-GPS densification can be carried out at the same time; the retro-densification result can be used as an input to the GPS-VLBI-SLR cross-technique densification; the cross-technique densification results can be used instead of the GPS-only result in the soft densification with InSAR; the soft densification and the hard densification can verify each other; and so on.

This thesis consists of 9 chapters. This chapter presents the background to GPS and CGPS. The research motivation, the methodology, and contributions of this research work are also outlined. In Chapter 2 the mathematical basis for this research, the adaptive filter based on the least-mean-square algorithm, is developed. Chapters 3 to 8 deal with each of the CGPS

densification schemes outlined above. Chapter 9 contains the summary, conclusions and recommendations arising from this research.

1.7 Contributions of the Research

While 'augmentations' are often used for GPS navigation applications, this research systematically studies the augmentations to continuous GPS networks/processing for crustal deformation monitoring applications. The four temporal densification schemes based on: high rate GPS-RTK, GPS multipath effects, and collocated VLBI and SLR, to augment the CGPS networks are the most significant contributions of this research. In addition, the two spatial densification schemes are also important new findings. The contributions of this research can be summarized as follows:

- The 'serial temporal densification scheme', in an attempt to use GPS as a seismometer, has been developed and tested. Simulated seismic signals have been extracted from very noisy, high rate (10Hz and 20Hz) GPS-RTK results, using an adaptive filter based on the least-mean-square algorithm. The extracted results are in very good agreement with those of collocated traditional seismometers. The proposed technique can also be used for other applications, such as the monitoring of tsunami and the deformation of large engineering structures.

- The proposed 'retro-active temporal densification scheme' takes advantage of the fact that the GPS multipath disturbance has a periodic characteristic (and is repeated between consecutive sidereal days). This densification scheme provides a means of correcting for multipath errors in the observation data themselves.

- The proposed 'all-GPS parallel temporal densification scheme' uses the multipath effects as a *signal* to, for example, monitor any change in the antenna environment. Each GPS satellite contributes an accurate, independent measure of the surrounding environment, because the multipath detected by the GPS receiver is actually an

interferometry between the direct and indirect GPS signals. Models relating the change of multipath to a change in the antenna environment have been derived.

- The proposed 'cross-technique parallel temporal densification scheme' integrates collocated CGPS, VLBI and SLR results. Whilst results from all these techniques are contaminated by various biases and errors, when GPS, VLBI and SLR instruments are installed at the same site, the same crustal displacement signature presents as a common-mode signal.

- The proposed 'soft spatial densification scheme' integrates CGPS with the InSAR technique. The Double Interpolation and Double Prediction (DIDP) approach has been developed, and combines the advantage gained from high temporal resolution (of the CGPS measurements) and with the high spatial resolution (of the InSAR result) for the same region. DIDP can generate deformation monitoring products of high resolution, in both a temporal and spatial sense. Quality assurance measures have also been developed for DIDP.

- A 'hard spatial densification scheme' has been developed and tested. There are two scenarios. One involves the deployment of a sub-network of single-frequency GPS receivers to in-fill an existing CGPS array using concept known as '*inward hard spatial densification'*. The other requires the deployment of receivers at some geophysically strategic sites outside an existing CGPS array, in the form of an '*outward hard spatial densification'*. The 'inward hard spatial densification' has been demonstrated to be a cost-effective approach to improving the CGPS spatial resolution and to providing some redundancy in hazardous environments such as active volcanoes. In the case of 'outward hard spatial densification', receivers can be used more efficiently to form combinations of different baselines which can, for example, separate plate tectonic and seismic fault movements.

These augmentations can be used either independently or collectively depending on the resources available in a CGPS array and at a specific site.

2 ADAPTIVE FILTER AND ASSOCIATED SIMULATION STUDIES

Conventional signal processing systems for the extraction of information from an incoming signal operate in an open-loop fashion. That is, the same processing function is carried out in the *present* time interval regardless of whether that function produced the correct result in the *preceding* time interval. In other words, conventional signal processing techniques make the basic assumption that the signal degradation is a known and time-invariant quantity.

Adaptive processors, on the other hand, operate with a closed-loop (feedback) arrangement. The incoming signal *x(n)* is filtered or weighted in a programmable filter to yield an output *y(n)* which is then compared against a desired, conditioning or training signal, *d(n)*, to yield an error signal, *e(n)*. This error is then used to update the processor weighting parameters (usually in an iterative way) such that the error is progressively minimized (i.e., the processor output *y(n)* more closely approximates the desired signal *d(n)*). Such processors fall into the class of adaptive filters.

Adaptive filters, which are the mathematical basis of this research, are concerned with the use of a programmable filter whose frequency response or transfer function is altered, or adapted, to pass without degradation the desired components of the signal and to attenuate the undesired or interfering signals, or to reduce any distortion on the input signal. These adaptive filters are frequently used to recover signals from channels whose characteristic is time varying.

Much of the early work on adaptive filters was arrived at by independent study in different organizations. Notable early developments occurred at the Technische Hochschule Karlsruhe in Germany and at Stanford University, where adaptive pattern recognition systems were initiated in 1959 (Rudin, 1967). Collaboration in 1964 between these institutions produced a comparative evaluation of their respective techniques which

subsequently led to the development of the most widely used algorithm for processor weight adjustment. Further relevant work was being conducted simultaneously at the Institute of Automatics and Telemechanics in Moscow. Now applications of adaptive filters can be found in such diverse fields as speech analysis, seismic, acoustic, and radar signal processing, and digital filter design (e.g. Haykin, 1996; Proakis & Mandakis, 1996; Solo & Kong, 1995).

2.1 The Adaptive Filter

An adaptive filter used for noise suppression is a dual-input, closed-loop adaptive feedback system. The operation of such an adaptive filter involves two basic processes: 1) a filtering process to produce an output in response to an input sequence; and 2) an adaptive process for the control of adjustable parameters used in the filtering process.

In the present application the dual-inputs to the adaptive filter are the primary input $d(n)$ and the reference input $x(n)$, which have sample size (vector length) N. The primary input $d(n)$ consists of the desired signal of interest $s(n)$ buried in (or contaminated by) noise $x'(n)$, that is

$$d(n) = s(n) + x'(n) \tag{2.1}$$

The reference input $x(n)$ supplies noise alone. In order to obtain a relatively noise-free signal using the adaptive filter output, $s(n)$, $x'(n)$, and $x(n)$ have to satisfy the following conditions:

1) the signal and noise in the primary input are uncorrelated with each other, that is

$$E[s(n)x'(n-k)] = 0 \quad n,k=0, \ldots, N-1 \tag{2.2}$$

Where $E[\ .\ ]$ denotes the expectation operator.

2) the noise in the reference input is uncorrelated with the signal $s(n)$ but is correlated with the noise component of the primary input $x'(n)$, that is

$$E[s(n)x(n-k)] = 0 \quad n,k=0, \ldots, N-1 \tag{2.3}$$

and

$$E[x(n)x'(n-k)] = p(k) \quad n,k=0, \ldots, N-1 \tag{2.4}$$

where $p(k)$ is an unknown cross-correlation for lag k.

2.2 The Filter Design

There are several types of programmable filters that can be used in the design of the adaptive filters. Here two basic filter designs are introduced briefly.

The most generalized digital filter structure is the recursive filter design, which comprises both feedforward and feedback multipliers, whose weight are controlled by some coefficients. The response of this filter is governed by the difference equation which shows that the value of the present filter output sample is given by a linear combination of the weighted present and past input samples as well as the previous output samples. This structure results in a pole-zero filter design where the pole locations are controlled by the feedback coefficients and the zero locations by the feedforward coefficients. The number of poles and zeros, or order of the filter, is given by the number of delay stages.

This recursive structure has theoretically an infinite memory and hence it is referred to as an infinite impulse response (IIR) filter design. It is not unconditionally stable unless restrictions are placed on the values of the feedback coefficients. However, the inclusion of poles as well as zeros makes it possible to realize sharp cutoff filter characteristics incorporating a low transition bandwidth with only a modest number of delay stages (i.e., low filter complexity). One drawback of the IIR design is that no control is offered on the phase (group delay) response of the filter. However, the major problem with adaptive IIR filter design is the possible instability of the filter due to poles straying outside the stable region.

One way to overcome the drawback of potential instability in the filter is to design an all-zero filter which uses only feedforward multipliers and is unconditionally stable (Fig. 2.1). This has only a limited memory, which is controlled by the number of delay stages and it results in the finite impulse response (FIR) filter design. The input signal is delayed by a number of delay elements, which may be continuous but usually are restricted to discrete

values. The outputs of these time-delay elements are subsequently multiplied by a set of stored weights and the products summed to form the output signal. This implies that the output is given by the convolution of the input signal with the stored weights or impulse response values. This filter incorporates only zeros (as there are no recursive feedback elements) and hence a large number of delay elements are required to obtain a sharp cutoff frequency response. However, the filter is always stable and can provide a linear-phase response.

Therefore, the Finite-duration Impulse Response (FIR) filter (Haykin, 1996), which is also known as a tapped-delay line filter, transversal filter, all-zero filter, or moving-average filter, is employed in this application due to its stability, versatility and ease of implementation.

As indicated in Fig. 2.1, the FIR consists of three basic elements:

- the unit-delay elements identified by the unit-delay operator z^{-1}, where the number of elements M refers to the filter length (its order is M-1);
- the multipliers, whose function is to multiply the tap input by a filter coefficient (tap weight); and
- the adders, which sum the individual multiplier outputs and yield an overall filter output:

$$y(n) = \sum_{i=0}^{M-1} \hat{w}_i(n)x(n-i) \qquad (2.5)$$

where M is the length of the adaptive FIR filter, $\hat{w}_i(n)$ denotes a time-varying transfer function (tap weight), which changes, or adapts, according to signal conditions, under the control of an algorithm which will be described in the next section.

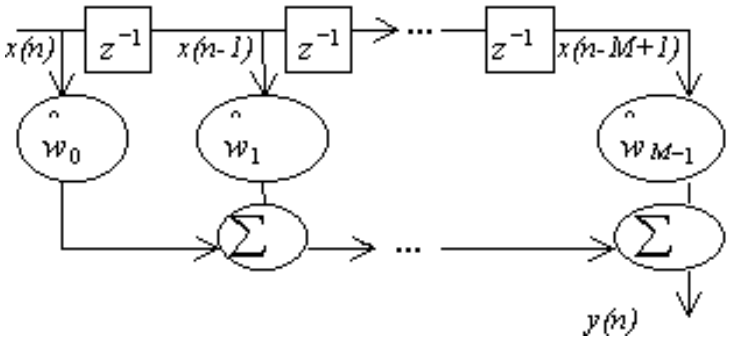

Figure 2.1 The FIR filter scheme.

2.3 The Adaptive Algorithm Design

In an adaptive system an absolute minimum of a priori information is necessary about the reference signal. The adaptive filter operates by estimating the statistics of the reference signal and adjusting its own response in such a way as to minimize some 'cost function'. This cost function may be derived in a number of ways depending on the intended application, but normally it is derived by the use of the primary (or desired) signal. The most commonly used cost function is the least-mean-squares (LMS) function. Alternatives are functions such as modulus of error and nonlinear threshold functions. The task of the adaptive algorithm is to adjust the weights in the programmable filter in such a way as to minimize the difference or error *e(n)* between the processor output *y(n)* and the primary input *d(n).*

Many methods exist to adjust the filter weight values to obtain the optimum solution. Random perturbation techniques have been applied, where the weights are altered and the output is examined to ascertain whether the random perturbation moves it toward or away from the desired solution. The least-mean-square (LMS) algorithm was first formally reported by Widrow (1971). It is now widely applied to the calculation of the adaptive filter weights, as it uses gradient search techniques, which converge toward the optimum solution much more efficiently than do other algorithms. It will be shown that this algorithm can maximize signal-to-noise ratio.

From Eqs. (2.1) and (2.5), the estimation error:

$$e(n) = d(n) - y(n) = s(n) + x'(n) - y(n) \tag{2.6}$$

is used to design an algorithm for the control of the FIR filter.

Using Eqs. (2.5) and (2.6), the mean square error (MSE) can be expressed as:

$$J = \sum_{n=0}^{N-1} e^2(n)$$

$$= \sum_{n=0}^{N-1} [d(n) - \sum_{i=0}^{M-1} \hat{w}_i(n) x(n-i)]^2$$

$$= \sum_{n=0}^{N-1} [d^2(n) - 2d(n) \sum_{i=0}^{M-1} \hat{w}_i(n) x(n-i) + \{\sum_{i=0}^{M-1} \hat{w}_i(n) x(n-i)\}^2]$$

Assume that $\hat{w}_i(n)$ can be approximated as constant with respect to n. Then we have:

$$J = \sum_{n=0}^{N-1} d^2(n) - 2\sum_{i=0}^{M-1} \hat{w}_i(n) r_{dx}(i) + \sum_{i=0}^{M-1} \sum_{l=0}^{M-1} \hat{w}_i(n) \hat{w}_l(n) r_{xx}(i-l) \tag{2.7}$$

where

$$r_{dx}(i) = \sum_{n=0}^{N-1} d(n) x(n-i) \tag{2.8}$$

$$r_{xx}(i) = \sum_{n=0}^{N-1} x(n) x(n+i) . \tag{2.9}$$

To minimize the MSE, J is partially differentiated with respect to the tap weights of the FIR filter:

$$\frac{\partial J}{\partial \hat{w}_i(n)} = 0$$

which is equivalent to:

$$\sum_{l=0}^{M-1} \hat{w}_l(n) r_{xx}(i-l) = r_{dx}(i),\ i=0, \ldots, M\text{-}1 \qquad (2.10)$$

This yields the set of linear equations that generate the optimum filter coefficients at time n. To solve the equations, both the auto-correlation sequence $\{r_{xx}(i)\}$ of the reference sequence $\{x(n)\}$ and the cross-correlation sequence $\{r_{dx}(i)\}$ between the primary sequence $\{d(n)\}$ and the reference sequence $\{x(n)\}$ are required.

The signal *s(n)* is part of the error signal *e(n)* and the noise component in the adaptive filter output is *x'(n)* - *y(n)*, as indicated in Eq. (2.6). While *s(n)* is essentially unaffected by the filter, minimizing *E* is equivalent to minimizing the output noise *x'(n)* - *y(n). Therefore, the signal-to-noise ratio of the output signal is maximized.*

There are two special cases when applying the adaptive filter:

1) The adaptive filtering is perfect when *y(n) = x'(n)*, and in this case the system output is noise-free, as can be seen from Eq. (2.6).

2) The adaptive filtering will be switched off automatically, as can be seen from Eq. (2.10), when the reference signal *x(n)* is completely uncorrelated with both the signal *s(n)* and the noise component *x'(n)* of the primary signal *d(n)*, i.e., $E[d(n)x(n-k)] = 0$ for $n,k=0, \ldots, N-1$. In this case, the primary signal is left intact and the output signal-to-noise ratio remains unchanged.

2.4 The Real-time Implementation of the Adaptive Filter

As mentioned above, in order to solve the equations, both the auto-correlation sequence $\{r_{xx}(i)\}$ of the reference sequence $\{x(n)\}$ and the cross-correlation sequence $\{r_{dx}(i)\}$

between the primary sequence {*d(n)*} and the reference sequence {*x(n)*} have to be calculated, which is almost impossible in real-time applications. Therefore the simplified least-mean-square (LMS) algorithm has been introduced as an alternative computational method to adaptively adjust the coefficients (weights) of an FIR filter, $\hat{w}_i(n)$, as in the following equation (tap-weight adaptation):

$$\hat{w}_i(n) = \hat{w}_{i-1}(n) + \mu\, e(n)x(n-i) \qquad (2.11)$$

where μ is the step-size parameter, i = 0, …., M-1 and n = 0,…,N-1.

In order to facilitate the comparison of Eqs. (2.10) and (2.11), the following matrix-vector notations are defined:

$\mathbf{X}^T(n) = [x(n)\ x(n-1)\ ...\ x(n-M+1)]$

$\mathbf{W}^T(n) = [\hat{w}_0(n)\ \hat{w}_1(n)\ ...\ \hat{w}_{M-1}(n)]$

$\mathbf{P} = E[d(n)\ \mathbf{X}(n)]$

$\mathbf{R} = E[\mathbf{X}(n)\mathbf{X}^T(n)]$

where the matrix transpose is defined by the superscript T.

Then Eqs. (2.5) and (2.6) can be rewritten as:

$$y(n) = \mathbf{W}(n)\ \mathbf{X}^T(n) = \mathbf{X}(n)\ \mathbf{W}^T(n) \qquad (2.5a)$$

$$\begin{aligned} e(n) &= d(n) - \mathbf{W}(n)\ \mathbf{X}^T(n) \\ &= d(n) - \mathbf{X}(n)\ \mathbf{W}^T(n) \end{aligned} \qquad (2.6a)$$

The cost function (or performance function) expressed in Eq. (2.7) can be rewritten as:

$$\begin{aligned} J &= E[e^2(n)] \\ &= D - 2\,\mathbf{W}^T(n)\mathbf{P} + \mathbf{W}^T(n)\,\mathbf{R}\mathbf{W}(n) \end{aligned} \qquad (2.7a)$$

where D is the expected power of d(n):

$D = E[\,|d(n)|^2]$

Note that J is a quadratic function of the weight vector **W**(n). The gradient of J becomes:

$$\frac{\partial J}{\partial W} = 2\ (\mathbf{RW}(n) - \mathbf{P}) \qquad (2.8a)$$

The solution of the optimal weight vector $\mathbf{W}_{opt}$ can be obtained by:

$$\frac{\partial J}{\partial W} = 0$$

i.e.,

$$\mathbf{W}_{opt} = \mathbf{R}^{-1}\mathbf{P} \qquad (2.10a)$$

On the other hand, the real-time LMS algorithm is using the squared-error as the cost function, i.e.,

$$G = e^2(n)$$

The gradient of G becomes:

$$\frac{\partial G}{\partial W} = 2\, e(n) \frac{\partial e(n)}{\partial W}$$

$$= -2\, e(n)\, \mathbf{X}(n)$$

This instantaneous gradient has been used in the real-time version of LMS to form an adaptive filtering algorithm which approximate a true gradient search of the cost function in the following:

$$\mathbf{W}(i) = \mathbf{W}(i-1) + \mu e(i)\, \mathbf{X}(i) \qquad (2.11a)$$

Note that

$$E\left[\frac{\partial G}{\partial W}\right] = E[-2\, e(n)\, \mathbf{X}(n)]$$

$$= 2\, E[\, -(d(n) - \mathbf{W}(n)\, \mathbf{X}^T(n))\, \mathbf{X}(n)]$$

$$= 2\ (\mathbf{RW}(n) - \mathbf{P})$$

$$= \frac{\P\ J}{\P\ W}$$

Thus the expected value of the approximate gradient equals the true gradient. Therefore, it has been shown that the LMS algorithm expressed in Eq. (2.11) can minimize the sum of squared errors as in the case of Eq. (2.10). Evidence has also been presented on the model-independence, and hence robust performance of the LMS algorithm (Solo & Kong, 1995), making the LMS algorithm the most widely known and used adaptive algorithm.

2.5 Evaluation of the LMS Algorithm

In this section, the solutions developed earlier for the optimal weight vector are used to add some intuitive insight into what the cost function J means and how the optimal weight vector depends on the characteristics of x(n) and d(n).

From Eqs. (2.7a) and (2.10a), the minimum value of J as the weight vector satisfies the normal equation can be found as:

$$J_{min} = D - 2\,\mathbf{W}^T_{opt}\,\mathbf{P} + \mathbf{W}^T_{opt}\,\mathbf{R}\mathbf{W}_{opt}$$

$$= D - 2\,\mathbf{W}^T_{opt}\,\mathbf{P} + \mathbf{W}^T_{opt}\,\mathbf{P}$$

$$= D - \mathbf{W}^T_{opt}\,\mathbf{P}$$

Thus the minimum value of J depends on D (the power or energy of d(n)), on the optimal weight vector $\mathbf{W}_{opt}$ and on P (the cross-correlation between d(n) and **X**(n)).

Given this minimum value, it is interesting to konw how large a price in performance is paid by not using the optimal vector. In particular, let **W**(n), the actual weight vector, be defined by:

$$\mathbf{W}(n) = \mathbf{W}_{opt} + \mathbf{V}$$

Where **V** is an M-dimensional vector representing the difference between **W**(n) and $\mathbf{W}_{opt}$. Substituting this value of **W**(n) into Eq. (2.7a), we find that:

$$J = D - 2(\mathbf{W}^T_{opt} + \mathbf{V}^T)\mathbf{P} + (\mathbf{W}^T_{opt} + \mathbf{V}^T)\mathbf{R}(\mathbf{W}_{opt} + \mathbf{V})$$
$$= D - 2\mathbf{W}^T_{opt}\mathbf{P} + \mathbf{W}^T_{opt}\mathbf{R}\mathbf{W}_{opt} - 2\mathbf{V}^T\mathbf{P} + \mathbf{W}^T_{opt}\mathbf{R}\mathbf{V} + \mathbf{V}^T\mathbf{R}\mathbf{W}_{opt} + \mathbf{V}^T\mathbf{R}\mathbf{V}$$
$$= J_{min} - 2\mathbf{V}^T\mathbf{P} + \mathbf{P}^T\mathbf{V} + \mathbf{V}^T\mathbf{P} + \mathbf{V}^T\mathbf{R}\mathbf{V}$$
$$= J_{min} + \mathbf{V}^T\mathbf{R}\mathbf{V}$$

This is the key result and forms the basis for much intuition about optimal squared error filters. It states that any excess squared error is a quadratic function of the difference between the actual weight vector $\mathbf{W}(n)$ and the optimal one $\mathbf{W}_{opt}$. Because $\mathbf{V}^T\mathbf{R}\mathbf{V}$ is never negative, J_{min} is in fact the minimum attainable value. For most well-behaved problems $\mathbf{V}^T\mathbf{R}\mathbf{V}$ is always positive for nonzero $\mathbf{V}$, meaning that any difference between $\mathbf{W}(n)$ and $\mathbf{W}_{opt}$, hence nonzero $\mathbf{V}$, will result in J being greater than the minimum possible value. Note that the penalty for poor choice of $\mathbf{W}(n)$ depends only on the reference input x(n) and not on the primary input d(n). Thus the character of the reference input affects the nature of the solution. Therefore, it is vital to choose an appropriate signal as the reference input.

2.6 Implementing Issues of the Adaptive Filter

However, special attention has to be paid to two closely related issues: the choice of suitable value for the step-size parameter m , and the filter length M.

1) It is important to select an appropriate m which controls the rate of convergence of the LMS algorithm to the optimum solution. The larger the m selected, the faster the convergence. However, too large a value of m may result in the LMS algorithm becoming unstable. To ensure stability, m should be in the range (Proakis, 1995):

$$0 < m < \frac{1}{10MPx} \qquad (2.12)$$

where M is the length of the adaptive FIR filter and Px is the power of the reference signal, which can be approximated by:

$$Px \approx \frac{1}{1+M}\sum_{n=0}^{N-1} x^2(n) = \frac{r_{xx}(0)}{M+1} \qquad (2.13)$$

where $r_{xx}(0)$ is the auto-correlation function of the reference sequence for zero lag.

2) The filter length (i.e., the number of independently adjusted parameters in the filter) should be selected so that the filter best models the regular features of a set of input data. The Minimum Description Length (MDL) criterion (Haykin, 1996) has been employed in this application. It is defined as:

$$MDL(M) = - L(\hat{q}_M) + \tfrac{1}{2} M \ln N \qquad (2.14)$$

where M is the filter length, N is the length of the input sequence, and $L(\hat{q}_M)$ is the logarithm of the maximum likelihood estimates of the filter parameters. The first term in the above equation tends to decrease rapidly with increasing M, while the second term increases linearly with increasing M. Therefore there is a value of M which can minimize MDL, representing the optimum length of the filter.

2.7 Adaptive Filtering of Simulated Data

When the FIR filter and the adaptive algorithm are integrated, an adaptive filter as shown in Fig. 2.2 is obtained. In this section, numerical simulation data are used to explore the features of such an adaptive filter, before applying it to the processing of CGPS results.

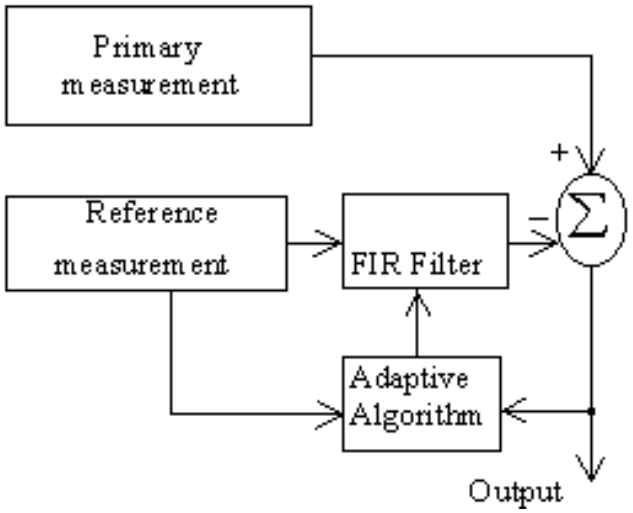

Figure 2.2 Adaptive filtering configuration.

Though ideally "true" noise has to be used as a reference signal in order to cancel it from the primary signal as discussed in previous sections, to derive true noise is as difficult as deriving a true signal for many practical applications. In fact, there are no fundamental differences between "signal" and "noise", except that a "signal" is a desired output and a "noise" is an undesired one. To address practical applications of the adaptive filter it is necessary to introduce the terms "coherent component" and "incoherent component" when discussing the compositions of the primary and reference signals. A "coherent component" is a composition of the primary signal which is correlated with a composition of the reference signal, while an "incoherent component" is a composition of the primary signal which is uncorrelated with any composition of the reference signal. In Fig. 2.2, the "coherent component" is the direct output of the FIR filter, and the "incoherent component" is the output of the whole adaptive filtering system.

In the case of CGPS measurements, the time series on a selected day can be expressed as:

$$r(n) = s'(n) + x'(n) \qquad (2.15)$$

where $s'(n)$ is the crustal deformation (signal free of multipath, etc.) and $x'(n)$ is the noise contribution respectively. And n is the epoch number.

The time series on the next day is expressed as:

$$d(n) = s(n) + x(n) \qquad (2.16)$$

where $s(n)$ and $x(n)$ are analoguous to $s'(n)$ and $x'(n)$.

From previous studies (e.g. Han & Rizos, 1997), $x(n)$ and $x'(n)$ are highly correlated in terms of multipath in nearly static antenna environments. But $s(n)$ and $s'(n)$ are uncorrelated, which means that the adaptive filtering conditions are only partially satisfied (a correlation between $s(n)$ and $s'(n)$ may become detectable in some stations caused, for example, by temperature expansion). In this case, can the adaptive filter be used to remove noise such as multipath from the results of the second day by employing the results of the first day as a reference signal?

As discussed in previous sections, and also in Ge (1999), there are two special cases to be considered in the application of an adaptive filter. Eq. (2.15) can be treated as a linear combination of the two cases. Therefore, theoretically it is possible to mitigate noise such as multipath by using CGPS results of two adjacent days as inputs to an adaptive filter.

Numerical simulation studies are carried out in order to demonstrate the feasibility of such filter schemes, and to explore some of the characteristics of the adaptive filter. In the first simulation both the reference (r(n)) and primary (d(n)) signals are composed of two sine waves, and all the components of r(n) and d(n) are uncorrelated:

r(n) = 10 cos(np/8+2)+25 cos(np/3);

d(n) = 25 cos(np/10+p)+10 cos(np/5);

where π=3.14159; *r(n)* and *d(n)* are in mm; n is the sample number and the sampling interval is 1 second.

Fig. 2.3 is the result of this simulation. It can be seen from both the time series and their Fast Fourier Transform (FFT) spectrum that although the coherent component is not zero, as it should be, the incoherent component is indeed left intact. Please note that the vertical scales of the coherent component plots are –5 to 5 for amplitude and 0 to $4*10^3$ for the FFT power respectively.

In the second simulation both the reference (r(n)) and primary (d(n)) signals are composed of two sine waves and the 0.05Hz component $25*\cos(n*\pi/10+\pi)$ in d(n) is introduced as the coherent component, and the 0.1Hz component $10*\cos(n*\pi/5)$ as the incoherent component (note also that the phase difference *p - 2* has been introduced on purpose between the two coherent components in *d(n)* and *r(n)*):

*r(n) = 10*cos(n*p/10+2)+25*cos(n*p/3);*

*d(n) = 25*cos(n*p/10+p)+10*cos(n*p/5);*

Fig. 2.4 is the result of this simulation. It can be seen from both the time series and their FFT spectrum that the coherent and the incoherent components of d(n) are successfully separated, despite that there is a phase difference between the two coherent components in *d(n)* and *r(n).*

To summarize the numerical simulation results, a truth table for adaptive filtering is presented in Table 2-1. From the table it can be concluded that the adaptive filter can be used as a powerful signal decomposer (analyser).

Table 2-1 Truth table for adaptive filtering.

Primary & reference	x, x' uncor. s, s' corr.	x, x' corr. s, s' uncorr.	x, x' uncor. s, s' uncorr.
Coherent	s	x	$\cong 0$
Incoherent	x	s	s+x

In the following chapters, the adaptive filter based on the least-mean-square algorithm will be used in various CGPS densification schemes.

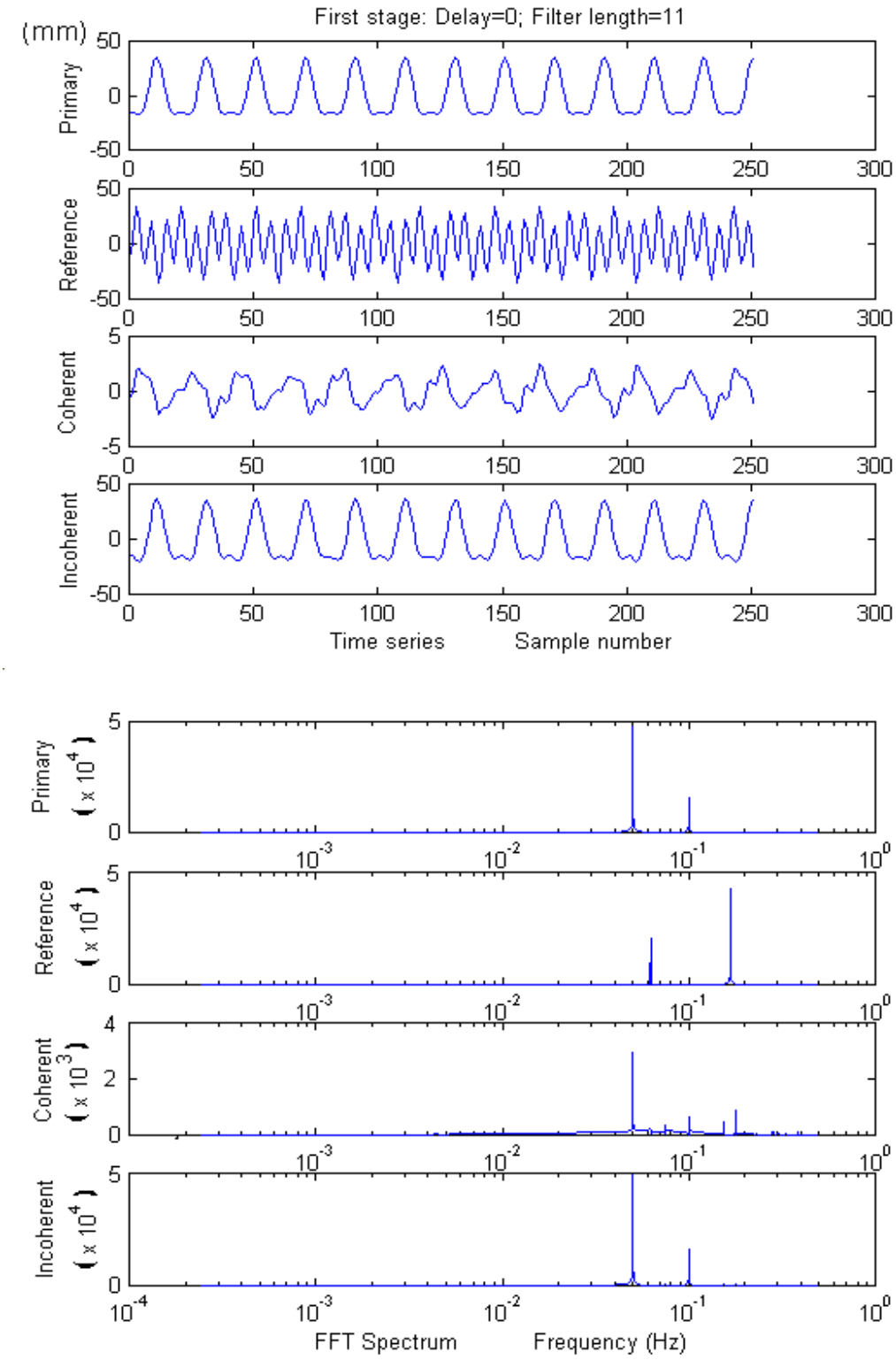

Figure 2.3 Numerical simulation result of adaptive filtering of uncorrelated signals.

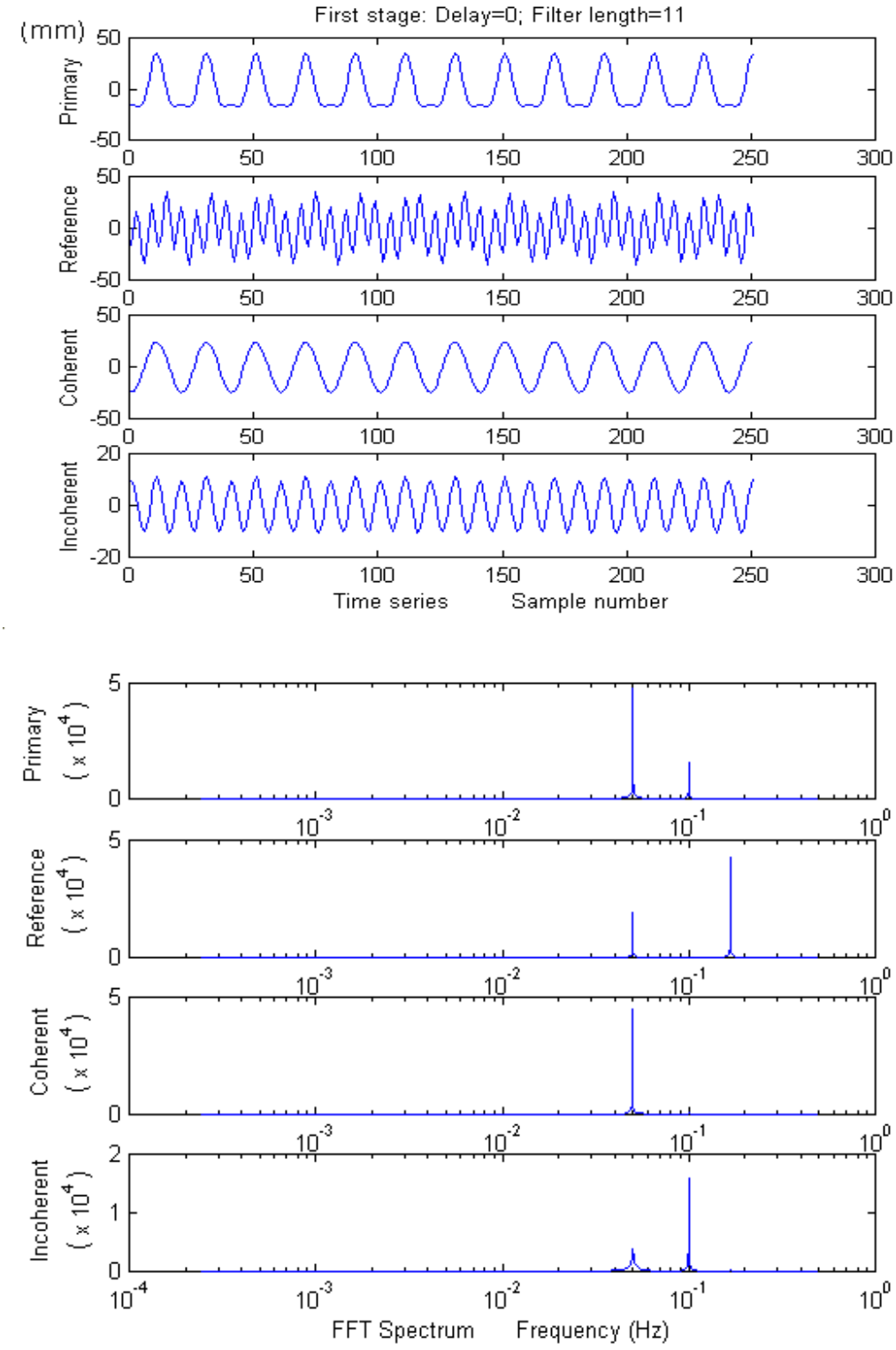

Figure 2.4 Numerical simulation result of adaptive filtering of partially correlated signals.

3 SERIAL TEMPORAL DENSIFICATION – THE 'GPS SEISMOMETER'

Serial temporal densification is realised by increasing the data sampling rate of GPS receivers and applying appropriate signal filtering techniques. It is typical that GPS receivers in CGPS networks typically make one set of measurements every 30 seconds. However, it is comparatively easy to increase this data rate to one sample per second (1Hz), since all currently deployed GPS receivers can support this rate (though the volume of data will be increased substantially!). Refer to Fig. 1.7 again, this 1Hz rate is equivalent to extend the dashed-line rectangle (the coverage of the current CGPS) in the negative direction of the vertical axis to 1 second. If it has to be further extended to 0.1 second, new receivers such as the Leica CRS1000 or Trimble MS750 would have to be introduced to satisfy the 10-20Hz sampling rate requirement for the detection of ground motion due to e.g. seismic waves (Ge, 1999).

Even with high sampling rates, the challenge still is to resolve the very weak signal from the noisy ‘kinematic' GPS solutions. This Chapter, focusing on the temporal densification and using the GPS seismometer concept to facilitate the discussion, starts with an introduction to GPS Real-Time Kinematic (RTK) applications. Two experiments are described in detail, that demonstrate a serial temporal densification scheme using the GPS RTK system as a 'GPS seismometer'. The last section of this Chapter discusses the implemention issues involved in using GPS as a seismometer.

3.1 GPS Real-Time Kinematic (RTK) Applications

3.1.1 Standard RTK

The standard GPS Real-Time Kinematic (RTK) technique is a relative (differential) positioning procedure whereby carrier phase measurements (or corrections) are transmitted in real-time from a reference or base station to a user's mobile receiver. Centimetre

accuracy is achieved without the need to record and post-process double-differenced carrier phase observables. The resolution of the carrier cycle ambiguities on-the-fly (OTF) is the key to modern RTK techniques. Due to the fact that atmospheric conditions can change rapidly, residual ionospheric and tropospheric biases (remaining after double-differencing the data) will grow in magnitude with increasing receiver separation. Hence the typical 'allowable' distance between user and base station receivers for OTF-RTK is only up to 10km. In the case of an instrument like the MS750 (Trimble, 2000), the stated accuracy is 1 cm+2ppm horizontal and 2cm+2ppm vertical in the so-called 'synchronized' RTK mode, and 2cm+2ppm horizontal and 3cm+2ppm vertical when used in the low latency mode. As will be seen in Section 3.5.1, this limitation is a serious concern when attempting to implement a 'GPS seismometer' based on the RTK positioning mode.

3.1.2 Network RTK (the Virtual Reference Station concept)

Standard (or traditional) GPS-RTK positioning is limited with respect to the distance between the reference station and the user receiver. CGPS networks such as the GEONET are able to provide services for traditional RTK positioning, but only because the residual systematic biases are relatively small due to the fact that the network of reference stations is very dense. However, the desired density of reference stations is a function of such factors as the 11 year solar sunspot cycle, with interstation distances being allowed to increase during solar minima, and decrease during solar maxima.

The concept of 'virtual reference stations' (VRS) is an effective way of eliminating/reducing systematic errors in reference station data, and hence allows for an increase in the distance between CGPS reference stations, while increasing the reliability of the RTK technique and reducing the initialization time. The 'virtual reference station' concept was first commercialized in Spectra Precision's GPS-Network software (Terrasat, 2000), although there have been many trials of similar systems over the last five years. Such network-based RTK systems require continuous modem line connections between the control centre and

all reference stations. GPS raw data is transmitted continuously to the centre. The control centre then performs the following standard tasks:

- Data archiving of all receivers in the RINEX format;
- Compression of RINEX files if required;
- Data quality analysis of the received GPS data;
- Visualization of remote station status; and most importantly
- Continuous computation of the systematic errors (mainly ionospheric biases, tropospheric biases, ephemeris errors and carrier phase ambiguities for L1 and L2) by analyzing the double-differenced carrier phase observations.

From these network results the interpolated systematic error for a specific user within the area defined by the reference station network can be estimated. The estimated systematic error when applied to the RTK processing overcomes the problems of distance-dependent errors. The interpolation requires an approximate position of the user receiver. The standard NMEA strings of the GGA message, which all major receivers provide, can be used for this purpose (it is a basic navigation solution using pseudo-range data). Hence, any off-the-shelf single- or dual-frequency GPS receiver capable of performing RTK positioning can be used without modification. From this position an 'optimized' RTCM data stream can be generated and input to the user receiver. Because this process is equivalent to creating raw reference station data for the approximate user position, it is often referred to as the "Virtual Reference Station (VRS)" technique. With these optimized RTCM messages it is possible to perform improved RTK positioning within the reference station network. Yet another approach is to simply create the VRS raw data itself. Position errors of 1-3cm horizontal and 4-6cm vertical using reference stations spaced at distances of approximately 50 km have been reported by Bücherl et al. (2000). Better accuracy for VRS-RTK is expected with advancs in receivers and orbit products (such as the use of IGS Ultra rapid products (IGSCB, 2000)). Another advantage of the VRS is the almost uniform accuracy, regardless of the distance of the user from any one reference station.

A VRS-RTK system connecting 85 stations from Switzerland, Finland, Sweden, and Germany is currently operating (Terrasat, 2000). A system implementing the Virtual Reference Station concept, Internet-connected reference station network and TV sound multiplexed sub-carrier data link has also been tested in Tokyo, Japan (Petrovski et al., 2000). This network covers a region of approximately 100 km in radius. Many more VRS-RTK system are likely to be installed in several regions and cities over the next few years.

As will be seen in Section 3.5.1, the VRS-RTK provides a good basis for implementing a 'GPS seismometer' based on the RTK technique.

3.2 GPS Seismometer – an Overview

The large near-field displacements before and during an earthquake are invaluable information for earthquake source study and for the detection of slow/silent quakes or pre-seismic crustal deformation events. However, none of the current seismometers can measure large near-field displacements directly. Typically, a seismometer (or seismograph) employs a pendulum to record seismic waves, because an "ideal pendulum" always stays in its original position regardless of the movements of the seismometer. Because the GPS satellites are not affected by earthquakes, the GPS constellation can be considered an "ideal pendulum". Therefore, a GPS receiver on the Earth can be used as a seismometer if its sampling rate is high enough to recover the signature of the antenna displacement.

Accurate time synchronization for seismic networks is vital for the determination of earthquake hypocentres. With no exact time, the seismic records are, as a rule, useless. Therefore, GPS has been widely used for accurate time-stamping of data collected by seismic networks. However, only recently have GPS receivers achieved very high data sampling rates. State-of-the-art GPS receivers with 10 to 20Hz sampling rates are now available (Leica, 2000; Timble, 2000). This means that such GPS receivers may be able to reproduce signals with frequencies from 0 HZ to (say) 10Hz, which is already compatible with some current seismic networks such as TERRAscope, a wide dynamic range, broad-

band (10 Hz to 0 HZ) seismographic network funded by the L. K. Whittier, ARCO Foundation and NSF/ARI, USA (Caltech, 2000). Hence, the concept of a 'GPS seismometer' appears feasible.

Is there a need for a 'GPS seismometer'? The largest amplitude of vibration accompanying an earthquake reported so far is 180mm for the 1923 Tokyo Quake, and the fault displacements associated with the largest earthquakes are of the order of 30m (Turcotte, 1982). Despite advancements in seismometer design, it is now still true, as Dr. Branson has claimed, that “Very probably, there have been earthquakes of larger movements which our seismographs were unable to record” (Branson & Tarr, 1952). As a matter of fact, though great efforts have been made to develop highly dynamic seismometers using the latest electronic technology, direct measurement of large co-seismic displacements with a flat frequency response remains elusive. The result is likely to be an under-estimation of earthquake sources. The development of a 'GPS seismometer' is therefore an option worth considering.

The first experiment concerning GPS seismometers was reported as early as 1994. It was carried out by the Disaster Prevention Research Institute (DPRI), Kyoto University, Japan (Hirahara et al., 1994). The experiment was performed at a user site equipped with a GPS antenna on a slider, and two reference sites at distances 160m and 160km away from this site. The slider oscillated horizontally with periods of 25-300sec and amplitude of 15cm. The sampling interval of the receivers was 1sec. A horizontal accuracy of 1-2cm was achieved in post-processing, and it was concluded that using GPS as a strain seismometer to obtain large amplitude, near-field ground motion was possible.

Another GPS seismometer experiment was carried out by the Geographical Survey Institute (GSI) of Japan, involving the kinematic processing of some GEONET data to derive ground motion due to the 4 October 1994, M8.1 Hokkaido-Toho-Oki earthquake (Hatanaka et al., 1994). The sampling rate of this continuous GPS (CGPS) data was 30sec. The P-wave arrival was successfully resolved in this case. Again, the experiment suggested the feasibility of a GPS seismograph if the receiver can observe with a high enough sampling

rate. Even at the 30sec sampling rate, GPS could detect slow/silent quakes or pre-seismic events. Short-term afterslip in the 1994 Sanriku-Haruka-Oki earthquake was an example of slow earthquake detection by GPS with 30 sec samling rate (Heki & Tamura, 1997). One Hz sampling GPS was also proposed to be used as an ultra-long-period seismograph by Miyazaki et al (1997).

On 11 November 1998 a GPS seismometer experiment was conducted at the University of New South Wales (the UNSW Experiment, see Section 3.3) (Ge, 1999). In that experiment two Leica CRS1000 receivers were used in the single-baseline RTK mode. One functioned as the mobile rover, the other as the reference receiver, both sampling at 10Hz. The sine-waves of 2.3Hz and 4.3Hz on the GPS antenna were generated using a mechanical shaker with amplitude of up to 12.7mm to simulate seismic waves. The signals as well as their harmonics and aliasing were resolved easily from the power spectrum of the RTK time series (even for the height component), although the time series itself was very noisy.

On 10 August 1999 a joint experiment between the University of New South Wales (UNSW) and the Meteorological Research Institute (MRI) (the UNSW-MRI Experiment, see Section 3.4) was performed in Tokyo, Japan. In the experiment, two Trimble MS750 GPS receivers were used in the RTK mode with a fast sampling rate of up to 20Hz. The GPS antenna, an accelerometer, and a velocimeter were installed on the roof of an earthquake shake-simulator truck. The simulated seismic waveforms resolved from the RTK time series are in very good agreement with the results from the accelerometer and the velocimeter.

3.3 GPS Seismometer – the UNSW Experiment

3.3.1 The UNSW GPS Seismometer Experiment

On 11 November 1998 at the University of New South Wales (UNSW), a GPS seismometer experiment was carried out using two Leica CRS1000 receivers (Ge et al, 1999d; Ge et al, 1999e). One functioned as the rover, the other as the reference receiver,

with both sampling at 10Hz and recording the raw observations. In addition, the rover was configured to record fast RTK position solutions. The experiment location was the roof of the Geography and Surveying Building (GAS) at UNSW (Fig. 3.1). The vibration on the GPS antenna was generated using a mechanical shaker with frequency higher than 2Hz and an amplitude of up to 12.7mm, which is more than one order improvement over previous experiments in terms of both frequency and amplitude. As shown in Fig. 3.2, the signal created by the sine random generator was power-amplified in order to drive the shaker. An accelerometer sensor was co-located on the GPS antenna fixture so that an independent measurement could be compared with the GPS result. The accelerometer output was recorded at 1200Hz by a Sony data logger.

Both standard and choke-ring antennas were used at the rover. In the case of the standard antenna, the shaker was operated both vertically and when inclined to 45 degrees to the horizontal (with the antenna facing north). The shaker was vibrated at 2.3Hz, and then at 4.3Hz. Table 3-1 shows how the various experimental sessions were organized.

Figure 3.1 Setup of the UNSW GPS Seismometer Experiment.

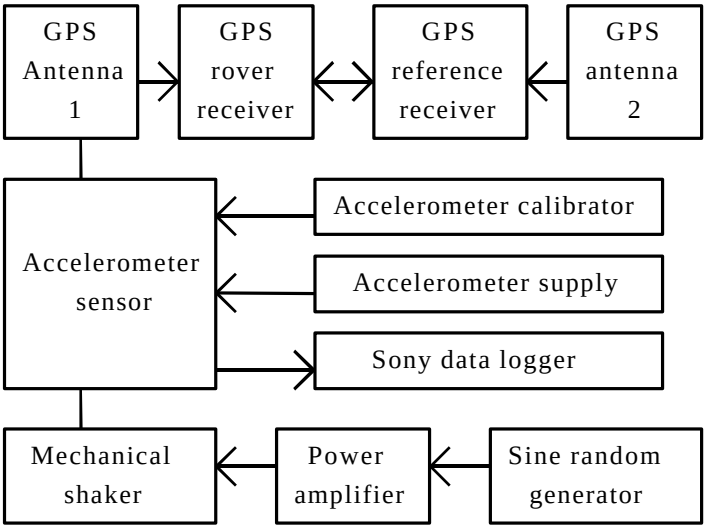

Figure 3.2 System configuration for the GPS Seismometer Experiment.

Table 3-1 The UNSW GPS seismometer experiment (11 November 1998).

Time	Frequency	Antenna	Vibration
13:50	0 HZ	Standard	Vertical
14:00	2.3Hz	Standard	Vertical
14:15	4.3Hz	Standard	Vertical
	Shaker inclined 45 degree		
14:30	0 HZ	Standard	45
14:35	2.3Hz	Standard	45
14:45	4.3Hz	Standard	45
	Change to Choke-Ring Antenna		
15:00	0 HZ	Choke-ring	Vertical
15:10	2.3Hz	Choke-ring	Vertical
15:20	4.3Hz	Choke-ring	Vertical

3.3.2 Fast RTK results

The recorded fast RTK results were downloaded from the rover receiver and converted to ASCII format. A number of Matlab programs were written to process the results.

In Fig. 3.3, the fast RTK time series of heights for the standard antenna when stationary (upper) and vibrating (lower) can be compared. In Fig. 3.4, the fast RTK time series (height) when the choke-ring antenna was used and vibrating at 2.3Hz (upper) and 4.3Hz

(lower) are shown. In all these figures, the horizontal axis indicates the number of samples and the vertical axis the height change in metres. All signals are very noisy when viewed in the time domain, however the series are quite different if inspected more closely.

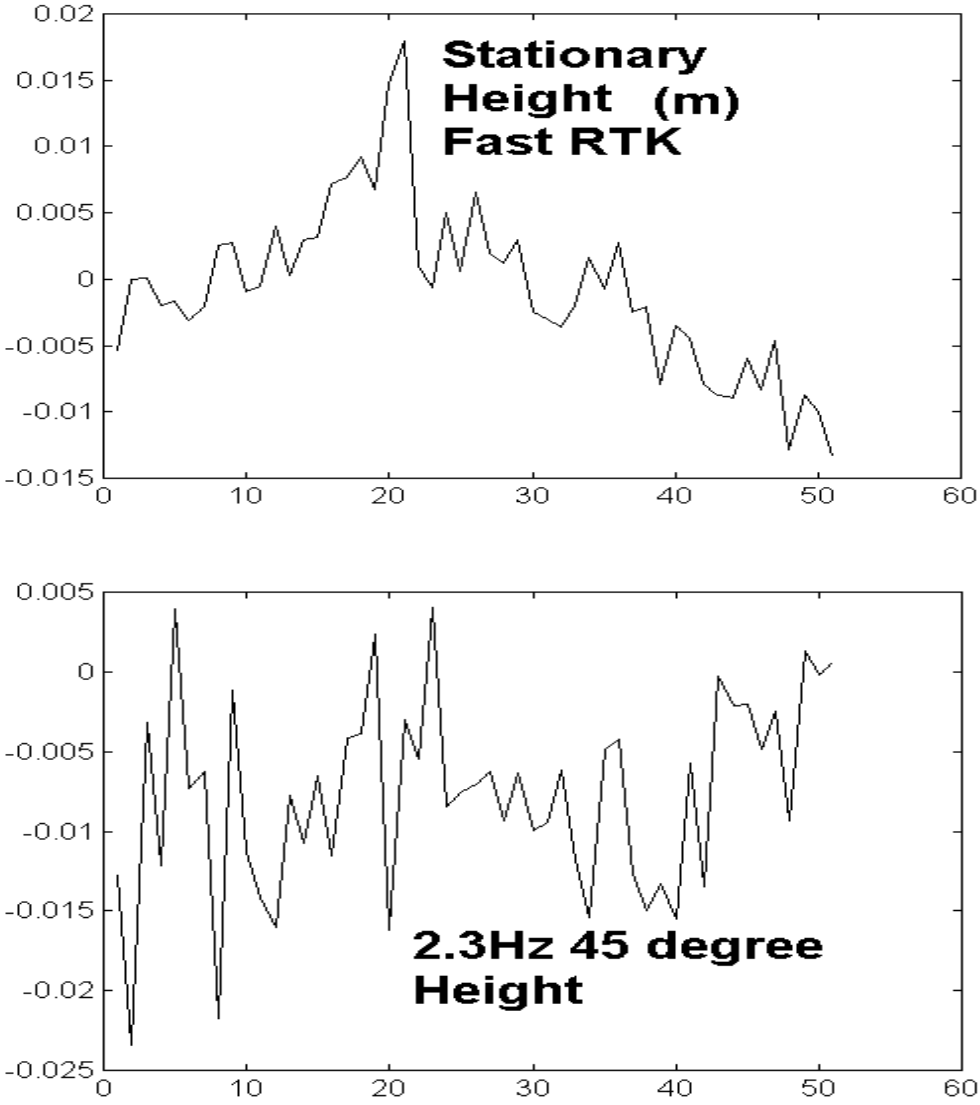

Figure 3.3 Comparison of fast RTK time series when the standard antenna is stationary (upper) and vibrating (lower).

Fig. 3.5 shows the frequency spectrum (after a Fast Fourier Transform operation on the time series) comparison when the shaker was vertical but vibrated at 0 HZ (top), at 2.3Hz

(middle), and at 4.3Hz (lower). The horizontal scale is in fs/2. For the UNSW experiments fs=10Hz. All three series have the same characteristics: it is noisier in the lower band than in the higher band. Though further research on the nature of the low frequency noise is needed, major sources of GPS errors by frequency band within the range of frequencies important for seismic wave detection are (Han & Rizos, 1997; Schwarz & Wei, 1994): (1) atmosphere: 0.00005-0.0008Hz; (2) multipath: 0.0008-0.01Hz; and (3) receiver noise: 0.0008-0.02Hz. There is also noise of an unknown source in the frequencies ranging from 0 HZ to 10Hz.

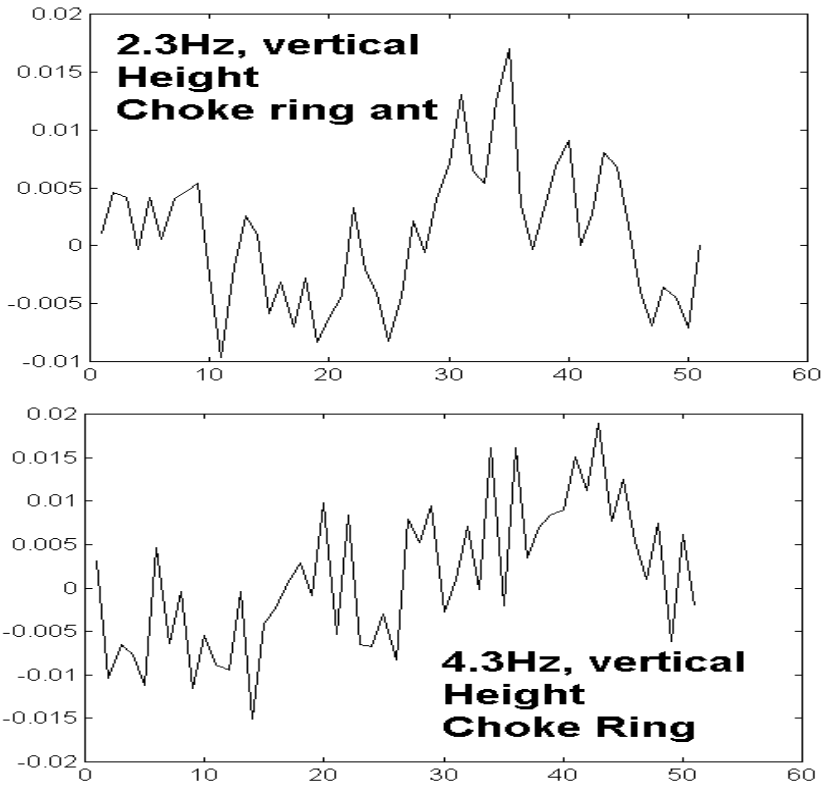

Figure 3.4 Fast RTK time series using choke-ring antenna.

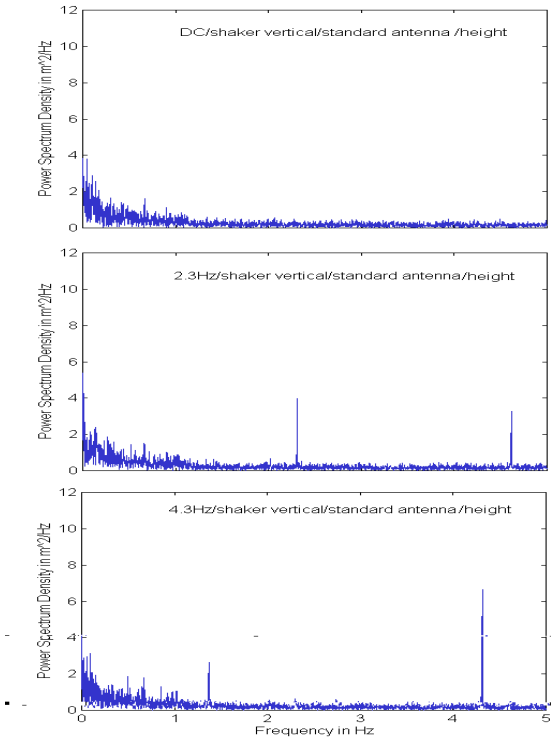

Figure 3.5 Frequency spectrum comparison, shaker vertical, 0 HZ-2.3Hz-4.3Hz, standard antenna.

The vibrations at both 2.3Hz and 4.3Hz are clearly resolved, although the height in Fig. 3.5 is the weakest of the three components. There is also a peak at 4.6Hz in the height component when 2.3Hz was applied because the shaker could not generate a perfect sine-wave. This fact had been noticed with a digital oscilloscope in the lab before the experiments and was also confirmed with the reference data from the accelerometer co-located under the GPS antenna (Fig. 3.6, acceleration data were resampled from 1200Hz to 64Hz when downloaded). With a 10Hz sampling rate for the GPS receiver, the 8.6Hz harmonic was removed in the case of 4.3Hz. However, the aliasing of the 8.6Hz harmonic is resolved at 1.4Hz in the lower plot of Fig. 3.5. It can also be seen that the 4.3Hz signal was resolved with an even better signal-to-noise ratio (SNR) than in the case of the 2.3Hz signal.

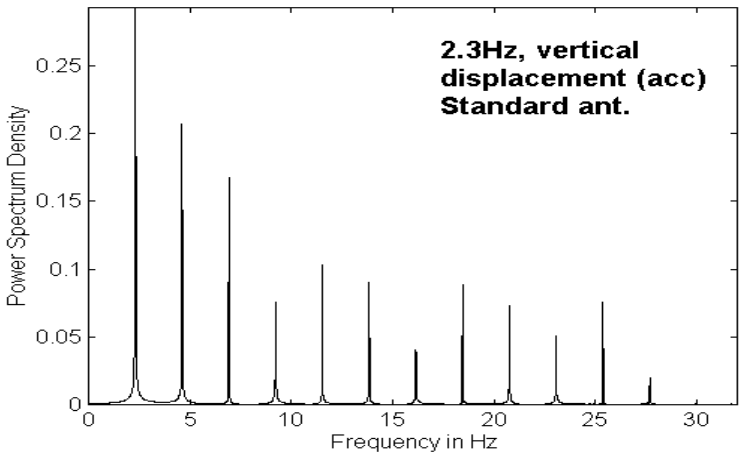

Figure 3.6 Frequency spectrum from the co-located accelerometer, 2.3Hz session.

The signals (in bold), their harmonics (in italics) and aliasing which can be detected with a 10Hz sampling-rate system are summarized in Table 3-2 for the convenience of later discussions (Praokis & Manolakis, 1996).

Table 3-2 Signals, their harmonic and aliasing (Hz).

signal/ harmonic	aliasing	signal/ harmonic	aliasing
2.3	-	**4.3**	-
4.6	-	*8.6*	1.4
6.9	3.1		
9.2	0.8		

The frequency spectrum when the shaker was inclined at 45 degree (facing north) and vibrated at 2.3Hz (Fig. 3.7) shows that the SNR of the latitude component is higher compared to the height component, though the displacements in the two components should be roughly the same. The peak at 2.3Hz for the longitude component indicates that the antenna was not exactly facing true north. Also the high order harmonic is seen clearly in both the height and latitude components at 4.6Hz; the aliasing of the 6.9Hz harmonic in height at 3.1Hz; and the aliasing of the 9.2Hz harmonic in both latitude and longitude at 0.8Hz, while it is too noisy to be seen in the height component.

Fig. 3.8 shows the frequency spectrum when the choke-ring antenna was used for the rover receiver and the shaker was vertical and vibrated at 2.3Hz, for the height, latitude, and longitude components respectively. The vibration at 2.3Hz is clearly resolved. There is also a peak at 4.6Hz in the height component. But there are no peaks at 2.3Hz for the latitude and longitude components, because this time a staff bubble was used to check the verticality of the shaker (which is also confirmed by a similar analysis of the data when 4.3Hz was applied). No aliasing is observed since the heavy choke-ring antenna has acted as an anti-aliasing filter and greatly attenuated the harmonics. See later discussion.

Fig. 3.9 shows the frequency spectrum comparison when the shaker was vertical but vibrated at 0 HZ, 2.3Hz, and 4.3Hz respectively. The aliasing of the 8.6Hz harmonic can be seen in the lower plot at 1.4Hz. It can be seen that the 4.3Hz signal is resolved with an even better SNR.

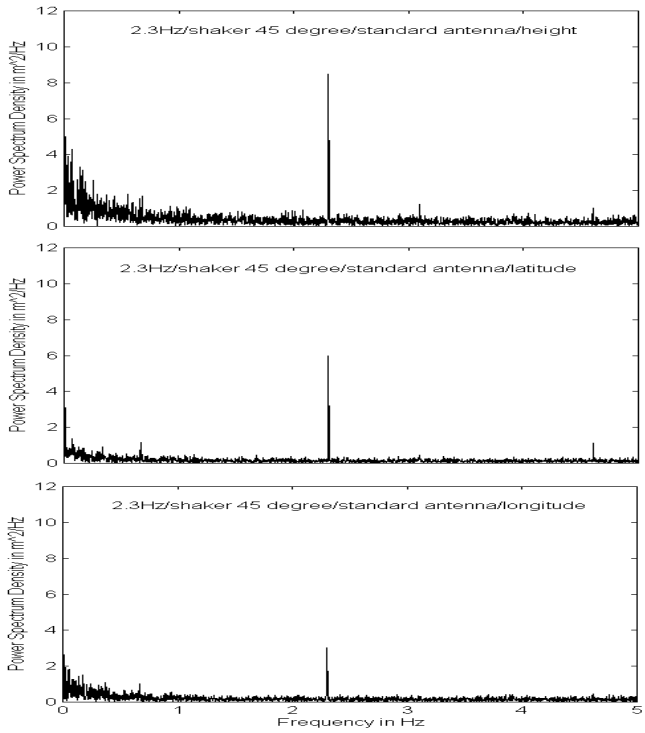

Figure 3.7 Frequency spectrum, 3 components, shaker 45 degree inclined, vibration 2.3Hz, standard antenna.

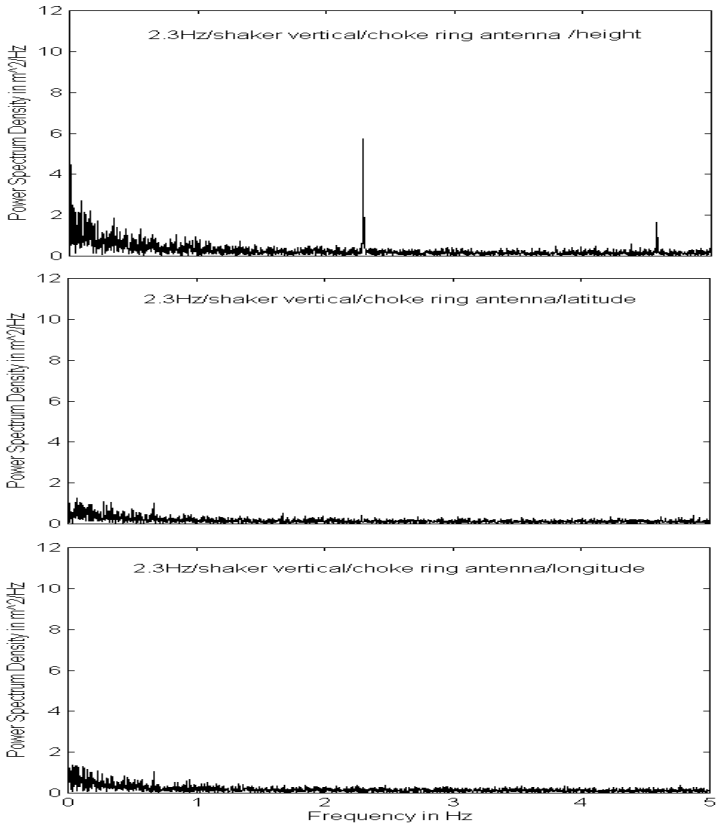

Figure 3.8 Frequency spectrum, 3 components, shaker vertical, vibration 2.3Hz, choke-ring antenna.

Fig. 3.10 shows the frequency spectrum comparison when the shaker was vertical and vibrated at 4.3Hz, for the height component, in the case of the standard antenna (upper) and the choke-ring antenna (lower).

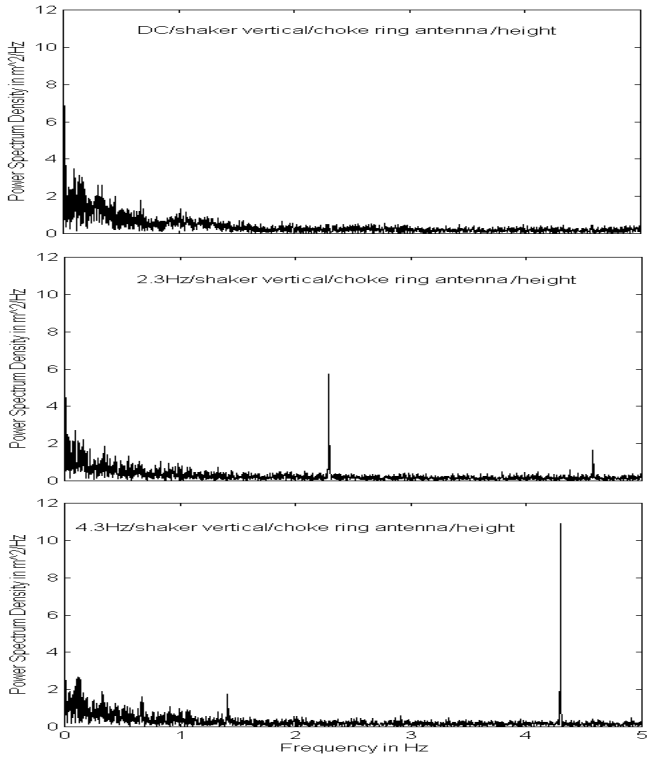

Figure 3.9 Frequency spectrum for height component, shaker vertical, 0 HZ-2.3Hz-4.3Hz, choke-ring antenna.

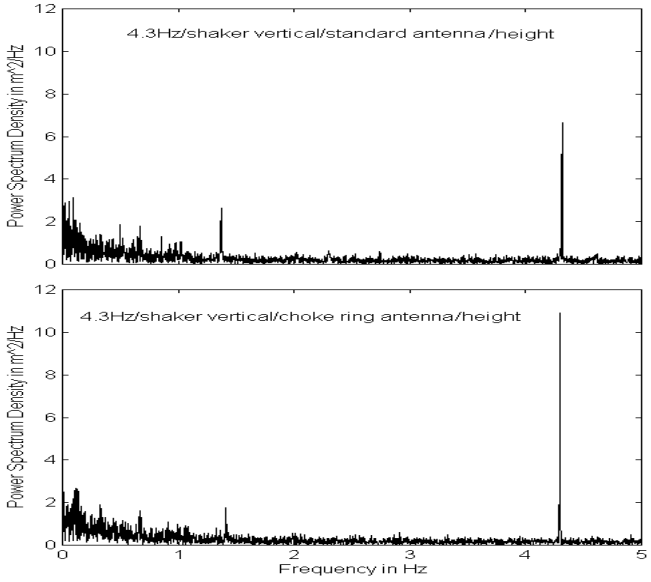

Figure 3.10 Frequency spectrum for height component, comparison of 4.3Hz results for the standard and choke-ring antennas.

The noise patterns are similar for both antennas, although the magnitude of the noise is smaller for the choke-ring antenna (i.e., the choke-ring antenna results again indicate higher SNR). The same conclusion can be reached if the other results in Fig. 3.9 are compared with their equivalents in Fig. 3.5. The high order harmonic and aliasing are also much smaller for the results using the choke-ring antenna due to the fact that it is much heavier than a standard antenna. (In fact, during the experiment, Prof. Randall from the School of Mechanical & Manufacturing Engineering, UNSW, suggested that a weight be added beneath the antenna to reduce the effects of high order harmonics.)

Although from the above analysis the 2.3Hz and 4.3Hz sine-waves used to simulate seismic waves can be recognized in both the time and frequency domain, they are more clearly resolved in the frequency domain. However, compared with current seismometers the results of a 'GPS seismometer' is hardly acceptable even when the choke-ring antenna is employed. Since the GPS noises (Han & Rizos, 1997; Lin & Rizos, 1997) and the broadband seismic waves fall in the same range of frequencies, and the noises are changing continuously, the unknown filter parameters must be estimated or tuned in real-time, and changed continuously, if a filter is used to track and suppress the noises. Therefore, it is essential that an *adaptive* filter rather than a fixed filter be used. In the following section, the adaptive filter based on the Least-Mean-Square algorithm, as described in Chapter 2, is employed to process the data collected from the UNSW GPS seismometer experiment.

3.3.3 Adaptive filtering of fast RTK results

As discussed in Section 2.2, in order to obtain a relatively noise-free signal from the adaptive system, the signal $s(n)$ has to be uncorrelated with not only the $x'(n)$ in the primary input, but also $x(n)$ in the reference input, while $x'(n)$ and $x(n)$ have to be correlated with each other. To meet these conditions, three data processing strategies have been developed, which represent three possible approaches in the implementation of a 'GPS seismometer'.

3.3.3.1 GPS-only approach

This approach is illustrated in Fig. 3.11, based on Fig. 2.2. Both the seismic wave *s(n)* and noise *x'(n)* are detected by the GPS receiver to generate *d(n)*,which is used as the primary input. The signal *d(n)* is delayed by D samples, i.e., *x(n) = d(n-D)*, where D is chosen so that *s(n)* and *s(n-D)* are uncorrelated but *x'(n)* and *x'(n-D)* are correlated (so that *s(n)* and x(n) are uncorrelated but *x'(n)* and *x(n)* remain correlated). (*s(n)* and *x'(n)* are uncorrelated because they are generated from completely different physical mechanisms.) The *x(n)* is used as the reference input to the adaptive filter. The rest of the figure is the same as Fig. 2.2.

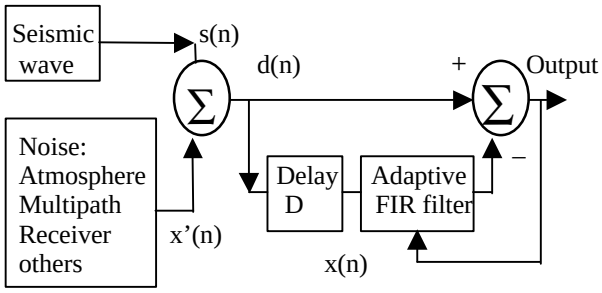

Figure 3.11 Adaptive filtering configuration using the GPS-only approach.

Fig. 3.12 is a sample of the result obtained using this approach to process the GPS seismometer experiment data with delay D=1 and filter order M=3 (for dataset: 2.3Hz, vertical vibration, with standard antenna).

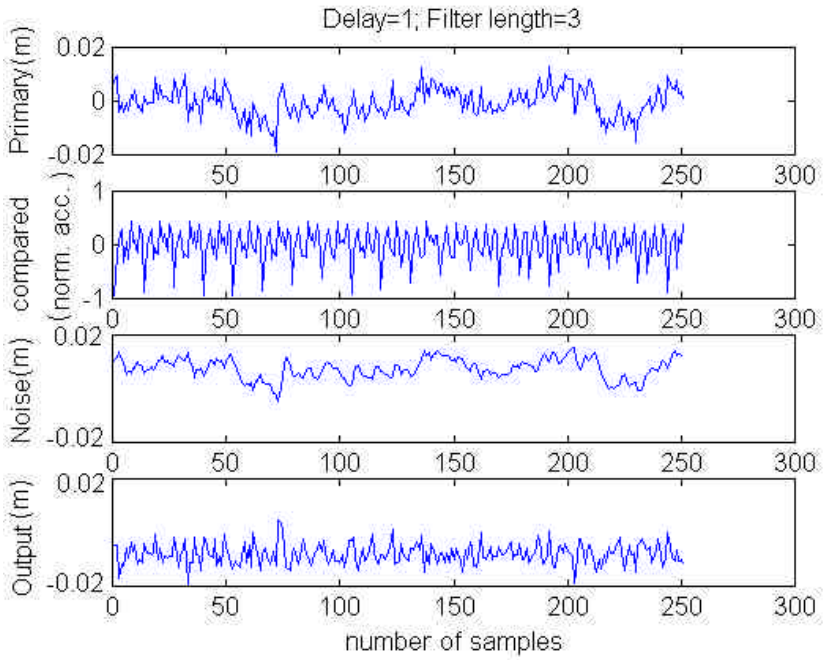

Figure 3.12 Adaptive filtering result using the GPS-only approach.

From top to bottom the plots are: the RTK GPS time sequence; accelerometer sequence for comparison only; extracted noise including atmospheric effect, multipath, receiver noise, etc.; and output from the adaptive system. In all these plots, except the second one, the horizontal axis indicates the number of samples and the vertical axis the height change in metres. In the second plot, the horizontal axis indicates the number of samples and the vertical axis the normalized acceleration. Comparing the first and fourth plots with the second one, it can be seen that the noise has been successfully mitigated, though it has not been completely eliminated.

3.3.3.2 GPS and accelerometer approach

Now replace Primary Measurement with GPS measurement of seismic wave (SW) and replace Reference Measurement with Accelerometer measurement of SW in Fig. 2.2 to obtain Fig. 3.13. As indicated in Fig. 3.13, assume that the GPS result is s + x and the accelerometer result is s' + x'. The s and s' are the measurements of the signal and x and x'

are the noises of the two sensors. According to the studies in Section 2.4, s can be derived as the coherent output from the adaptive filter.

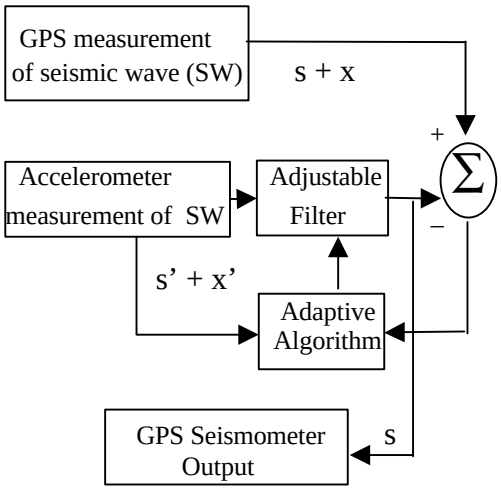

Figure 3.13 Adaptive filtering configuration using the GPS and accelerometer approach.

Fig. 3.14 illustrates the result obtained using the GPS and accelerometer approach on a sample of data. From top to bottom: the fast RTK GPS results (displacement in metres); the accelerometer measurement; the noise sequence derived by the filter; and the output from the filter. In all these plots, except the second one, the horizontal axis indicates the number of samples and the vertical axis the height change in metres. In the second plot, the horizontal axis indicates the number of samples and the vertical axis the normalized acceleration. Comparing the first and fourth plots with the second one and with the fourth one in Fig. 3.12, it can be seen that although the noise has not been removed completely, the SNR has been improved and it is now better than that obtained by the GPS-only approach.

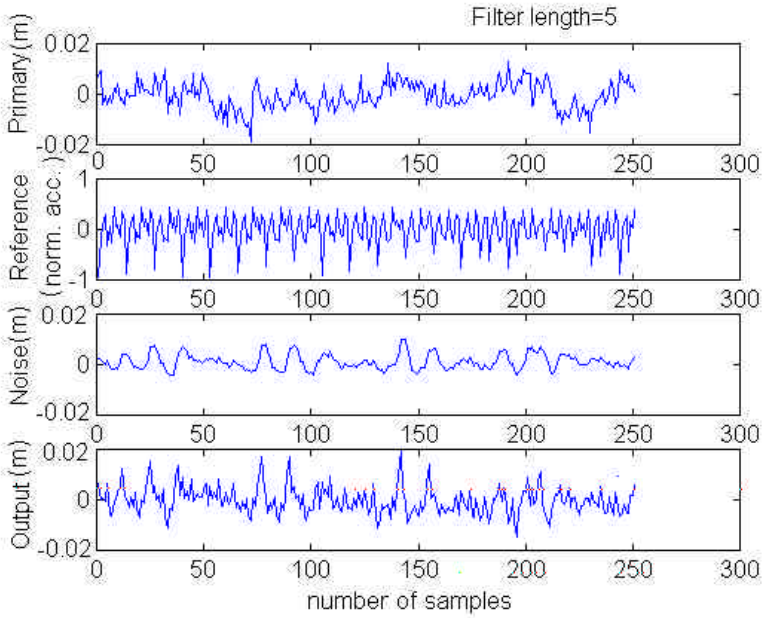

Figure 3.14 Adaptive filtering result using the GPS and accelerometer approach.

Some stations in current continuous GPS arrays such as GSI's GEONET are already configured so that a CGPS receiver is co-located with a three-component accelerometer, which can be upgraded to a GPS seismometer using this approach. On the other hand, as mentioned earlier, GPS receivers have been widely used at many seismic stations, such as the K-NET of the National Institute for Earth Sciences and Disaster Prevention of Japan, to provide a precise time service. These stations can, therefore, be easily upgraded to output both acceleration and displacement by employing this approach.

3.3.3.3 Multi-template approach

Fig. 3.15 illustrates the configuration for the multi-template approach, based on Fig. 2.2. The primary input is the GPS measurement of seismic waves. The reference input is separated into several “templates”, which can be generated using different resources. For example, the atmospheric template can be generated using observations from adjacent GPS seismometers, the multipath template can be generated using observations on the previous day at the same site (Lin & Rizos, 1997), and so on.

Though these resources were not available for the UNSW GPS seismometer experiments, Fig. 3.16 indicates adaptive filtering results using a multipath template. From top to bottom: the multipath time series of pseudo-range observations of the second day; the time series of the first day, which is used as the template; the derived noise from the adaptive filter; and the output from the adaptive filter (which shows the multipath effect has been successfully removed). The GPS data used here were the same as used in a previous study on multipath (Han & Rizos, 1997), which is actually a special case for the GPS seismometer (when there are no seismic events).

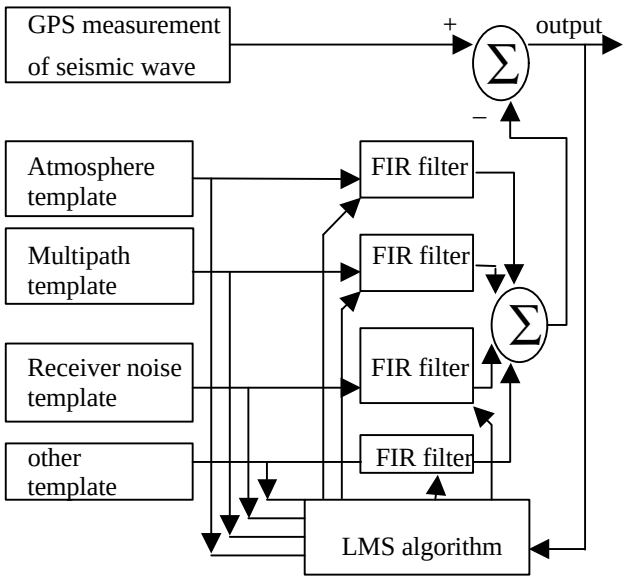

Figure 3.15 Adaptive filtering configuration using the Multi-template approach.

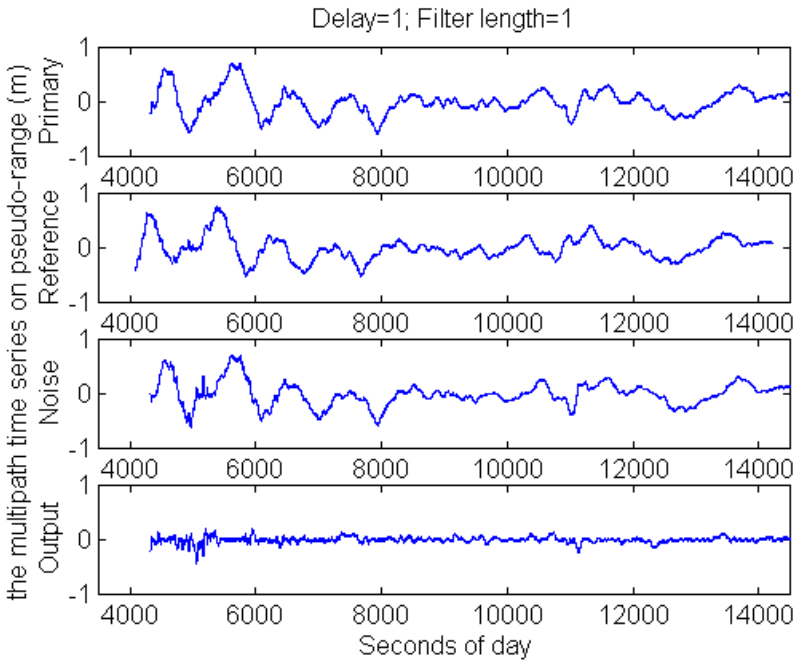

Figure 3.16 Adaptive filtering result using the multipath-template approach.

3.3.4 Concluding remarks

Two Leica CRS1000 GPS receivers have been used in the fast RTK mode to study the feasibility of using GPS as a broadband and highly dynamic seismometer. The sampling rates of both the rover and reference receivers were 10Hz. The rover antenna was mounted on a mechanical shaker which generated vibrations to simulate displacements due to seismic waves.

Though there was much noise in the low frequency band due to the effects of atmosphere, multipath, receiver noise, etc., FFT analysis of the fast RTK outputs indicate that vibrations of 2.3Hz and 4.3Hz with an amplitude of 12.7mm, applied to the rover antenna to simulate seismic waves, can be recognized in both the time and frequency domain (though they are more clearly resolved in the frequency domain), not only in the latitude and longitude components, but also in the height component. The fast RTK results at 0 HZ, 2.3Hz and 4.3Hz were found to exhibit similar noise patterns. The choke-ring antenna is shown to

yield results with higher SNR than the standard antenna. In addition to the signals, harmonics and aliasing were also detected. Data from a reference accelerometer confirmed that the harmonic was generated by the shaker and is not an artifact of the GPS experiment.

Compared with current seismometers, the output of this 'GPS seismometer' is not yet acceptable even when the choke-ring antenna is employed. Therefore, an adaptive filter based on the Least-Mean-Square algorithm which can track and eliminate noise in real-time has been used to process the RTK data. Three novel approaches, namely the GPS-only approach, the GPS and accelerometer approach, and the multi-template approach, have been developed and used to process the GPS seismometer experiment data. The former two have improved the SNR of the UNSW GPS seismometer significantly, while the latter has been proved to be very effective in cancelling the multipath effects using data collected on a previous day. An operational GPS seismometer can therefore be developed using a high sampling rate GPS receiver and a LMS adaptive filter.

3.4 GPS Seismometer – the UNSW-MRI Experiment

3.4.1 The UNSW-MRI GPS seismometer experiment

The current wide dynamic range, broadband seismic networks are sensitive to the frequency band from 10Hz to 1/300Hz. Therefore a GPS system with 10Hz sampling rate (i.e. up to 5Hz frequency coverage) seems still not sufficient to justify a GPS seismometer network. However, very recently GPS receivers have achieved 20Hz sampling rates which means that such receivers may be able to detect signals with frequencies from 0 HZ to 10Hz.

In a joint experiment on 10 August 1999 between the University of New South Wales (UNSW) and the Meteorological Research Institute (MRI) (Ge et al, 1999c; Yoshida et al, 1999), two Trimble MS750 GPS receivers were used in the RTK mode with a fast sampling rate of up to 20Hz. As can be seen from Fig. 3.17, the GPS antenna, an accelerometer, and a velocimeter were installed on a metal plate, which was mounted with bolts and adhesive tape on the roof of an earthquake shake-simulator truck, shown in Fig. 3.18 .

Figure 3.17 Setup of the UNSW-MRI GPS Seismometer Experiment.

Figure 3.18 Earthquake shake-simulator truck used in the UNSW-MRI GPS Seismometer experiment.

Table 3-3 UNSW-MRI experiment sessions (10 August 1999).

Session	Time (JST15h m s)	Intensity *	GPS
		Horizontal	
1	1314-1344	2	
2	1417-1447	2	
3	1532-1552	3	
4	1602-1622	3	
5	1642-1702	3	
6	1712-1732	4	
7	1748-1808	4	
8	1817-1837	4	
9	1902-1922	5L	
10	1932-1952	5L	
11	2002-2022	5L	
12	2032-2052	5H	
13	2102-2122	5H	
14	2132-2152	5H	
15	2212-2222	6	20Hz
		Up & down	
16	2402-2422	4	
17	2512-2532	4	
18	2542-2602	4	
19	2612-2632	5L	
20	2642-2702	5L	
21	2712-2732	5L	
22	2742-2802	5H	
23	2812-2832	5H	
24	2842-2902	5H	
25	2932-2942	6	
26	3341-		
		Horizontal	
27	4112-4132	2	
28	4142-4202	3	
29	4212-4232	4	
30	4242-4302	5L	
31	4312-4332	5H	
32	4352-4402	6	10Hz
		Up & down	
33	4442-4502	4	
34	4512-4532	5L	
35	4542-4602	5H	
36	4627-4637	6	
		Horizontal	
37	4857-4917	2	
38	4927-4947	3	
39	4956-5017	4	
40	5026-5046	5L	
41	5056-5116	5H	5Hz
42	5132-5142	6	
		Up & down	
43	5156-5216	4	
44	5226-5246	5L	
45	5256-5316	5H	
46	5326-5336	6	
47	5517-5707	1923 Kanto	
48	5813-5840	1995 Kobe	20Hz

*Japan Meteorological Agency scale

Table 3-3 outlines the 48 experiment sessions in which earthquakes of different intensities, including such past quakes such as the 1923 Kanto Quake and the 1995 Kobe Quake (recorded at the Kobe Kaiyou Meteorological Observatory), were simulated. GPS sampling rates used were 20Hz, 10Hz and 5Hz, while the sampling rates for the seismometers were 100Hz (acceleration data logging started at 14:03:50 JST, and velocity data logging started at 14:27:29 JST).

3.4.2 Results and comparison

The GPS receiver on the truck was used the a 'rover receiver' while a reference station was setup 10m away from the truck. The GPS-RTK results for the experiments were recorded on files, in the GGK message format, which includes information on time, position, position type and DOP (Dilution of Precision) values. Acceleration and velocity data from the seismometers were recorded concurrently. According to the MS750 Manual, the accuracy of the MS750 in low latency mode, in which it was configured for the UNSW-MRI experiment, is 2cm + 2ppm for horizontal and 3cm + 2ppm for vertical.

In Figure 3.19, the GPS-RTK time series of selected segments of the 20Hz session are compared with acceleration integrated twice and velocity integrated once. The later two are bandpass filtered (passband: 0.1 to 8Hz). The three results are in very good agreement in all the experimental sessions (where there were vibrations). But the GPS results indicate that the shaft of the shake-simulator truck did not return to its original position after the sessions, and indeed no effort was made to do so in the experiment.

In Figure 3.20, the three results were bandpass filtered (passband: 0.1 to 8Hz). The acceleration and velocity results were offset 2cm and –2cm respectively in the vertical axis direction for better viewing. (As a matter of fact, when the results are superimposed in a colour plot they agree with each other very well.) The GPS result is much better than expected (although the origin of the trace offsets in the GPS result that occur every 5

seconds is not clear at present). As can be seen from the figure, sine waves of 10cm amplitude peak-to-peak and 1-5 sec periods were generated by the truck in this session.

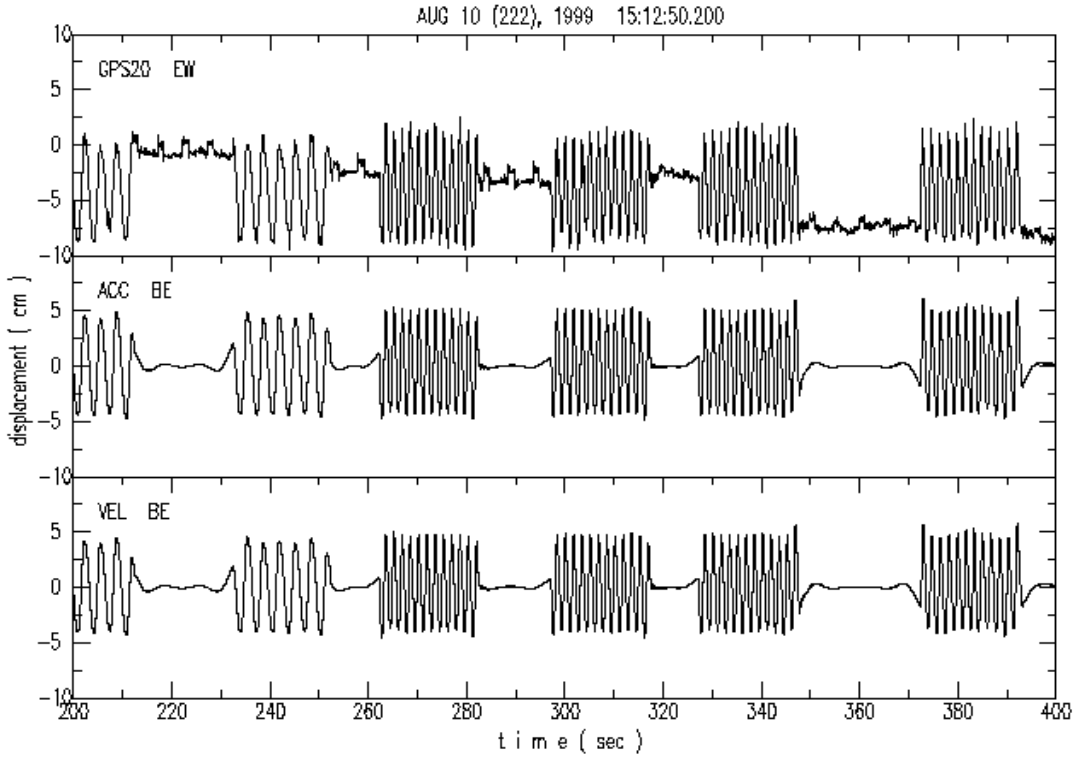

Figure 3.19 GPS RTK result compared with acceleration integrated twice and velocity integrated once.

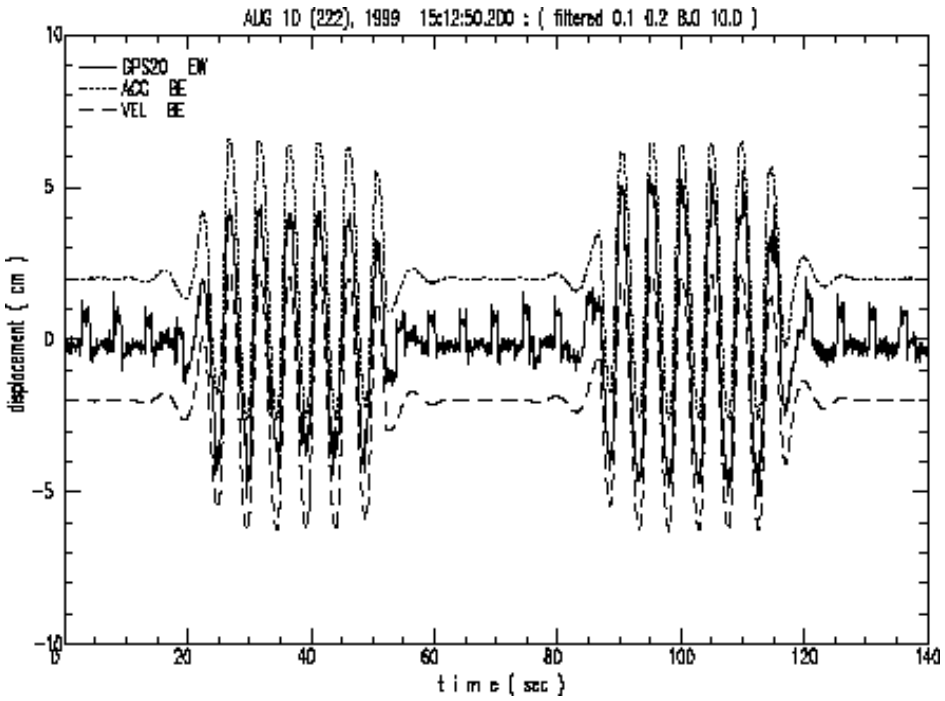

Figure 3.20 GPS RTK, acceleration and velocity after bandpass filtering.

3.4.3 Concluding remarks

The joint UNSW-MRI experiment involved using two Trimble MS750 GPS receivers, operating in the Real-Time Kinematic mode, to detect seismic signals generated by an earthquake simulating truck. The GPS-RTK result is in very good agreement with the results of the accelerometer and velocimeter, indicating again that a fast sampling rate (up to 20Hz) GPS system can be used as a 'GPS seismometer' for measuring displacements directly.

3.5 GPS Seismometer – the Implementing Issues

Although the GPS seismometer experiments have demonstrated very encouraging results, several implementing issues have to be investigated before the concept of a 'GPS seismometer' can be considered operationally feasible (Ge et al, 2000c). Therefore, the

focus of this section is to investigate some of the implementation issues, i.e. the layout of reference and rover receivers, noise reduction using measurements from adjacent days, correlation between measurements, data communication, and the pros and cons of using GPS as a seismometer.

In order to design the layout of reference and rover stations for distant seismic events, a configuration consisting of a reference station in the centre of a ring formed by a few rover stations is proposed. For seismic events local to the ring (within the "rover ring"), combined processing of moving baseline RTK and DGPS positioning can be a solution. Detailed discussions are given in Section 3.5.1.

To test the possibility of noise reduction using measurements from adjacent days, two Trimble MS750 GPS receivers were connected with a null modem to collect data at 20Hz rate at UNSW for about 3 hours, each day on 5 successive days. By using an adaptive filter for processing the various combinations of the RTK time series, it has been shown that the noise can be reduced significantly (Section 3.5.2).

In Section 3.5.3 a zero-baseline test at 10Hz sampled dual-frequency data indicates that the L1 phase measurements are truly independent, L2 phase measurements are partially independent, and the pseudo-range measurements of P1 and P2 are highly correlated.

Since Frame Relay circuits have already been used in some broadband seismic networks, it would appear that data communication is not a big problem if using high data rate GPS as a seismometer (Section 3.5.4).

3.5.1 The layout of reference and rover receivers

The first issue is the pattern of deployment of the reference and rover stations. Ideally seismic waves originating from a hypocentre arrive at the rover first and the reference station remains stationary during the whole earthquake event. However, because the

hypocentre can be located anywhere relative to the GPS seismometer, and the waves may travel as fast as 8km/s, neither of the above two conditions can be satisfied.

It is not easy to ensure that seismic waves arrive at the rover receiver first, since unlike tsunamis (for which the receivers on the land can always be used as reference stations, while those on the sea are the 'rovers'), earthquake waves can arrive from any direction relative to the rover and reference receivers. However, for distant events a configuration consisting of a reference station in the centre of a ring formed by a few rover stations could be used (Fig. 3.21). In fact this configuration is very similar to the first seismoscope invented by Zhang Heng in A.D. 136 for locating earthquakes. For an event as indicated in the figure, rover receivers at R1 and R8 are set active for detecting seismic waves while the rest of rovers work in the usual Continuous GPS (CGPS) mode (e.g., sampling at 30 sec interval). In fact, no matter in which direction the seismic waves approach the ring, one or two rover receivers can be activated to ensure seismic wave detection.

Although sub-decimetre precision in kinematic positioning over baselines of more than 1000km has been reported (e.g. Colombo, 1999), commercial VRS-RTK systems are suitable for baseline lengths up to about 50km. Therefore, the choice of rover ring radius is problematic. If two complete periods of the seismic waves are to be recorded, using the data which are given in Table 3-5 of Section 3.5.5, the radius should be 48km, 100km and 120km for P-, S- and Rayleigh–waves respectively. A GPS seismometer will be able to meet the requirements of real-time earthquake location if the GPS-RTK capability can be extended to baselines of 100km, because only P- and S-waves are normally used for real-time location. The rest of the seismic waves can be studied from the post-event analysis of the RTK results.

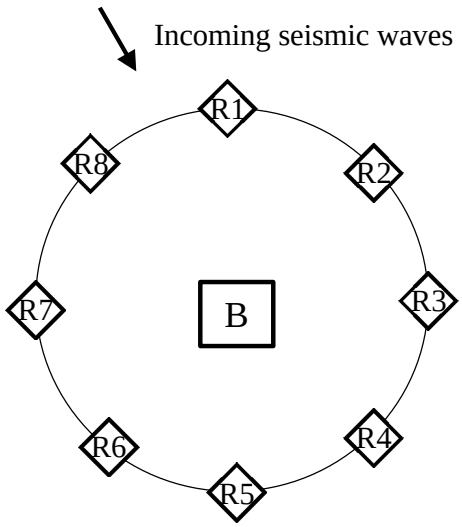

Figure 3.21 Configuration of reference and rover receivers in a GPS seismometer system (B: reference receiver; R1-R8: rover receivers).

For seismic events local to the ring (i.e. within the “rover ring”), a combined strategy of processing moving baseline RTK (Trimble, 1999) and DGPS positioning will have to be used (Fig. 3.22). This was originally implemented in the Trimble MS750 GPS receiver for vehicle orientation applications and precise relative displacement tracking of two moving vehicles. With the moving baseline RTK technique, the reference receiver (B) broadcasts Compact Measurement Record (CMR) data and station location data every epoch and the rover receiver (R1) performs a synchronized baseline solution (currently at 1 or 5Hz for the MS750). The accuracy of the baseline solution is at centimetre-level (horizontal: 1 cm, vertical: 2cm), while the absolute location of the reference-rover vector is only accurate to a few tens of metres. However, when the moving reference receiver (B) is performing DGPS or RTK relative to a fixed reference station (FR), the accuracy of the absolute location of the reference-rover vector can be improved to the metre-level for DGPS or the centimetre-level for RTK. The fixed reference station receiver (FR), unlike the moving reference receiver (B) and rover receiver (R1), is not immediately affected by the co-seismic movement. In this enhanced moving baseline RTK, the moving reference station (B) receives differential corrections from the fixed reference station (FR) and generates position solutions. CMR data is output by the moving reference station (B) to the rover

(R1). The rover accepts these CMR data and generates a vector solution. Now that the moving reference station (B) is differentially corrected, both the vector displacement and the absolute location of the moving baseline are derived, which are all very important in real-time determination of the near-field displacement in a seismic event.

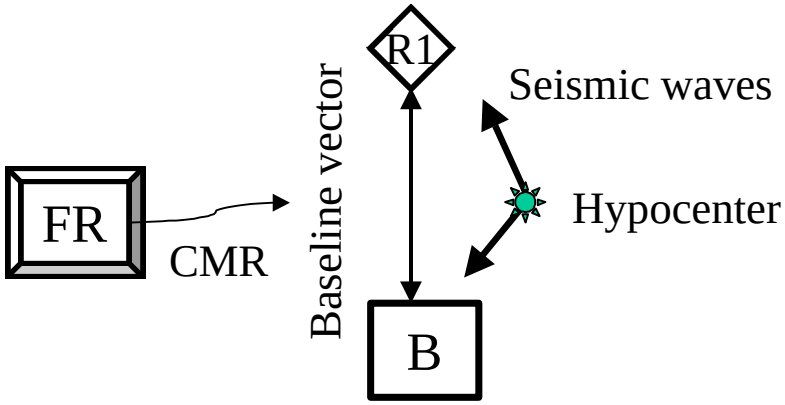

Figure 3.22 Moving baseline and DGPS positioning

(B: moving reference receiver; R1: rover receiver; and FR: fixed reference receiver).

3.5.2 Noise reduction using measurements from adjacent days

To test the possibility of noise reduction using measurements from successive days, two Trimble MS750 GPS receivers were connected with a null modem to collect data at UNSW for about 3 hours each day, on 5 successive days starting 3 March 1999. Fig. 3.23 is a plot of the variations of the RTK positions about the known position of the rover antenna from Day1 (bottom) to Day5 (top) (vertically shifted for easy viewing). The vertical axis is the variation in the latitude component in mm, and the horizontal axis is the second of the day. The multipath effect is clearly seen in the series. Suppose the RTK sequence on a selected day can be expressed as (Ge et al., 2000):

$$r(t) = s'(t) + x'_{mul}(t) \qquad (3.1)$$

where $s'(t)$ and $x'_{mul}(t)$ are the signal free of multipath (i.e. ground displacement due to seismic waves) and the noise contribution from multipath respectively.

The RTK sequence on the next day is expressed as:

$$d(t) = s(t) + x_{mul}(t) \qquad (3.2)$$

where $s(t)$ and $x_{mul}(t)$ have similar meanings as $s'(t)$ and $x'_{mul}(t)$ in Eq. (3.1).

According to previous studies (e.g. Han & Rizos, 1997), $x_{mul}(t)$ and $x'_{mul}(t)$ are highly correlated due to the repeat geometry of GPS satellites. Studies have shown that an adaptive Finite-duration Impulse Response filter, based on a least-mean-square algorithm, can reliably extract $x_{mul}(t)$ from the RTK sequence by using *d(t)* and *r(t)* as the primary- and reference-input to the adaptive filter (Ge, 1999; Ge et al., 2000).

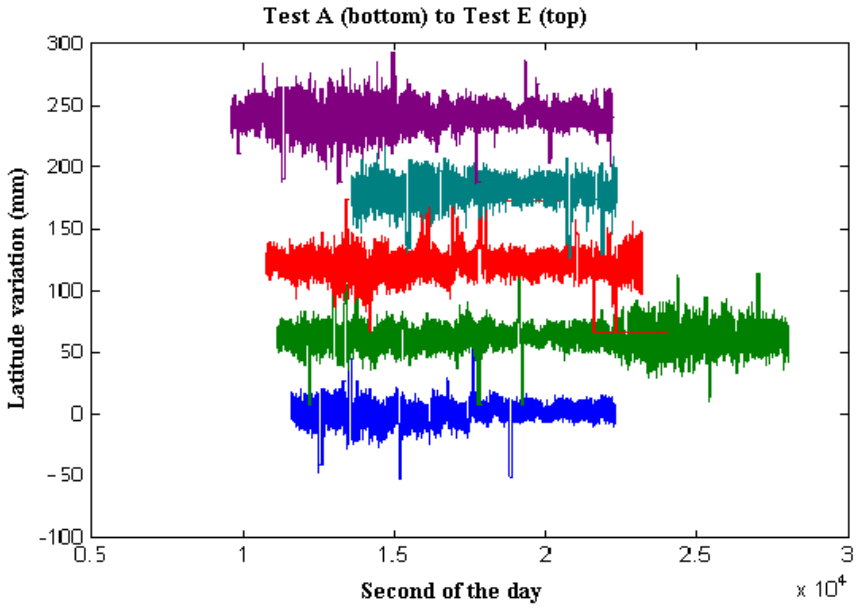

Figure 3.23 Latitude variations of the rover RTK series on 5 successive days.

Fig. 3.24 is an example of noise reduction using the adaptive filter. From top to bottom the plots are: the GPS-RTK time sequence of Day 5 as primary input; the RTK time sequence of Day 1 as reference input; extracted noise (multipath) as coherent output; and the incoherent output from the adaptive filtering system. In all these plots, the horizontal axis indicates second of the day and the vertical axis the latitude change in mm. In this particular case, the noise is reduced by about 30%. Table 3-4 is a summary of the noise reduction results for different combinations. The noise reduction in the latitude component (LTr) ranges from 11% to 62%; in the longitude component (LNr) 14% to 59%; in the height component (HTr) 8% to 42%; in the average of the three components (Ar) 12% to 54%; and in the average of the horizontal components (Hr) 13% to 60%. Because of the generally lower noise level in the horizontal components compared to the height component for the GPS-RTK result, much better noise reduction has been achieved for the horizontal components than for the height component.

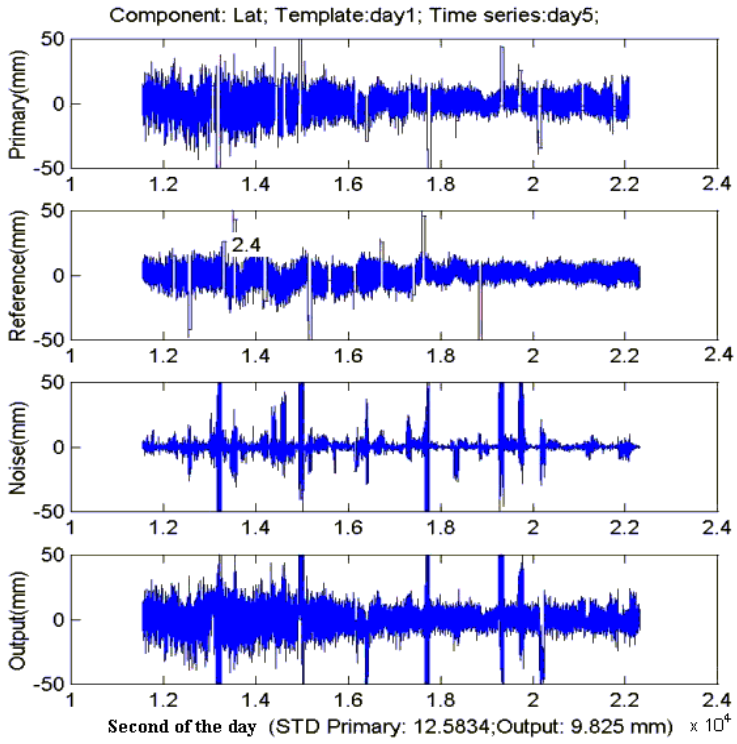

Figure 3.24 Adaptive filtering used in noise reduction.

Table 3-4 Summary of noise reduction results using adaptive filtering.

P	R	STDp (mm)	STDo (mm)	LTr (%)	LNr (%)	HTr (%)	Hr (%)	Ar (%)
2	1	13.98	10.99	21			18	15
		11.22	9.49		15			
		25.63	23.5			8		
3	1	17.98	13.58	24			21	19
		14.69	12.11		18			
		28.07	23.52			16		
	2	19.72	15.96	19			19	18
		15.85	12.85		19			
		29.37	24.83			15		
4	1	21.41	19.04	11			13	12
		18.35	15.78		14			
		31.05	27.51			11		
	2	21.46	17.92	16			19	17
		18.28	14.47		21			
		30.76	26.29			15		
	3	10.2	3.92	62			60	54
		12.49	5.11		59			
		25.5	14.89			42		
5	1	12.58	9.77	22			25	21
		13.93	10		28			
		28.31	25.08			11		
	2	12.78	9.37	27			25	20
		13.36	10.27		23			
		27.29	24.11			12		
	3	12.81	6.32	51			51	47
		14.15	6.91		51			
		27.29	16.71			39		
	4	11.31	6.38	44			50	44
		15.01	6.53		56			
		28.12	18.74			33		

Remarks:

For every combination between primary and reference sequences, the first row is latitude, the second longitude and the third height;

P: primary sequence;

R: reference sequence;

STDp: the standard deviation (STD) of primary sequence;

STDo:the STD of output sequence;

LTr: noise reduction in the latitude component;

LNr: noise reduction in the longitude component;

HTr: noise reduction in the height component;
Ar: averaged noise reduction in the three components; and
Hr: averaged noise reduction in the horizontal components.

3.5.3 Correlation between measurements

State-of-the-art GPS receivers with high sampling rates up to 20Hz have been available recently and can be used to track high-frequency displacement signals. In order to obtain true and real-time deformation information, measurements between trajectory epochs at such a high sampling rate should be independent, otherwise the high rate data would only achieve the same as low rate data interpolated to a high rate in post-processing. In practice, errors and biases in non-zero-baseline data processing, such as multipath effects, residual atmospheric biases and orbital errors, may exist in GPS pseudo-range and carrier phase observations, and will lead to significant correlation between trajectory measurements. To overcome this problem, zero-baseline data can be used to analyze whether the high sampling rate data is truly independent or not because these biases will disappear after double-differencing.

Based on the above considerations, a zero-baseline test using two Leica CRS1000 GPS receivers operating at 10Hz sampling rate was carried out on 4 August 2000 for half-hour at UNSW. During data collection, the observation mode without smoothing in carrier phase and pseudo-range observations has been specified. From the observation data, double-differenced residuals of the L1 and L2 carrier phase, and P1 and P2 pseudo-range can be calculated. The auto-correlation function is then used to describe the degree of similarity between a random process (residual sequence) and itself at different shifts or lags. Figures 3.25 to 3.28 show the residual series and their auto-correlation function for the L1 and L2 carrier phase and the P1 and P2 pseudo-range data respectively, between satellite pairs 5 and 30.

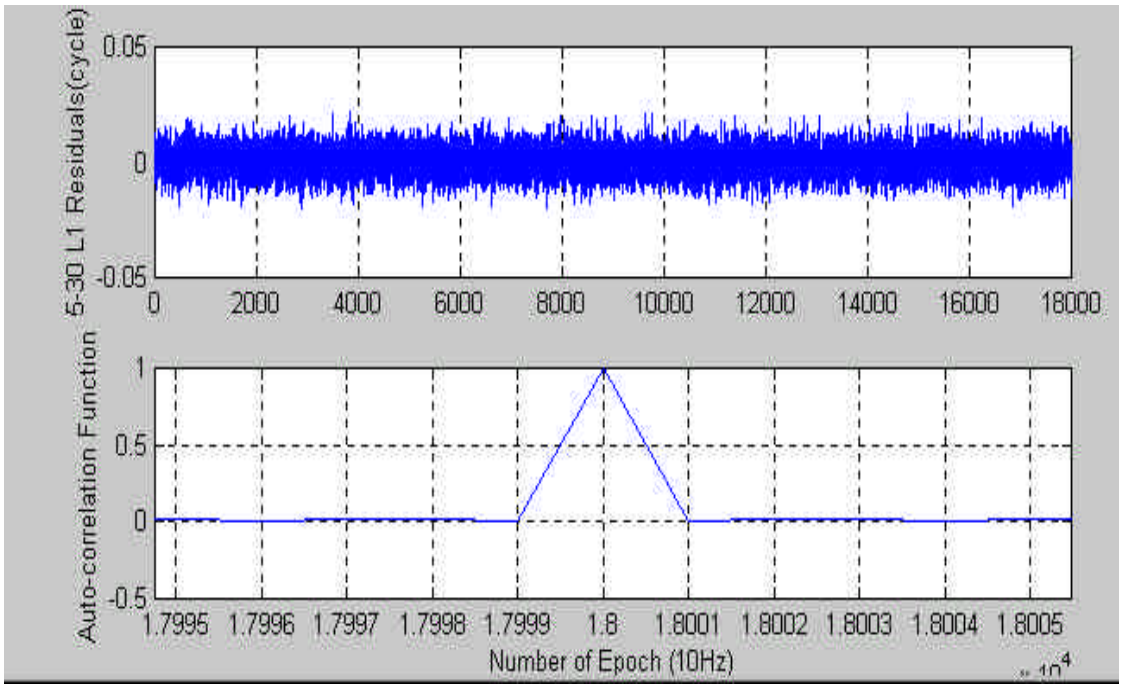

Figure 3.25 Correlation analysis for L1 carrier phase (PRN5, 30).

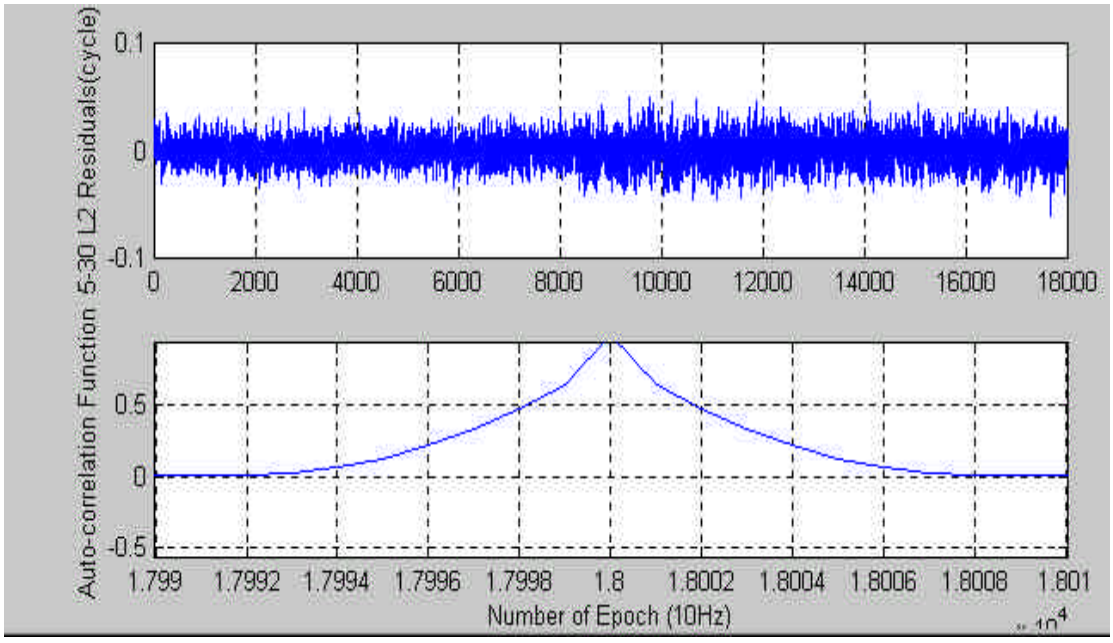

Figure 3.26 Correlation analysis for L2 carrier phase (PRN5, 30).

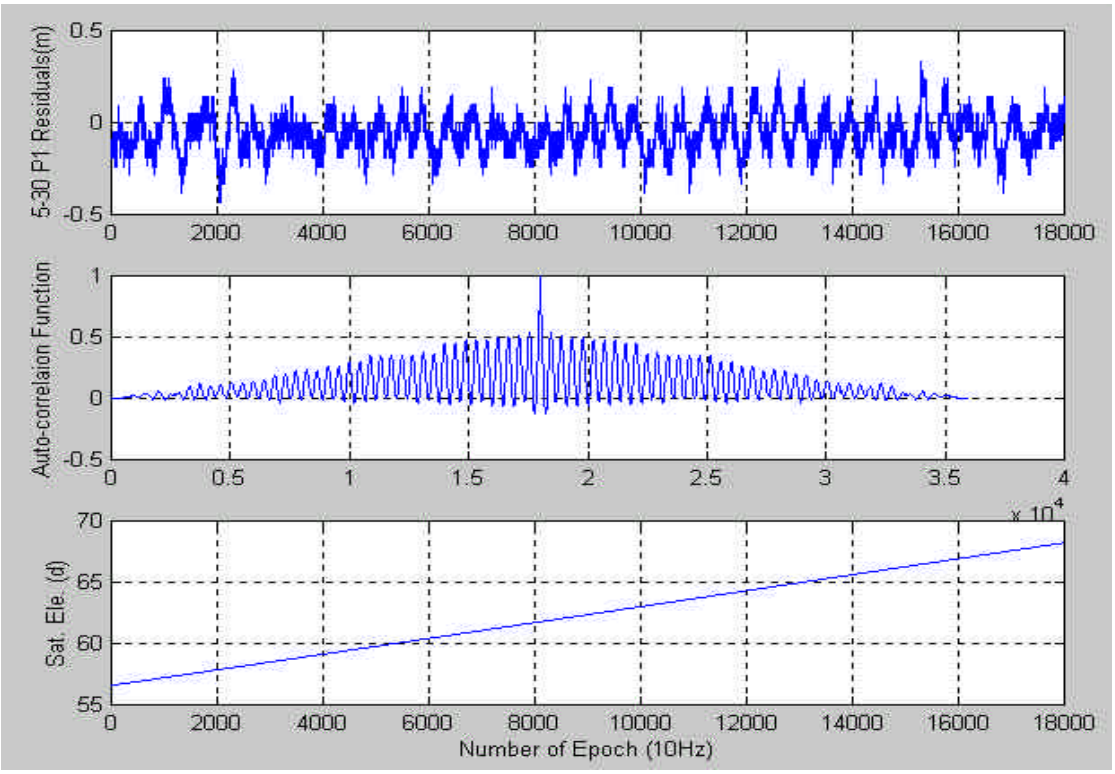

Figure 3.27 Correlation analysis for P1 pseudo-range (PRN5, 30).

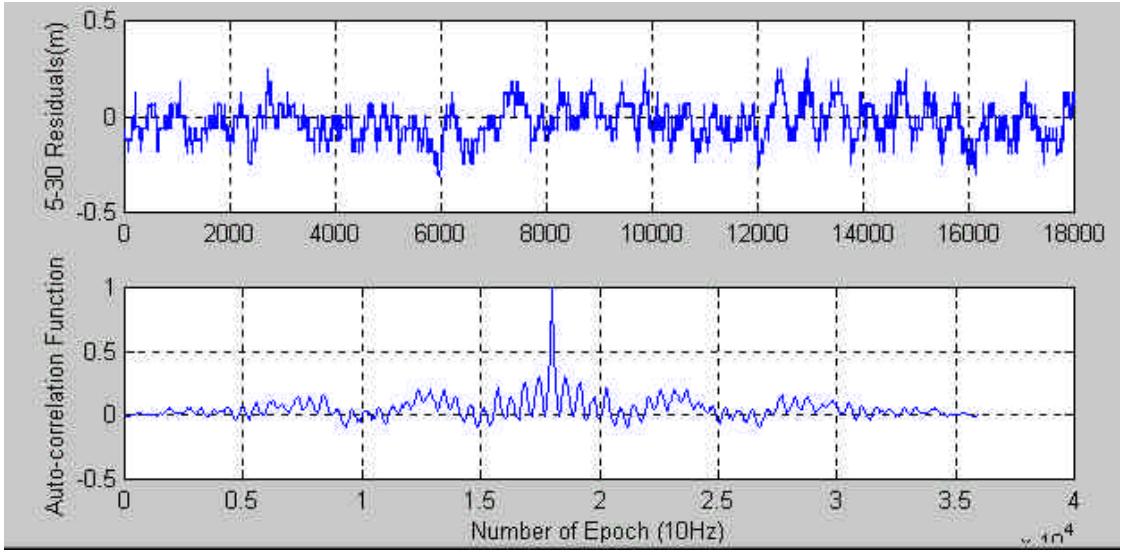

Figure 3.28 Correlation analysis for P2 pseudo-range (PRN5, 30).

From Fig. 3.25 it can be seen that the auto-correlation coefficient rapidly decreases from 1 to zero after shifting only one epoch, which indicates that the L1 phase measurements are truly independent for up to 10Hz sampling rate. From Fig. 3.26, the auto-correlation coefficient gradually decreases to zero after shifting 10 epochs. This suggests that the L2 phase measurements are partially independent. From Figs. 3.27 and 3.28 it can be concluded that the P1 and P2 pseudo-range measurements are highly correlated even though no smoothing option has been chosen. Further tests are needed to determine whether GPS receivers can provide independent measurements with up to 20Hz rate.

3.5.4 Data communication

The size of the RINEX observation and navigation file for a CGPS station working at the 30 second sampling rate is typically 1.6Mbytes and 0.1Mbytes respectively per day, although it may vary due to the geographical location of the station and the available satellites. Hence, the daily data volume (when raw observations are transferred) for a GPS seismometer sampling at 20Hz is:

(1.6 + 0.1) * 30 * 20 = 1020 Mbytes

The yearly data volume is:

1020 * 365 = 372300 Mbytes or about 0.4 terabytes.

If only the RTK results are sent, as in the case of the experiment described in Section 3.5.2, the daily data flow would be only 120Mbytes.

Many seismic stations around the world are now connected using technologies varying from long distance phone lines, commercial Internet, INMARSAT satellites, and VSAT systems. Although the amount of data transferred in this manner varies, typically 4 - 10 megabytes per day are transmitted. Moreover, Frame Relay circuits, which can handle a

data flow of about 5 - 10 terabytes / year (Stallings, 1999), have already been used in some broadband seismic networks. Therefore, data communication is not a crushing problem for a GPS seismometer system.

A GPS seismometer array could prove very cost-effective because the real-time, high-rate capability can be used to support many other applications such as atmosphere studies (Ware et al., 1999).

3.5.5 The Pros and Cons of using GPS as a seismometer

To assist discussions, definitions of some fundamental concepts are reproduced here (Gubbins, 1990). A *seismoscope* is an apparatus or device which only indicates that an earthquake has occurred, but which does not record anything. A *seismograph* is an instrument which gives a continuous record of the motion of the ground, i.e. a seimogram. A *seismometer* is a seismograph whose physical constant are so well known that the true ground motion can be calculated from the seismogram. Since the GPS receiver is measuring the true ground motion, it is best referred to as a 'GPS seismometer'.

In a traditional seismometer, everything in connection with the Earth, such as the seismometer pier, the frame of the seismometer, etc., takes part in the motion generated by the seismic waves. In order to record the waves, it is required to have some fixed point not taking part in this motion. This fixed point corresponds to the seismometer pendulum, which has been made independent of its surroundings by delicate suspension.

A completely statical pendulum is an ideal case; because in the traditional seismometer, even the pendulum gets its own small motion due to some friction. What is recorded is always the *relative motion* between pendulum and frame. In order to overcome the friction in the recording system, pendulum masses weighing as much as 20 tons are used in some Wiechert seismographs. (Some of which are still in operation not only out of pious

considerations but also due to the fact that they are the very best for recording the motions associated with the largest earthquakes (Båth, 1973).)

In contrast to the traditional seismometer, with the support of VLBI and SLR, the GPS constellation can be considered completely statical in terms of the influence from earthquakes on the Earth. The measurements from a GPS seismometer is thus due to absolute motion. With digitization and the application of Very Large Scale Integration (VLSI) electronic circuits, the GPS receivers are becoming cheaper, lighter and smaller.

For the traditional seismometer, when a record of an earthquake has been obtained, the first task is to determine the arrival times of the various phases, and the periods and amplitudes for the different waves, which defines two important aspects of seismology: accurate timing and calibration.

Accurate timing is vital for accurate location of seismic events. With no exact time, the seismic records are, as a rule, all but useless. Quartz crystal clocks with an accuracy of 0.1sec for several weeks have been used widely, and short wave radio receivers for direct recording of a time signal on the records were also used for quite a while. However, as soon as GPS established its importance to surveying, GPS timing has replaced virtually all these timing systems because it is much more accurate and easier to maintain. This implies that many of the current seismic stations could potentially be upgraded to have GPS seismometer capability. In a GPS seismometer, since all the measurements are taken together and tagged with the GPS time stamp, there is no need for an additional timing system.

Every seismic 'wave' actually consists of a whole spectrum, and to be able to reproduce this it is necessary for the seismometer to record in different period ranges, from a second up to several minutes. There has long been requirements to extend the period range considerably, partly towards shorter periods (around 1 sec and below) to be able to record local shocks, and also to get more exact information on P-waves from distant events, as well as towards longer periods (of the order of several minutes) to better record long-period surface waves

from distant quakes. Also, parallel instruments with different sensitivity are needed to a certain extent, because of the great variation in the amplitudes of the incoming signals. Hence, highly dynamic broadband seismometers have been developed to address all these requirements. However, it is still not possible for these traditional seismometers to achieve the same good reaction to all these waves with one and the same instrument (the reaction is best for those waves whose periods agree with the free period of the seismometer). For example, the long-period range seismometers are very sensitive to drift of the equilibrium position of the pendulum, due to variations in the atmospheric temperature and pressure. Thus the sensors have to be enclosed in an airtight case and a sophisticated temperature compensation system has to be used, which contributes significantly to the cost of the seismometers. Therefore sometimes there are up to a dozen instruments in a well-equipped station to simultaneously record seismic waves.

GPS seismometers, on the other hand, provide flat response to signals from 20Hz to 0 HZ without any calibration, although they cannot provide any magnification of the ground motion (although the modern seismographs, which have to be calibrated regularly, generally have a magnification which is too high to give really good records of the largest shocks (Bath, 1973)). Table 3-5 compares the GPS seismometer with current seismic instruments in their ability to detect seismic waves. At present many different instruments are used in order to recover different kinds of seismic waves, while a GPS seismometer has the potential to cover the whole seismic wave spectrum. Furthermore, with no fine mechanical parts such as the pendulum, and no need for a temperature compensation system, a GPS seismometer is much cheaper than a traditional seismometer.

In the case of a traditional seismometer, if the pendulum period is much longer than the ground period, the deflections on the record are proportional to the displacement (amplitude) of the ground and the seismometer is an amplitude meter. Conversely, if the pendulum period is much shorter than the ground period, then the deflections are proportional to the ground acceleration and the seismometer is an accelerometer. Finally, when the two periods are about equal, the deflections are proportional to the velocity of the ground motion. Due to the problem of the drift of the equilibrium position for the long-

period pendulum mentioned earlier, most of the installed seismometers are in fact accelerometers. Moreover, because of the very large amplitude in the near-field coseismic deformation, it can not be recorded directly by a traditional seismometer. However, such a deformation can be easily detected by a GPS seismometer.

Table 3-5 Comparison of the GPS seismometer with current seismic instruments in detecting seismic waves.

Seismic waves		Speed (km/sec)	Period (sec)	Current instruments	GPS seismometer
Body waves	P-waves	7.8 - 8.2	0.1 - 6	1	√
	S-waves	4.6 - 4.7	10 - 20	2	√
Surface waves	Love waves	3.7 – 4.2	20- 500	4, 5, 7	√
	Rayleigh waves	3.0 – 4.0	10 - 30	2, 3, 5	√
	Stonley waves	3.1 – 4.5	10 - 30	2, 3, 5	√
	Free oscillations	Standing	2500, 3200	5, 6, 7, 8	√

Remarks:

1. Short-period seismograph
2. long-period seismograph
3. strainmeter
4. tiltmeter
5. extensometer
6. gravimeter
7. quartz strainmeter (resolution: 10^{-9})
8. dual-frequency laser strainmeter (resolution: 10^{-12})

3.5.6 Concluding remarks

Using a GPS receiver as a seismometer was first proposed in 1994. Recent experiments on the feasibility of GPS seismometers with GPS-RTK systems have demonstrated very encouraging results. In this Chapter, several implementing issues associated with making a GPS seismometer system operational have been investigated.

In order to design the layout of reference and rover stations for distant seismic events, a configuration consisting of a reference station in the centre of a ring formed by a few rover stations is proposed. In such a configuration the GPS seismometer will be able to meet the requirements of real-time earthquake location if the GPS-RTK capability can be extended to baselines of 100km length, which has been partly fulfilled by the commercialization of the Virtual Reference Station concept. For seismic events local to the ring (within the "rover ring"), combined processing of moving baseline RTK and DGPS positioning is an option.

To test the possibility of noise reduction using measurements from adjacent days, two Trimble MS750 GPS receivers were connected with a null modem to collect data on 5 successive days. By employing an adaptive filter on various combinations of the RTK time series, it has been shown that the noise can be reduced significantly (latitude: 11% to 62%; longitude: 14% to 59%; height: 8% to 42%; the average of three components: 12% to 54%; and the average of horizontal components: 13% to 60%).

Zero-baseline tests at a 10Hz sampling rate indicate that the L1 phase measurements are truly independent, L2 phase measurements are partially independent, and the P1 and P2 pseudo-range measurements are highly correlated. These characteristics need to be further investigated for different types of GPS receiver.

Since Frame Relay circuits, which can handle a data flow of about 5 - 10 terabytes / year, have already been used in some broadband seismic networks, data communication is not quite a problem when seeking to use GPS as a seismometer.

Discussions on the pros and cons of using GPS as seismometer reveal that a GPS-RTK system can be used as a strong motion amplitude seismometer, which complements current seismometers. **Therefore, there are no major technological obstacles in upgrading current continuous GPS arrays to implement the serial temporal densification scheme.**

4 RETRO-ACTIVE TEMPORAL DENSIFICATION – MULTIPATH MITIGATION

One of the biggest advantages of the CGPS technique is that the GPS receivers are operating 24 hours a day, 7 days a week. However, when one processes the CGPS data for deformation monitoring one always focusses on the *current* data only, although one does compare the *current* result with *past* results in order to trace the evolution of the deformation.

On the other hand, although extreme care has always been taken in the selection of the site and the construction of the CGPS station, it is inevitable that some stations simply have to be deployed in harsh or non-ideal environments. For example, the strongly multipath-affected stations within the German CGPS network comprise about 20% of the total stations (Wanninger & Wildt, 1997).

Since the geometry relating the GPS satellites and a specific receiver-reflector location repeats every sidereal day (because the antenna environment is constant in the case of CGPS), the multipath disturbance has a periodic characteristic and is repeated between consecutive days (see, e.g., Han & Rizos, 1997). Therefore, it is useful to estimate the multipath effects in the **current** CGPS data from the **past** CGPS data, and then attempt to remove them from the **current** data before they are used in the GPS solution. This is, in fact, a retro-active temporal densification of the **current** CGPS data (refer to Fig. 1.8). This densification scheme, aimed to improve precision of the CGPS results rather than pushing the temporal limits of Fig. 1.7, can provide a mechanism to correct multipath errors from the observation data themselves. Hence, there will be no need to change the operational mode of CGPS arrays by, for example, seeking to find 'perfect', multipath-free sites. Using the data from the immediate past, the algorithms developed here should be flexible enough to enable the correction of multipath errors that vary seasonally as well.

4.1 Multipath Mitigation – An Overview

No matter how well such CGPS arrays are designed, multipath is a common concern as it impacts on the quality of the CGPS outputs or 'products'.

As is well known, multipath effects occur when GPS signals arrive at a receiver site via multiple paths due to reflections from nearby objects, such as the ground and water surfaces, buildings, vehicles, hills, trees, etc. Multipath distorts the C/A-code and P-code modulations, as well as the carrier phase observations. However, multipath signals are always delayed compared to line-of-sight signals because of the longer travel paths caused by reflections. Although use of choke-ring antennas and the careful selection of antenna site can effectively mitigate multipath, it cannot always be eliminated and sometimes the residual multipath disturbance remains a major contributor of error in continuous GPS results. There are also some applications, such as volcano and opencut mine slope monitoring, for which it is often impossible to identify antenna sites which are not vulnerable to mulipath. In the case of volcano monitoring, all the GPS receivers have to be placed on the slope or at the foot of the mountain. The only antenna site which may be free of multipath is the one on the summit, where there is often a great reluctance to install a receiver!

The importance of multipath has long been recognized by the GPS community. Many methods, both on-receiver and post-reception processing, have been developed. Much effort has been invested in refining on-receiver processing algorithms, both to reduce the threshold for multipath detection and rejection, and to simultaneously improve the measurement accuracy. Fenton et al. (1991) described one of the first low-cost receivers employing narrow correlation tracking techniques, as well as providing useful background on the theory concerning achievable pseudo-range measurement accuracy. Other on-receiver processing methods to reduce carrier phase and pseudo-range multipath have been also explored. These efforts have resulted in a new generation of C/A-code receivers that make use of narrow correlator spacing techniques. Dierendonck et al. (1992) describes the theory and performance of narrow correlator technology. Most of state-of-the-art receivers

now employ techniques similar to the Multipath Elimination Technology and the Multipath Elimination Delay Lock Loop (Townsend & Fenton, 1994) to eliminate, as far as possible, multipath in the receiver signal processing stage. But multipath cannot be removed completely, and the residual may still be too significant to ignore when compared to, for example, the crustal deformation signal being sought in the GPS results. Hence, it is still necessary to investigate post-reception data processing techniques for mitigating multipath.

Fortunately, since the GPS satellite ground tracks repeat every sidereal day (23 hours and 56 minutes), the multipath errors experienced today, for example, from 1:00pm – 2:00pm will be very similar to those experienced tomorrow, but will occur from 12:56pm – 1:56pm, provided that the antenna environment is constant. In recent years several post-reception methods to reduce multipath have been proposed. For example, one suggestion is to map the multipath environment surrounding a GPS antenna so that the multipath corrections for each satellite signal as a function of its azimuth and elevation can be determined (Haji, 1990; Cohen & Parkinson, 1991). One of the limitations of such an approach is that the antenna environment has to be mapped repeatedly if there are any changes to it. In 1998 a group of researchers headed by Jim Davis of the Harvard-Smithsonian Center for Astrophysics was funded to build an Antenna and Multipath Calibration System (AMCS) (Meertens, 2000). In their design, a parabolic reflector radio antenna with high directivity will be connected to a standard geodetic receiver, providing a signal free of multipath effects. By comparing with the signal received through the nominal GPS antenna, one can assess the multipath enviroment. When completed, the AMCS will provide important information about the multipath characteristics of many CGPS sites. Nevertheless, it is unlikely that many AMCS will be built due to their high cost. Hence a few AMCS have to be shipped from site to site, and they will certainly not be available on a daily basis at each of the thousands of CGPS sites around the world. Thus any multipath error that is affected by changes in the weather (and thus reflectivity of the nearby surfaces), changes in vegetation, and skyview, cannot be calibrated by the AMCS.

To identify and eliminate multipath sources, Axelrad et al. (1994) has suggested analysing the signal-to-noise ratio (SNR) of GPS signals. Multipath reflectors are identified by

isolating segments of the SNR data with strong spectral peaks. A model of the phase errors is generated based on the frequencies of these peaks, which is then used to reduce multipath. The shortcoming of such a method is that it cannot be implemented in real-time, and may need some changes to be made in the CGPS operation. The use of a ‘multipath template’ for the purpose of multipath mitigation was first proposed by Bishop et al. (1994). An ideal compliment to these techniques would be a multipath calibration method that could estimate and remove the multipath error from the CGPS data. Han & Rizos (1997) proposed the use of bandpass finite impulse response (FIR) filters to extract and eliminate multipath based on the CGPS observations. These do not only significantly mitigate multipath but can also generate a multipath model that can be used for real-time applications. However, the limitation of such an approach is that signals (for example, crustal deformation induced by an earthquake) falling in the same frequency band as the FIR filters will be filtered out.

Since the GPS noises and crustal deformation signals (particularly in the case of silent/slow seismic events) tend to fall in the same range of frequencies, and the noises are changing continuously (Han & Rizos, 1997; Lin & Rizos, 1997), the unknown filter parameters must be estimated or "tuned" in real-time, and altered continuously, in order to track and suppress the noises. Therefore, it is preferable that an *adaptive* filter rather than a *fixed* filter be used for multipath mitigation (Ge et al, 2000d). In this Chapter, the adaptive filter based on the least-mean-square algorithm described in Chapter 2 is used as the mathematical basis for multipath mitigation. The filter is employed to process the multipath series of both pseudo-range and carrier phase measurements.

4.2 Multipath Combination

To estimate multipath, it is not possible to simply compare the measured pseudo-range or carrier phase to the true geometric range since the error is a combination of many effects in addition to multipath. Therefore, multipath isolation or the formation of a 'multipath data combination' is necessary. The following pseudo-range combination is achieved through

judicious combination of pseudo-range and carrier phase measurements, taking advantage of the fact that the noise and multipath effects on the carrier phase are negligible compared to those of the pseudo-range yet most other error sources are the same (Rizos, 1996):

$$\mathrm{MP}_{\mathrm{P}_1} = \mathrm{P}_1 - \frac{9529}{2329}\cdot\phi_1 + \frac{7200}{2329}\cdot\phi_2 + \mathrm{K}_1 \tag{4.1}$$

$$\mathrm{MP}_{\mathrm{P}_2} = \mathrm{P}_2 - \frac{11858}{2329}\cdot\phi_1 + \frac{9529}{2329}\cdot\phi_2 + \mathrm{K}_2 \tag{4.2}$$

where MP_{P_1} and MP_{P_2} are the pseudo-range multipath effects on L1 and L2; P_1 and P_2 are pseudo-range data on L1 and L2; f_1 and f_2 are carrier phase data on L1 and L2; and K_1 and K_2 are functions of the receiver noise, the multipath on carrier phase and include the unknown integer ambiguities (which can be assumed constant if there is no cycle slip in the carrier phase data). All terms are expressed in units of metres. After the combination, the result is the pseudo-range multipath mixed with the receiver noise.

For the estimation of carrier phase multipath, one starts with the one-way carrier phase equation (Rizos, 1996),

$$L_i = r + dr + dtrop - dion_i + (dt - dT) - l_i.N_i + MC_i + uC_i \tag{4.3}$$

where

i = subscript indicates a certain frequency of signal (i=1 or 2);
L = phase measurement in range units;
ρ = geometric range between the antenna and satellite;
dρ = ephemeris (orbital) error;
dtrop = tropospheric bias;
dion = ionospheric bias;
dt,dT = receiver and satellite clock errors;
λ = the wavelength;
N = phase ambiguity (integer);

MC = phase multipath; and

νC = phase noise.

If the two GPS stations are very close to each other, after the between-satellite and between-receiver differencing (double-differencing: DD), Eq. (4.3) reduces to:

$$\nabla\Delta L_i = \nabla\Delta\rho - \lambda_i.\nabla\Delta N_i + \nabla\Delta MC_i + \nabla\Delta \upsilon C_i \quad (4.4)$$

where $\nabla\Delta$ is the DD operator. In Eq. (4.4), although $\nabla\Delta L_i$ can be directly calculated from the RINEX files of the two stations, $\nabla\Delta\rho$ and $\nabla\Delta N_i$ have to be estimated before the DD phase multipath $\nabla\Delta MC_i$ can be derived. Therefore the combination result is also the carrier phase multipath mixed with the phase noise. When one of the two stations is relatively multipath free, the DD multipath can, therefore, be considered as the carrier phase multipath signature for the other station.

Based on the above analysis, the multipath sequence derived using the multipath combinations on a selected day can be expressed as:

$$r(n) = N'(n) + x'_{mul}(n) \quad (4.5)$$

where $N'(n)$ and $x'_{mul}(n)$ are the noise free of multipath and the noise contribution from multipath, respectively.

The multipath sequence on the next day is expressed as:

$$d(n) = N(n) + x_{mul}(n) \quad (4.6)$$

where $N(n)$ and $x_{mul}(n)$ have similar definitions as $N'(n)$ and $x'_{mul}(n)$.

According to previous studies (e.g., Han & Rizos, 1997), $x_{mul}(n)$ and $x'_{mul}(n)$ are highly correlated. But $N(n)$ and $N'(n)$ are uncorrelated, which means that Eqs. (2.1) - (2.4) are only partly satisfied. In this case, as demonstrated in Chapter 2, the adaptive filter can still be used to extract multipath from the results of the second day by employing the results of the first day as a reference signal. The benefit of this is the ability to then correct the affected observable sequences using the extracted multipath, and to use these corrected observables in the GPS solution to improve the quality of the GPS coordinate results.

In the following sections the adaptive filter is used first to extract the multipath model and then to eliminate the multipath from the GPS results, using three data sets. The first two data sets are the same as were used in the Han & Rizos (1997) study.

In the first data set, the pseudo-range data over a period of nearly 3 hours for four successive days, collected on the roof of the Geography and Surveying (GAS) building, at the University of New South Wales (UNSW), from 30 September to 3 October 1997, using an Ashtech Z12 GPS receiver, were used to compute the pseudo-range multipath time series according to Eq. (4.1) (In this study only the 'pseudo-range multipath time series' on L1 for satellite PRN 9 are used.) This is Data set 1.

In the second data set, multipath series of double-differenced carrier phase measurements over a period of nearly 2 hours on four successive days for two satellites (PRNs 1 and 21) were calculated from data collected in an experiment carried out on the roof of the GAS building at UNSW, from 28 April to 1 May 1997, using two Leica SR299 GPS receivers, with a baseline length of about 6 metres. Here the residual series of double-differenced carrier phase observations are used as the 'carrier phase multipath time series' because they reflect the multipath disturbance and observation noise (it is assumed that all the other errors and biases are negligible because the baseline length is only a few metres), as analyzed in Eq. (4.4). This is Data set 2.

With the third data set, the filter is used to first *extract* the multipath model from an analysis of the time series, and then to *eliminate* the multipath effect from the GPS results

of the BRAN station in the Southern California Integrated GPS Network (SCIGN). The pseudo-range multipath time series on L1 for satellite PRN 2 is derived using Eq. (4.1). This is Data set 3.

4.3 Pseudo-Range Multipath Mitigation Using The Adaptive Filter

All the analyses in this section are based on Data set 1. Fig. 4.1 illustrates the forward adaptive filtering results for pseudo-range multipath for the Day 1 and Day 2 pair. Forward filtering means that GPS results on a day are used to correct results on a following day. From top to bottom in the figure: the multipath time series of the pseudo-range observations of Day 2, which is used as primary input to the filter; the time series of Day 1, which is used as the reference input to the filter; the multipath model derived by the adaptive filter (noise); and the output from the adaptive filter. Note that the output's standard deviation (STD) is only one fourth of the primary input, which indicates that the multipath effect has been indeed successfully reduced. (The horizontal axis indicates seconds of the day and the unit of the vertical axis is the metre.)

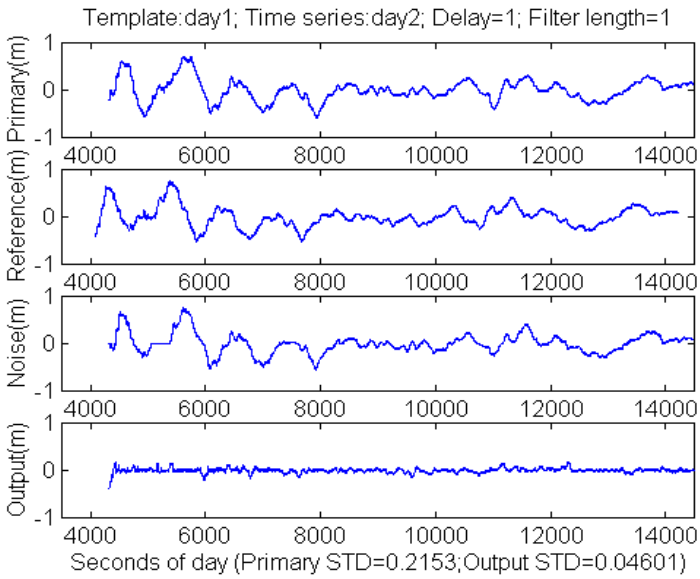

Figure 4.1 Forward adaptive filtering results for pseudo-range multipath for the Day 1 and Day 2 pair.

Figs. 4.2 and 4.3 show forward adaptive filtering results for the pseudo-range multipath time series for pairs of days: Day 2 & Day 3 and Day 3 & Day 4. The results are illustrated in the same format as Fig. 4.1. Similar multipath mitigation results have been achieved. It is also interesting to note that although in Figs. 4.1, 4.2, and 4.3 different pairs of time series are used, the multipath model derived is almost identical, which demonstrates the strength of an adaptive filter for such an application.

In order to investigate the influence of the "age" of the reference signal on multipath mitigation, Figs. 4.4 and 4.5 illustrate the forward adaptive filtering results for pseudo-range multipath time series for pairs of days: Day 1 & Day 3 and Day 1 & Day 4. Comparing these with the results for the Day 1 & Day 2 pair in Fig. 4.1, the output STD rises from 0.046m for Day 1 & Day 2 pair, to 0.059m for the Day 1 & Day 3 pair, and to 0.071m for the Day 1 & Day 4 pair. Hence, one can see that the "older" the reference signal, the less effective the multipath mitigation. Hence, the "age" of the reference signal does influence the multipath mitigation, even when the antenna environment remains largely unchanged (as in the case of CGPS).

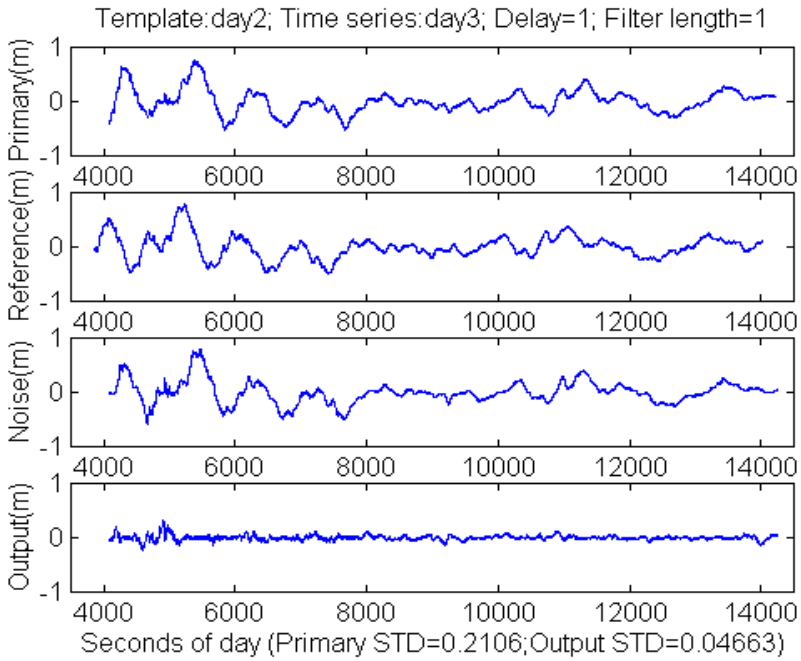

Figure 4.2 Forward adaptive filtering results for pseudo-range multipath for the Day 2 and Day 3 pair.

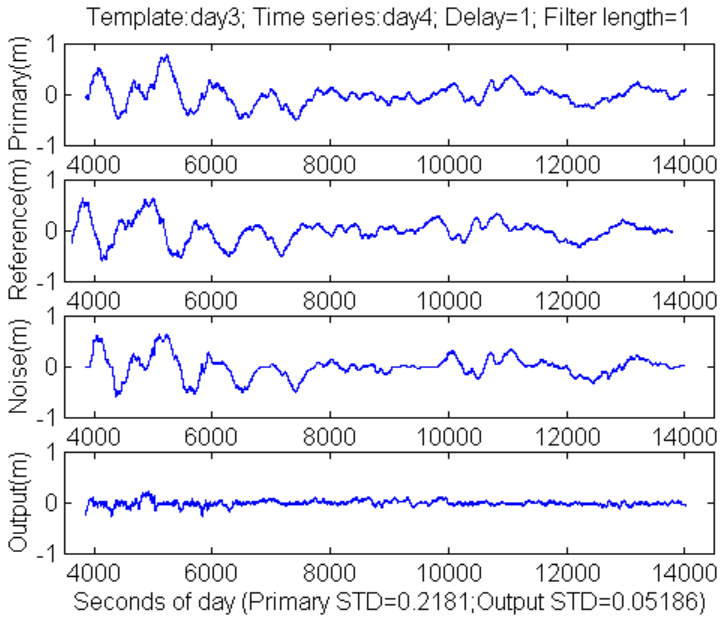

Figure 4.3 Forward adaptive filtering results for pseudo-range multipath for the Day 3 and Day 4 pair.

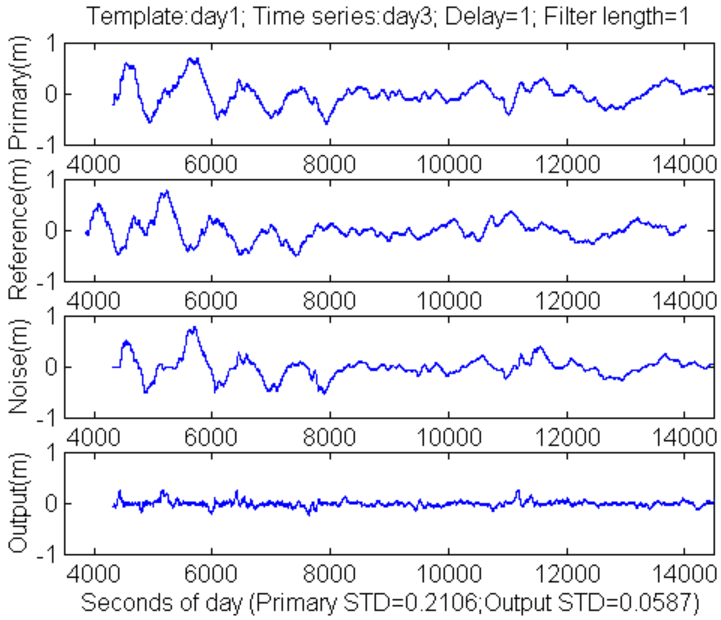

Figure 4.4 Forward adaptive filtering results for pseudo-range multipath for the Day 1 and Day 3 pair.

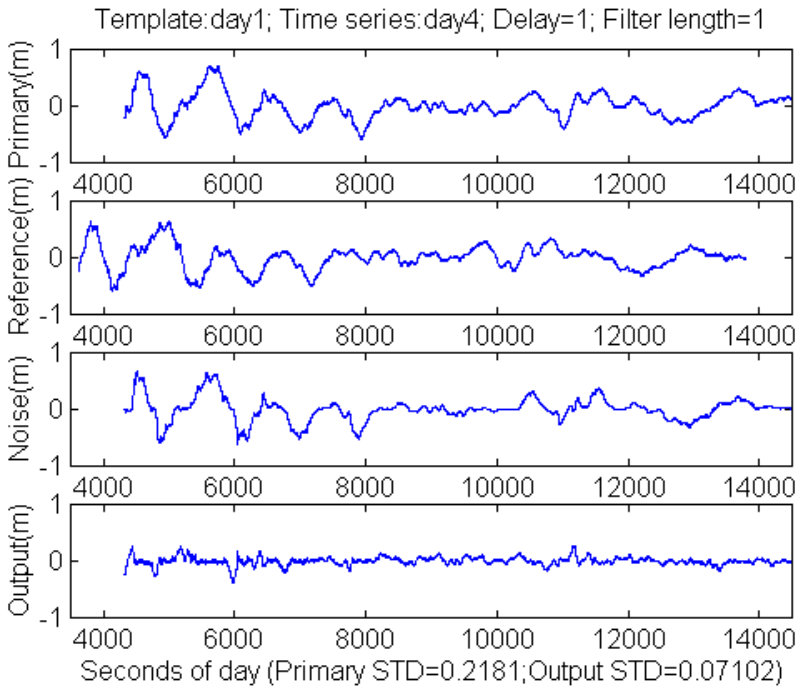

Figure 4.5 Forward adaptive filtering results for pseudo-range multipath for the Day 1 and Day 4 pair.

It is also evident that although the multipath mitigation is not as good as the previous results using pairs of adjacent days, the multipath model derived is still almost identical to that obtained from the previous results.

Although forward filtering discussed so far already significantly mitigates multipath, CGPS results are never "too accurate" for crustal deformation monitoring. In order to explore the full potential of the adaptive filtering technique for multipath mitigation, backward filtering was also investigated. Backward filtering means that GPS results for a particular day are used to correct results from a previous day. Fig. 4.6 illustrates the backward adaptive filtering results for pseudo-range multipath time series for the pair of days Day 4 & Day 1. Comparing this result with the forward filtering result for the Day 1 & Day 4 pair in Fig. 4.5, the backward filtering output STD 0.078m is a little worse than 0.071m for the forward

filtering case. Hence, a tentative conclusion is that forward correction is better than backward correction.

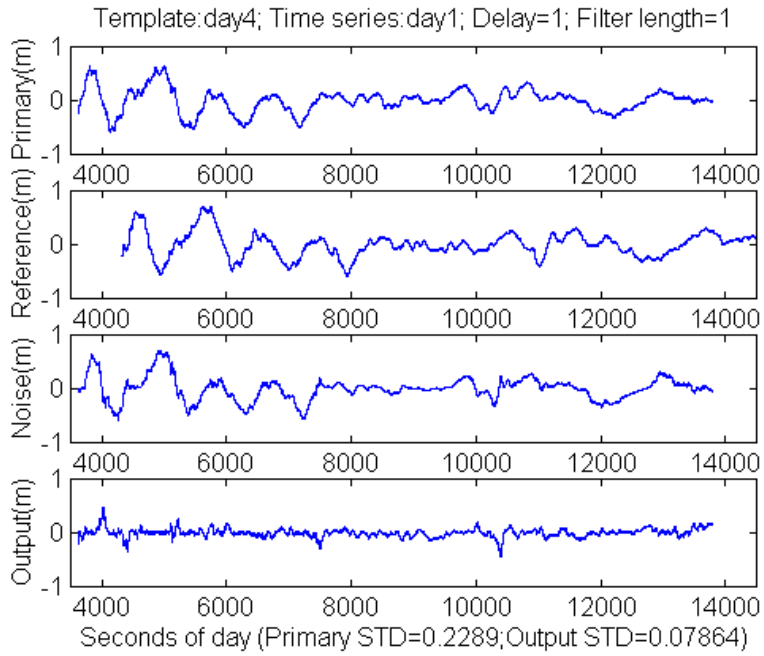

Figure 4.6 Backward adaptive filtering results for pseudo-range multipath for the Day 4 and Day 1 pair.

Other combinations of pseudo-range multipath time series have also been calculated using the adaptive filter. All of the results (including those not illustrated in the figures here) are summarised in Table 4-1.

The standard deviations of the pseudo-range time series before multipath correction are given in italics on the diagonal of the table. The standard deviations of the pseudo-range time series after multipath correction using forward filtering are given in the triangle above the diagonal while the backward filtering results are presented in the triangle below the diagonal.

Table 4-1 Standard deviation of pseudo-range time series before (in *italic*) and after multipath correction (unit: m).

Ref\Prim	Day 1	Day 2	Day 3	Day 4
Day 1	*0.229*	**0.046**	0.059	0.071
Day 2	0.054	*0.215*	**0.047**	0.065
Day 3	0.068	0.048	*0.211*	**0.052**
Day 4	0.079	0.063	0.048	*0.218*

Considering these results, it can be concluded that:

- a pseudo-range multipath model can be reliably derived using an adaptive filter, independent of the combinations of pseudo-range time series pairs used, as long as the antenna environment remains unchanged;
- the older the reference signal, the less accurate the pseudo-range multipath correction;
- forward filtering is better than backward filtering; and
- the best pseudo-range multipath mitigation strategy is forward filtering using data on two consecutive days (as indicated by the results in bold in Table 4-1), which reduces the STD of the pseudo-range multipath time series to about one fourth.

4.4 Carrier-Phase Multipath Mitigation Using The Adaptive Filter

All the analyses in this section are based on Data set 2. Fig. 4.7 illustrates the forward adaptive filtering results for carrier phase multipath for the Day 1 and Day 2 pair. From top to bottom in the figure: the multipath time series of carrier phase results on Day 2, which is used as primary input to the filter; the time series of Day 1, which is used as the reference input to the filter; the carrier phase multipath model derived by the adaptive filter (noise); and the output from the adaptive filter. Noted that its STD is only half of the primary input, which indicates that the multipath effect has been reduced. The horizontal axis indicates the seconds of the day and the unit of the vertical axis is millimetres.

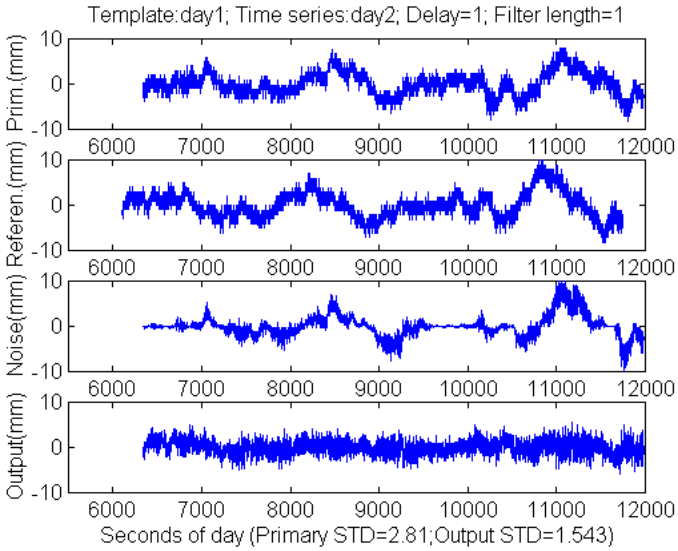

Figure 4.7 Forward adaptive filtering results for carrier phase multipath for the Day 1 and Day 2 pair.

As in the case of the pseudo-range analyses described in Section 4.3, other combinations of carrier phase multipath time series have also been calculated using the adaptive filter described here. All of the results are summarised in Table 4-2.

The standard deviations of the carrier phase time series before multipath correction are given in italics on the diagonal of the table. The standard deviations of the carrier phase time series after multipath correction using forward filtering are given in the triangle above the diagonal, while the backward filtering results are presented in the triangle below the diagonal.

Table 4-2 Standard deviation of carrier phase time series before (in *italic*) and after multipath correction (unit: mm).

Ref\Prim	Day 1	Day 2	Day 3	Day 4
Day 1	*2.54*	**1.54**	1.51	1.51
Day 2	1.47	*2.81*	**1.41**	1.47
Day 3	1.60	1.58	*2.33*	**1.46**
Day 4	1.60	1.69	1.48	*2.43*

Considering these results, it can be concluded that:

- a carrier phase multipath model can be reliably derived using an adaptive filter, independent of the combinations of time series pairs used, as long as the antenna environment remains unchanged;
- the older the reference signal, the less accurate the multipath correction to carrier phase;
- forward filtering is better than backward filtering; and
- the best carrier phase multipath mitigation strategy is forward filtering using data on two consecutive days (as indicated by the results in bold in Table 4-2), which reduces STD of the residual double-differenced time series to about one half.

4.5 Multipath Mitigation Using Adaptive Filtering Applied To CGPS Data

CGPS data in the RINEX format from the BRAN station in the SCIGN network for 4 days beginning on 28 November 1999 (DOY 332) were used in this study of multipath mitigation using an adaptive filter. An Ashtech Z12 GPS receiver was deployed at the station. The data sampling interval is 30 seconds. The pseudo-range multipath time series on L1 (Data set 3) over about 4 hours each day, for satellite PRN 2, were generated (Fig. 4.8), and then used in the adaptive filtering step (see Fig. 4.9, in layout similar to Fig. 4.1). In this example, the multipath is reduced from 0.28m in the primary sequence to 0.15m in the output.

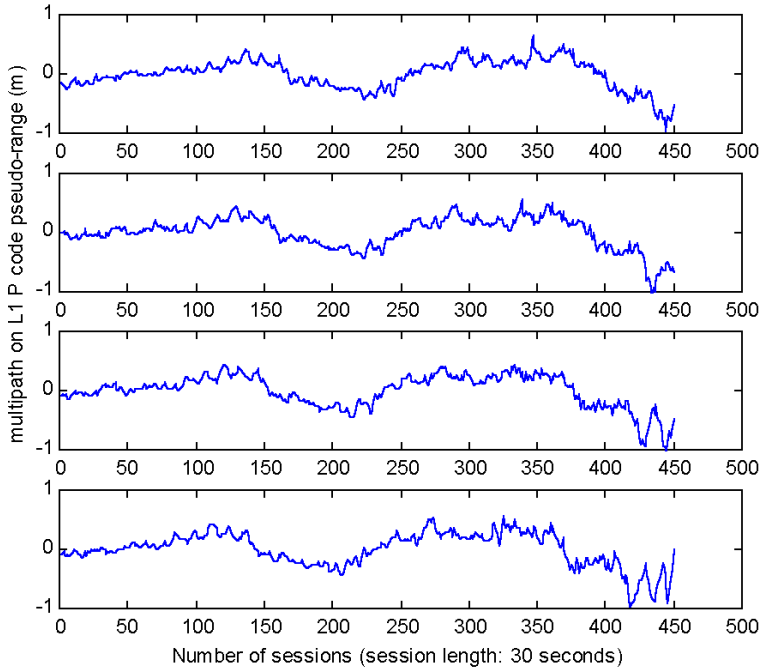

Figure 4.8 Pseudo-range multipath for station BRAN of SCIGN (top to bottom plot: DOY 332 to 335).

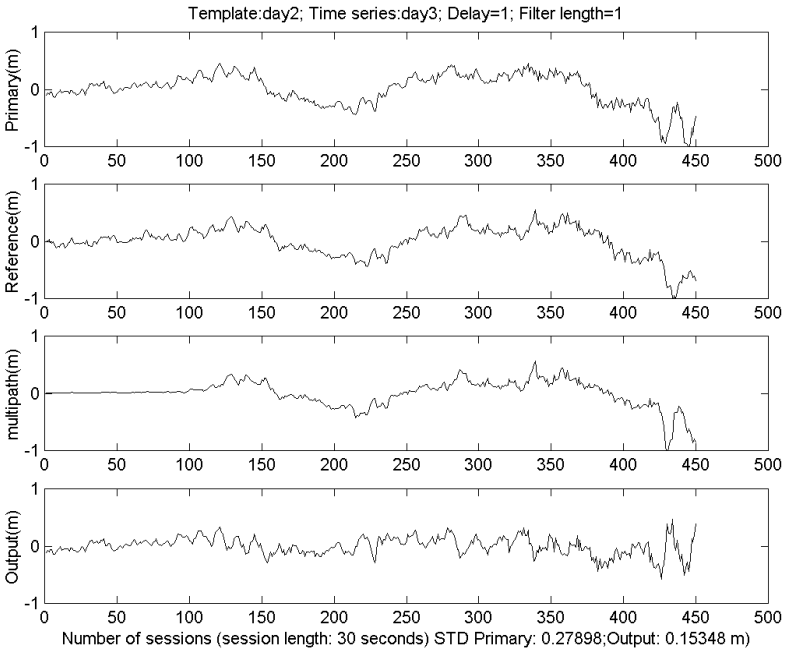

Figure 4.9 Forward adaptive filtering results for pseudo-range multipath for the Day 2 and Day 3 pair.

The adaptive filtering results are summarised in Table 4-3, arranged in the same format as Tables 4-1 and 4-2. Conclusions similar to those in Section 4.3 can also be drawn, though the STD in the output is only reduced to about half of the primary signal.

Table 4-3 Standard deviation of the pseudo-range time series before (in *italic*) and after multipath correction (unit: m).

Ref\Prim	Day 1	Day 2	Day 3	Day 4
Day 1	*0.26*	**0.14**	0.17	0.20
Day 2	0.13	*0.26*	**0.15**	0.19
Day 3	0.16	0.15	*0.28*	**0.16**
Day 4	0.18	0.17	0.16	*0.29*

4.6 Implementing Procedures For Retro-Active Temporal Densification

There are three major steps in implementing an algorithm for multipath mitigation based on adaptive filtering. The first step is to derive the necessary pseudo-range or carrier phase multipath time series from GPS measurements. Since the pseudo-range "multipath combination" (Eqs. (4.1) and (4.2)) is formed from one-way, dual-frequency phase and pseudo-range data, which are available from a single GPS receiver, pseudo-range multipath mitigation can be carried out on a single receiver basis.

In contrast, the carrier phase multipath series are obtained by double-differencing (Eq. (4.4)) the phase measurements from two relatively closely-spaced receivers (close enough to make the assumption of effective cancellation of spatially-correlated atmospheric biases), one subject to multipath disturbance, and the other in a multipath-free environment. This may become a limitation in a sparse CGPS array. However, in an array such as the Japanese GEONET, it is always possible to identify some reference stations free of multipath, and to generate the RINEX data for a Virtual Reference Station (VRS) located close enough to the CGPS station targeted for multipath mitigation.

The second step is to input the derived multipath series into the adaptive filter to extract the multipath model as was done in the studies reported in the previous sections. In the third step, the multipath model (one-way pseudo-range, or double-differenced carrier phase) are used to generate the multipath-corrected observable (pseudo-range or double-differenced carrier phase) sequence, which can then be used for point positioning, baseline solutions, etc.

4.7 Concluding Remarks

An adaptive filter based on the least-mean-square algorithm has been used to extract and eliminate multipath. This algorithm can be used in real-time. The adaptive filter is a powerful signal decomposer, able to distinguish the underlying coherent component of multipath on consecutive days even though the pseudo-range and carrier phase data series are significantly different. The extracted pseudo-range multipath behaves very much like that of carrier phase, except that the variation is much larger (in the examples in this study, it is two orders of magnitude larger).

Multipath models for both pseudo-range and carrier phase have been reliably derived using the adaptive filter, independent of the combinations of time series pairs used, as long as the antenna environment remains unchanged. However, it is found that the older the multipath reference signal, the less accurate the multipath correction. Forward filtering is better than backward filtering, and hence the best multipath mitigation strategy is forward filtering using data on two consecutive days. Such a strategy reduces standard deviations of the pseudo-range multipath time series to about one fourth the original values, and in the case of carrier phase to about a half, based on the experimental GPS data considered here. In the case of CGPS data from the SCIGN, the standard deviations of the pseudo-range multipath time series is reduced to about a half. The results in Table 4-1 are much better than those in Table 4-3 because the two antenna environments are very much different.

This multipath reduction technique can be used both on older data sets as well as new GPS data, and because the technique uses pseudo-range and carrier phase data collected simultaneously, it is sensitive to time-varying environmental effects at CGPS sites.

As a further study, GPS solutions with and without the multipath corrections can be compared to assess improvements in precision and accuracy. The identification of multipath reflectors at CGPS sites can be compared with site descriptions and changes in environmental factors. Also, where possible, multipath-corrected solutions can be compared with independent techniques such VLBI and SLR to test the effectiveness of this retro-active temporal densification scheme.

In the next Chapter, the tools developed here to extract and mitigate multipath noise will be used as a basis for using multipath effect as a signal.

5 ALL-GPS PARALLEL TEMPORAL DENSIFICATION – THE USE OF MULTIPATH EFFECTS AS A SIGNAL

As reviewed in Chapter 4, multipath has long been considered a major error source in deformation monitoring using CGPS. In this Chapter, an attempt is made to use multipath as a **signal**. As mentioned in Chapter 1.1, measurements from at least four GPS satellites have to be used in order to solve for the three dimensional position of the GPS antenna and the receiver clock. Using multipath as a signal to, e.g., monitor any change in the antenna environment, it is proposed that each GPS satellite produce an independent result of the monitoring of the environment, because multipath errors detected by the GPS receiver is actually the outcome of interferometry between the direct and indirect GPS signals. Because eight or more GPS satellites may be tracked from a single receiver, there are many more measurements in the same epoch. Hence, this approach of using multipath as a signal, according to Fig. 1.8, is in fact an **all-GPS parallel temporal densification** *(Ge et al, 2000g)*. This scheme is aimed to take advantage of the GPS noise rather than pushing the temporal limits of Fig. 1.7.

In this Chapter the procedures to extract multipath and to detect its change using the adaptive filter are discussed in detail. Then the methodology is used to process CGPS data from both a stationary and a changing antenna environment. Before concluding the Chapter, mathematical models relating the multipath change to the change of the GPS antenna environment, e.g. due to the movement of a slope, are derived, suggesting another promising application of this all-GPS parallel temporal densification scheme.

This technique provides an easy-to-implement, quality assurance tool for CGPS antenna environmental sensing after events such as typhoons, cyclones, snowfalls, volcano

eruptions, earthquakes, etc. Other possible applications include the monitoring of slope stability and ground subsidence.

5.1 Introduction

No matter how well continuously operating GPS (CGPS) networks are designed, multipath is a significant concern as it impacts on the quality of the CGPS outputs or 'products'. Moreover, it may change slowly on a seasonal basis, or abruptly due to events such as a snowfall.

Recently effort has also been made to make use of multipath, i.e. to use it as a signal rather than a noise (e.g. Ding et al., 1999). The idea of analysing GPS errors and biases for signal is not a new one. The best example is the so-called “GPS Meteorology”, which uses the atmospheric refraction effects on GPS measurements as its input. Therefore, instead of focusing on multipath mitigation, in this Chapter GPS multipath is used as a signal to sense the change in the GPS antenna environment. This capability is very useful in the maintenance and quality assurrance of CGPS networks such as the GEONET, where the GPS monitoring environment can be changed not only by natural phenomenon such as snow accummulation and tree growth, but also by disasters such as volcanic eruption, typhoon and earthquake.

5.2 Multipath Extraction

Based on the analysis in Chapter 4, in the case of multipath extraction the multipath residual sequence derived using the multipath combinations on a selected day can be expressed as:

$$D_1(t) = MP_1(t) + N_1(t) \qquad (5.1)$$

where $N_1(t)$ and $MP_1(t)$ are the noise free of multipath and the noise contribution from multipath respectively.

The multipath sequence on the next day is expressed as:

$$D_2(t) = MP_2(t) + N_2(t) \qquad (5.2)$$

where $N_2(t)$ and $MP_2(t)$ have similar definitions as $N_1(t)$ and $MP_1(t)$.

According to previous studies (e.g. Han & Rizos, 1997), $MP_1(t)$ and $MP_2(t)$ are highly correlated. But $N_1(t)$ and $N_2(t)$ are uncorrelated, which means that the two conditions of using the adaptive filter as mentioned in Chapter 2 are only partly satisfied. In this case, as demonstrated in a numerical simulation study in Chapter 2.4, the adaptive filter can still be used to extract multipath from the combination results of the second day by employing those of the first day as a reference signal. And $N_2(t)$ and $MP_2(t)$ will be outputs from the filter as the "incoherent component" *e(n)* and "coherent component" *y(n)* respectively.

In order to extract multipath, M days worth of GPS data are divided into M-2 sets, each of which consists of data from three consecutive days, as follows:

Set	Consecutive days
1	1, 2, 3
2	2, 3, 4
3	3, 4, 5
…….	
M-2	M-2, M-1, M

That is, there are 3 days in each set and among them there are 2 days overlapping in two consecutive sets. After the multipath combination, following Eqs. (5.1) and (5.2) the multipath residual sequences can be expressed as:

Day 1 in Set i, $D_{i1}(t) = MP_{i1}(t) + N_{i1}(t)$

Day 2 in Set i, $D_{i2}(t) = MP_{i2}(t) + N_{i2}(t)$

Day 3 in Set i, $D_{i3}(t) = MP_{i3}(t) + N_{i3}(t)$

Or for Day j in Set i, $D_{ij}(t) = MP_{ij}(t) + N_{ij}(t)$

Where, i=1, 2, …, M-2

j=1, 2, and 3

We define @ as the adaptive filtering operator and A@B as the adaptive filtering process using A as the primary input and B as the reference input. Then for the Day 1 and Day 2 pair:

$$D_{i2}(t) @ D_{i1}(t) = [\hat{MP}_{i2}(t) \quad \hat{N}_{i2}(t)] \tag{5.3}$$

where $\hat{MP}_{i2}(t)$ is the adaptive filter estimated multipath for Day 2 in Set i (coherent output) and $\hat{N}_{i2}(t)$ is the estimated receiver noise (incoherent output). Similarly for the Day 2 and Day 3 pair:

$$D_{i3}(t) @ D_{i2}(t) = [\hat{MP}_{i3}(t) \quad \hat{N}_{i3}(t)]$$

The estimated multipath for Day j in Set i can be further expressed as:

$$\hat{MP}_{ij}(t) = MP_{ij}(t) + d\,MP_{ij}(t) \tag{5.4}$$

where $d\,MP_{i2}(t)$ is the multipath estimation error. If there is no change in the antenna environment then:

$$MP_{i\ j}(t) = MP_{i\ j-1}(t + \Delta t) \tag{5.5}$$

Δt is typically 236sec although it may be different for different satellites (Wanninger & May, 2000).

5.3 Multipath Change Detection

If there is a change of the antenna environment between Days 2 and 3, then:

$$MP_{i\,3}(t) = MP_{i\,2}(t + \Delta t) + \Delta MP_i(t) \tag{5.6}$$

and

$$\hat{MP}_{i3}(t) @ \hat{MP}_{i2}(t) = [MP_{i2}(t + \Delta t) \quad \Delta MP_i(t)] \tag{5.7}$$

where $\Delta MP_i(t)$ is the multipath change between Days 2 and 3 in Set i.

This approach to multipath change detection resembles the 3-pass differential radar interferometry (InSAR) technique (Gabriel et al., 1989; also Chapter 7), in which the elevation change is extracted by InSAR from the terrain model that is also constructed by InSAR.

To summarize, as illustrated in Fig. 5.1, there are three main steps in implementing multipath change detection based on adaptive filtering. The first step is to derive the pseudo-range or carrier phase multipath residual time series through multipath combination of the GPS measurements. Since the pseudo-range "multipath combination" is formed from one-way, dual-frequency phase and pseudo-range data, which are available from the same GPS receiver, pseudo-range multipath extraction can be implemented on a single receiver basis.

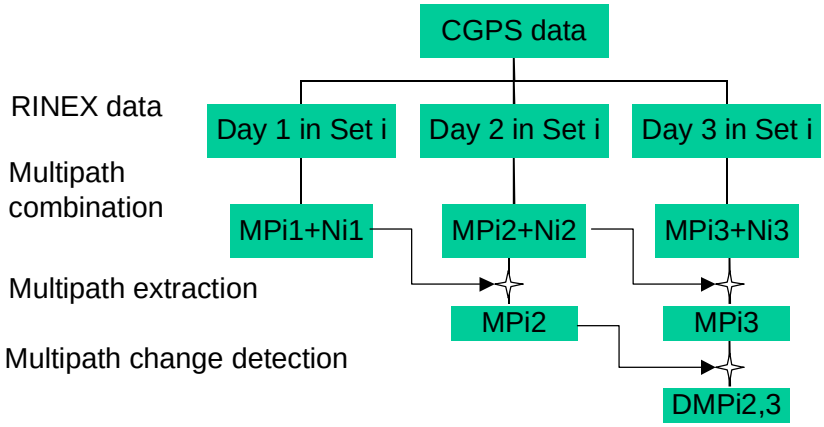

Figure 5.1 Multipath change detection procedures.

On the other hand, the carrier phase multipath series are obtained by double-differencing the phase measurements from two relatively closely spaced receivers (close enough to make the assumption of effective cancellation of spatially-correlated atmospheric biases), one subject to multipath disturbance, and the other in a multipath-free environment. This may be a severe limitation in a sparse CGPS array. However, in an array such as the GEONET of Japan, it is always possible to identify some reference stations free of multipath, and then generate the *apparent* RINEX data for a Virtual Reference Station (VRS) (Bücherl et al., 2000) located close enough to the CGPS station considered for multipath extraction.

In the second step, the adaptive filter (indicated by the star in Fig. 5.1) is used first to extract the multipath from the residual series from two consecutive days, obtained from the multipath combination (Eqs. (5.3) and (5.4)). Two multipath series will be obtained for each 3 day set as a result.

In the third step, the adaptive filter is used again to detect the multipath change between the two multipath series derived in the second step (Eq. (5.7).

In the following two sections this technique is first used for multipath change detection in a stationary antenna environment to test if the detected change is zero when there is no

change in the antenna environment. Then it is applied for multipath change detection in a changed antenna environment to test if the technique can identify the change when there is indeed a change in the multipath disturbance caused by snowfall.

5.4 Multipath Change Detection in a Stationary Antenna Environment

Two data sets were used in this test, which were the same as those used in the Han & Rizos (1997) study. In the first data set, the pseudo-range data over a period of nearly 3 hours for four successive days, collected on the roof of the Geography and Surveying (GAS) building, at the University of New South Wales (UNSW), from 30 September to 3 October 1997, using an Ashtech Z12 GPS receiver, were used to compute the pseudo-range multipath time series. (In this study only the 'pseudo-range multipath time series' for L1 for satellite PRN 9 are used.)

In the second data set, multipath series of double-differenced carrier phase measurements over a period of nearly 2 hours on four successive days for two satellites (PRNs 1 and 21) were calculated from data collected in an experiment carried out on the roof of the GAS building at UNSW, from 28 April to 1 May 1997, using two Leica SR299 GPS receivers with a baseline length of about 6 metres. Here the residual series of double-differenced carrier phase observations are used as the 'carrier phase multipath time series' because they reflect the multipath disturbance and observation noise (it is assumed that all the other errors and biases are negligible because the baseline length is only of the order of 6 metres).

Fig. 5.2 shows the results of the pseudo-range multipath combination. From top to bottom the plots represent the pseudo-range multipath residual sequences from Day 1 to Day 4. It can be seen that although they look very similar there are differences between them due to the change of uncorrelated noise from day to day. Also the Δt (about 236sec) advance between two consecutive days can be clearly seen.

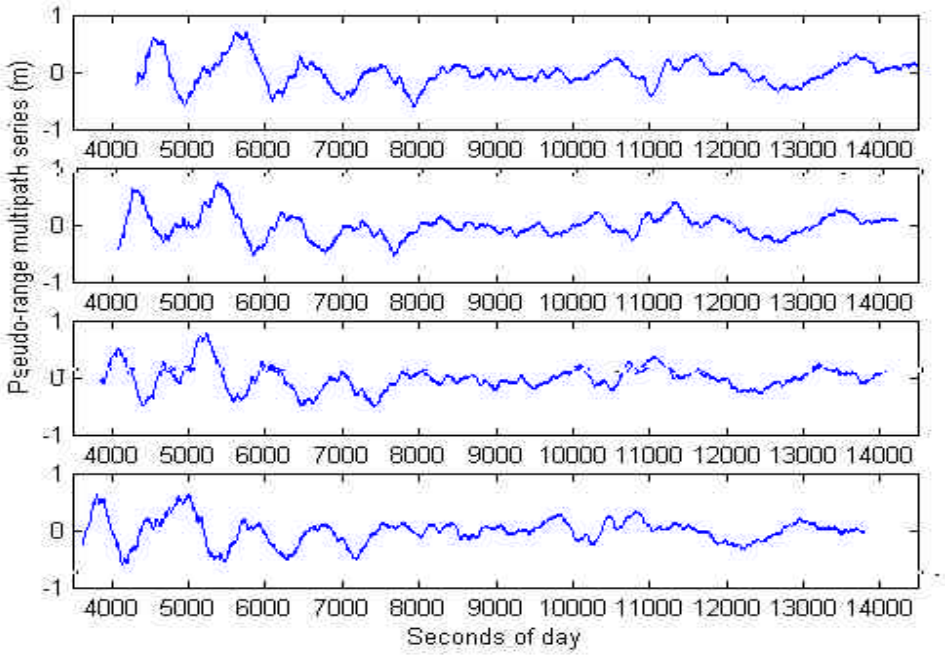

Figure 5.2 Pseudo-range Multipath Combination Results.

Fig. 5.3 shows the multipath extraction result for Day 2 using the multipath residual sequence of Day 1 as reference input. The extracted multipath on Day 2 (MP2) is displayed in the third plot and the fourth one gives the uncorrelated noise. Similar extraction is done on pairs of days: Day 2 & Day 3, and Day 3 & Day 4 so that MP2, MP3 and MP4 are all obtained.

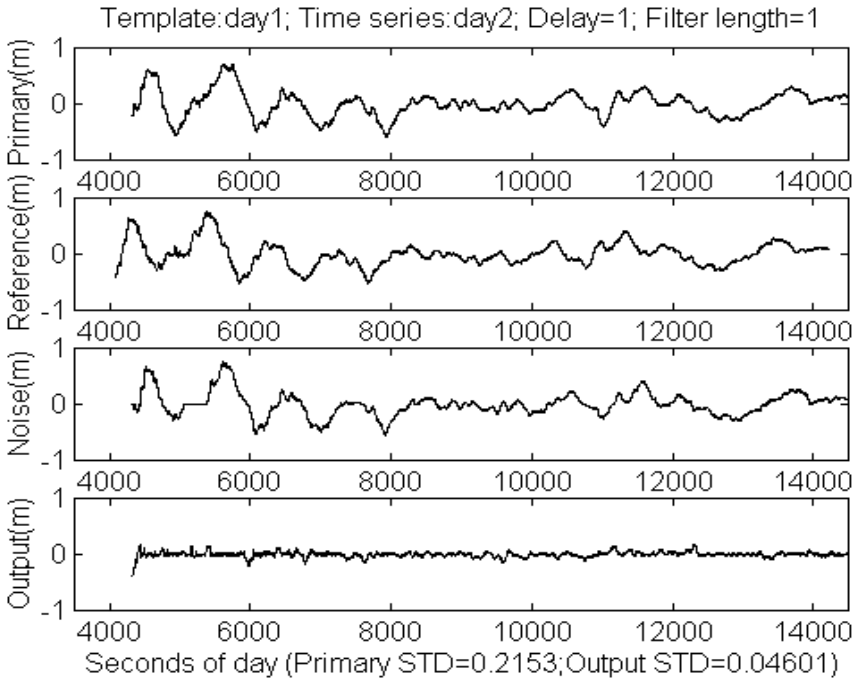

Figure 5.3 Multipath Extraction Result.

Figs. 5.4 and 5.5 display the multipath change detection results for pairs of days Day 2 & Day 3 and Day 3 & Day 4. The multipath change is given in the fourth plot. Comparing the plots for MP2, MP3, and MP4 in these figures, they look much more similar to each other than the multipath residual sequences for Day 1 to Day 4, which highlights the importance of multipath extraction for reliable multipath change detection.

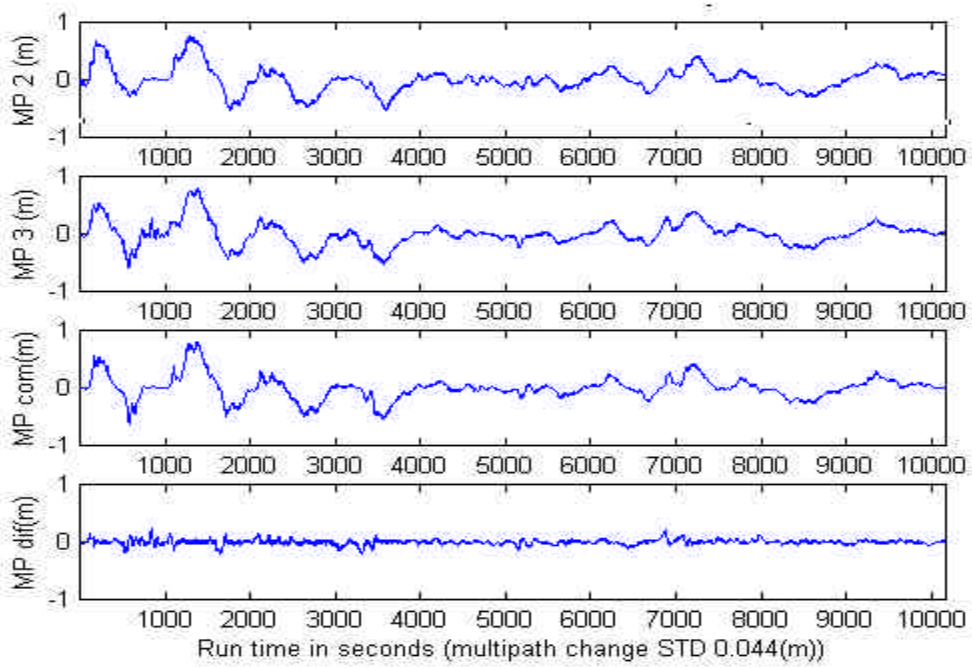

Figure 5.4 Multipath Change Detection Result (Day 2-3).

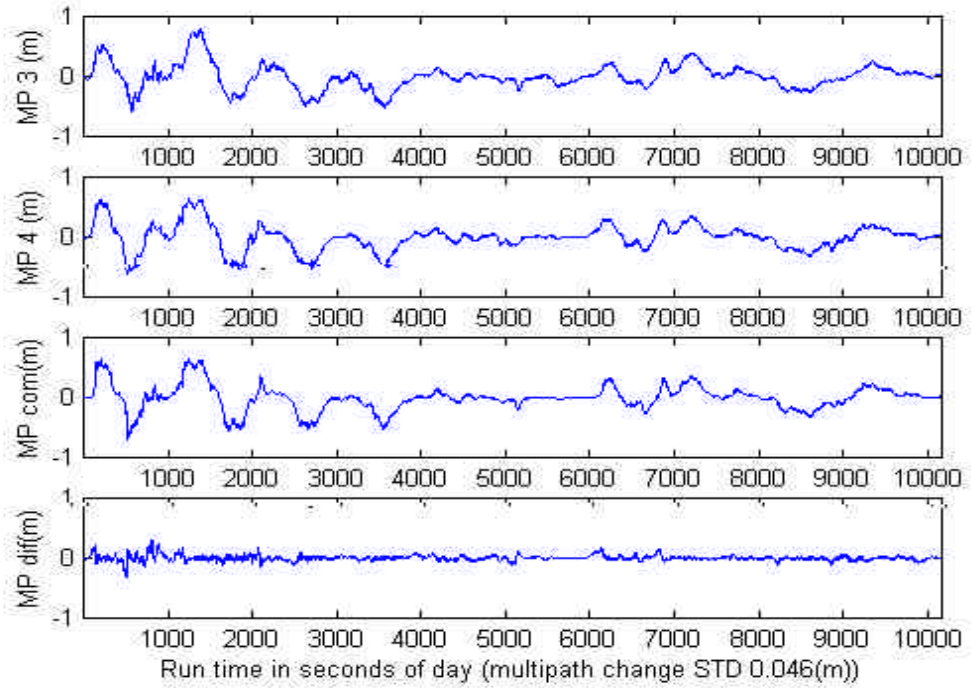

Figure 5.5 Multipath Change Detection Result (Day 3-4).

Table 5-1 summarizes the standard deviations (STD) of the pseudo-range multipath extraction (the first three rows) and change detection (the last two rows) results. Note that in the multipath extraction step, the incoherent output is the uncorrelated noise and the coherent output is multipath, while in the multipath change detection step the incoherent output is the change of multipath and the coherent output is correlated multipath. Note that the changes of multipath detected are not zero as they should be, but are 0.044 and 0.046m in the pairs Day 2 & Day 3 and Day 3 & Day 4 respectively, which are nevertheless smaller than the derived uncorrelated noise. Therefore, a tentative conclusion is that any multipath change smaller than the uncorrelated noise (mainly the receiver noise) will go undetected.

Table 5-1 Multipath Extraction and Change Detection: Pseudo-Range Result.

Day	Incoherent Output STD (m)	Coherent Output STD (m)
2	0.046	0.210
3	0.047	0.205
4	0.052	0.212
2-3	0.044	0.201
3-4	0.046	0.207

Now the technique is used to detect the multipath change of the carrier phase. Fig. 5.6 shows the results of the carrier phase multipath combination. From top to bottom the plots represent the carrier phase multipath residual sequences from Day 1 to Day 4. As in the case of pseudo-range, it can be seen that although they look very similar there are differences between them due to the change of uncorrelated noise from day to day. Also the Δt (about 236sec) advance between two consecutive days can be clearly seen.

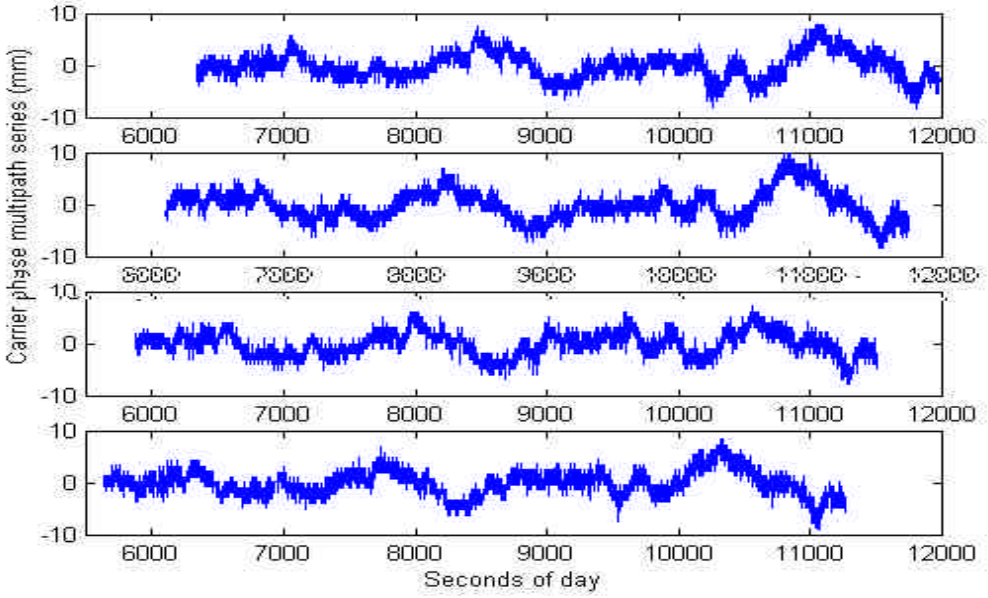

Figure 5.6 Carrier phase multipath combination result.

Fig. 5.7 shows the carrier phase multipath extraction result for Day 2 using the multipath residual sequence of Day 1 as reference input. The extracted multipath on Day 2 (MP2) is displayed in the third plot and the fourth one gives the uncorrelated noise. Similar extraction is done on pairs of days: Day 2 & Day 3, and Day 3 & Day 4 so that MP2, MP3 and MP4 are all obtained.

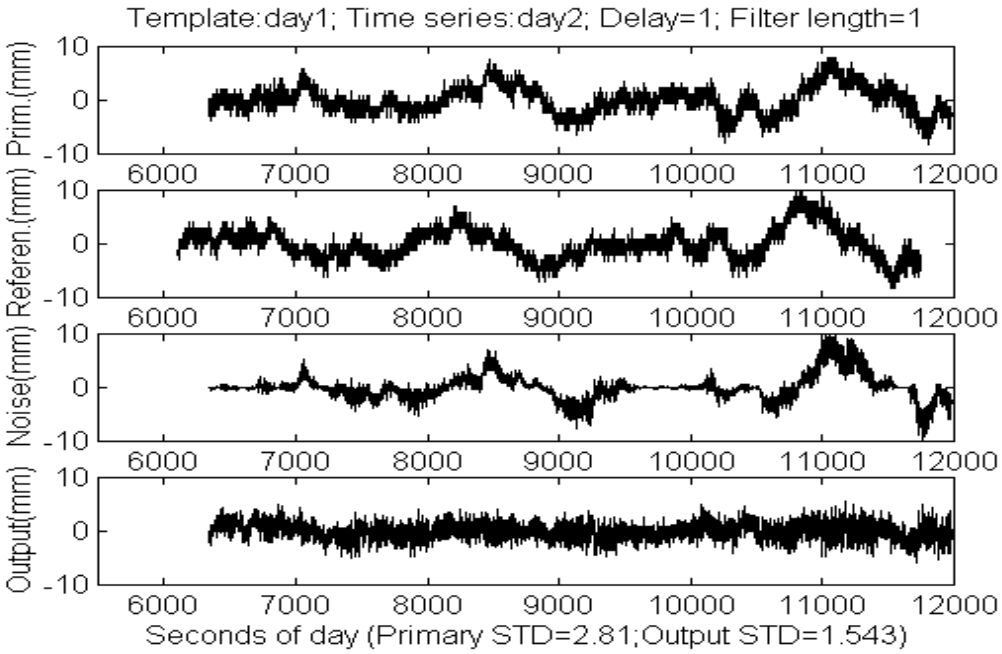

Figure 5.7 Multipath Extraction Result.

Figs. 5.8 and 5.9 display the carrier phase multipath change detection results for pairs of days Day 2 & Day 3 and Day 3 & Day 4. The multipath change is given in the fourth plot. Comparing the plots for MP2, MP3, and MP4 in these figures, they look much more similar to each other than the multipath residual sequences for Day 1 to Day 4, which highlights the importance of carrier phase multipath extraction for reliable multipath change detection.

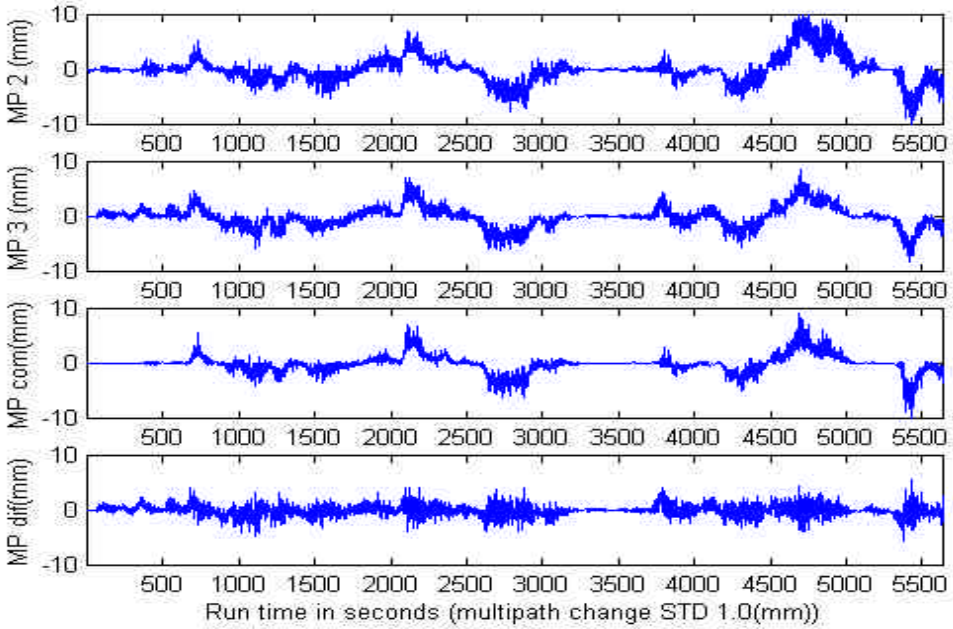

Figure 5.8 Multipath Change Detection Result (Day 2-3).

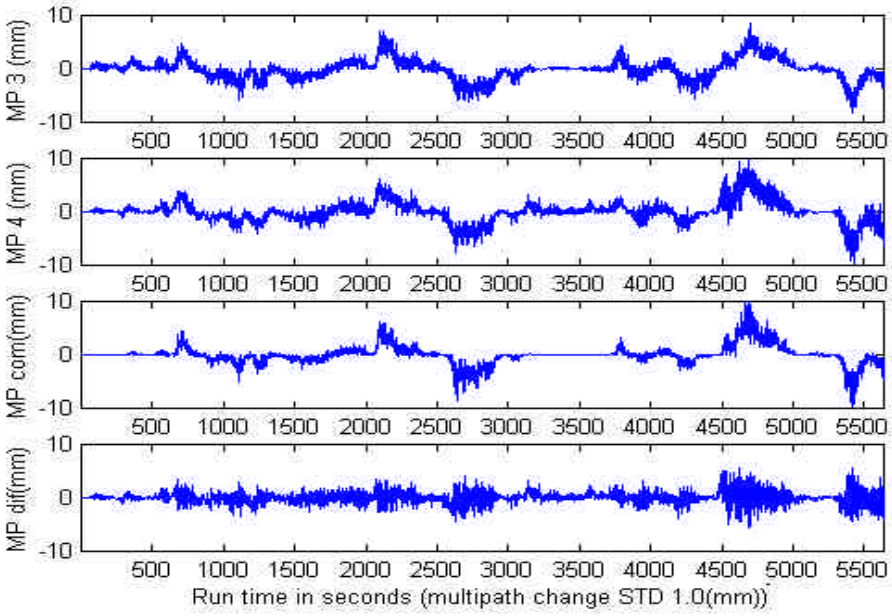

Figure 5.9 Multipath Change Detection Result (Day 3-4).

Table 5-2 summarizes the standard deviations (STD) of the carrier phase multipath extraction (the first three rows) and change detection (the last two rows) results. Note that in the multipath extraction step, the incoherent output is the uncorrelated noise and the coherent output is multipath while in the multipath change detection step the incoherent output is the change of multipath and the coherent output is correlated multipath. Note that the changes of multipath detected are not zero as they should be, but are 0.966 and 1.010m in the pairs Day 2 & Day 3 and Day 3 & Day 4 respectively, which are nevertheless smaller than the derived uncorrelated noise. Therefore, a tentative conclusion, similar to the pseudo-range case, is that any carrier phase multipath change smaller than the uncorrelated noise (mainly the receiver phase noise) will go undetected.

Table 5-2 Carrier Phase Multipath Extraction and Change Detection Result.

Day	Incoherent Output STD (mm)	Coherent Output STD (mm)
2	1.543	2.367
3	1.409	1.866
4	1.457	1.969
2-3	0.966	1.624
3-4	1.010	1.718

Therefore, one conclusion is that multipath change (either in pseudo-range or carrier phase) above the receiver noise level (in the case of this study: code: 0.05m; phase: 1.5mm) could be detected using this technique.

5.5 Multipath Change Detection in a Changed Antenna Environment

To test the capability of this technique in detecting multipath change, continuous GPS data from two Japanese GEONET stations 960627 and 92110 located in the Tsukuba City were used. In both Station 960627 and Station 92110, a Trimble 4000SSI receiver and a Permanent L1/L2 antenna are installed at each station. The approximate coordinates X, Y and Z for Station 960627 are -3957244.2254m, 3310369.6968m, and 3737538.8800m (WGS84). Data from DOY 60 to 99 in the year 1998 are used in this test. While at Station

92110, the approximate coordinates X, Y and Z are -3957164.7499m, 3310202.7523m and 3737759.8264m. Data used are from DOY 60 to 88 in the year 1998 (unfortunately the RINEX files for DOY 89 to 99 were corrupted when writing to a CD). Hence the distance between the two stations is about 286m.

An abnormal change as large as 3cm in the time series of the baseline length between the two stations was detected by Hatanaka & Fujisaku (1999). In their study, the elevation-dependent antenna phase centre was compared for both L1 and L2, calculated every 3 hours from 15:00 Japan Standard Time (JST) on March 5 (DOY 64) to 9:00 JST on March 6. A big offset was seen in the result for the period 0:00 to 3:00 on March 6 compared to those of the other segments, which corresponds to the time of a snowfall, as illustrated in Fig. 5.10. Moreover, the phase change on L2 was more significant that on L1.

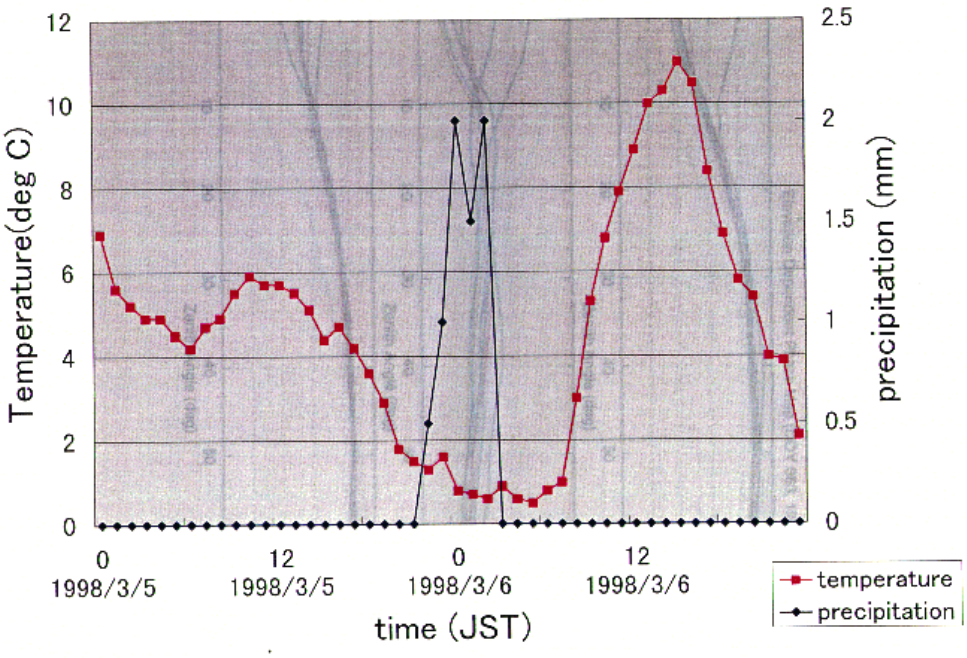

Figure 5.10 Precipitation and temperature in Tsukuba from 5 March (DOY 64) to 6 March (DOY 65) 1998.

In order to test whether the adaptive filtering technique can detect this change in the antenna environment, the CGPS data were processed following the procedures outlined in the previous sections.

Fig. 5.11 is the pseudo-range multipath STD change on the C1 code at Station 960627 for satellite PRN25. The total change (the biggest one in the figure) in the multipath STD from DOY 64 to 65 is 0.19m, while the second biggest change is 0.10m from DOY 87 to 88, which is an almost 100% increase.

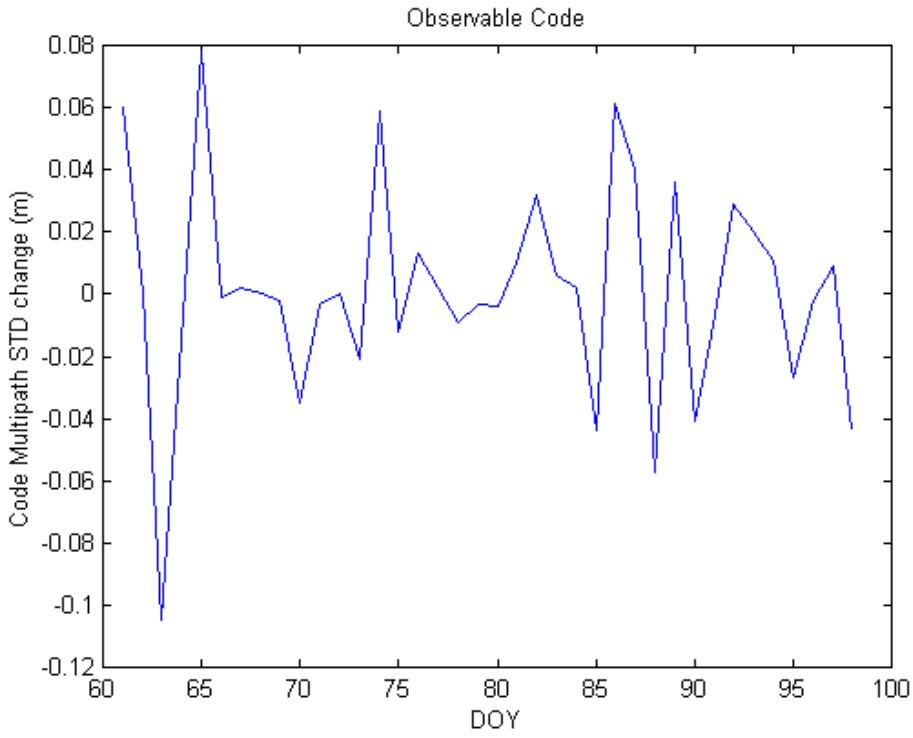

Figure 5.11 Pseudo-range multipath change on C1 code at Station 960627 for satellite PRN25.

Fig. 5.12 is the pseudo-range multipath STD change on the C1 code at Station 92110 for satellite PRN 22. The total change (the biggest one in the figure) in the multipath STD from DOY 64 to 65 is almost 0.09m, while the second biggest change is less than 0.07m from DOY 72 to 73, which is not as significant as in Fig. 5.11. This might indicate that Station 92110 is less vulnerable to multipath.

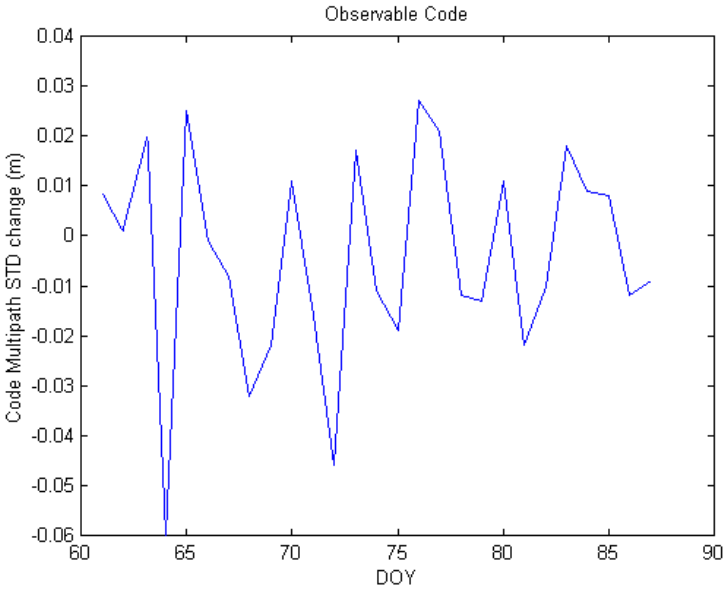

Figure 5.12 Pseudo-range multipath change on C1 code at Station 92110 for satellite PRN 22.

Figs. 5.13 and 5.14 are the results of carrier phase multipath change on L1 and L2 respectively in DD between Stations 92110 and 960627, for satellite pair PRNs 22 and 25. In the two results, the biggest changes all occur on DOY 64 to 65, although the L2 result gives a much better "signal-to-noise ratio", which is in agreement with the result of Hatanaka & Fujisaku (1999).

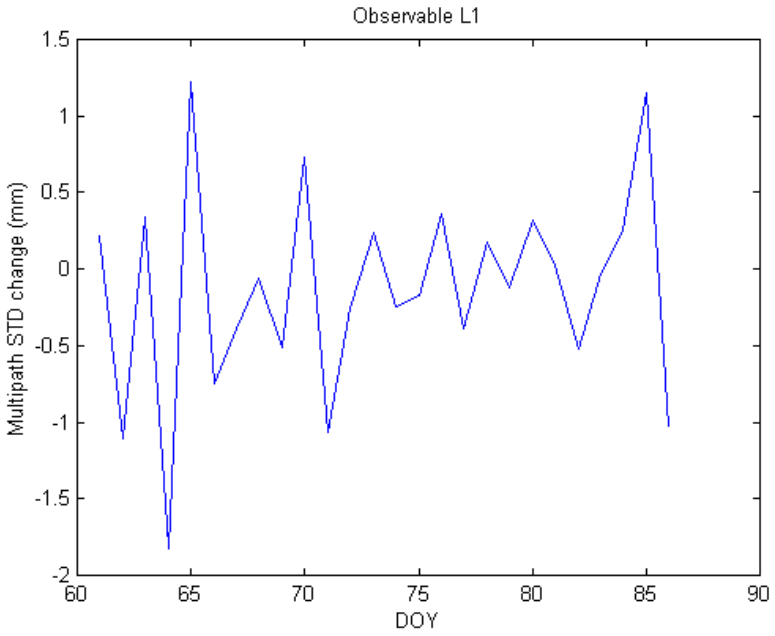

Figure 5.13 Carrier phase multipath change on L1 in DD between Stations 92110 and 960627 for satellite pair PRNs 22 and 25.

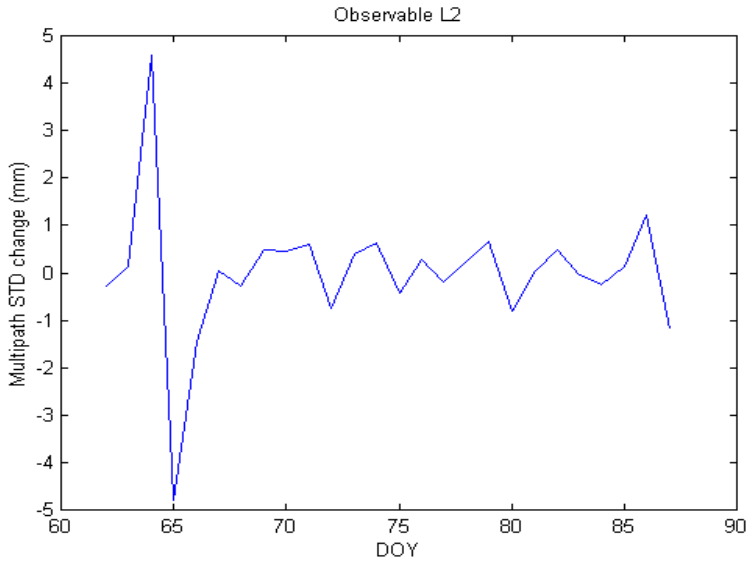

Figure 5.14 Carrier phase multipath change on L2 in DD between Stations 92110 and 960627 for satellite pair PRNs 22 and 25.

Therefore, it seems that when there is indeed a change in the antenna environment it will be detected using this technique.

5.6 Slope Stability Monitoring Using Multipath Change

In this Section multipath has been used as a signal in a technique for slope stability monitoring. The multipath combination, the multipath extraction and the detection of multipath change are the same as described in previous sections. The change of multipath is used in a least square process to estimate the slope movement parameters by employing the mathematical models developed in this Section. The technique can also be used for applications such as ground subsidence monitoring due to mining or underground water extraction.

Traditional slope stability monitoring equipment and techniques include:

- Survey techniques (e.g., EDM and GPS leveling or photogrammetric surveys);
- Displacement monitoring pins and tape extensometers fixed across cracks or major rock defects;
- Borehole inclinometers; and
- Extensometers anchored within the rock mass via boreholes drilled into slopes.

Compared to these techniques, there are obvious advantages in using the multipath effect for slope stability monitoring. Multipath signals have common transmission time at the satellite, almost common course through the atmosphere and are received by the same receiver at the same time. Therefore, they are less noisy than the satellite-receiver double-differenced observable. This ensures that the technique could achieve very high accuracy. Other advantages include the movement of the slope at multiple reflecting points can be monitored, which contributes to higher efficiency; moreover, the technique is relatively cheap and highly automatic because a GPS receiver is a general purpose equipment compared to the equipment used in some of the traditional techniques.

In this Section the mathematical models necessary to employ the GPS multipath effect for slope stability monitoring are derived.

5.6.1 Models for relating multipath to slope movement

5.6.1.1 Two dimensional model for relating multipath to slope movement

Fig. 5.15 is a slope in the 2D illustration monitored by the GPS multipath. For the application of slope stability monitoring using multipath effects, the antenna has to be installed at the foot of the slope instead of on the slope itself. In the figure, a is the satellite elevation angle, b is the incident angle of incoming GPS signal B'B on the slope, and the slope is in angle q to the ground. C'C is the direct line-of-sight signal from a GPS satellite and RC is the reflected signal by the slope. The GPS antenna phase centre C is *d* metres away from the foot of the slope and *h* metres above the ground DE. For the convenience of calculation, AC is parallel to the ground DE, CB is perpendicular to RB and DF is perpendicular to AC respectively.

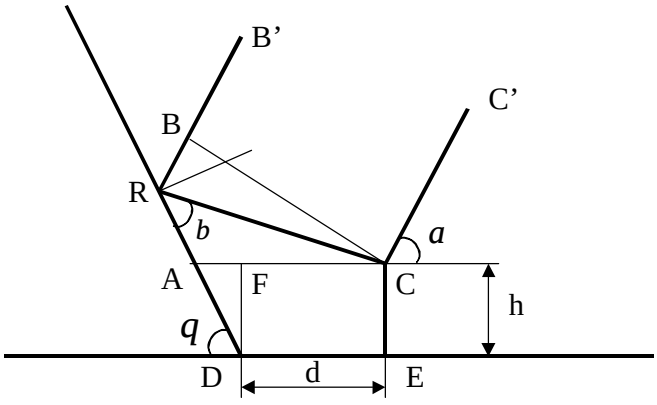

Figure 5.15 A slope in the 2D illustration monitored by the GPS multipath.

In ΔADF, DF = h and $\angle$DAF = q . Hence, AF = h / (tan$q$) and

$$AC = d + h / (\tan q) \quad (5.8)$$

In ΔACR, $b = 180^0 - (q + a)$ (5.9)

and $\angle CAR = 180^0 - q$. Hence, $CR / \sin(\angle CAR) = AC / \sin b$ or

$$CR = AC \sin q / \sin b \quad (5.10)$$

In ΔCBR, $\angle CRB = 180^0 - 2b$. Thus

$$BR = CR \cos(\angle CRB) \quad (5.11)$$

Therefore the geometric path length difference between the direct and reflected signals is: L = BR + CR or by using Eqs. (5.8) to (5.11),

$$L = 2 \sin(q + a)(d \sin q + h \cos q) \quad (5.12)$$

As will be seen from later discussions, Eq. (5.12) can be used to relate multipath to slope movement.

5.6.1.2 Three dimensional model for relating multipath to slope movement

Fig. 5.16 is a slope in the 3D rectangular coordinate system monitored by the GPS multipath. In the figure, the slope to be monitored is represented by a plane containing the y-axis and point *R*. The slope is in angle q to the horizontal plane xoy. j is the orientation of the slope. C'C is the direct line-of-sight signal from a GPS satellite and RC is the reflected signal by the slope. The GPS antenna phase centre C is *d* metres away from the foot of the slope and *h* metres above the ground DE. For the convenience of calculation, CB is perpendicular to RB.

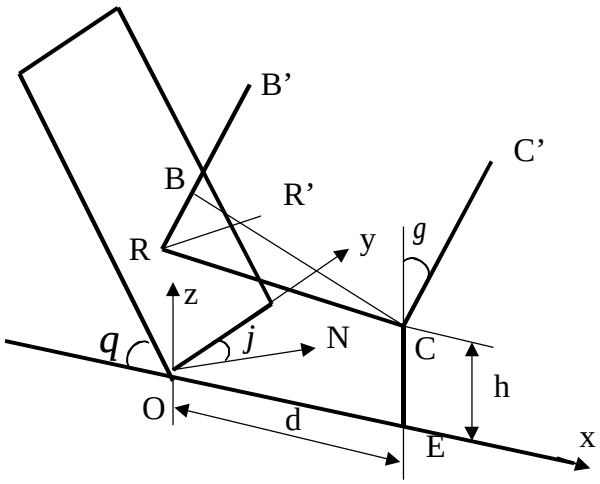

Figure 5.16 A slope in the 3D rectangular coordinate system.

Denoting the unit vectors along the x, y and z axes by $\vec{i}$, $\vec{j}$, and $\vec{k}$, the direction vector of the incident GPS signal is given by

$$\vec{B'B} = \vec{i}\cos a + \vec{j}\cos b - \vec{k}\cos g \qquad (5.13)$$

where, α, β, and γ, which are linked to the satellite elevation angle and slope orientation φ relative to north, can be calculated from the Keplerian elements of the GPS satellite and the location of the antenna.

The normal to the reflecting surface is

$$\vec{RR'} = \vec{i}\tan q + \vec{k} \qquad (5.14)$$

The direction vector of the reflected ray is (Stavroudis, 1972)

$$\vec{RC} = -\vec{B'B} + 2\cos d\ \vec{RR'} \qquad (5.15)$$

where d is the incident angle and

$$\cos d = \frac{\vec{B'B} \bullet \vec{RR'}}{|\vec{B'B}| \cdot |\vec{RR'}|}$$

$$= \cos a \sin q - \cos g \cos q \qquad (5.16)$$

Since the coordinates of point C are (d, 0, h), the equation of the line R C is

$$\begin{aligned} x &= d + (2 \cos d \tan q - \cos a)\, v \\ y &= (-\cos b)\, v \\ z &= h + (\cos g + 2 \cos d)\, v \end{aligned} \qquad (5.17)$$

Where -¥ < v < ¥.

Since the equation of the slope surface is $x \tan q + z = 0$, the coordinates of reflecting point R (x_R, y_R, z_R) can be calculated using Eq. (5.17) by using v defined as

$$v = \frac{h + d \tan q}{\cos a \tan q - \cos g - 2 \cos d / \cos^2 q} \qquad (5.18)$$

With the coordinates of point R known, the length of RC is

$$RC = \sqrt{(x_R - d)^2 + y_R^{\,2} + (z_R - h)^2} \qquad (5.19)$$

Therefore the geometric path length difference between the direct and reflected signals is

$$L = BR + RC = (1 + \cos 2d)\, RC \qquad (5.20)$$

As will be seen from later discussions, Eq. (5.20) can be used to relate multipath to slope movement.

5.6.2 The movement of slope and the change of geometric path length difference between the direct and reflected signals

5.6.2.1 The 2D model

Eq. (5.12), the geometric path length difference between the direct and reflected signals is

$$L = 2 \sin (q + a) (d \sin q + h \cos q) \quad (5.12)$$

By taking the partial derivative of L with respect to d and q

$$\partial L / \partial d = 2 \sin (q + a) \sin q \quad (5.21)$$

$$\partial L / \partial q = 2 d (\sin 2q \cos a + \sin a) + 2 h \cos a \cos 2q \quad (5.22)$$

The relationship between the movement of slope and the change of geometric path length difference between the direct and reflected signals can be expressed as

$$\Delta L = \Delta d (\partial L / \partial d) + \Delta q (\partial L / \partial q) \quad (5.23)$$

5.6.2.2 The 3D model

Eq. (5.20), the geometric path length difference between the direct and reflected signals is

$$L = (1 + \cos 2d) RC \quad (5.20)$$

By taking the partial derivative of L with respect to d and q

$\partial L / \partial d = (1 + \cos 2d)\,(\partial RC / \partial d)$ (5.24)

$\partial L / \partial q = (1 + \cos 2d)\,(\partial RC / \partial q) - 2\,RC \sin 2d\,(\partial d / \partial q)$ (5.25)

Using Eqs. (5.16) to (5.19)

$$\partial RC / \partial d = [(x_R - d)(\frac{\partial x_R}{\partial d} - 1) + y_R \frac{\partial y_R}{\partial d} + (z_R - h)\frac{\partial z_R}{\partial d}] / RC$$

$$\partial RC / \partial q = [(x_R - d)\frac{\partial x_R}{\partial q} + y_R \frac{\partial y_R}{\partial q} + (z_R - h)\frac{\partial z_R}{\partial q}] / RC$$

$\partial d / \partial q = \cos a \cos q + \cos g \sin q$

where

$\partial x_R / \partial d = 1 + (2 \cos\delta \tan\theta - \cos\alpha)\,(\partial v / \partial d)$

$\partial y_R / \partial d = (-\cos b)\,(\partial v / \partial d)$

$\partial z_R / \partial d = (\cos g + 2 \cos d)\,(\partial v / \partial d)$

$\partial x_R / \partial \theta = (2 \cos\delta \tan\theta - \cos\alpha)\,(\partial v / \partial \theta) - 2\,v \sin\delta \tan\theta\,(\partial \delta / \partial \theta) + 2\,v \cos\delta / \cos^2\theta$

$\partial y_R / \partial q = (-\cos b)\,(\partial v / \partial q)$

$\partial z_R / \partial q = (\cos g + 2 \cos d)\,(\partial v / \partial q) - 2\,v \sin d\,(\partial d / \partial q)$

$$\partial v / \partial d = \frac{\tan q}{\cos a \tan q - \cos g - 2 \cos d / \cos^2 q}$$

$$\partial v / \partial q = \frac{v}{h + d \tan q} \cdot \frac{d \cos q - v(\cos a \cos q + 2 \cos d \sin q)}{\cos^3 q}$$

Therefore, just as in the case of 2D model, the relationship of the 3D model between the movement of slope and the change of geometric path length difference (between the direct and reflected signals) can be expressed using Eq. (5.23).

5.6.3 The change of multipath and the movement of slope

The effect of multipath is characterized by four parameters (all of which are relative to the direct signal): 1) amplitude; 2) time delay; 3) phase; and 4) phase rate of change. For this analysis only 1) and 3) are significant.

Now consider first the case in which only one reflected signal from a planar surface interferes with the direct line-of-sight carrier signal. The direct and the reflected signals can be expressed as

$$\begin{aligned} S_0 &= A\cos j^{\,p} \\ S_1 &= a^{\,p} A\cos(j^{\,p} + q^{\,p}) \end{aligned} \tag{5.26}$$

where, S_0 is the direct signal from the satellite and S_1 is the reflected signal from the surface; A and $j^{\,p}$ are the amplitude and the phase of the signal, respectively; $a^{\,p}$ is the amplitude reduction factor which fulfills the inequality $0<a^{\,p}<1$; $q^{\,p}$ is the phase shift caused by multipath. To avoid confusion of notations with the previous discussions, a “p” in superscript is used to denote variables specific to multipath once inside the receiver.

Suppose the geometric path length difference between the direct and reflected signals is L and the microwave refractive index at the antenna site is n. L can be linked to slope parameters using Eqs. (5.12) (the 2D model) or (5.20) (the 3D model). The phase shift can be written in radians as

$$q^{\,p} = \frac{2pnL}{l} \tag{5.27}$$

where l is the length of the code (pseudo-range) or wavelength (carrier phase) of the signal.

When the two signals interfere at the antenna centre, the composite signal is (e.g., Leick, 1995)

$$S = S_0 + S_1 = A'\cos(j^{\,p} + y^{\,p}) \tag{5.28}$$

where the resultant amplitude A' is

$$A' = A(1 + 2a^{\,p}\cos q^{\,p} + (a^{\,p})^2)^{1/2} \tag{5.29}$$

and the phase delay $y^{\,p}$ is

$$y^{\,p} = \tan^{-1}\left(\frac{a^{\,p}\sin q^{\,p}}{1 + a^{\,p}\cos q^{\,p}}\right) \tag{5.30}$$

For the planar surface, the multipath error can be found by

$$MP = \frac{y^{\,p}}{2p}\,l \tag{5.31}$$

Because in Eq. (5.30) both $q^{\,p}$ and $2Np + q^{\,p}$ (N is an integer) will give the same $y^{\,p}$, there is a problem with the integer ambiguity N when trying to link multipath MP with L using Eqs. (5.31), (5.30) and (5.27). To address this problem, Eq. (5.27) is rewritten as

$$q^{\,p} + 2Np = \frac{2pnL}{l} \tag{5.27a}$$

Suppose there is still another planar surface to reflect the GPS signals, and the reflected signal is

$$S_2 = a^{p}_{1} A\cos(j^{p} + q^{p}_{1}) \tag{5.32}$$

By introducing, $j^{p}_{new} = j^{p} + y^{p}$; $q^{p}_{new} = q^{p}_{1} - y^{p}$; and

$$a^{p}_{new} = a^{p}_{1} / (1 + 2a^{p}\cos q^{p} + (a^{p})^2)^{1/2}$$

Eqs. (5.26) and (5.32) can be re-written as

$$\begin{aligned} S &= A'\cos j^{p}_{new} \\ S_2 &= a^{p}_{new} A'\cos(j^{p}_{new} + q^{p}_{new}) \end{aligned} \tag{5.33}$$

Hence, the new composite signal can be written as

$$S_m = S_0 + S_1 + S_2 = (S_0 + S_1) + S_2 = A'_m \cos(j^{p}_{new} + y^{p}_{m}) \tag{5.34}$$

where A'_m and y^{p}_{m} can be calculated using equations similar to Eqs. (5.29) and (5.30).

Therefore, an "equivalent ideal slope" with planar surface can always be found for the practical slopes which can reflect the GPS satellite signals to the antenna from multiple points. The following discussion on the single reflected signal case are equally valid for the multiple reflected signal case.

To avoid the integer ambiguity as describe in Eq. (5.27a), the change of multipath rather than the multipath itself is used to estimate the slope movement. The change of multipath can be expressed as

$$\Delta MP = \Delta d \bullet (\partial MP / \partial d) + \Delta q \bullet (\partial MP / \partial q)$$

$$= \Delta d \bullet PMP_{d} + \Delta q \bullet PMP_{\theta} \tag{5.35}$$

where

$$PMP_{d} = \partial MP / \partial d = \frac{dMP}{dy^{p}} \cdot \frac{dy^{p}}{dq^{p}} \cdot \frac{dq^{p}}{dL} \cdot \frac{\partial L}{\partial d} \tag{5.36}$$

$$PMP_{\theta} = \partial MP / \partial q = \frac{dMP}{dy^{p}} \cdot \frac{dy^{p}}{dq^{p}} \cdot \frac{dq^{p}}{dL} \cdot \frac{\partial L}{\partial q} \tag{5.37}$$

From Eqs. (5.31), (5.30) and (5.27a)

$$\begin{aligned} \frac{dMP}{dy^{p}} &= \frac{l}{2p} \\ \frac{dy^{p}}{dq^{p}} &= \frac{(a^{p})^{2} + a^{p}\cos q^{p}}{1 + (a^{p})^{2} + 2a^{p}\cos q^{p}} \\ \frac{dq^{p}}{dL} &= \frac{2np}{l} \end{aligned} \tag{5.38}$$

$\partial L / \partial d$ and $\partial L / \partial q$ are calculated using Eqs. (5.21) and (5.22) (for 2D model) or (5.24) and (5.25) (for 3D model). Note also that the integer ambiguity is not present in Eq. (5.38), which indicates that *ambiguity resolution has been avoided by using the change of multipath rather than the multipath itself*.

Considering that MP, a, q and d are all changing with respect to time t due to the movement of the slope, and satellite and MP and a are different for different satellites, Eq. (5.35) can be re-written as

$$\Delta\ MP^{i}(t) = \Delta d(t)\ (\partial MP^{i}(t) / \partial d(t)) + \Delta q\ (t)\ (\partial MP^{i}(t) / \partial q\ (t)) \tag{5.39}$$

where i stands for the PRN of the satellite. For the convenience of later discussions, let

$$PMP_d^i(t) = \partial MP^i(t) / \partial d(t) \quad (5.40)$$

$$PMP_\theta^i(t) = \partial MP^i(t) / \partial q(t) \quad (5.41)$$

Then Eq. (5.39) can be further re-written as

$$\Delta MP^i(t) = \Delta d(t) \bullet PMP_d^i(t) + \Delta q(t) \bullet PMP_\theta^i(t) \quad (5.39a)$$

Hence, using this equation the change of multipath $\Delta MP^i(t)$ can be related to the movement of slope $\Delta d(t)$ and $\Delta q(t)$. *Note that if q is held as zero, this technique can also be used for applications such as ground subsidence monitoring due to mining or underground water extraction.*

5.6.4 Least square estimation of slope movement using the change of multipath

Because there are at least four GPS satellites (even more than eight if low-elevation angle ones are also considered) in the field of view of an antenna anywhere on the Earth, but there are only two variables of slope movement to be estimated, there are many redundant measurements (a result of all-GPS parallel temporal densification!). Consider the vector of unknowns or the slope movement vector

$$\mathbf{X} = [\Delta d(t) \quad \Delta q(t)]^T \quad (5.42)$$

Hence, least square estimation is introduced into the data analysis. Denote the observation vector which consists of the change of both pseudo-range ($\Delta MP^i(t)$) and carrier phase ($\Delta MP^{phi}(t)$) multipath calculated by Eq. (5.39a) for satellites PRN1 to PRNi all available at time *t* as

$$\mathbf{L} = [\Delta\ MP^{PRN1}(t) \quad \Delta\ MP^{PRN2}(t) \quad \ldots \quad \Delta\ MP^{PRNi}(t)$$
$$\Delta\ MP^{phPRN1}(t) \quad \Delta\ MP^{phPRN2}(t) \quad \ldots \quad \Delta\ MP^{phPRNi}(t)]^T \tag{5.43}$$

Then the coefficient matrix can be determined using Eqs. (5.40) and (5.41)

$$\mathbf{B} = \begin{bmatrix} PMP_d{}^{PRN1}(t) & PMP_q{}^{PRN1}(t) \\ PMP_d{}^{PRN2}(t) & PMP_q{}^{PRN2}(t) \\ .... & \\ PMP_d{}^{PRNi}(t) & PMP_q{}^{PRNi}(t) \\ PMP^{ph}{}_d{}^{PRN1}(t) & PMP^{ph}{}_q{}^{PRN1}(t) \\ PMP^{ph}{}_d{}^{PRN2}(t) & PMP^{ph}{}_q{}^{PRN2}(t) \\ .... & \\ PMP^{ph}{}_d{}^{PRNi}(t) & PMP^{ph}{}_q{}^{PRNi}(t) \end{bmatrix} \tag{5.44}$$

Assume the vector of observation errors is Δ, then the observation equation is

$$\mathbf{L = B\ X + \Delta} \tag{5.45}$$

Therefore, the least square estimation of the slope movement is (Giordano & Hsu, 1985)

$$\hat{X} = \mathbf{(B^T\ P\ B)^{-1}\ B^T\ P\ L} \tag{5.46}$$

where $\mathbf{P} = D_{\Delta}^{-1}$ and D_{Δ} is the variance matrix of Δ.

*5.7 **Concluding Remarks***

The all-GPS parallel temporal densification scheme is proposed for the detection of multipath change as a signal at permanent GPS stations based on an adaptive filter using the least-mean-square algorithm. The technique was tested on some experimental data,

indicating that the multipath change above the receiver noise level can be detected. A further test was done with some CGPS data from the Japanese GEONET when there was a snowfall. The results indicate that if there is a change in the antenna environment the proposed technique will indeed detect it in both the pseudo-range and carrier phase data.

For applications of pseudo-range multipath change detection, data from a single dual-frequency receiver is sufficient. For applications of carrier phase multipath change detection, data from two closely-spaced receivers have to be used. This may become a limitation in a sparse CGPS array. However, in an array such as the GEONET it is always possible to identify some reference stations free of multipath, and to generate the RINEX data for a Virtual Reference Station located close to the CGPS station targeted for multipath change detection. For reliable multipath change detection, the temporal resolution of this method is 24 hours.

As an application of the technique, the mathematical models for slope stability monitoring using the change of GPS multipath effects have been given in this Chapter. *It is found that an "equivalent ideal slope" with planar surface can always be found for the practical slopes which can reflect the GPS satellite signals to the antenna from multiple points. Moreover, ambiguity resolution has been avoided by using the change of multipath rather than the multipath itself in the monitoring of slope movement.* The change of multipath is used in a least square process to estimate the slope movement parameters by employing the mathematical models developed. The system is designed to function as an early warning system through monitoring the sliding precursors. When the sliding is imminent, the system has to be withdrawn.

This all-GPS parallel temporal densification scheme provides an easy-to-implement quality assurrance tool for CGPS antenna environment sensing after disasters such as typhoons, cyclones, and earthquakes. Other possible applications include the monitoring of slope stability and ground subsidence.

6 CROSS-TECHNIQUE PARALLEL TEMPORAL DENSIFICATION – THE INTEGRATION OF GPS WITH VLBI AND SLR

In recent years space geodetic techniques such as the Global Positioning System (GPS), Very Long Baseline Interferometry (VLBI), and Satellite Laser Ranging (SLR) have been collocated to address many applications in geoscience. Cross-technique parallel temporal densification requires the integration of the continuous GPS (CGPS) results with VLBI and SLR data. In other words, an appropriate fusion of these multi-technique space geodetic results must be developed. VLBI measures the difference between the arrival times, at two Earth-based antennas, of a radio wavefront emitted by a distant quasar. SLR measures the round-trip-time of travel of a signal between a ground-based laser transmitter/receiver and a satellite equipped with optical corner reflectors. Whilst results from all these techniques are contaminated by various biases and errors, when GPS, VLBI and SLR instruments are installed at the same site, the same crustal displacement signature will be present as a common-mode signal. The results can therefore be fused, GPS-VLBI and GPS-SLR, using the adaptive filtering approach based on the Least-Mean-Square algorithm described in Chapter 2, or by extending the adaptive filter to a three input (one primary, two references) and two output system (Ge et al, 2000b). The GPS-VLBI and GPS-SLR outputs can be used to verify each other as well.

In this Chapter, data from the Matera Station in Italy and the Wettzell Station in Germany have been used to test this densification scheme.

6.1 Introduction

The space geodetic techniques of GPS, VLBI, and SLR have been used to address applications such as the monitoring of plate and polar motion of the Earth. In recent years,

GPS, VLBI and SLR instruments have been collocated for the purpose of monitoring active fault movement in campaigns such as the Key Stone Project (KSP) of Japan. In 1999 the common-mode signal from the GPS, VLBI and SLR techniques, extracted from the published KSP results (Takahashi & Ichikawa, 1999), was analysed using the proposed methodology. This methodology has also been validated by researchers from M.I.T. (Herring, 1999).

In the case of GPS measurements, the biases and errors include ephemeris uncertainties, satellite clock errors, selective availability effects (before 1 May 2000), receiver clock errors, reference station coordinate uncertainties, ionospheric delay, tropospheric delay, carrier phase ambiguity, unmodelled residual biases, carrier phase cycle slips, multipath disturbance, antenna phase centre offset, and random observation error. In the case of the VLBI measurements, the biases and errors may include the effects of temperature variations on the hydrogen maser, the ionosphere, the wet component of the troposphere, the structure of the radio sources used in the observations, and so on. In the case of SLR measurements, the biases and errors may include the effects of the satellite ephemeris uncertainties, the precession and nutation uncertainties, satellite libration theory, elastic deformations of the Earth surface, atmospheric retardation of photons and the behavior of terrestrial clocks. Despite the fact that, for example, dual-frequency data can be used to negate the effect of the ionosphere, and water vapour radiometers can be used for wet tropospheric calibration, many of these biases and errors contaminate the final GPS, VLBI and SLR results.

In Section 2 of this Chapter, detailed analyses and intercomparisons of the biases and errors in the GPS, VLBI and SLR results are presented. The decorrelation among the baises and errors makes it feasible to extract the crustal movement as the common-mode signal from collocated GPS, VLBI and SLR results.

In Section 3 of this Chapter, the common-mode signals from the results of collocated GPS, VLBI and SLR at Matera (Italy) and Wettzell (Germany), extracted using an adaptive filter based on the Least-Mean-Square algorithm, are presented.

6.2 Analyses And Comparisons of The Biases And Errors In The GPS, VLBI And SLR Results

In the case of GPS, VLBI and SLR results, the time series for a station can be expressed as:

$$d(n) = s(n) + x_{co}(n) + x_{inco}(n) \tag{6.1}$$

$$r'(n) = s'(n) + x'_{co}(n) + x'_{inco}(n) \tag{6.2}$$

$$r''(n) = s''(n) + x''_{co}(n) + x''_{inco}(n) \tag{6.3}$$

where *s(n), s'(n),* and *s"(n)* are the signals free of noise (true crustal movement) detected by GPS, VLBI, and SLR respectively; and $x_{co}(n)$ and $x_{inco}(n)$ are the contributions to GPS results from noises and biases which are coherent and incoherent, respectively, with those in VLBI and SLR results. $x'_{co}(n)$ and $x'_{inco}(n)$ and $x''_{co}(n)$ and $x''_{inco}(n)$ are analoguous to $x_{co}(n)$ and $x_{inco}(n)$. As a result, $s(n) + x_{co}(n)$ will behave as the common-mode signal amongst the GPS, VLBI and SLR results.

In this case, can the adaptive filter be used to extract the true crustal movement *s(n)* from the GPS result *d(n)* by employing the VLBI result *r'(n)* and/or SLR result *r"(n)* as reference signals? As discussed in Chapter 2.4, and also in Ge (1999), there are two special cases to be considered in the application of an adaptive filter. Eq. (6.1) can be treated as a linear combination of the two cases. Therefore, by decorrelating the noises and biases in collated GPS, VLBI and SLR results theoretically it is possible to obtain the true crustal movement *s(n)* by using GPS, VLBI and SLR results as inputs to an adaptive filter. Hence, the success of the cross-technique parallel temporal densification scheme in integrating collocated GPS, VLBI, and SLR results using the adaptive filter depends on the decorrelation among the noises and biases in the results, i.e. $x_{co}(n) \to 0$ in Eq. (6.1).

In GPS measurements, the biases and errors include satellite ephemeris uncertainties, satellite clock errors, selective availability effects, receiver clock errors, reference station coordinate uncertainties, ionospheric delay, tropospheric delay, carrier phase ambiguity, unmodelled residual biases, carrier phase cycle slips, multipath disturbance, antenna phase centre offset, and random observation error (Rizos, 1996).

The satellite ephemeris uncertainties (bias) is the discrepancy between the true position (and velocity) of a satellite and its known value. In the Broadcast Ephemerides within the GPS Navigation Message, the bias can range from (usually) less then 10m to (very rarely) up to 100m. In the post-processed ephemerides the bias is well below the metre level.

The satellite clock errors consist of the offset, drift and drift-rate of the satellite clocks with respect to GPS Time. These errors are modelled to an accuracy of about 20 nanoseconds. Selective Availability (SA) is a further artificial dithering of the satellite clocks causing several dekametres error in the range (or phase-range equivalent). Fortunately SA has been switched off since 1 May 2000.

The receiver clock errors due to the use of quartz crystal oscillators in GPS receivers include the error in defining the time origin (tying the clock to a well established time scale, such as GPS Time, to the 0.01 microsecond level with SA off) and the clock drift.

The reference station coordinate uncertainties in differential GPS positioning (essential for overcoming the satellite dependent biases described above) will cause a bias in the solution because the coordinates of the reference station are held fixed during data processing. Hence, in effect, only the relative position (or baseline components) relating the second receiver to the first (reference) receiver are estimated.

In terms of the atmospheric effects, the ionospheric and tropospheric delays will affect both pseudo-range and carrier phase measurements. However, the dispersive nature of the ionosphere can be used in actually removing *most* of the ionospheric delay effect by making pseudo-range and/or carrier phase measurements on both L-band frequencies, and

forming the "ionosphere-free" combination. In the case of the tropospheric delay bias, 90% due to the dry atmosphere can be modelled very well, while 10% due to the wet component of the atmosphere is difficult to account for.

The ambiguity and cycle slips are specific to the carrier phase observable, and hence are relevant to GPS only.

The unmodelled residual biases remaining after the appropriate differencing of phase data, collected simultaneously by two GPS receivers, are primarily due to the:

- differential ionospheric refraction between the two sites (if not eliminated by the "ionosphere-free" combination);
- differential tropospheric refraction between the two sites; and
- second-order effect of orbit error on the baseline solution.

The multipath disturbance is caused by extraneous reflections of GPS signals from nearby metallic objects, ground or water surfaces reaching the antenna. Whilst both on-the-receiver and post-processing techniques have been used to mitigate the multipath effects as reviewed in Chapter 4, the disturbance is still common in the final GPS result.

The antenna phase centre offset is the distance between the physical and the electrical centres of the antenna. Because the electrical centre varies with the direction and strength of the incoming signal, a variation in the satellite-receiver geometry will cause the position of the electrical centre to also vary, which introduces errors into the GPS result.

The random observation error for GPS is typically at the millimetre level.

In VLBI measurements, the biases and errors may include the effects of temperature variations on the hydrogen maser, the ionosphere, the wet component of the troposphere, the structure of the radio sources used in the observations, and so on. Measuring the difference between the arrival times at two or more Earth-based antennas of the radio wavefronts, at S-, X- and sometimes K-bands (Takashima et al, 2000), emitted by many

distant quasars, VLBI is free of the satellite-dependant biases and errors. Instead, the structure of the radio sources used in the observations will introduce some errors, which are of course very unlikely to be correlated to the satellite-dependant biases and errors in the GPS result.

However, when the radio signals from these quasars travel through the atmosphere, biases correlated to the ionospheric and tropospheric biases in GPS result will be introduced because the S- (f=2100-2450MHz, $\lambda \approx 15$cm), X- (f=8100-9000MHz, $\lambda \approx 3$cm) and K- (f= 19500-25000 MHz, $\lambda \approx 1.5$cm) bands used by VLBI as well as the L-band (f_{L1}= 1575.42MHz, $\lambda_{L1} \approx 19$cm; f_{L2}=1227.60MHz, $\lambda_{L2} \approx 24$cm) used by GPS are all in the microwave band. For example, the ionospheric group delay d_{ion} and the ionospheric phase delay f_{ion} for a microwave propagating from a quasar or GPS satellite to the ground is approximated by (Rizos, 1996):

$$\begin{aligned} d_{ion} &= -f_{ion}\frac{c}{f} \\ &\approx 40.28 \cdot \frac{STEC}{f^2} \\ &\approx \frac{40.28}{\cos ec z} \cdot \frac{VTEC}{f^2} \end{aligned} \qquad (6.4)$$

where:

d_{ion} is the ionospheric group delay in units of metres;

ϕ_{ion} is the ionospheric phase delay in units of cycles;

c is the speed of electronic magnetic radiation in a vacuum (m/sec);

cosec ζ is the cosecant of the zenith angle of the line-of-sight to the microwave source;

f is the signal frequency (Hz);

STEC is the Slant Total Electron Content, expressed as the number of free electrons per square metre (el/m^2); and

VTEC is the Vertical Total Electron Content (zenith direction) (el/m^2).

Note, from Eq. (6.4), the higher the frequency, the smaller the ionospheric delay effect. Let us assume that VTEC is 10^18 electrons per square meter. This is a high but not unrealistic value. Then the contribution at GPS L band frequencies is of the order of 1 for VTEC/(f**2). It is only marginally greater than 10mm at the top end of X band and is negligible for optical wavelengths. Note that at K band frequencies the VLBI contribution is only 1.6mm. Thus the ionosphere impacts differently upon the three techniques.

In addition, the tropospheric water vapour leads to correlations between VLBI and GPS observations.

The effects of temperature variations on the hydrogen maser on the VLBI result are analogous to the receiver clock errors in the GPS result. But correlation between them is expected to be low since different types of clock are used in VLBI and GPS.

Since a VLBI antenna is quite unidirectional due to it's large diameter, there shouldn't be any multipath effect in VLBI observations.

In the case of SLR measurements, the biases and errors may include the effects of the satellite ephemeris uncertainties, the precession and nutation uncertainties, satellite libration theory, elastic deformations of the Earth surface, atmospheric retardation of photons and the behavior of terrestrial clocks. Among them, the effects of the satellite ephemeris uncertainties will be a correlated error between GPS and SLR if a GPS satellite is used as a SLR target as well. As a matter of fact, optical corner reflectors have been installed on two of the GPS satellites. Fortunately, they do not normally contribute to a SLR solution which is usually restricted to LAGEOS type satellites. Again the atmospheric biases will contaminate the SLR result but would not correlate with those in GPS as strongly as in the case of VLBI because the wavelength of the laser pulse used in SLR is usually at 532nm, which is in the visible light band, rather than the microwave band.

Table 6-1 summarizes the above discussion and indicates the degree of decorrelation of GPS noises and biases in various combinations with VLBI and SLR. From the table, it can be concluded that noises and biases in GPS result can be significantly reduced by integrating with collocated VLBI and SLR results, which makes the cross-technique parallel temporal densification scheme feasible.

Table 6-1 Decorrelation of GPS noises and biases in various combinations with VLBI and SLR.

Combinations / Noises and biases	GPS-VLBI	GPS-SLR	GPS-VLBI-SLR
satellite ephemeris uncertainties	0	0.5	0
satellite clock errors	0	0	0
Selective availability effects	0	0	0
receiver clock errors	0	0	0
Ref. station coordinate uncertainties	0	0	0
ionospheric delay	1	0	0
tropospheric delay	1	0.5	0.5
carrier phase ambiguity	0	0	0
carrier phase cycle slips	0	0	0
multipath disturbance	0	0	0
antenna phase centre offset	0	0	0
Random observation error	0	0	0

Remarks: 0 uncorrelated;
0.5 partially correlated; and
1 correlated.

6.3 The Integration of Collocated GPS, VLBI And SLR Results

In this section, data from two stations Matera and Wettzell are used in the integration of collocated GPS, VLBI and SLR results using the adaptive filter.

Details of the two stations are summarized in Table 6-2. From the table the distances from the VLBI Monument to the GPS Mark and from the SLR Monument to the GPS Mark are 58.000m and 38.334m respectively at Matera Station. Hence, an absolute collocation is not possible. Even for the collocated GPS and GLONASS (and in the future Gelileo) which share the same antenna, there is the problem of phase centre differences. Therefore, it is important to ensure that the distances between the marks are so small that they will not lead to the decorrelation of *s(n), s‘(n),* and *s“(n)* in Eqs. (6.1) to (6.3).

Table 6-2 Details of the Matera and Wettzell stations

Station		MATERA	WETTZELL
City or Town		Matera	Koetzting
State or Province		Basilicata	Bavaria
Country		Italy	Germany
Tectonic Plate		Adriatic-African	Eurasian
Parent/Funding organization		Agenzia Spaziale Italiana (Asi), Italy	Bundesamt fuer Kartographie und Geodasie (BKG) Forschungseinrichtung Satellitengeodaesie der Technischen Universitaet Muenchen (FESG)
Collocated space geodetic techniques		GPS SLR VLBI PRARE*	GPS SLR VLBI PRARE GLONASS
Other collocated techniques			Gravimeter (super conducting) seismometer time & frequency laboratory meteorological sensors water vapour radiometer
Station configura-tions	GPS	Monument Inscription: Stable pillar on the roof Approximate Position (m): X: 4641949.709 Y: 1393045.298 Z: 4133287.333 Latitude (deg): 40.6491 N Longitude (deg): 16.7044E Elevation (m): 535.65 GPS Receiver: TRIMBLE 4000SSI GPS Antenna: Trimble L1/L2 Dorne Margolin element with Choke-rings	Monument Inscription: Pillar Approximate Position (m): X: 4075580.695 Y: 931853.668 Z: 4801568.036 Latitude (deg): 49.144197129 N Longitude (deg): 12.878907601 E Elevation (m): 666.024 GPS Receiver: AOA SNR-8000 ACT GPS Antenna: AOAD/M_T
	VLBI	Rack: Mark IIIA Recorder: VLBA Hydrogen-maser model: OSCILLOQUARTZ EFOS-8 Other frequency standards: 2 CESIUM (HP 5061) GPS timing receiver model: FTS-8400 X/S receiver RF bandwidths: 2210-2450 8180-8980 MHz Differential Components from VLBI Monument to GPS Mark dx (m): -10.946 dy (m): -42.246 dz (m): 38.203 Accuracy (mm):6 Date Measured: 01-NOV-1991	Rack: Mark IIIA Recorder: Mark IIIA Hydrogen-maser model: EFOS-1, EFOS-3, and EFOS-13 Other frequency standards: HP Cesium standard GPS timing receiver model: ALLAN OSBORNE TTR-6 X/S receiver RF bandwidths: 8100-9000 MHz, 2100-2300 MHz Differential Components from VLBI Monument to GPS Mark dx (m): -40.802 dy (m): -118.398 dz (m): +61.317 Accuracy (mm): 1 Date Measured: 13-FEB-1995
	SLR	Instrument: permanent Differential Components from SLR Monument to GPS Mark dx (m): 15.172 dy (m): 24.826 dz (m): -24.959 Accuracy (mm):2 Date Measured: JUL-1996	Instrument: permanent Differential Components from SLR Monument to GPS Mark dx (m): -3.828 dy (m): -68.200 dz (m): +15.517 Accuracy (mm): 1 Date Measured: 13-FEB-1995

* PRARE (the Precision RAnge and Range-rate Experiment)

In order to integrate the collocated results of GPS, VLBI and SLR, two configurations can be designed for the adaptive filter: a two-input-and-two-output, and a three-input-and-two-output. In the two-input-and-two-output configuration, the inputs consist of a primary input (GPS result) and a reference input (VLBI or SLR result) and the outputs consist of the common-mode signal between the primary and reference inputs and the uncorrelated component in the primary signal. This configuration enables the comparison between the common-mode signals derived from GPS-VLBI and GPS-SLR combinations. In the three-input-and-two-output configuration, the inputs consist of a primary input (GPS result) and two reference inputs (VLBI and SLR results) and the outputs consist of the common-mode signal among the primary and the two reference inputs and the uncorrelated component in the primary signal. This configuration enables the extraction of the common-mode signal by the integration of collocated GPS, VLBI and SLR results.

In the GPS-VLBI combination, the overlap period of GPS and VLBI results for Matera is from 25 May 1992 to 1 May 1999, and for Wettzell from 9 January 1996 to 22 July 1998. Coordinates for the two stations were estimated on a daily and fortnightly basis using GPS and VLBI data respectively, resulting in two time series for each station. The GPS time series are given in ellipsoidal coordinates while the VLBI results are in Cartesian coordinates. Hence, the VLBI time series were converted to ellipsoidal coordinates before being used in the filtering.

Fig. 6.1 is the integration of GPS and VLBI at Matera for the longitude component. From top to bottom the plots are: the GPS time sequence as primary input; the VLBI time sequence as reference input; extracted common-mode signal as coherent output; and the incoherent output from the adaptive filtering system. In all these plots, the horizontal axis indicates year and the vertical axis the longitude change in centimetres. The blue (black) curves are the respective data while the red (or grey) straight lines in the first three plot are the least-squares fits of the data, so that the rate of movement in the stations and the repeatability of the results can be estimated. It can be seen that the repeatability of the derived common-mode signal (0.46cm) is better than that of GPS (0.59cm) and that of

VLBI (0.62cm) and perhaps 2.38cm/yr is a more realistic estimate for the rate of plate movement (further study is needed to compare these results with the NUVEL-1 Model, DeMets et al., 1990).

Calculations on other components for station Matera and all three components for station Wettzell were also done (Figs. 6.2 to 6.6), and the results were summarized in Table 6-3. In the table, mLatitude, mLongitude and mHeight stand for the three components of the Matera Station while wLatitude, wLongitude and wHeight are those of the Wettzell Station. Conclusions similar to that for the longitude component of Matera can be made for the other results in the table. The differences between GPS and VLBI results in this study and the JPL (the Jet Propulsion Laboratory) GPS and GSFC (the Goddard Space Flight Center) VLBI (Ma & Ryan, 1998) results are due to the data length used in the estimations. For example, data from 16 November 1983 to 22 July 1998 were used in the GSFC VLBI estimation for Wettzell, whilst in this study only data from 9 January 1996 to 22 July 1998 were used, due to the availability of collocated GPS result.

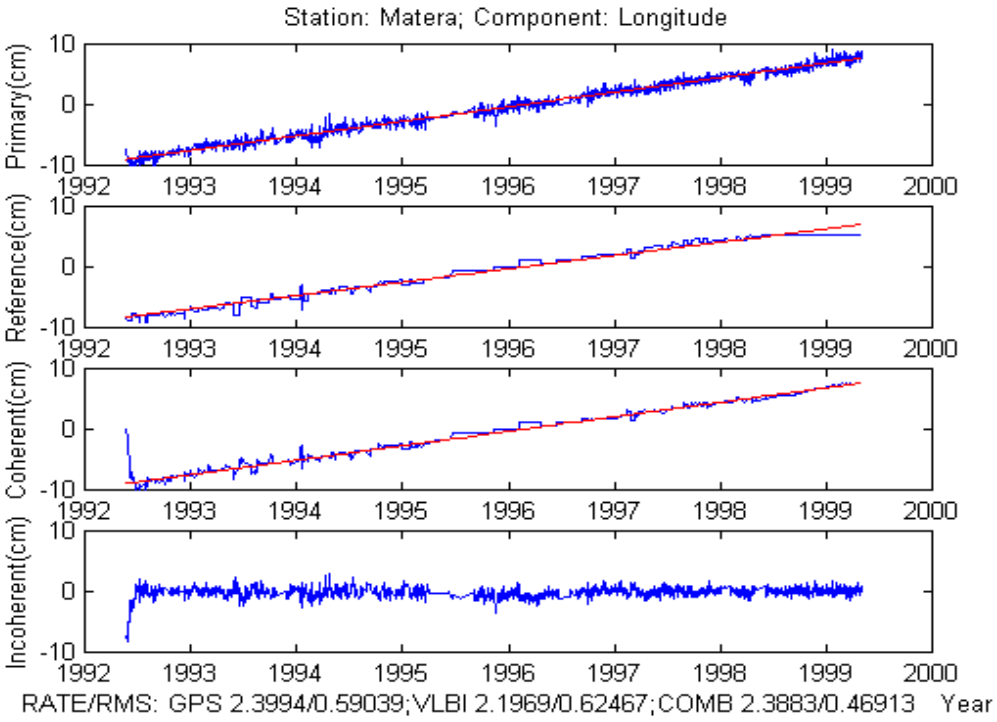

Figure 6.1 Integration of GPS and VLBI at Matera: the longitude component.

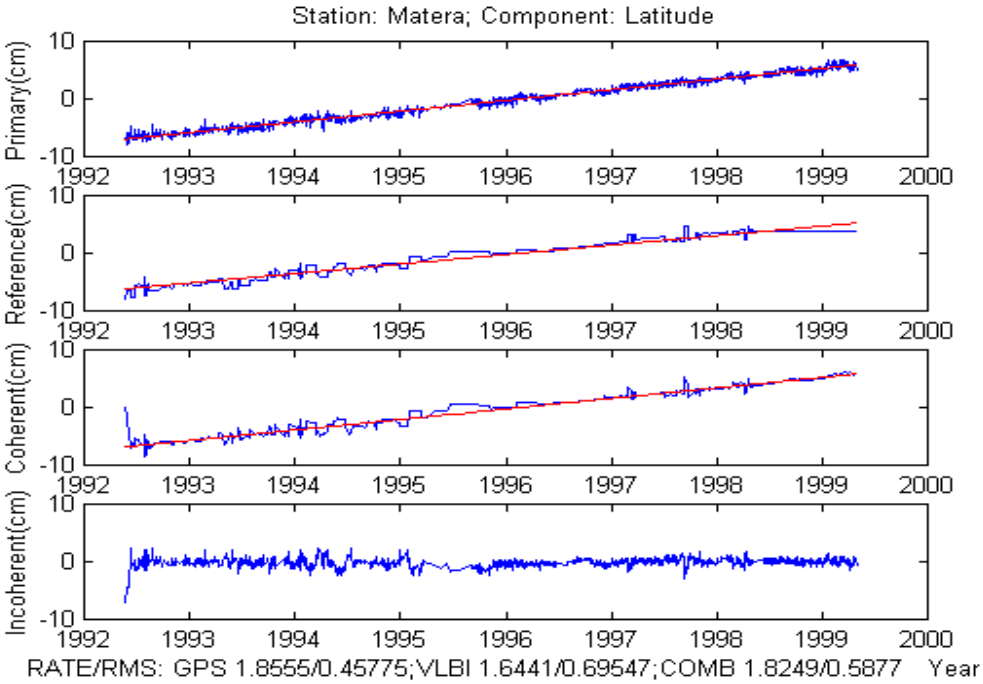

Figure 6.2 Integration of GPS and VLBI at Matera: the latitude component.

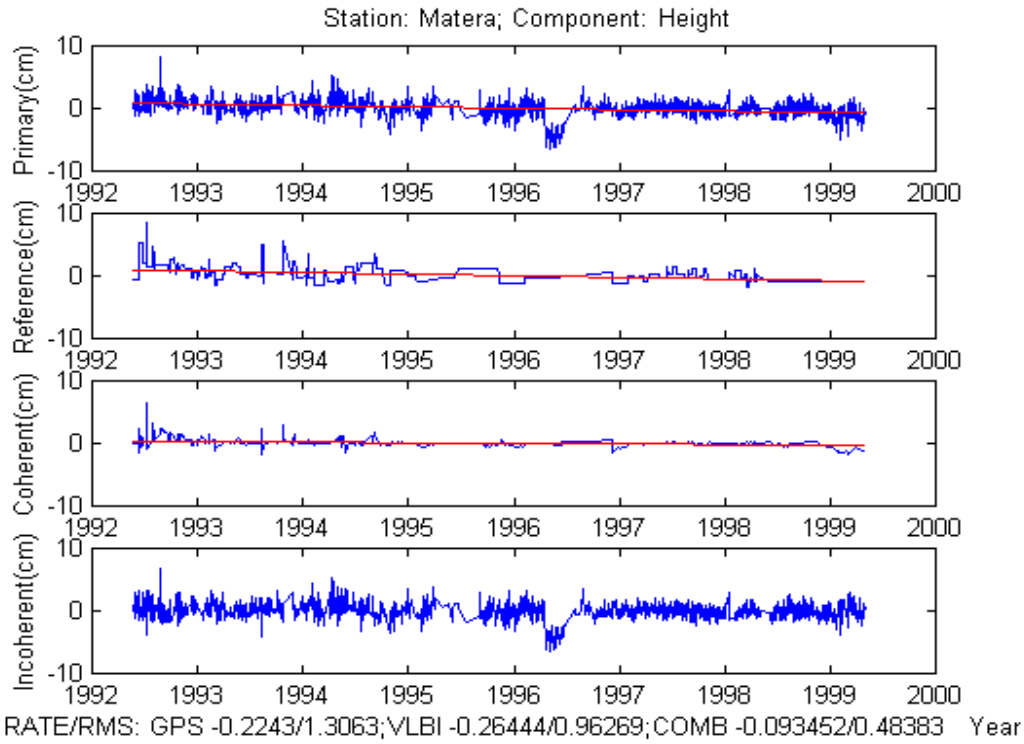

Figure 6.3 Integration of GPS and VLBI at Matera: the height component.

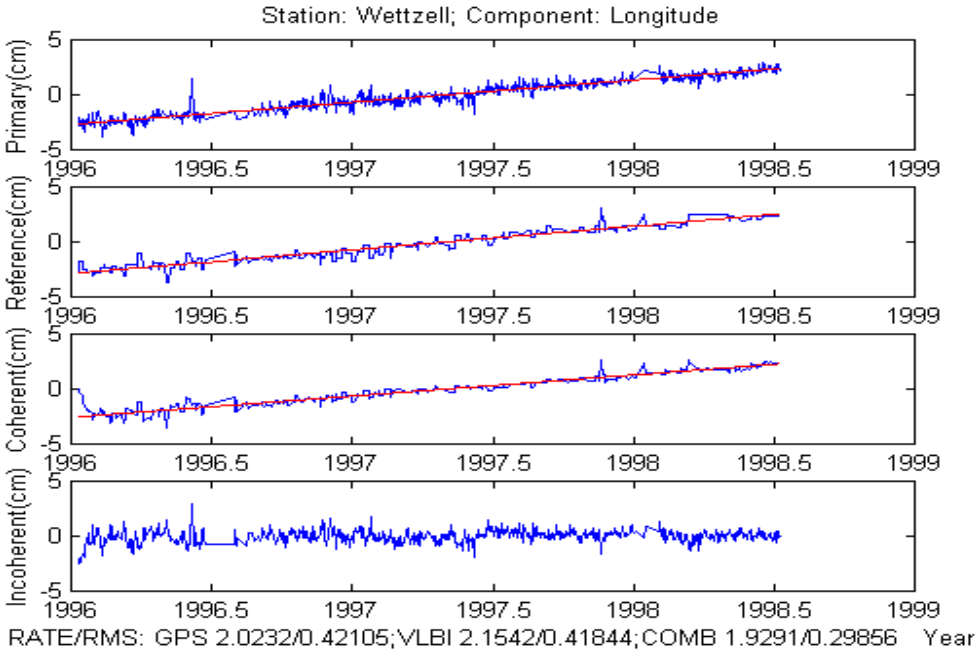

Figure 6.4 Integration of GPS and VLBI at Wettzell: the longitude component.

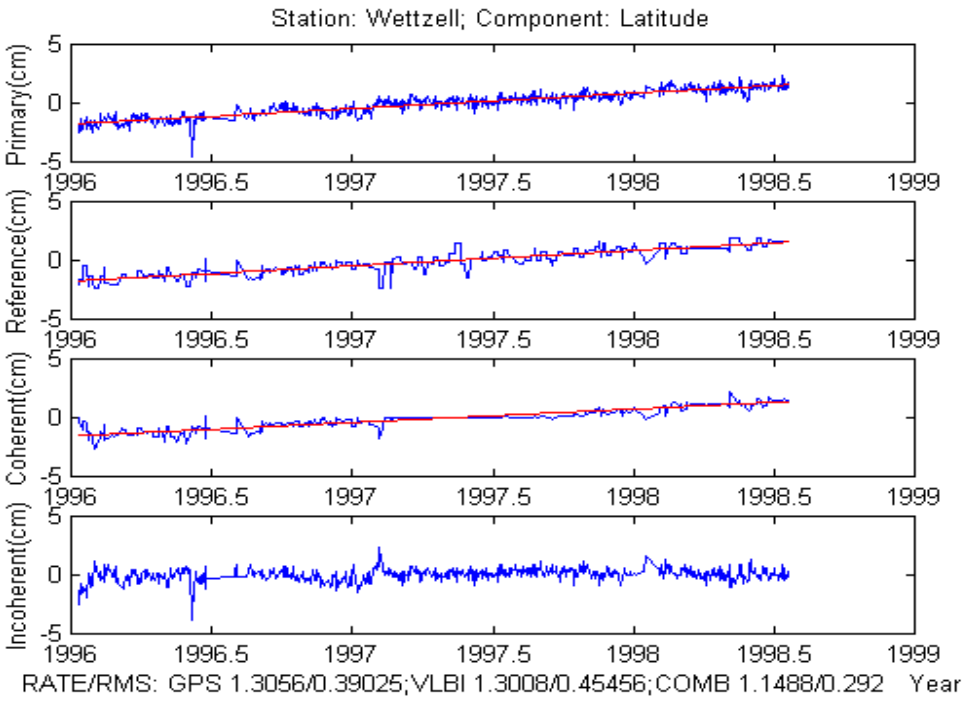

Figure 6.5 Integration of GPS and VLBI at Wettzell: the latitude component.

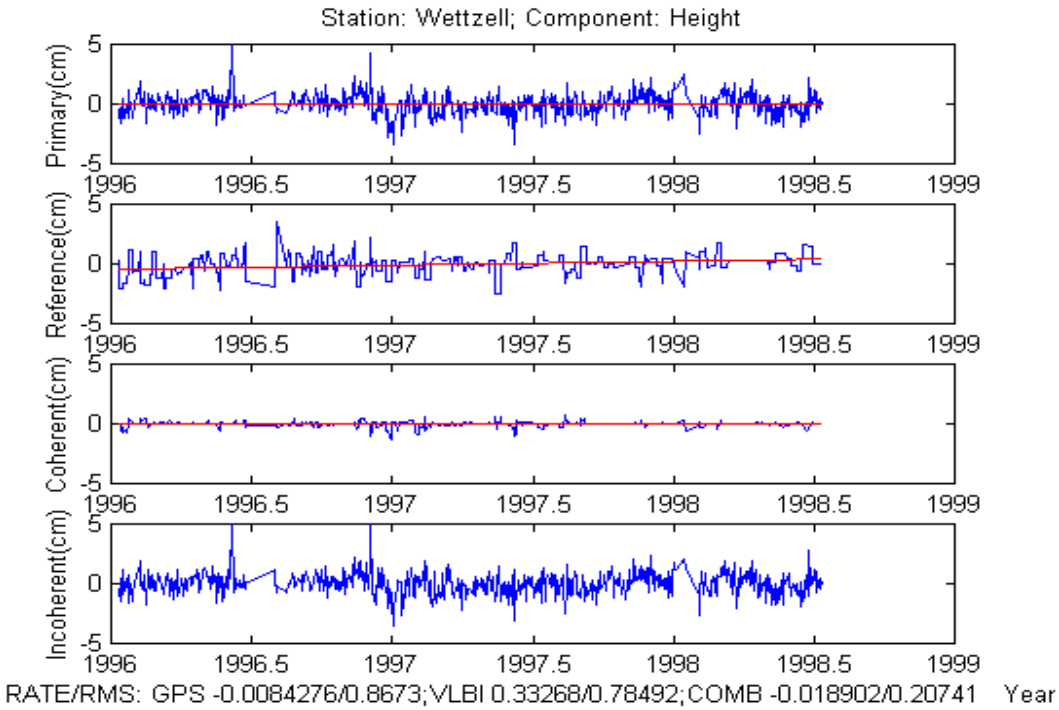

Figure 6.6 Integration of GPS and VLBI at Wettzell: the height component.

Table 6-3 Summary of GPS, VLBI, SLR and the integrated results (in cm).

Solutions		combined	GPS	VLBI	JPL GPS[1]	GSFC VLBI[2]
mLati-tude	rate	1.82	1.85	1.64	1.84	1.74
	rms	0.58	0.45	0.69	0.42	0.34
mLon-gitude	rate	2.38	2.39	2.19	2.33	2.36
	rms	0.46	0.59	0.62	0.53	0.28
mHeig ht	rate	-0.09	-0.22	-0.26	-0.39	-0.12
	rms	0.48	1.30	0.96	1.04	0.99
wLati-tude	rate	1.14	1.30	1.30	1.32	1.35
	rms	0.29	0.39	0.45	0.39	0.40
wLon-gitude	rate	1.92	2.02	2.15	2.05	2.04
	rms	0.29	0.42	0.41	0.43	0.40
wHeig ht	rate	-0.01	-0.01	0.33	-0.12	-0.10
	rms	0.20	0.86	0.78	0.91	1.01

[1]: http://sideshow.jpl.nasa.gov/mbh/all/MATE.gif
http://sideshow.jpl.nasa.gov/mbh/all/WTZR.gif

[2]: http://lupus.gsfc.nasa.gov/vlbi.html

For the GPS-SLR combination, although generally the coordinates and velocities of each SLR stations are estimated as global parameters and therefore the time series is not directly available from such a process, it is possible to obtain a SLR time series if one evaluates the coordinates of each station as local parameters (for single arcs).

Once the SLR time series is available, the common-mode signals derived from the three combinations (GPS-VLBI, GPS-SLR, and GPS-VLBI-SLR) can be compared to see if they are in agreement for both the Matera and Wettzell stations, which could facilitate the more realistic determination of plate or fault movement. At Matera, also collocated is the space geodetic technique PRARE, while at Wettzell available collocated techniques include PRARE, GLONASS, gravimeter (super conducting), seismometer, meteorological sensors,

and water vapour radiometer. In future it is proposed to also integrate results from some of these techniques.

6.4 Concluding Remarks

Space geodetic techniques such as the GPS, VLBI, and SLR have been collocated at many sites to address applications in the geosciences. A common-mode signal has been found among the collocated results (coordinate time series) of GPS, VLBI and SLR, although results from all these techniques are contaminated by different biases and errors. An adaptive filter based on the Least-Mean-Square algorithm is proposed as the cross-technique parallel temporal densification scheme to extract this common-mode signal by inputting to the filter the GPS result as the primary sequence and VLBI and/or SLR results as the reference sequences. Data from the Matera Station in Italy and the Wettzell Station in Germany have been used to test the algorithm. The derived common-mode signal has better repeatability than the individual results of GPS, VLBI and SLR. Further study is needed to establish whether the movement rate determined by the derived common-mode signal is more realistic than the individual results by comparing them with that from the NUVEL-1 Model.

In the following two chapters, spatial densification of CGPS measurements will be discussed.

7 SOFT SPATIAL DENSIFICATION – THE INTEGRATION OF GPS WITH RADAR INTERFEROMETRY (INSAR)

The approach suggested for so-called 'soft spatial densification' is the “double interpolation and double prediction” (DIDP) technique for GPS and InSAR integration (Ge et al, 2000f; Ge et al, 2000h). This Chapter begins with a brief introduction to the radar interferometry (InSAR) technique. Then a detailed comparison between the two techniques - GPS and InSAR shows that they are in fact very complementary to each other for crustal deformation monitoring applications. For example, InSAR is very sensitive to a range of errors such as atmospheric biases, satellite orbit errors, ground cover and temporal decorrelation. While the latter two effects can only be reduced by careful selection of radar band and SAR image pairs, the former two types of biases can only be significantly reduced by incorporating GPS data. The DIDP technique is designed to take advantage of the complementarity of GPS and InSAR.

7.1 Review of Radar Interferometry (InSAR)

There is a need in many fields of Earth science for accurate knowledge of topography and topographic *change* at a variety of spatial scales and coverage areas. Radar interferometry (or Interferometric synthetic aperture radar, InSAR for short) is a technique first suggested in 1974 (Graham, 1974). After more than two decades of development, InSAR is now well developed with many applications in mapping topography, topographic change determination, and so on.

An image resulting from the phase difference between two SAR images acquired over the same region is called an *interferogram*. The two SAR images may be acquired in the same pass, as in the case of the Shuttle Radar Topography Mission (SRTM) and Airborne Synthetic Aperture Radar (AIRSAR) (JPL, 1999). In this configuration the two antennas are installed on the same platform, one of them sends out the radar signal while both

receive the reflected signals from the surface of the Earth. This is referred to as 'single-pass InSAR', and has the advantage that there is no problem of *temporal decorrelation* while the disadvantage is that such a space-borne SAR system provides a big challenge in the orbit maneuver and attitude control of the space vehicle, as was experienced during the SRTM mission (SRTM, 2000).

If the two SAR images are acquired from two repeated SAR coverages of the same region, the technique is referred to as 'repeat-pass InSAR'. It is much easier to build and deploy such a SAR system. However, the temporal decorrelation is a big problem, which may limit the SAR images that are suitable for InSAR processing. Nevertheless, for the purpose of continuous crustal deformation monitoring, repeat-pass InSAR is the most suitable. Hence, this Chapter will focus on the repeat-pass InSAR technique.

The SAR repeat-pass interferometry can generate digital elevation models (DEMs), deformation maps, and temporal change maps (Zebker & Goldstein, 1986). Topographic change measurement by InSAR was first demonstrated for Seasat L-band data (Gabriel et al., 1989), and later with the spectacular contour map of co-seismic deformation associated with the 1992 Landers earthquake in southern California obtained with the ERS-1 data (Massonnet et al., 1993).

During the last decade SAR repeat-pass interferometry has been the subject of intensive research. Although it is still not as operational a technique as GPS, it has been recognized as a technique that yields important quantitative information such as height, large scale deformation and (subtle) elevation change. It has the potential to routinely provide DEMs, maps of deformation and change, and to allow a full geocoding of SAR imagery. A growing number of applications have become feasible, and even more are being currently investigated. Perhaps the most exciting new application of SAR interferometry is the 2-dimensinoal mapping of crustal deformation with very high accuracy (mm- to cm-level). Applications include earthquake deformation detection and monitoring, monitoring of crustal movements, volcanic movement, landslides and land subsidence. Another interesting area of research is the use of phase coherence for classification and change

detection. To exploit InSAR, two basic ingredients are required. The first is the acquisition of two phase preserved SAR images of the same region but obtained at slightly different viewing angles. These images may be obtained by the space-based SARs aboard ERS-1 (until June 2000), ERS-2, JERS-1 (until October 1998), and RADARSAT. Alternatively, these images may be acquired by an airborne SAR sensor, either in single-pass or repeat-pass modes. The second requirement is a set of image processing tools that combine the two SAR images to create an interferogram and extract information from it.

InSAR is a process of using interference effects to determine lengths or changes in lengths very accurately. This technique has some similarities to stereo-optical imaging in that two images of the same area, viewed from different angles, are appropriately combined to extract topographical information. However, a major difference between interferometry and stereo imaging lies in the painstaking manual effort required in obtaining topographic information from stereo-optical images. Meanwhile, inherent in SAR data, is distance information that enables the automatic generation of topography models. This means that DEMs can be generated using InSAR with greater automation than optical techniques. Also, using the technique known as *differential* InSAR, surface deformations can be measured with an accuracy and spatial measurement density which is unprecedented. Add to this the ability of SAR to penetrate clouds and provide day and night operation, and it becomes clear that InSAR has definite advantages over many conventional deformation monitoring techniques.

SAR interferometry is possible because the technique measures both distance and radar “brightness”. The distance information is encoded in phase, which is a fine scale measurement of distance that is measured twice in two separate SAR passes. Distance combined with incidence angle, and with the location of the SAR platform on each of the two passes, gives a three-dimensional localization of points on the Earth’s surface. The two SAR images, each containing brightness and phase information, can be used to produce one interferometric data set from which height and other information is extracted.

In repeat-pass InSAR, interferograms are formed from repeated observations of the same platform. With respect to the Earth, the satellite goes through a cycle of orbits, for example, every 35 days in the case of ERS-2. This means that the satellite returns almost exactly to the same position with respect to the Earth after 35, 70, 105, … days. On the first pass of the satellite, a SAR image is acquired. After a period of time (one or more orbit repeat cycles), the same area may be imaged again, thus acquiring the second SAR image.

The two SAR images are individually processed by a precision, phase preserving, SAR processor to convert the "raw" radar signals into the black and white SAR images with the phase information carefully preserved (e.g., the single look complex (SLC) image). Sophisticated InSAR processing is then applied to register the two SAR images to an accuracy of $1/8^{th}$ of a pixel. Next, the phase differences in the two images are calculated by subtracting the phase in one image from the phase in the other. The result is called an interferogram. These phase differences in the interferogram wrap around in cycles of 360 degrees and must be unwrapped to obtain the absolute phase. The problem is very similar to the carrier phase integer ambiguity resolution in GPS. It suffices to say that phase unwrapping, although a complex process, is the key to high precision positioning. After phase unwrapping, the absolute phase is converted to the various data products through further processing.

In radar interferometry, two synthetic aperture radar images of a surface area are acquired and combined into an interferogram, which contains the phase difference between the two images. If the two images are acquired at the same time but at different sensor locations, then the phase difference is related to the topography. If the scene is imaged from the same location but at different times, then the phase difference is a record of topographic change. If the scene is imaged from different locations and at different times, then the phase difference is a record of both topography and topographic change. In a simplified geometry where the radar antennas are looking directly orthogonal to their orbit motion, the differential phase is given by (Zebker & Goldstein, 1986):

$$\Delta f = \frac{4p}{l} B \sin(q - a) + \frac{4p}{l} \Delta r \qquad (7.1)$$

where q is the look angle to a given image point,

B is the magnitude of the distance between the antenna locations, known as the baseline vector,

a is the angle of the baseline vector measured from the orbital horizontal,

l is the radar wavelength, and

Δr is the displacement of the image point along the radar line-of-sight from one observation time to the next.

If the natural variation in Δf due to a reference surface at zero elevation is removed from Eqn. (7.1), then

$$\Delta f_{\text{flat}} = \frac{4p}{l} B \cos(q_0 - a) \frac{z}{r_0 \sin q_0} + \frac{4p}{l} \Delta r \qquad (7.2)$$

where q_0 is the look angle not to the image point but to the reference surface,

r_0 is the range to the reference surface, and

z is the height of the image point above the reference surface.

Eqn. (7.2) indicates that the first term is proportional to topography and the second term is proportional to the topographic change.

7.1.1 Environment of InSAR studies

Through the development of over two decades, more and more platforms are available to provide images for InSAR studies. Though most remote sensing radars operate at wavelength between 0.5cm to 50cm, L, C, and X are the most common radar bands used for InSAR.

SAR data are available on C band (3.8-7.5cm) from the ERS-1, ERS-2 and RADARSAT missions, on L band (15-30cm) from the JERS-1 and SEASAT missions, and on X band (2.4-3.8cm) from the X-SAR mission. The characteristics of these platforms are summarized in Table 7-1. Many organizations and companies in Australia, US, Japan, Canada, France, Germany, Italy, China, etc., are providing SAR data.

The orbital parameters of ERS-1/ERS-2 could be adjusted to realize the three planned repeat cycles of 3, 35 and 168 days. The transition from one orbital configuration to another, to adjust the repeat cycle, requires up to two weeks to stabilize the orbits to within 1km of the nominal ground track. Therefore most of the time ERS-1/ERS-2 are running in the 35 day repeat cycle.

SAR data are quite cheap compared to setting up a GPS reference station. Some SAR data are actually provided free of charge for disaster-related InSAR studies (e.g., under the "Open Sky" policy of NASA).

In order to obtain high quality InSAR images, the repeat cycle should be as short as possible to provide a wide choice of SAR image pairs for processing. However, as mentioned earlier, it takes some time for ERS-2 to stabilize after an orbit adjustment. Furthermore, an exact repeat orbit is required for topographic change detection. Therefore even a 3-day repeat cycle is not easy to achieve. With advances in space technology, twin-satellite or shuttle SAR systems have been suggested to ensure a pair of correlated SAR images are always available.

While the space shuttle is playing a more and more important role for InSAR studies, many exciting new SAR missions are planned by different space agencies for the 21st century (e.g. SAR 2000 by NASA). In short, the future InSAR application environment is very favourable, and research on InSAR/CGPS integration is very topical.

Table 7-1 Most commonly used spaceborne platforms for InSAR.

Satellite	SEASAT	ERS-1/ERS-2	JERS-1	RADARSAT	X-SAR
Organization	NASA/ JPL	European Space Agency	NASDA of Japan	Canadian Space Agency	NASA/JPL
Time of launch	28 June, 1978	July 1991 / 1995	11 February, 1992	1995	9 April, 1994 (first flight)
SAR band	L-band (23.5cm wavelength)	C-band (6cm wavelength)	L-band (24cm wavelength)	C-band	X band (3cm)
polarization	HH	VV	HH	HH	VV
Orbit height	800km	785km	568km		
Repeat cycle		3, 35, or 168 days	44 days	24 days	
SAR Antenna	10.74 x 2.16m	10.0 x 1.0m			4 x 12m
Resolution	25m	25m	18m	25m	10-200m
Incidence angles	22 degrees	20-26 degrees	32-38 degrees	20-50 degrees	
Number of Looks	4	4	3		
Swath Width	100km	100km	75km	500km	15-90km
Typical image area		80 x 80km	80 x 75km		
Remarks	first SAR satellite operated for 105 days until October 10, 1978			first commercial SAR satellite	first landing April 20, 1994; part of SIR-C/X-SAR

In the following sections some of the exciting applications of InSAR are briefly reviewed.

7.1.2 InSAR for DEM

Experience with the ERS-1, JERS-1, RADARSAT, and ERS-2 missions, even prior to the SRTM mission, had established InSAR as a method for generating detailed and accurate Digital Elevation Models (DEM) of the Earth's surface. Two missions, the ERS Tandem

Mission and the SRTM Mission, have contributed significantly to research on the use of InSAR for DEM generation.

The ERS Tandem Mission started on the 16th August 1995 for a period of 9 months up to end-May 1996, in which the two satellites ERS-1 and ERS-2 were both in 35-day repeat orbits, but with ERS-2 following approximately 30 angular minutes behind ERS-1 in the same orbital plane so that there was a 1-day interval between ERS-1 & ERS-2 observing the same area of ground. The main driver for the Tandem Mission has been SAR Interferometry and as a result a series of new and improved observations of geophysical phenomena was made possible using the InSAR technique.

For the total period until May 1996, about 79% of all Tandem mission InSAR pairs are suitable for DEM generation, 20% for potential use for Differential InSAR (ie land change detection), and just 1% are unsuitable for InSAR. This high rate of suitable SAR images is mainly due to the significant improvement in the phase coherence. The overall improvement of interferogram quality (phase coherence) from the 1-day Tandem Mission configuration, with respect to the 35-day and 3-day single satellite repeat cycles, has been confirmed, although it is diffcult to quantify due to the strong dependence of coherence on specific terrain conditions. Values of coherence as high as 0.7/0.8 have been observed for some areas. However, there have been some snow-covered regions with extremely low coherence (possibly due to summer melting).

Based on results achieved with ERS-1 and ERS-2, the improved coherence from the Tandem Mission data is estimated to result in DEM rms height errors of less than 10m across the complete 100 x 100km image, and less than 2m for local regions within the image, under favourable conditions. This highly accurate and consistent DEM can play a very important role in the DEM + InSAR approach for deformation monitoring.

The Shuttle Radar Topography Mission (SRTM) is illustrated in Fig. 7.1, in the form of a computer-generated view of the Space Shuttle Endeavour flying above Earth's surface during 11-22 February 2000. The SRTM Mission has collected three-dimensional

measurements of nearly 80% of the Earth's land surface, home to nearly 95% of the world's population, except near the poles, with an accuracy of better than 16 metres.

With its radars sweeping most of the land surfaces of the Earth, SRTM acquired enough data during its ten days of operation to obtain the most complete near-global, high-resolution database of the Earth's topography. To acquire topographic (elevation) data, the SRTM payload was outfitted with two radar antennas. One antenna was located in the shuttle's payload bay, the other on the end of a 60m mast that extended from the payload pay once the shuttle was in space. Additional C-band imaging antenna and improved tracking and navigation devices were also incorporated.

All of the radar data was collected during the single, 11-day shuttle mission, and will be processed to the same specification. Collecting and processing the data in this way ensures that the SRTM-generated topographic maps will have the same quality. The resulting data will provide 3-D images of the Earth's surface, which can be used to help study drainage patterns and land surface changes over time. The data's military applications include mission planning and rehearsal, modelling and simulation.

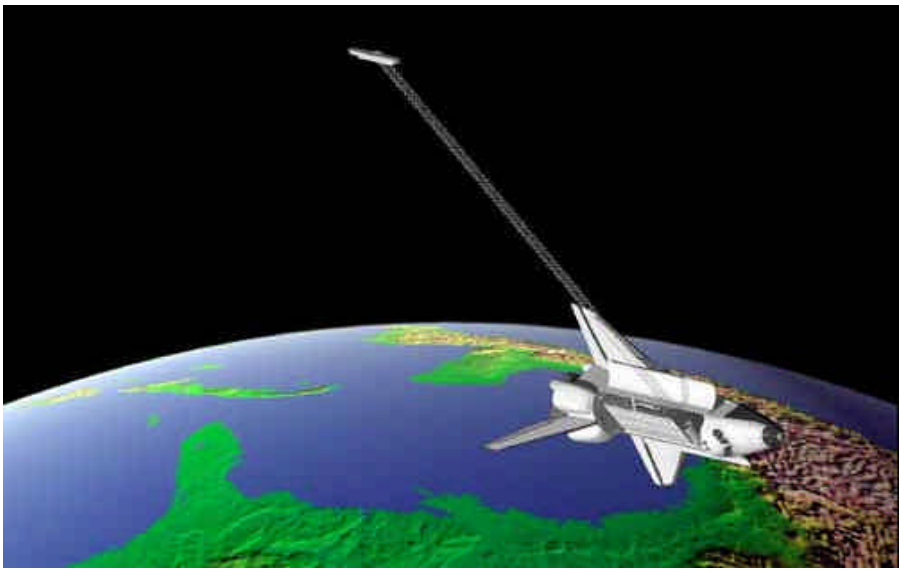

Figure 7.1 Computer-generated view of the Space Shuttle flying above Earth's surface in the Shuttle Radar Topography Mission (SRTM) (JPL, 1999).

The ERS Tandem Mission and the SRTM Mission generated a unique and valuable data set with important exploitation potential for years to come.

7.1.3 InSAR for deformation (elevation change)

Each year there are about 10 large earthquakes globally (among them about 3 occurring on land which can be studied with InSAR). These events cause thousands of deaths and considerable property damage. For example, the 1995 Kobe earthquake in Japan resulted in over 5000 fatalities and damage estimates exceeding $100 billion. The geoscience community therefore has a pressing need of a global data set of densely sampled pre-seismic, co-seismic and post-seismic observations of crustal deformation. SAR Interferometry has the potential to provide that data set, together with other techniques such as GPS. As an extension of the basic InSAR technique, the *Differential* InSAR could allow the detection of very small (mm to cm level) movements of the land surface, as demonstrated with the ERS-1 repeat data for the 1992 Landers earthquake in California (Massonnet et al., 1993).

As a matter of fact, due to its very high spatial coverage and cost effectiveness, many earthquakes have been studied using InSAR:

- 28 June 1992 - Landers, California (Massonnet et al., 1993a; 1994; 1996);
- 17 January 1994 - Northridge, California (Murakami et al., 1996);
- 17 January 1995 - Kobe, Japan (Ozawa et al., 1997);
- 27 May 1995 - Sakhalin, Russia (Fielding et al., 1996,;Tobita et al., 1998);
- 13 May 1995 - Kozani-Grevena, Greece (Clarke et al., 1997);
- 17 May 1993 - Eureka Valley, California (Peltzer & Rosen, 1995);
- 1995 - Hyogoken-Nanbu, Japan (Murakami et al., 1995);
- 1993 - Izu Peninsula, Japan (Fujiwara et al., 1998a); and
- 26 March 1997 - Kagoshima-ken-hokuseibu, Japan (Fujiwara et al., 1998b).

This is far from a complete list. Some of the earthquakes were studied by several researchers from different institutions, some were studied by the same researcher several times, and some researchers have studied several quakes. More recently, InSAR has also been applied to study the Mw 7.1 Hector Mine Earthquake in near-real time (Sandwell et al., 2000). Colourful InSAR results on earthquakes have been used to derive fault models that can be compared with those derived from seismic data; to estimate the co-seismic deformation; to detect the fault-zone collapse; and so on. Seismologists have benefit greatly from the InSAR results, as never before has the co-seismic deformation on seismic faults been observed in such a comprehensive manner.

The following volcanoes have been studied with InSAR:

- Mount Etna, France (Briole et al., 1997);
- New Trident, Alaska (Lu et al., 1997);
- Merapi, Indonesia (Briole et al., 1997);
- Kilauea, Hawaii (Gaddis et al., 1989);
- Kunlun Mountains, western China (Guo et al. ,1997); and
- Mt. Vesuvius, Italy (Mouginis-Mark et al., 1993).

Volcanoes are ideal test sites for InSAR due to the absence of vegetation.

Other InSAR applications of elevation change determination include landslides (Fruneau et al., 1996) and terrain subsidence (Rosen et al., 1997).

7.1.4 Other InSAR applications

Other main application domains of InSAR include: ice surface motion (for glaciology) (e.g., Goldstein et al., 1993), and land surface change/classification (for forestry / agriculture) (Wegmuller & Werner, 1995). For the study of glacial motion, maps of ice motion velocity vectors have been derived from both ERS and JERS InSAR. It is thought that the technique will work best during winter when the potential for daytime melting (and

consequent loss of coherence) is minimized. For land surface change / classification, results with the ERS Tandem Mission confirm the potential for land surface cover discrimination when coherence is combined with the radiometry.

However, the most exciting new application of InSAR is the two-dimensional mapping of large scale surface deformation with very high sensitivity. These deformation maps can be used to detect and monitor land deformation due to earthquakes, crustal movements, landslides, volcanic activity (subsidence and absidence), underground mining activity and water or fluid extraction (causing land subsidence).

7.2 Comparison Between CGPS and InSAR

Global continuous GPS (CGPS) stations, such as deployed for the International GPS Service (IGS), provide the tracking data for determining precise satellite ephemerides and for defining the terrestrial reference frame. The IGS therefore supports the wide application of continuous GPS regional arrays for geodetic studies of crustal deformation. Many CGPS networks have been set up in recent years, such as the Japanese GEONET, and the Southern California Integrated GPS Network (SCIGN), by the Jet Propulsion Laboratory. Many more countries are constructing their own CGPS networks, such as China, South Korea, Taiwan, Hong Kong, Germany, U.K., Singapore, Russia, to name but a few. Data from CGPS arrays are also used in meteorological research projects to test the feasibility of operational mapping of the tropospheric water vapour, and ionospheric disturbances.

Most CGPS arrays are now sampling data at an interval of 30 seconds, although some can sample at a one second interval. New GPS receivers can make as many as 10 to 20 samples per second. Therefore CGPS receivers could provide temporally very dense GPS observations. The high temporal resolution is the most significant characteristic of CGPS. These CGPS arrays may be spatially dense enough for applications such as navigation, RTK, etc. They are not dense enough, as a rule, for characterizing or monitoring seismic faults. For this purpose sub-km level spatial resolution is required, which is hard to achieve with CGPS networks. GEONET, the world's densest CGPS array, has receivers spaced at

an average 25km.

InSAR, on the other hand, exhibits around 25m spatial resolution (Table 7-1). Without the need for any ground-based receiver or cooperative target, InSAR can virtually monitor every corner of the Earth. But InSAR is very sensitive to errors such as atmospheric effects (tropospheric delay, ionospheric delay, etc.), satellite orbit error, condition of ground surface and temporal decorrelation. When present in the InSAR image, these errors can be very misleading and lead to misinterpretation. However, there is no way to eliminate them using only SAR data. Furthermore the repeat cycle of 35 to 44 days of SAR satellites can not provide enough temporal resolution for applications such as monitoring terrain subsidence due to underground mining, distinguishing deformations before, during, and after earthquakes or volcano eruptions, and so on.

Table 7-2 provides a brief comparison of the two techniques. Since data from CGPS arrays can be used to map tropospheric water vapour and ionospheric disturbances, these results can be used to remove atmospheric effects in InSAR. With the support of SLR and VLBI, GPS coordinates can be considered as being 'absolute' in the sense that they are tied to a well-defined terrestrial reference system. While assuming that there are no displacements at a few points (reference points) in a radar image in data processing, InSAR results are relative measurements. GPS measurements on the reference points in a SAR image can also be used as constraints to mitigate the influence of SAR satellite orbit errors. On the other hand, InSAR results, with its high spatial resolution, can be used to densify GPS observations in a spatial sense. Moreover, even when the GPS networks are densified, in order to recover the signature of active faults the station configuration design may not be ideal. Interpolation at these points, based on the GPS results from a well-designed station network, can provide a good quality control measure.

Therefore it is obvious that the two techniques are complementary. The integration of InSAR/GPS could measure deformation to 1 mm/yr precision with unprecedented spatial coverage. Such a InSAR/GPS system would be able to determine displacement at millions of points, rather than the few hundred being measured with current geodetic methods (e.g.

the 947 stations of the GEONET).

Table 7-2 Comparison of CGPS and InSAR.

	CGPS	InSAR
Observable	three component displacement (horizontal and vertical, accurate in horizontal, inaccurate in vertical)	change of distance from ground to satellite (one component, may be divided to an accurate vertical and inaccurate horizontal)
Temporal resolution	almost continuous (usually daily position solutions, can be one or even 30 samples per second)	periodical (every 35 days for ERS-1, 44 days for JERS-1, 1 day for ERS Tandem Mission)
Spatial coverage and resolution	discrete stations (highest resolution of about 25km in Japan)	continuous global coverage (25m x 25m resolution)
Satellite	24 GPS satellites	one SAR satellite
Receiver on ground	required (at least two to achieve high accuracy)	None

The integration of InSAR and GPS was first suggested in 1997 (Bock et al., 1997). The Double Interpolation and Double Prediction (DIDP) approach for InSAR/GPS integration was proposed in 1997 (Ge et al., 1997a&b). The algorithmic basis and some results of DIDP are presented in this Chapter.

7.3 GPS and InSAR Integration – the "Double Interpolation and Double Prediction" (DIDP) Approach

In the DIDP approach the first step is to derive atmospheric corrections to InSAR from CGPS analyses. Analysis of the GPS data can give estimates of precipitable water vapour (in a technique referred to these days as "GPS meteorology"), as well as the ionospheric delay (possible because of the available dual-frequency GPS observations). The second step

is to remove or mitigate the SAR satellite orbit errors by using GPS results as constraints. In a third step the CGPS observations, separated by one or several InSAR repeat cycles within the SAR image, are 'densified' onto a grid. This is done by interpolation in the spatial domain using as a basis a distribution model derived from the GPS-corrected InSAR results. The densified gridded values are then interpolated in the time domain using as a basis a dynamic model derived from the daily, hourly, or even 30 second sampling rate of the CGPS data series, incorporating known geophysical information such as the locations and geometries of active faults (Ge et al., 1999b). The adaptive filter can be used in this step. In a fourth step, based on the double interpolation result, forward filtering (e.g. Kalman filtering) can be used to predict the crustal deformation at all points on the grid - in effect a double prediction in both the temporal and spatial domains.

7.3.1 Deriving atmospheric correction to InSAR from CGPS

In the DIDP approach the first step is to derive atmospheric corrections to InSAR using CGPS data (Bevis et al, 1992). It is well known that the accuracy of InSAR measurement is limited mostly by atmospheric propagation *heterogeneity* (due to the highly variable distribution of atmospheric water vapour) in space and time (e.g. Massonnet et al, 1995). Atmospheric refraction artefacts in the InSAR result may introduce errors as large as three fringes locally, in the case of exceptional conditions. Therefore they have to be corrected before InSAR results can be used for deformation analysis.

On the other hand, although the primary purpose of almost all CGPS arrays is to address geodetic applications, they may also produce estimates of the tropospheric zenith delay in the immediate vicinity of the GPS station as a byproduct of data processing. Using CGPS data it is possible to map the tropospheric zenith delay with high resolution in both space and time. This, in turn, can be used as an atmospheric 'correction' to the InSAR result. Such atmospheric 'corrections' generated from CGPS data will soon be generally available through the IGS and other services, as there is a growing interest in the monitoring of atmospheric water vapour.

Water vapour is one of the most significant constituents of the atmosphere since it is the means by which moisture and latent heat are transported, and hence cause "weather". Water vapour is also a greenhouse gas that plays a critical role in the global climate system. Despite its importance to atmospheric processes over a wide range of spatial and temporal scales, water vapour is one of the least understood and poorly described components of the Earth's atmosphere.

While an important goal in modern weather prediction is the improvement of short-term cloud and precipitation forecasts, the ability to do so is severely limited by the lack of timely and accurate water vapour information. Traditional water vapour observing systems include radiosondes, surface-based radiometers, satellite-based radiometers, and some research aircraft. Each of these systems has advantages and limitations. Although it also has limitations, many researchers believe that ground-based CGPS will be most useful as an element of a composite upper-air observing system. In this role it will provide frequent water vapour measurements to constrain numerical weather prediction models, as well as independent calibration and validation of satellite measurements.

The principle of using GPS data to measure water vapour is based on the fact that GPS radio signals are slowed as they propagate from the GPS satellites to ground-based receivers, passing through layers of the Earth's atmosphere: the ionosphere and the neutral atmosphere. This slowing delays the arrival time of the transmitted signal from that expected if there were no intervening media. It is possible to correct for the ionospheric delay, which is frequency dependent, by using dual-frequency GPS measurements. The delays due to the neutral atmosphere, however, are effectively non-dispersive at GPS frequencies and so cannot be corrected in this way. They depend on the constituents of the atmosphere, which are a mixture of dry gases and water vapour.

In a ground-based GPS system, the signal delays from several (at least four, but typically six or more) satellites in view are simultaneously measured. These delays are mathematically adjusted (scaled) such that all satellite signals are treated as having been transmitted from directly overhead (at the zenith) simultaneously, using the mapping

function:

$M_T(q) = 1/\sin q$ (7.3)

where θ is the elevation angle from receiver to the satellite. The averaged vertically-scaled signal delay introduced by the atmospheric constituents is called the Zenith Total (or Tropospheric) Delay (ZTD). ZTD can be separated into two components, the zenith hydrostatic delay (ZHD) and the zenith wet delay (ZWD):

$$\Delta L = \Delta L_h^0 M_h(q) + \Delta L_w^0 M_w(q) \quad (7.4)$$

where $M_h(q) \_ and \_ M_w(q)$ are the hydrostatic and wet mapping functions respectively. $\Delta L_h^0 \_ and \_ \Delta L_w^0$ are ZHD and ZWD respectively (in mm).

The ZHD is calculated by measuring the surface pressure and applying a mapping function. The ZWD can be viewed as a stochastic process, and the process parameters can be estimated using a Kalman filter. In fact, both stochastic and deterministic algorithms for atmospheric modeling are employed in high precision GPS software such as GIPSY, GAMIT and the Bernese package.

Suppose the ZTD at GPS station i at the SAR image acquisition time t is $\Delta L_i(t)$ using Eqn. (7.4), the atmospheric correction derived from GPS data to the InSAR result on the image point of station i will be:

$$d\ L_i = \Delta L_i(t_2) - \Delta L_i(t_1) \quad (7.5)$$

where t_1 and t_2 correspond to the imaging time of the two SAR images used in the interferometric processing. The atmospheric correction for other image points can be interpolated from the GPS stations.

7.3.2 Remove or mitigate SAR satellite orbit errors by using GPS results as constraints

The second step of DIDP is to remove or mitigate SAR satellite orbit errors by using GPS results as constraints. For this purpose, metal corner reflectors can be co-located with, or 'tied' precisely to, some GPS sites on the ground. The SAR data covering each of these GPS sites thus correspond to a precisely-located point, and hence could be used to provide 3-D corrections to the spacecraft orbit, and hence improve the accuracy of the ground displacement measurement.

Fig. 7.2 illustrates the InSAR geometry. The radar beam is transmitted to the ground from antenna A_1. After scattering at the ground point G, the radar wave is received by antennas at both A_1 and A_2. The distance between A_1 and A_2 (the baseline length) is B (exactly 60m in the case of the Shuttle Radar Topography Mission, the length of the mast (JPL, 1999)) and the radar look angle is θ. The GPS heights of the antenna A_1 and the ground point G are H and h respectively. H can be estimated from the SAR satellite ephemeris, but usually not precisely enough for deriving DEM or deformation information (because it is one of the orbit errors to be mitigated), although for SRTM data it is precisely known because GPS receivers were flown aboard the space shuttle. The h is usually an unknown to be solved by InSAR but is known precisely if a GPS receiver and corner reflector are employed at the control point. Suppose $\beta = \angle G\, A_1\, A_2$ can be calculated from the orientation of the baseline, then the geometric distance r between A_1 and G can be calculated as:

$$r = \frac{B^2 - d^2}{2d + 2B\cos b} \tag{7.6}$$

where δ can be calculated from the phase difference φ from InSAR as:

$$d = \frac{j}{2p} l \qquad (7.7)$$

where λ is the radar wavelength. Therefore, the SAR vehicle height estimated from the ground control point information is:

$$H = h + r\cos q \qquad (7.8)$$

Several estimations of H can be obtained if there are several ground control points. By giving different weights to both these estimates and the H derived from the SAR satellite ephemeris in a least-squares process (Giordano & Hsu, 1985), the orbit errors can be effectively reduced.

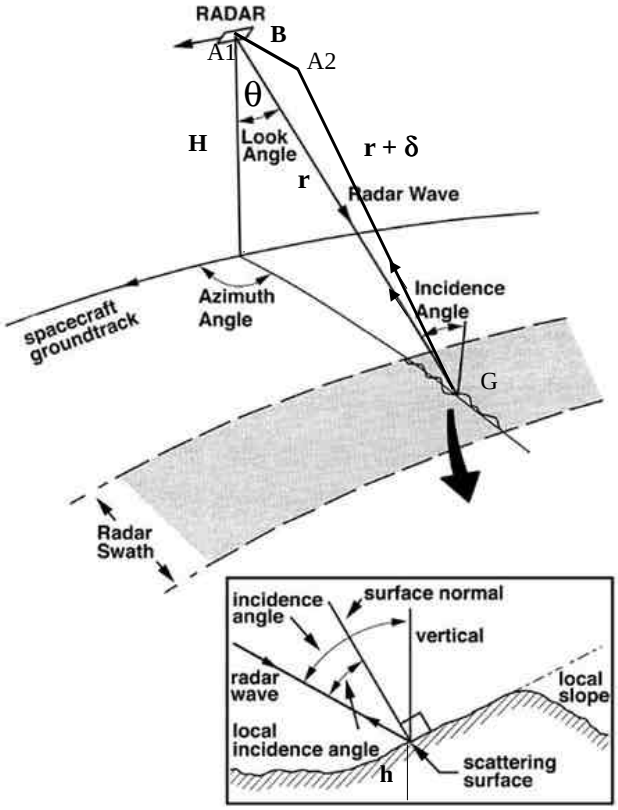

Figure 7.2 The radar interferometry geometry (after Mouginis-Mark, 2000).

7.3.3 Densify observations by double interpolation

The atmospheric and orbit corrections dealt with in the previous two sections yield GPS-corrected InSAR results. In the third step of DIDP, the CGPS observations separated by one or several InSAR repeat cycles are densified in a grid manner by interpolation in the spatial domain based on the GPS-corrected InSAR results (geophysical information has been incorporated in the distribution model for this interpolation) (Ge et al., 1999). Then the densified grid observations are interpolated in the time domain based on the daily, hourly, or even 30 second sampling rate CGPS time series (adaptive filtering based on the least-mean-square algorithm has been used to extract the dynamic model for this interpolation) (Ge, 1999).

7.3.3.1 Distribution Model For Interpolation Based on InSAR Result and Incorporating Geophysical Information

To start the interpolation process, an irregular grid pattern is formed based on the locations of the stations in the GPS network.

As indicated in Fig. 7.3, the latitudes and longitudes of the GPS stations are read from a (sequential) data file. Here Nij (i, j=1, 2, 3, and 4) refers to the latitude for the ith station in the file and it ranks j among the latitudes for all the GPS stations. Eij stands for longitude and is analogous with Nij. Then the latitudes Nij and longitudes Eij are sorted according to their values (i.e. index j). The sorted latitudes and longitudes are then combined to form the grid (Nij, Eij), consisting of both existing GPS stations (denoted by “G”) and points to be interpolated (denoted by “I”). The important feature of the two dimensional sorting is that the attributes of GPS stations (index i) are maintained so that no interpolation operation is needed on grid points of GPS stations. Therefore, the algorithm carries out an “indexed sorting”.

It can be seen from Fig. 7.3 that there is one and only one GPS station in both the rows and the columns on the transformed grid. In practical applications, however, there may be two or more when the CGPS array is very dense and some of the stations are very close, or in the contrary situation, there may be none in a row or column when the CGPS array is very sparse but a relatively dense 'densification' is desired.

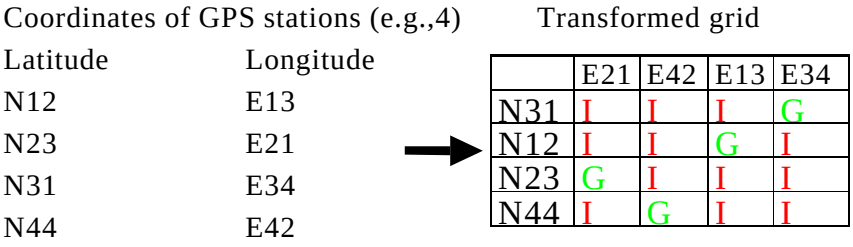

Figure 7.3 An irregular grid formed by indexed sorting.

In order to interpolate objectively, it is proposed that geophysical information be incorporated. It is well known that the movements of GPS stations on the two sides of a fault can be significantly different, therefore it is important to classify the stations and the intended interpolating points according to their positions in relation to the fault. The open- (Fig. 7.4) and closed- (Fig. 7.5) curve models have been designed to describe the geometric characteristics of faults. In the open-curve model the region of interest is divided into upper (or left) and lower (or right) sub-regions by an open curve. This model should be adequate for most seismic faults.

An algorithm has been developed to automatically identify to which sub-region a station or an interpolating point belongs. Assume the unit vectors of latitude is $\vec{i}$ and longitude is $\vec{j}$, from an arbitrary point on the fault (N_i, E_i) to the GPS station (GS) at (N_G, E_G) the vector can be expressed as:

$$\vec{G} = (N_G - N_i) \bullet \vec{i} + (E_G - E_i) \bullet \vec{j} \qquad (7.9)$$

A minimum search of vector length is performed to find $|\vec{G}|_{(N_i, E_i)} = \min$

Therefore, a GS local fault vector can be written as:

$$\vec{F}_G = (N_{i+1} - N_i) \bullet \vec{i} + (E_{i+1} - E_i) \bullet \vec{j} \qquad (7.10)$$

From an arbitrary point on the fault (N_j, E_j) to the interpolating point (IP) at (N_I, E_I) the vector can be expressed as:

$$\vec{I} = (N_I - N_j) \bullet \vec{i} + (E_I - E_j) \bullet \vec{j} \qquad (7.11)$$

A minimum search of vector length is performed to find $|\vec{I}|_{(N_j, E_j)} = \min$

Then, an IP local fault vector can be written as:

$$\vec{F}_I = (N_{j+1} - N_j) \bullet \vec{i} + (E_{j+1} - E_j) \bullet \vec{j} \qquad (7.12)$$

From Eqs. (7.9) to (7.12) a "decision" can be made: if $(\vec{F}_G \times \vec{G}) \bullet (\vec{F}_I \times \vec{I}) > 0$ the GPS station and the interpolating point are on the same side of the fault. Otherwise they are on different sides of the fault.

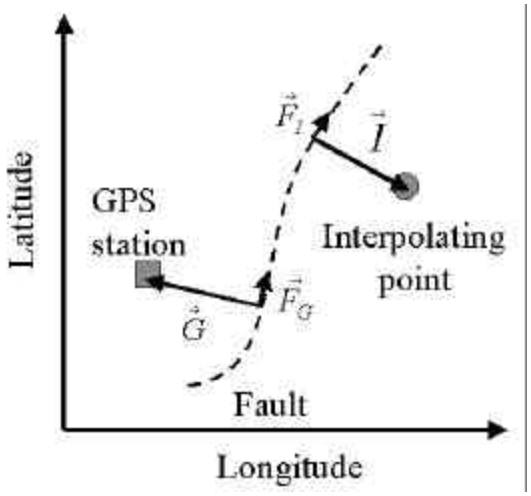

Figure 7.4 Open-curve model: one GPS station and one interpolating point case.

In the closed-curve model the region to be studied is divided into 'outside' and 'inside' sub-regions by a closed curve. This model is appropriate for applications such as volcano deformation monitoring.

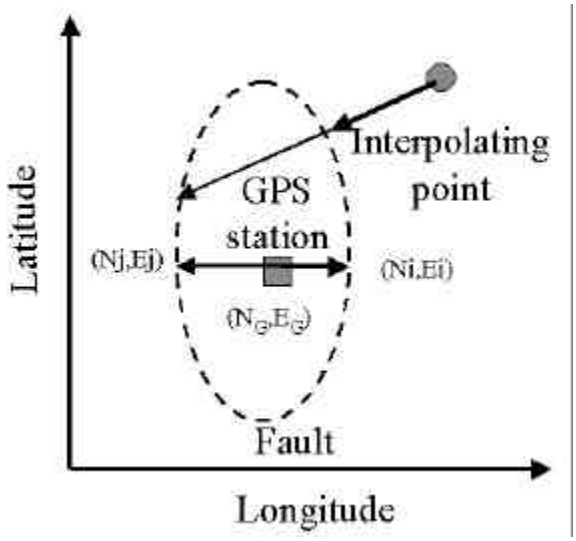

Figure 7.5 Closed-curve model: one GPS station and one interpolating point case.

A different algorithm for this model is developed to automatically identify in which sub-region a station or interpolating point belongs to. Again assume the unit vectors of latitude is $\vec{i}$ and longitude is $\vec{j}$. From the GPS station (GS) at (N_G, E_G) to an arbitrary point on the fault (N_i, E_i) the vector can be expressed as:

$$\vec{G} = (N_i - N_G) \bullet \vec{i} + (E_i - E_G) \bullet \vec{j} \qquad (7.13)$$

A minimum search of vector length is performed to find $|\vec{G}|_{(N_i,E_i)} = \min$

The GS primary vector is thus determined as:

$$\vec{L}_1 = \vec{G} \qquad (7.14)$$

Then a minimum distance search from an arbitrary point on the fault to the GS primary vector can determine (N_j, E_j), which is used to calculate the GS secondary vector:

$$\vec{L}_2 = (N_j - N_G) \bullet \vec{i} + (E_j - E_G) \bullet \vec{j} \qquad (7.15)$$

From Eqns. (7.14) and (7.15), a "decision" can be made: if $\vec{L}_1 \bullet \vec{L}_2 > 0$ the GPS station is outside of the fault. Otherwise it is inside the fault. The position of the interpolating point relative to the fault can be determined in the same way.

The combination of open- and closed-curve models can deal with comparatively complex fault systems. After the classification of GPS stations and the intended interpolating points into different groups, a distribution model for interpolation for each group based on the GPS-corrected InSAR results is proposed, as illustrated in Table 7-3. After developments over more than two decades, InSAR is now capable of addressing many applications such as mapping topography, detecting topographic change, etc. InSAR has approximately 25m spatial resolution. Without the need for any ground-based receiver or cooperative target, it can virtually monitor every corner of the Earth. But InSAR is very sensitive to errors such as atmospheric effects (tropospheric delay, ionospheric delay), satellite orbit error, conditions of the ground surface and temporal decorrelation. When presented in the InSAR image, these errors can result in misleading interpretation. There is at present no way to eliminate them using SAR data alone. Therefore, a distribution model for interpolation based on both GPS and InSAR results is proposed, as given in Table 7-3. In some sites of interest (Sites 1 to 4) there are both GPS and InSAR results for the deformation (the CGPS results may have to span one or more InSAR repeat cycles depending on the availability of suitable SAR image pairs). But in most other sites (Sites 5, 6, …) there will only be InSAR-derived results. All of the results are input into a least-squares adjustment (e.g. Giordano & Hsu, 1985). The adjusted results, which form the distribution model for interpolation in spatial domain, are used as constraints later on to scale the time series generated at the interpolated points based on the dynamic model.

Table 7-3 Distribution model based on InSAR information.

Interested site	GPS result	InSAR result	Least-square adjusted result
1	G1	S1	A1
2	G2	S2	A2
3	G3	S3	A3
4	G4	S4	A4
5		S5	A5
6		S6	A6

It is important to have overlapping GPS and InSAR results over the active fault region so that the GPS results can be used to calibrate out some errors in the InSAR results. But this condition is very hard to satisfy (Bock & Williams, 1997). It is hoped that the densification of CGPS and new missions for InSAR such as the Shuttle Radar Topography Mission (SRTM), Airborne Synthetic Aperture Radar (AIRSAR), Geographic Synthetic Aperture Radar mission (GeoSAR), and Lightweight Synthetic Aperture Radar (LightSAR) (JPL, 1999), will ease such difficulties.

Fig. 7.6 is an example of the deformation distribution model based on both InSAR and GPS for the 1992 Landers Earthquake, obtained following such an approach. The geocoded InSAR result and GPS result for 38 sites for the 1992 Landers Earthquake epicenter region were kindly provided by courtesy of Dr Massonnet of CNES, France (Massonnet et al., 1993) and Dr Freymueller of the University of Alaska (Freymueller et al, 1994) respectively. In order to derive the distribution model for interpolation in the spatial domain, GPS sites were first matched with their imaging points in the InSAR result. Then the GPS displacements were projected to the change in range in the direction which points towards the satellite. Meanwhile, the InSAR result was resampled. Having obtained both InSAR and GPS results, they were least-square adjusted as outlined above. Fig. 7.6 is a plot of the adjusted result (Ge et al, 1999b), which is not significantly different from the InSAR alone result (Massonnet et al., 1993) due to the fact that some GPS stations have been used as ground control points in the InSAR data processing, and that the InSAR and GPS results employed are generally in good agreement. However, this will by no means lessen the importance of InSAR/GPS integration for deriving the distribution model.

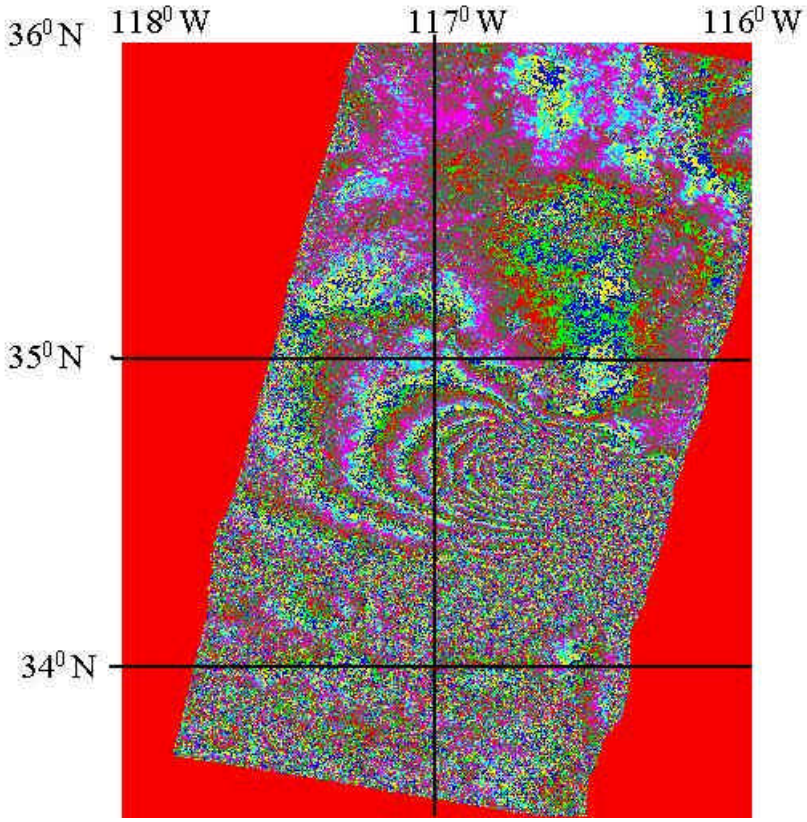

Figure 7.6 A deformation distribution model based on both InSAR and GPS for the 1992 Landers Earthquake.

7.3.3.2 Dynamic Model For Interpolation Based on CGPS Times Series

After the classification of GPS stations and the intended interpolating points into different groups, CGPS results sampled daily, hourly, or even every 30 second from stations in the same sub-region are used to derive a dynamic model, which is then used to interpolate in the time domain at grid points in the same sub-region. Figs. 7.7 to 7.9 shows an example of a dynamic model extracted using an adaptive filter based on the least-mean-square algorithm (Ge, 1999) for daily CGPS results from two closely located stations in the same classified group: stations BRAN and LEEP of the Southern California Integrated GPS

Network (SCIGN).

In each figure, the first two plots are latitude time series for stations BRAN and LEEP respectively. The third plot is the model derived using an adaptive filter, which can be used as a dynamic model for interpolation in temporal domain. The characteristic change in the model near day 300 indicates that the filter does need some time before it can identify the coherent features between the two inputs. The last plot is the local monument movement at BRAN output by the filter. It is well known that the local monument movement for a continuous GPS station can lead to very misleading results. Although much effort has been made to improve the design of the monument, this local movement remains a significant concern in any interpretation. If the GPS time series from individual CGPS stations, as shown in the first two plots of Figs. 7.7 to 7.9, are used directly as dynamic model for interpolation, all the deformations at grid points around the stations will be biased. Therefore it is important to separate the local monument movement from the crustal deformation due to plate or fault motion. Fortunately, since the local monument movements are independent, while the crustal deformations at stations in the same sub-region are strongly correlated (as evident in Figs. 7.7 to 7.9), the adaptive filtering can be employed to decompose them. Even though the two time series from BRAN and LEEP are very different, the derived model in the third plot can function reliably as the dynamic model.

If there is only one CGPS station in the sub-region, its time series is used directly as the dynamic model. If there are more than two CGPS stations in the same sub-region, one of them is used as the primary station and the others are used to provide reference sequences, and the adaptive filter is extended to handle a single primary input and multiple reference inputs system, rather than the single reference input system as shown in Figs. 7.7 to 7.9.

After the double interpolation in this step, deformations at the GPS sites and interpolated points are both spatially and temporally dense enough to be used to prepare an 'animation' of how the crust deforms.

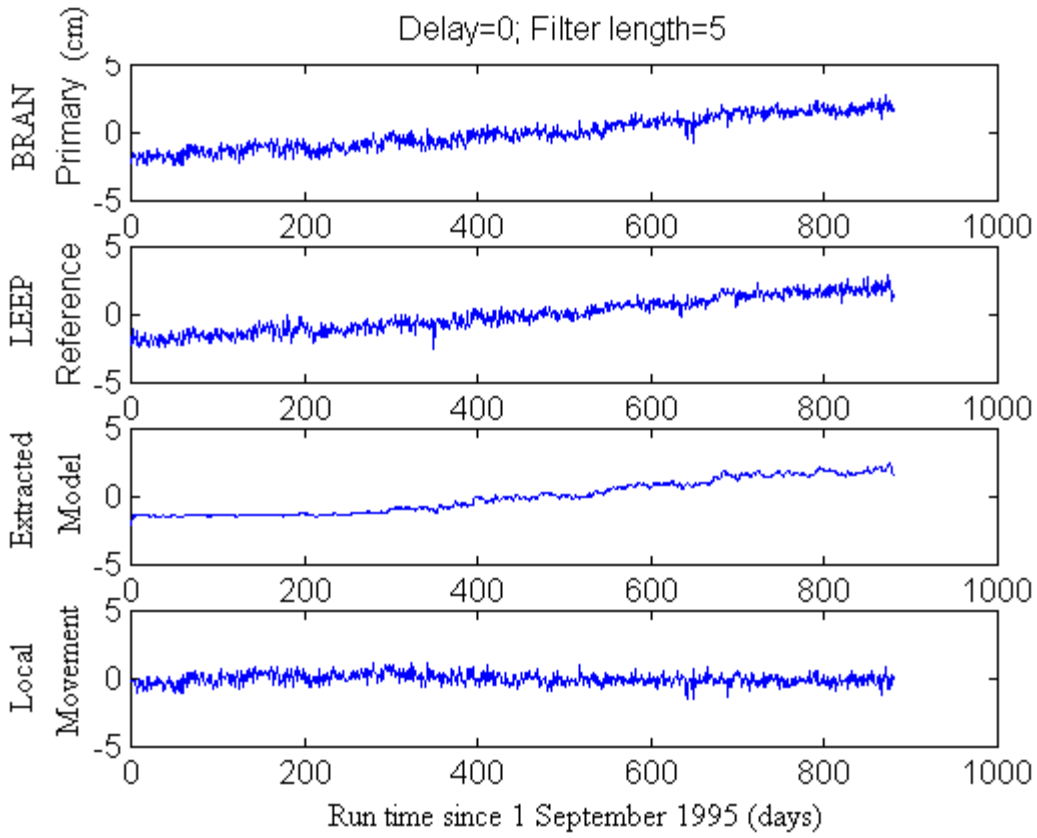

Figure 7.7 Dynamic model extracted using adaptive filtering on CGPS results from BRAN and LEEP stations of SCIGN (latitude component, data courtesy of Jet Propulsion Laboratory, NASA, USA).

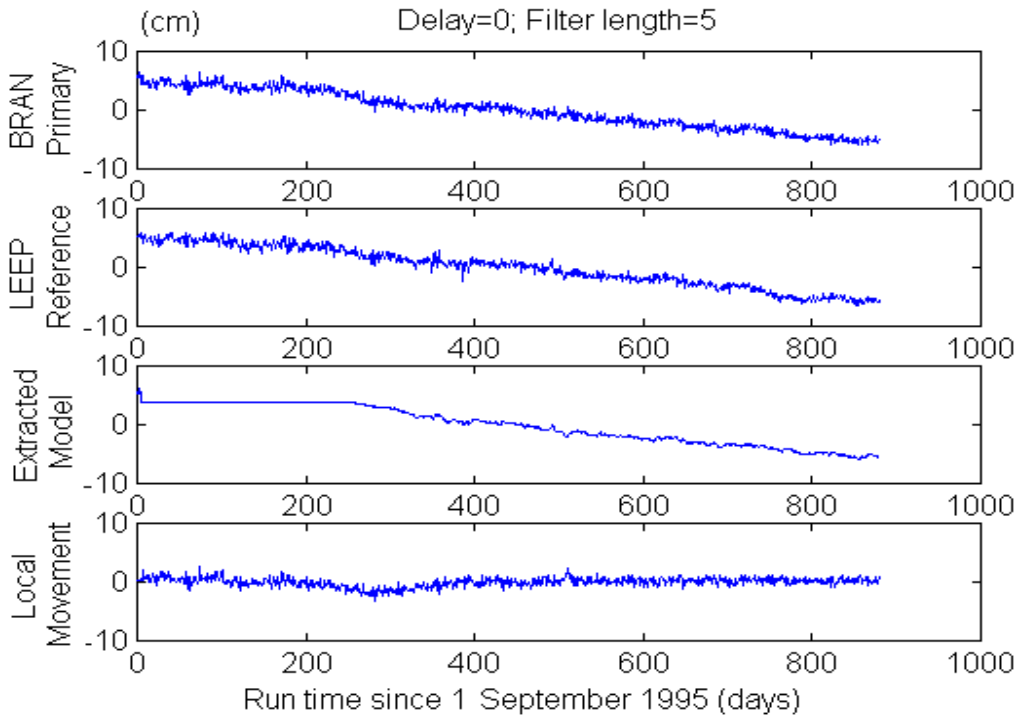

Figure 7.8 Dynamic model for the longitude component.

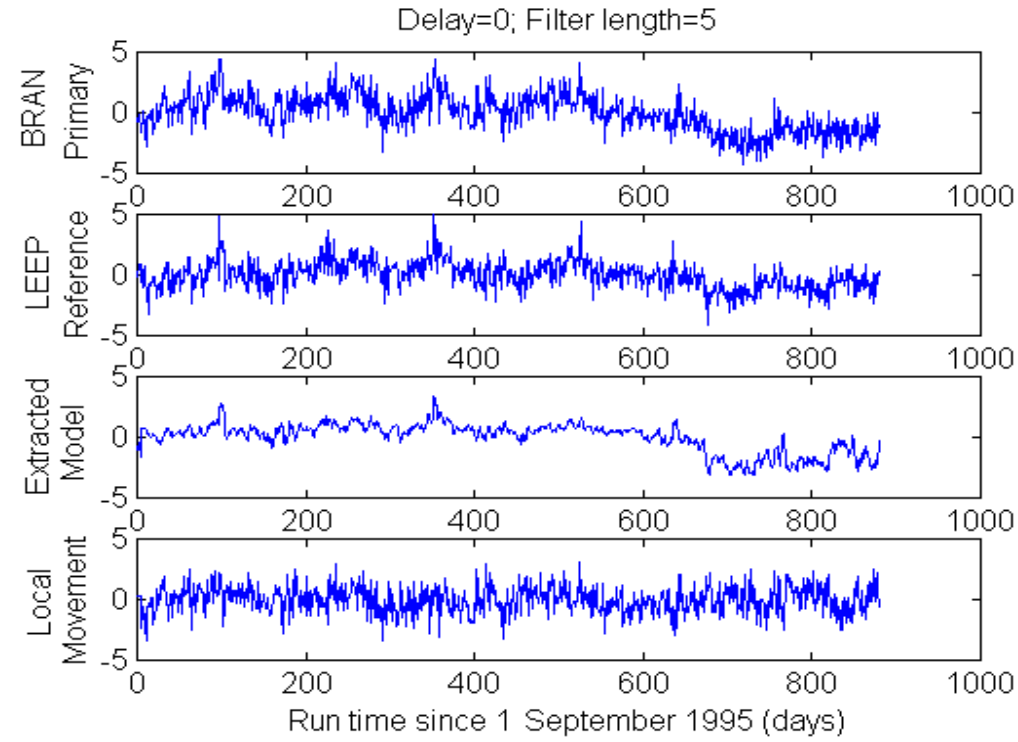

Figure 7.9 Dynamic model for the height component.

7.3.4 Extrapolate quasi-observations by double prediction

In the fourth step of DIDP, based on the double interpolation result (quasi-observations) of the third step, forward filtering (Kalman filtering) is used to predict the crustal deformation at all points on the grid. This is in fact a double prediction in both the time and spatial domains, which could facilitate the use of the DIDP technique for applications such as the prediction of volcano eruption or earthquake ruptures. Moreover, this step is very important in the three-step reliability test (RT) for DIDP. In the first step of RT, the CGPS and SAR data are processed to yield a CGPS time series and the InSAR image respectively. In the second step of RT, the CGPS time series from some of the sites are used together with the InSAR image in the double interpolation to predict CGPS time series for the rest of the CGPS sites. The CGPS time series for these latter sites, from both observation and prediction, are compared to test the reliability of the double interpolation. In the third step of RT, the CGPS time series from all the sites in one SAR repeat cycle are used, together with the InSAR image for the same SAR repeat cycle in the double interpolation, to generate quasi-CGPS time series for all the points on a grid. These quasi-CGPS time series are then used in the double prediction to yield the deformation in the next SAR repeat cycle. The predicted deformation is compared with the CGPS and InSAR results in the next repeat cycle to further test the reliability of the double prediction.

7.4 Concluding Remarks

The Double Interpolation and Double Prediction (DIDP) approach for integrating InSAR and GPS results in the soft spatial densification scheme has been described in this Chapter. In the DIDP approach, the first step is to derive the atmospheric corrections to InSAR from the CGPS measurements.

The second step is to remove or mitigate the SAR satellite orbit errors by using GPS results as constraints. Metal corner reflectors are co-located with (or tied precisely to) some GPS sites. The SAR data covering each of these GPS sites thus correspond to a precisely-located point, and hence could be used to provide 3-D corrections to the spacecraft orbit, thus

improving the accuracy of the ground displacement measurement. These atmospheric and orbit corrections yield GPS-corrected InSAR results.

In the third step, the CGPS observations separated by one or several SAR repeat cycles are densified in a grid by interpolation in the spatial domain, based on the GPS-corrected InSAR results but according to a distribution model. Then the densified grid observations are interpolated in the time domain, based on a dynamic model derived from the daily, hourly, or even 30 second sampling rate of the CGPS time series.

Geophysical and InSAR information have been incorporated in the interpolation of GPS measurements. *The indexed sorting algorithm is very effective in forming an irregular grid pattern for interpolation and maintaining the "attributes" of the GPS stations.* The combination of open- and closed-curve models of a fault is suitable for dealing with comparatively complex fault systems. CGPS data from the SCIGN have been used to demonstrate that adaptive filtering can be successfully used to extract a dynamic model from the GPS time series of stations in the same classified group. A deformation distribution model for interpolation in spatial domain was derived based on both InSAR and GPS results for the 1992 Landers Earthquake.

In the fourth step, based on the double interpolation result of the third step, forward filtering (using a Kalman filter) is used to predict the crustal deformation at all points on the grid, which is in fact a double prediction in both the time and spatial domains.

Since a single SAR image usually covers an area of only 50km by 50km, the reliability of spatial interpolation is guaranteed. Because GPS receivers are operating continuously, and can achieve high accuracy, the DIDP method is, refer to Fig. 1.7, a promising strategy for soft spatial densification to significantly improve the spatial, temporal and magnitude resolution of ground deformation monitoring to 25m, 30 second and mm level respectively.

8 HARD SPATIAL DENSIFICATION – INTEGRATING SINGLE- AND DUAL-FREQUENCY GPS RECEIVERS

Hard spatial densification can be achieved either by deploying a sub-network of single-frequency GPS receivers to in-fill the present CGPS arrays, typically involving the integration of single- and dual-frequency GPS receivers in a so-called '*inward hard spatial densification'*, or by deploying receivers at some geophysically strategic sites outside the existing CGPS array so that combinations of different baselines can be used to, for example, separate plate tectonic and seismic fault movements, in a so-called '*outward hard spatial densification'*.

The 'inward hard spatial densification' is a cost-effective way of deploying many extra receivers in local areas where the deformation patterns are likely to be very complex, such as the junction of several active seismic faults, or where the receivers are more vulnerable to damage (hence some backups are necessary), such as at active volcanoes. In this densification scheme, the dual-frequency measurements are used to generate "error-correction terms", which are used in a linear combination observation model for the processing of the single-frequency measurements. In this way any GPS satellite orbit bias and ionospheric delay can be largely eliminated, and the tropospheric delay, multipath and observation noise can be significantly reduced. In this way it is possible to ensure sub-centimetre relative accuracy (Rizos et al., 1999). Such a scheme is essentially the same as that of the Virtual Reference Station (VRS) concept introduced in Chapter 3, although different algorithms may be used to generate the "error-correction terms".

To test the effectiveness of such an 'inward hard densification' scheme, in August 1999 researchers from The University of New South Wales (UNSW) and from Japan's Geographical Survey Institute (GSI) tested a hardware/software system design for a continuously-operated ground deformation monitoring system based on low-cost GPS receiver technology (Rizos et al, 1999). This UNSW-GSI experiment was undertaken using

data from the GEONET.

In order to densify such CGPS networks (important when high spatial resolution for the monitoring of the deformation phenomenon is required), and to promote the use of the CGPS technique in lesser developed countries, a significantly cheaper system architecture is needed. The proposed design is an integrated, dual-mode network consisting of low-cost, single-frequency GPS receivers across the area of interest, surrounded by a sparser network of dual-frequency GPS receivers. Initial tests using the dual-frequency data collected at selected stations in the GEONET network to simulate single-frequency data have already shown that through enhanced data processing algorithms a CGPS network containing both single-frequency and dual-frequency receivers would be able to deliver better than centimetre level relative positioning accuracy (Rizos et al., 1998).

Chapter 8.3 will report the results of the first field tests carried out in the Tsukuba area of Japan. The test network consisted of: (a) several stations of the GEONET network, surrounding (b) an inner network of four single-frequency Canadian Marconi GPS receivers installed by UNSW researchers (single- and dual-frequency GPS receivers are compared in Chapter 8.1). The data from both the GEONET and the UNSW receivers were processed using a modified version of the Bernese GPS Software Package. The software first processes the GEONET GPS station data in order to generate empirical "corrections", which are then applied to the double-differenced data of the GPS baselines located within the test area enclosed by the dual-frequency CGPS stations (the algorithm and procedures are briefly discussed in Chapter 8.2). These corrections have the effect of improving baseline solution accuracy by up to an order of magnitude, even for baselines ranging up to 100km in length. The baselines connecting the inner network to the surrounding GEONET stations are processed in a number of modes, including 24hr files (as is the standard practice for geodynamic applications), and hourly data files (as in volcano deformation monitoring applications). Chapter 8.5 draws conclusions on the basis of the results of the UNSW-GSI experiment.

The 'outward hard spatial densification' is described in Chapter 8.4. To test this densification scheme, CGPS observations from four stations distributed on both sides of the Longitudinal Valley Fault in Taiwan and one station in Tsukuba (Japan) are processed to generate baseline solutions, which are then used to separate plate tectonic and seismic fault movements.

8.1 Comparison Between Single- And Dual-Frequency GPS Receivers

GPS-based volcano monitoring at Miyake-jima Island in Japan (Fig. 8.1) an example that illustrates why the spatial densification is necessary. Four GEONET stations have been installed on the Island: Stations 93059 (latitude 34 07 03 and longitude 139 30 25) and 93060 (latitude 34 03 20 and longitude 139 33 01) were installed in 1993, while Stations 960599 (latitude 34 05 25 and longitude 139 33 53) and 960600 (latitude 34 04 20 and longitude 139 28 55) were installed in 1996. On 27 June 2000 the GPS Observation Group was formed at the Earthquake Research Institute (ERI) of Tokyo University in response to the increased volcanic activity associated with an earthquake swarm on 26 June 2000. Since 15 July 2000 the three ERI CGPS stations and the 13 temporary CGPS stations have become operational, and 32 temporary rapid static points have been surveyed on a regular basis. Although *3 out of the 4 GSI CGPS stations were damaged during the volcanic activity*, crustal movements associated with the magma intrusion beneath the summit of Mt. Oyama on the Island on June 26 and 27, the August 18 10:52 M6.0 earthquake, and the August 18 17:00 eruption have been successfully monitored by this dense GPS network.

In summary, as is apparent from the figure, in an area smaller than 10km by 10km, there are four GSI GEONET CGPS stations, three ERI CGPS stations, 13 temporary CGPS stations, and 32 temporary GPS-surveyed points, all of which have played an important role in mitigating the effects of the disaster. Without the newly installed ERI CGPS stations, the temporary stations and the surveyed points, prediction of the volcanic eruption would not have been so successful. Spatial densification of a GPS network such as this, therefore, can provide not only necessary input to geophysical modelling but also some redundancy. *Note also that this is not an experiment run by a GPS manufacturer to promote the sale of*

receivers, rather it is real and very recent field work carried out by ERI, which has extensive expertise in the modelling of earthquakes and volcanoes.

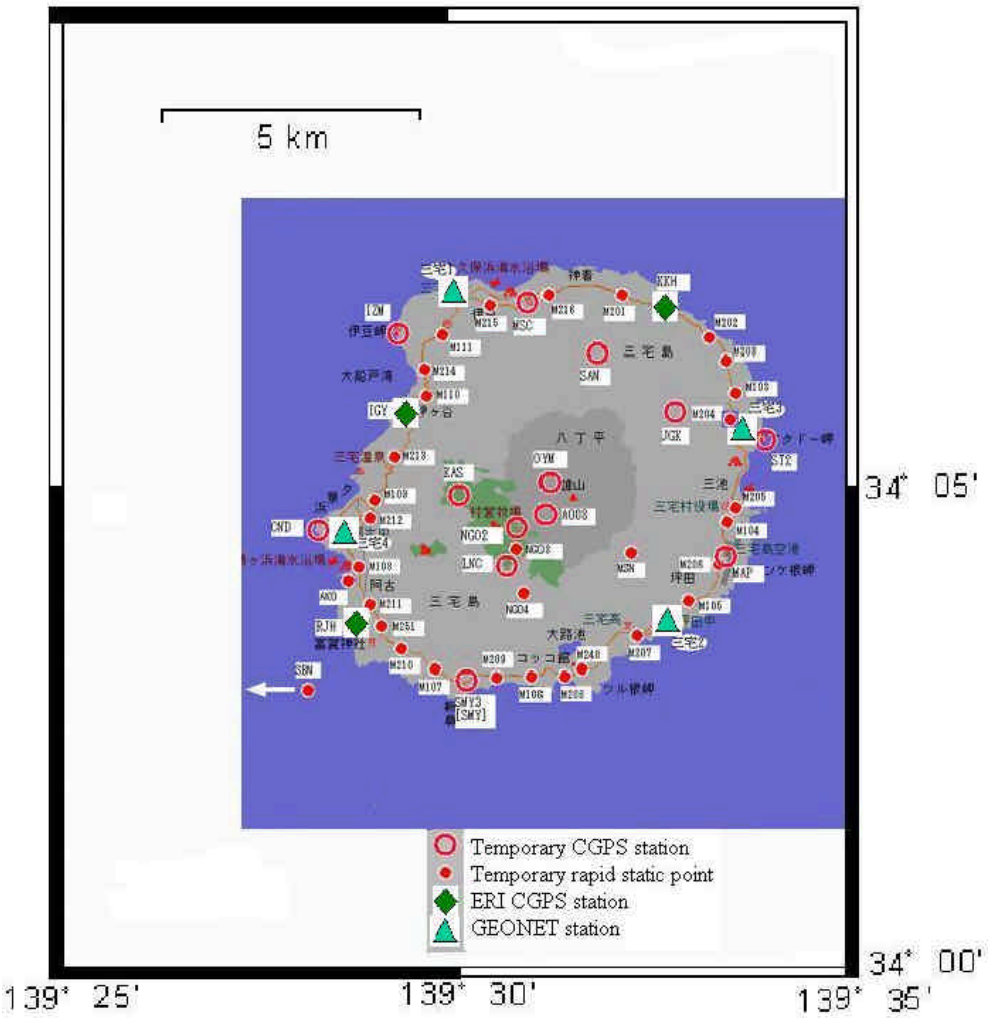

Figure 8.1 GPS network for volcano monitoring at Miyake-jima, Japan (after ERI, 2000).

While it is important for the CGPS network to have a high enough spatial resolution in order to monitor the deformation phenomenon associated with earthquakes and volcanoes, Japan may be one of the few countries (if not the only one) which are capable of densifying an existing CGPS network in such a short time, and with such a density. Moreover, even in this example many rapid-static-surveyed points had to be established, which posed potential

threats to the lives of the GPS surveyors. Therefore, the proposed 'inward hard spatial densification' scheme based on integrating single- and dual-frequency receivers is a worthwhile topic of study.

Single-frequency receivers are widely used in navigation (in space and in the air, on land, or at sea). Single-frequency observations are also adequate for short baselines using conventional GPS surveying techniques.

However, dual-frequency receivers do offer significant advantages. They can be used to eliminate the effects of ionospheric delay (which is a problem for baselines greater than about 20-30km in length), they increase the reliability of the results over long baselines, and they certainly increase the scope of GPS procedures available to the receiver operators. Dual-frequency instrumentation is also essential for high productivity "rapid-static", "stop-&-go" and "kinematic" GPS surveying procedures because of the advantages of dual-frequency phase and pseudo-range data for rapid ambiguity resolution.

There is intensive R&D to improve the tracking performance on the L2 carrier wave. In order to recover both carrier and code on the L2 signal when Anti-Spoofing is on, receivers have to be built using techniques such as squaring, cross-correlation, code-correlation-plus-squaring, and Z-tracking (Rizos, 1996). As a result, dual-frequency instruments usually are hybrid, with code-correlating on L1, and proprietary codeless technology on L2.

Dual-frequency instruments are used mainly on geodetic and geodynamic applications, which comprises a much smaller market than in the case of navigation applications. Moreover, as mentioned above, they are much more complex and therefore are more expensive than single-frequency receivers.

Is there an approach which can take the advantages of both single- and dual-frequency receivers and yet still deliver high accuracy? The next section describes the proposed scheme.

8.2 Inward Hard Spatial Densification – Integrating Single- And Dual-Frequency GPS Receivers

Permanently operating GPS networks have been used for many years in support of geodetic applications. Data from these networks are usually collected on a daily basis, centrally archived at data centres, and are available via the Internet to users. Many of these users, through the application of special carrier phase processing techniques, are able to achieve relative station coordinate accuracies as high as a "few parts per billion" (sub-centimetre accuracy for receiver separations up to a thousand kilometres or more). However, typically "sub-parts-per-million" accuracies (sub-ppm: 0.1ppm implies an accuracy of 1cm in 100km baseline) are considered to be indicative of "GPS Geodesy" techniques. The range of applications that can be addressed using GPS Geodesy techniques is growing rapidly.

Though the CGPS spatial resolution, such as that of the GEONET, is now as high as about 25km, due to the high cost of dual-frequency GPS receivers they may not be established in a dense enough configuration to address all of the geodetic applications. One of them, the monitoring of pre-seismic or post-seismic faulting, requires sub-km resolution, as indicated by the faulting length in Table 1-1.

One option for increasing the geodetic network's spatial resolution is to use low-cost GPS receivers to densify the dual-frequency network, that is, the 'inward hard spatial densification' scheme. The dual- and single-frequency stations are treated as reference and user stations respectively. Another option is to integrate CGPS with techniques such as differential Synthetic Aperture Radar Interferometry (InSAR) (i.e. the 'soft spatial densification' scheme discussed in Chapter 7). As described in several previous studies (e.g. Han, 1997; Rizos et al., 1998; Chen et al., 1999), hard densification data processing strategies have been developed by the UNSW Group that can deliver sub-ppm relative accuracy even for baselines up to 100km in length. Here the data processing algorithm is briefly outlined.

The double-differenced observable can be written as:

$$\nabla\Delta f = \nabla\Delta r + \nabla\Delta dr + l \cdot \nabla\Delta N - \nabla\Delta d_{ion} + \nabla\Delta d_{trop} + \nabla\Delta d^{j}_{mp} + e_{\nabla\Delta f} \qquad (8.1)$$

where $\Delta\nabla$ represents the double-differencing operator; ϕ: the carrier phase observation in units of metres: $\rho := \left(\mathrm{x}^{\mathrm{S}} - \mathrm{x}\right)$, x^{S} is the satellite position vector, x is the station position vector; $\mathrm{d}\rho$: the effect of ephemeris errors (including SA effects, if any); l: the wavelength of the carrier; N: the integer ambiguity for a particular satellite-receiver pair; d_{ion}, d_{trop}, d^{f}_{mp} and $e_{\nabla\Delta f}$ are the ionospheric delay, tropospheric delay, multipath effect and the carrier phase observation noise for a particular one-way observation, respectively (Han, 1997).

From Ibid (1997), Eq (8.1), through a linear combination (assume the number of GPS reference stations is three), can be written as:

$$\nabla\Delta f_{u,3} - \left[a_1 \cdot V_{1,3} + a_2 \cdot V_{2,3}\right] = \nabla\Delta r_{u,3} + l \cdot \nabla\Delta N_{u,3} + e_{\sum_{i=1}^{3} a_i \cdot \nabla\Delta f_i} \qquad (8.2)$$

The subscripts refer to the receiver stations: 1, 2, 3 are the reference stations, and u is the user station(s). It is assumed here that reference station 3 is the "primary" one, used to generate double-differences with the various user stations (u). The parameters α_i can be determined, based on the conditions given in Han & Rizos (1996) and Wu (1994):

$$\sum_{i=1}^{3} a_i = 1 \qquad (8.3)$$

and

$$\sum_{i=1}^{3} a_i \cdot \left(\vec{X}^{S} - \vec{X}_i\right) = 0 \qquad (8.4)$$

The residual vectors are formed from the double-differenced observations between reference stations 1 & 3, and 2 & 3:

$$V_{1,3} = \nabla\Delta f_{1,3} - \nabla\Delta N_{1,3} - \nabla\Delta r_{1,3}$$
$$V_{2,3} = \nabla\Delta f_{2,3} - \nabla\Delta N_{2,3} - \nabla\Delta r_{2,3} \qquad (8.5)$$

By comparing Eqs (8.1) and (8.2), it can be seen that the orbit bias, ionospheric delay, tropospheric delay and multipath bias have been eliminated or significantly reduced. This means that once the reference station data have been used to estimate the ambiguities and coordinates, the residual vectors can be created using Eq. (8.5). Then every user receiver station can receive the correction term $\left[a_1 \cdot V_{1,3} + a_2 \cdot V_{2,3}\right]$ (reference station number 3 is assigned as an original point) and use Eq. (8.2) to aid in the determination of the double-differenced ambiguities.

From the algorithm discussed above, the data processing procedure involves two steps. The first step is to derive the residuals from the three or more reference stations using Eq. (8.5). Based on the approximate position of any single-frequency receiver, the linear combination coefficients can be derived and the correction term (the second term on the left-hand side of Eq. (8.2)) can be generated. The second step is to apply this correction term to the double-differenced carrier phase observations between the one primary reference receiver and a single-frequency receiver. The standard rapid-static positioning procedure can then be used to resolve integer ambiguities and derive the ambiguity-fix solution for the coordinates. This correction term can also be applied to two single-frequency receivers for determining the baseline between these receivers. This procedure is depicted in Fig. 8.2, and has been implemented within the Bernese GPS Software Package by UNSW researchers.

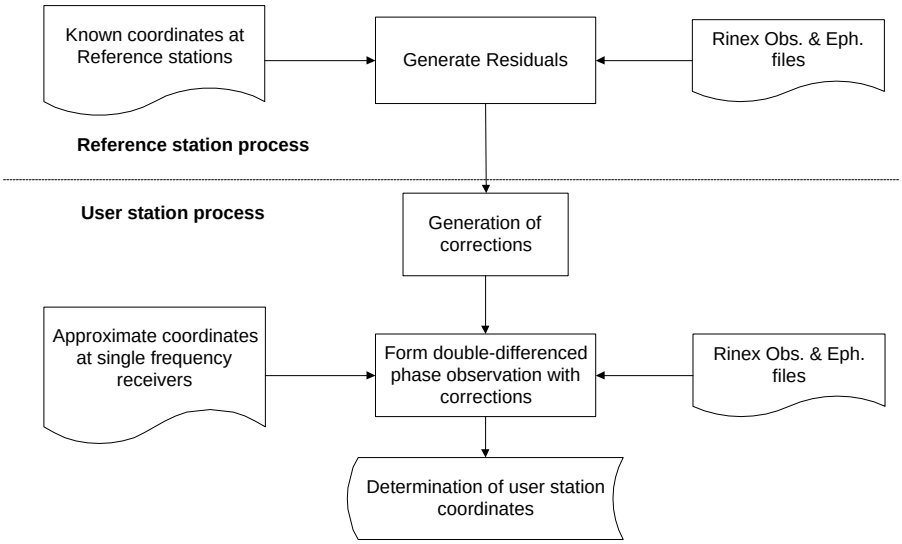

Figure 8.2 Flow chart of data processing procedure.

8.3 The UNSW-GSI Hard Spatial Densification Experiment

In August 1999, the UNSW-GSI experiment was carried out within the GEONET around Tsukuba, Japan (Fig. 8.3), to field test low-cost, single-frequency GPS receivers (Canadian Marconi Company (CMC) receivers) side-by-side with geodetic-type GPS receivers (Trimble 4000SSE). The objectives were to test the UNSW method of integrated data processing, to analyse the coordinate results obtained by this procedure compared with standard multi-station processing using the Bernese Software, and to establish a test network for future UNSW-GSI tests. Four temporary sites, equipped with both CMC and Trimble receivers, with antennas atop two closely spaced tripods, were set up as user stations in the Goka, Hojo, Niihari, and Yatabe districts of Tsukuba. The tripods initially occupied by the CMC antennas are denoted as GOKA, HOJO, NIIH, and YATA. The tripods initially occupied by Trimble antennas are denoted as GOKT, HOJT, NIIT, and YATT. GEONET stations 93002, 93006, 93012, 960582, 960583, and 960584 were used as reference stations in this experiment.

The experiment consisted of two phases. In phase 1 both the UNSW single-frequency receivers and the GSI dual-frequency receivers were operating continuously, side-by-side, for two days. In phase 2 the four test sites were divided into two groups, with two sites in each group. An antenna swapping test was carried out in the first group (Niihari and Yatabe) (Fig. 8.4), while antenna sharing was implemented in the second group (Goka and Hojo) (Fig. 8.5). Data were collected for 8 hours each day over a three day period.

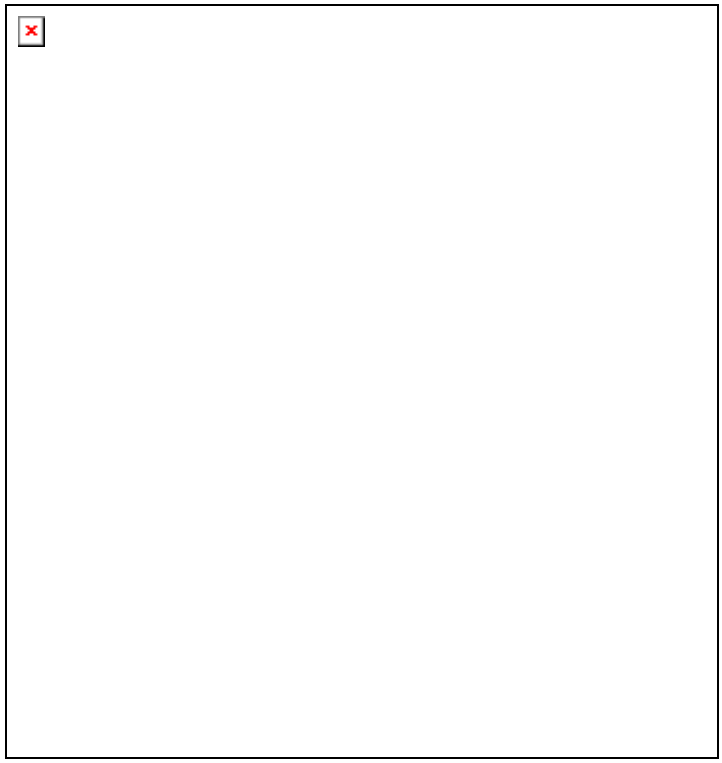

Figure 8.3 The UNSW-GSI test network around Tsukuba, Japan.

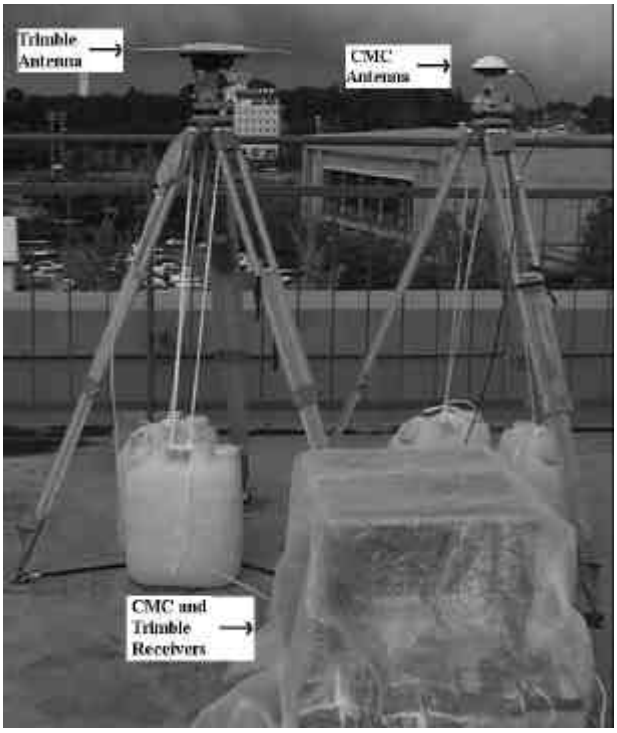

Figure 8.4 Configuration at antenna swapping site.

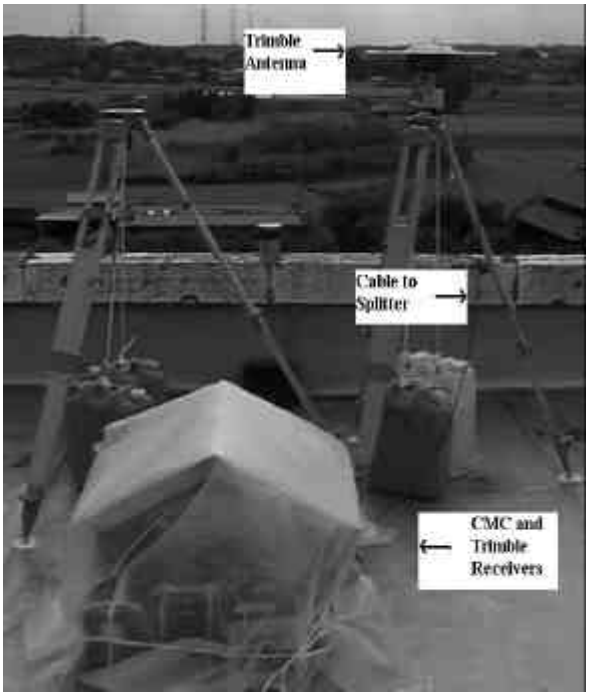

Figure 8.5 Configuration at antenna sharing site.

The “true” coordinate values for the four temporary sites were computed using data from the whole campaign (from DoY 214 to 224 1999). The GEONET station 93012 coordinate was held fixed, and in all the following analysis the true values have been removed from the latitude, longitude, height and length components. The comparisons have been made for both the long-session and the hourly-session tests. ('Long-session' refers to 24 and 8 hour data sets for phases 1 and 2, respectively.) In the hourly-session processing there were 387 and 475 data files, for the dual-frequency and single-frequency receivers respectively. (The single-frequency receivers logged data during the weekend, 7-8 August, hence there are more single-frequency files than dual-frequency ones.)

Table 8-1 shows the mean values and standard deviations of the long-session results for the different stations. Some stations were only occupied once, therefore no standard deviations are shown. Comparing the mean value and standard deviation derived from the analysis of dual-frequency data with those derived from the single-frequency data with corrections (as determined using Eq. (8.5) results), the horizontal components (latitude, longitude and length) are not significantly different. In the case of the height component, the variations of the single-frequency-with-correction results are larger, especially at station GOKA. In general, single-frequency-with-correction processing can achieve accuracies better than 5mm in the horizontal components, and 3cm in height, while dual-frequency processing can achieve better than 2mm in the horizontal components and 6mm in height. The column labelled “Distance” is the approximate distance from station 93012 to the user stations.

Table 8-1 Comparison of single-frequency (with correction) and dual-frequency long-session results (mean & std. devs.).

Stations	Frequency	Obs.	Latitude (mm)	Longitude (mm)	Height (mm)	Length (mm)	Distance (km)
YATA	Dual	1	-3.0	3.0	-1.4	-0.7	12.9
	Single	5	1.6±5.5	-3.2±2.5	-11.0±5.2	-0.5±5.8	
YATT	Dual	4	1.2±0.7	-1.0±1.7	0.9±3.2	0.4±1.5	12.9
	Single	2	1.9±0.2	0.1±4.7	-13.4±4.5	1.6±2.8	
GOKA	Dual	Nil					14.4
	Single	5	-0.8±1.8	0.0±2.7	-24.3±4.7	-0.8±1.6	
GOKT	Dual	4	0.6±2.5	-0.5±1.6	0.4±6.4	0.5±2.4	14.4
	Single	2	3.6±0.2	2.1±2.2	-9.6±1.9	3.6±0.4	
NIIH	Dual	1	-2.3	1.1	-7.0	-1.3	26.1
	Single	2	-3.3±7.9	-2.3±1.6	20.7±4.5	-4.0±7.4	
NIIT	Dual	4	1.5±1.2	-0.5±1.1	2.1±10.1	1.1±1.6	26.1
	Single	1	-1.6	1.3	13.5	-0.4	
HOJO	Dual	Nil					27.2
	Single	4	-5.1±1.8	-6.9±0.8	-1.4±8.3	-7.0±1.8	
HOJT	Dual	4	0.6±0.9	-0.4±0.9	0.0±6.5	0.4±1.0	27.2
	Single	1	-5.4	-4.9	-4.0	-6.7	

Table 8-2 gives the ambiguity resolution success rate and the standard deviations of relative positioning. The QIF (Quasi Ionosphere-Free) method is used to fix the integer ambiguity on the hourly dual-frequency data, while the search method is used to process the single-frequency data (Rizos et al., 1998). The variations of the dual-frequency and single-frequency-with-correction results are similar for all the components. Because the biases (e.g. ionospheric delay, tropospheric delay and orbit error) are effectively reduced, the ambiguity resolution success rates are higher in the case of the single-frequency-with-correction results.

In order to compare the single-frequency and the dual-frequency receiver in terms of relative positioning ability, splitters were used in phase 2 of the experiment so that the two

receivers shared the same Trimble antenna. According to the results in Table 8-3, the height component from the single-frequency-with-corrections processing is 9mm worse than that from the dual-frequency processing, while the latitude, longitude and length results are virtually the same.

Table 8-2 Comparison of single-frequency (with corrections) and dual-frequency hourly-session results (mean & std. devs.).

Frequency	Ambiguity success rate	Latitude (mm)	Longitude (mm)	Height (mm)	Length (mm)
Dual	91% (352/387)	0.6±5.5	0.0±6.4	-3.2±22.9	0.5±5.3
Single	99% (471/475)	0.2±5.9	-2.3±5.9	-9.9±18.0	-0.8±5.8

Table 8-3 The antenna sharing results (mean & std. devs.).

Frequency	Latitude (mm)	Longitude (mm)	Height (mm)	Length (mm)
Dual	1.9±2.2	-0.6±1.7	3.1±4.9	1.7±2.1
Single	2.9±1.1	0.3±3.4	-11.9±4.2	2.3±2.3

8.4 Outward Hard Spatial Densification - Separating Tectonic And Fault Movements From Combinations of Baseline Solutions

While the 'inward spatial densification' scheme can provide enough information for geophysical modelling, there are also other important needs such as to decompose the tectonic movement, the fault movement, and the local monument variations from the results of precise point positioning, baseline solution, and so on. This decomposition is not possible with a single station (in the case of precise point positioning), or with a few stations concentrated in a small region (in the case of baseline solutions), rather additional station(s) have to be located in some geophysically strategic sites to assist the

decomposition. The configuration is termed ‘outward hard spatial densification’ (Ge et al, 2000e).

In precise point positioning, the crustal deformation signal (a combination of the tectonic and the fault movements) is always corrupted by the local monument variations. The power of outward densification using adaptive filtering in recovering the underlying signal from the precise point positioning results is illustrated in Fig. 8.6. The latitude component of coordinate time series during 1 September 1995 and 31 October 1998 for two close stations, BRAN (latitude: 34.18489296, longitude: -118.27704570, and elevation: 246.2551) and LEEP (latitude: 34.13459941, longitude: -118.32174987, and elevation: 485.0621) of the Southern California Integrated GPS Network (SCIGN) has been filtered. From top to bottom the plots are: CGPS series for LEEP; series for BRAN; the coherent component; and the incoherent component (the horizontal zero lines in these plots represent the average of the data used within each plot). In this configuration, BRAN is used as an outward densification to LEEP. This figure shows the decomposition of the observed data into tectonic signal and measurement noise. The filter is able to distinguish the underlying coherent signal even though the two data series are significantly different when zoomed in.

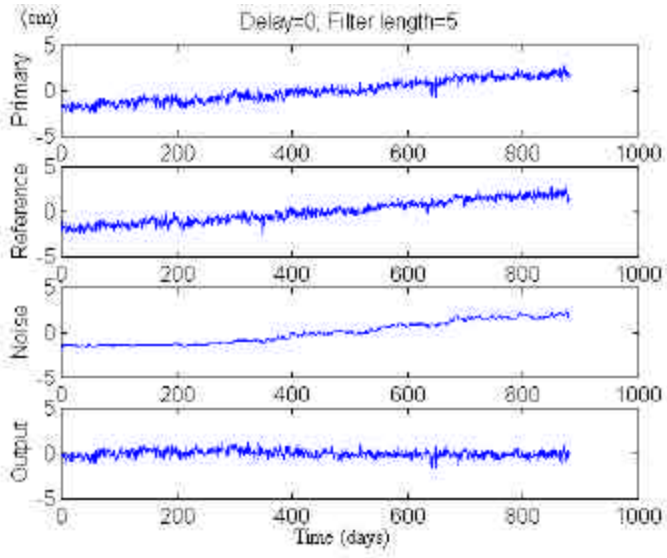

Figure 8.6 Adaptive filtering on CGPS results from two closely located stations: BRAN and LEEP of SCIGN (latitude component, GPS data courtesy of JPL).

Though the baseline solution is the most accurate method of describing the relative motion between two GPS stations, the tectonic movement, the fault movement, the local monument variations, etc., are all included in the baseline result if the two stations are on different plates. To explore the outward densification using baseline solution results, a CGPS array of five stations as shown in Fig. 8.7 is considered. In the array there are four stations distributed on both sides of an active fault. The fifth station (S0) is on a different continental plate (which is 'geophysically strategic') from the other four stations. S0 is the outward densification to the other four stations. Baseline solutions between stations S0 and S1 (S0-S1) will contain the following components: the relative tectonic movement between the two plates; fault movement at S1; local monument movements at both S0 and S1; and other measurement noises. Meanwhile, S0-S3 will contain the following components: the relative tectonic movement between the two plates; fault movement at S3; local monument movements at both S0 and S3; and other measurement noises. If all the CGPS stations S0, S1, and S3 are well designed, the only significant coherent component between the two baseline solutions S0-S1 and S0-S3 will be the relative tectonic movement between the two plates. Therefore, the tectonic movement can be derived with the adaptive filter by using these baseline solutions as inputs. Since both tectonic movement and fault movement will be coherent between baseline solutions S0-S1 and S0-S2, they cannot be used as inputs to the adaptive filter for the purpose of deriving tectonic movement. A similar analysis can identify the combinations of baseline solutions for deriving fault movement. All combinations which may be used to derive tectonic or fault movement are listed in Table 8-4.

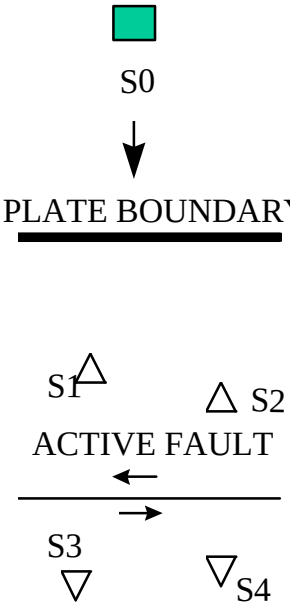

Figure 8.7 CGPS array configuration for signal decomposition.

To test the above analysis, the adaptive filter is used to process baseline solutions from CGPS observations at four stations distributed on both sides of the Longitudinal Valley Fault in Taiwan, and one station in Tsukuba (Japan), which comprise an array as illustrated in Fig. 8.7. Details of these stations are given in Table 8-5. Data collected by the five stations during GPS day 97001 to 98167 (532 days in total) are used in the various baseline solutions listed in Table 8-4.

Table 8-4 Baseline combinations for signal decomposition.

Signal to derive	Tectonic	Fault
Combination 1	S0-S1	S1-S4
	S0-S3	S2-S3
Combination 2	S0-S1	S1-S3
	S0-S4	S2-S4
Combination 3	S0-S2	
	S0-S3	
Combination 4	S0-S2	
	S0-S4	

Table 8-5 Continuous GPS stations used in the experiment.

Station	Code	Name & Location
S0	TSKB	Tsukuba, Japan
S1	S058	Changping, Taiwan
S2	S104	Fushan, Taiwan
S3	S105	Mingyeh, Taiwan
S4	S23R	Pingtung, Taiwan

Adaptive filtering results for the baseline length from different combinations of baseline solutions are given in Fig. 8.8 to Fig. 8.13. In Fig. 8.8 from top to bottom the plots are: the primary input of baseline solutions (S105-TSKB); the reference input of baseline solutions (S058-TSKB); the derived tectonic movement (labelled “noise”); and the baseline solution series with tectonic movement being removed (the horizontal zero lines in these plots represent the average of the data used within each plot). The other figures are arranged in a similar layout. These results have different lengths due to data gaps in different combinations.

Fig. 8.8 to Fig. 8.11 present the results of four combinations for deriving tectonic movement. The derived tectonic movements are in good agreement among the four combinations, indicating that the two plates are moving towards each other at a rate of 10mm/year along the baseline direction. This result is in good agreement with a previous study (Yu et al., 1997). But the tectonic movement derived in Combination 3 is much noisier compared to the other results, which can be well explained by the fact that stations S104 and S105 are very close to each other. In fact, they are so close (16km) that the coherent noises between their observations have become significant compared to the tectonic movement signature.

Fig. 8.12 and Fig. 8.13 illustrate the results of two combinations for deriving fault movement which are in agreement with each other. Combining the two results, the movement along the fault is about 13mm/year, which is in agreement with the previous study (Ibid, 1997).

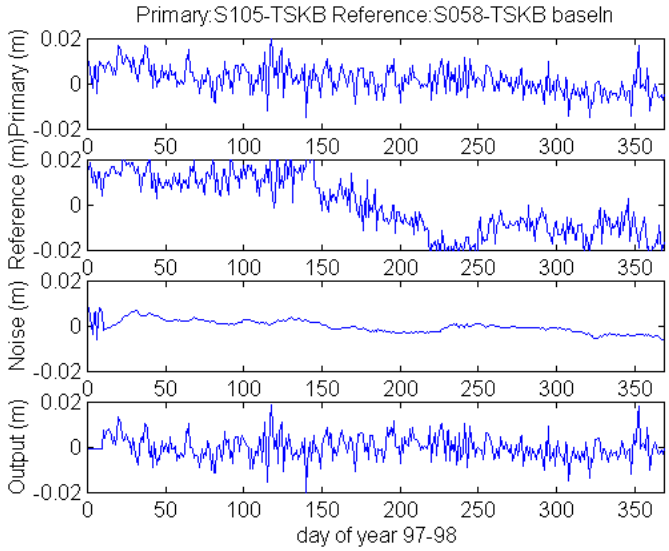

Figure 8.8 Adaptive filtering result of Combination 1 for deriving tectonic movement.

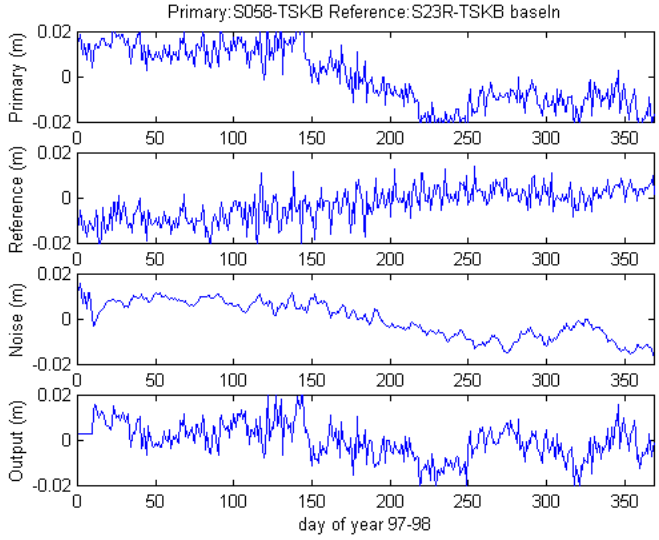

Figure 8.9 Adaptive filtering result of Combination 2 for deriving tectonic movement.

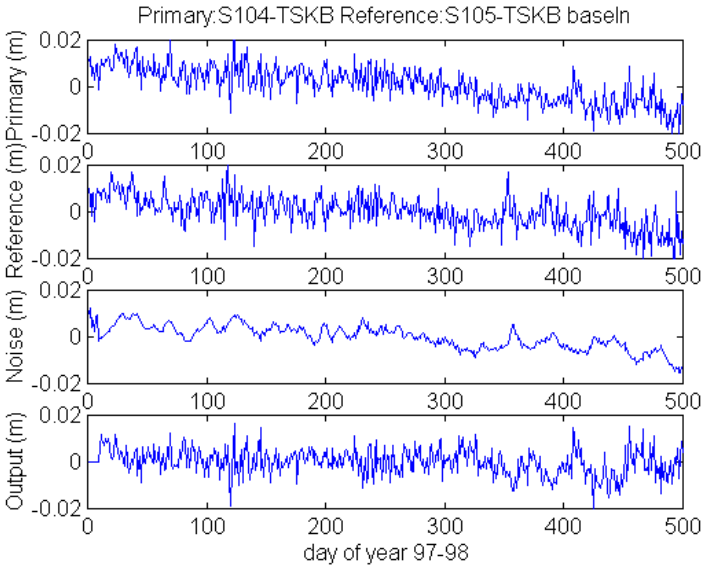

Figure 8.10 Adaptive filtering result of Combination 3 for deriving tectonic movement.

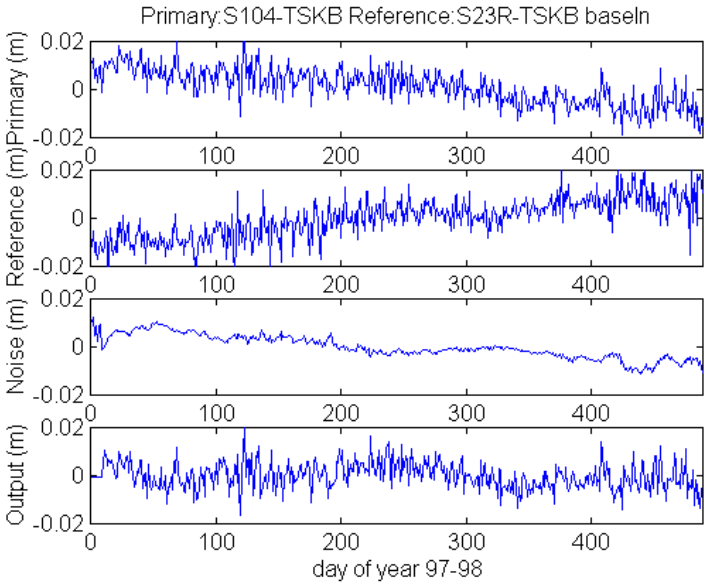

Figure 8.11 Adaptive filtering result of Combination 4 for deriving tectonic movement.

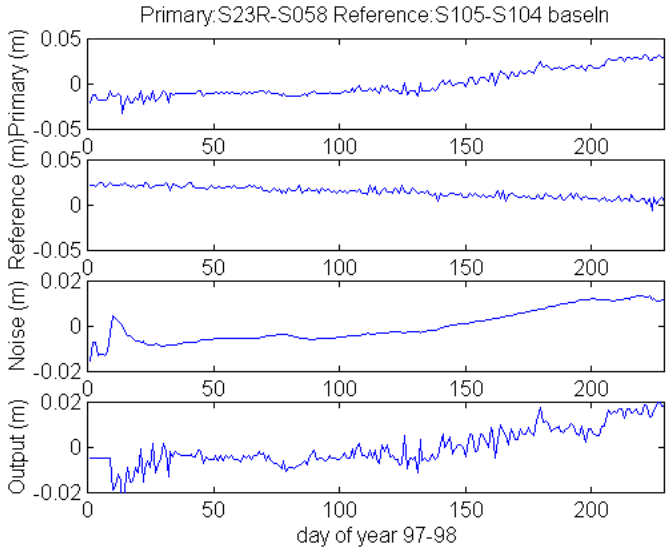

Figure 8.12 Adaptive filtering result of Combination 1 for deriving fault movement.

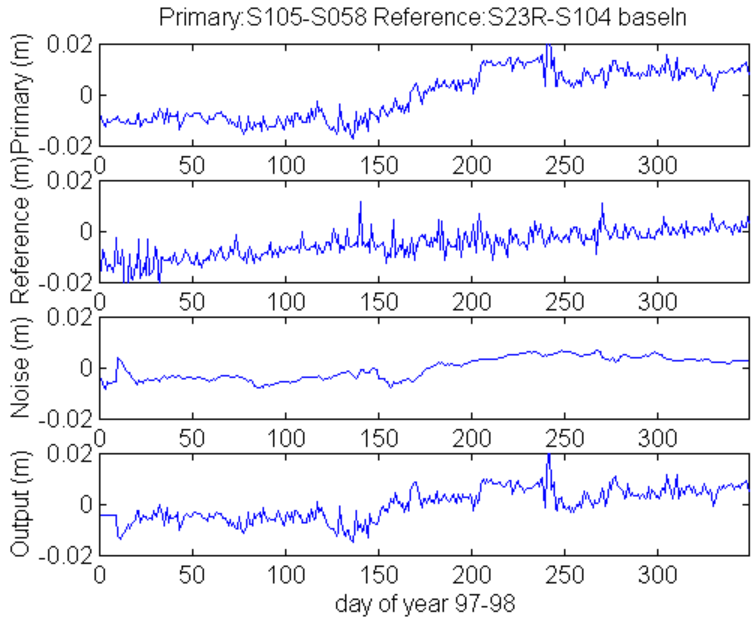

Figure 8.13 Adaptive filtering result of Combination 2 for deriving fault movement.

From the above analyses, it can be concluded that by carefully selecting point positioning or baseline solutions as primary and reference inputs to the adaptive filter, tectonic and fault movements can be resolved, which are in good agreement with previous studies

involving the analysis of many more CGPS stations.

8.5 Concluding Remarks

The following comments concerning the inward and outward hard spatial densification schemes can be made:

1. The long-session (24 & 8hr sessions) results indicate that single-frequency-with-correction processing can achieve accuracies of better than 5mm in the horizontal components and 3cm in height, while the dual-frequency results can achieve accuracies better than 2mm in the horizontal components and 6mm in height.

2. It has been shown in the antenna sharing experiment that the single-frequency and dual-frequency results have similar quality (especially for the horizontal components).

3. Hourly-session results indicate that the ambiguity resolution success rate of dual-frequency processing is less than that of single-frequency-with-correction processing. When ambiguities are resolved, there are no significant differences between the results.

4. Tectonic and fault movements have been derived using the adaptive filter from point positioning and baseline solutions of CGPS array. The results are in good agreement with each other, using different baseline combinations, and with results from previous published studies.

9 SUMMARY, CONCLUSIONS AND RECOMMENDATIONS

9.1 Summary and Conclusions

While augmentations of various types are used for the GPS navigation applications, this research for the first time deals with augmentations for crustal deformation monitoring. Several techniques that take advantage of continuous GPS receiver networks have been identified, the necessary algorithms and procedures developed, and subsequently tested.

For many geodynamic applications the arrays of continuously-operating GPS (CGPS) receivers are not capable, on their own, of determining the characteristics of crustal motion at the fine temporal or spatial scales required. For example, the monitoring of pre-seismic or post-seismic faulting requires sub-kilometre spatial resolution (from a study of the faulting lengths of some past earthquakes), while the measurement of co-seismic displacement require 0.1sec (10Hz) temporal resolution. **Although several 'modernizations' to the Global Navigation Satellite Systems (GNSS) have been proposed in recent years, they are almost all only of benefit to navigation applications. As a result, crustal deformation monitoring can only benefit from augmentations specific to CGPS and similar geodetic procedures and techniques.**

In this research, four temporal densification schemes based on: (a) high rate GPS-RTK, (b) GPS multipath effects, and (c) the use of VLBI and SLR to augment CGPS networks for crustal deformation monitoring, have been developed and tested. In addition, two spatial densification schemes have also been developed and tested.

9.1.1 Serial temporal densification – GPS seismometer

The 'serial temporal densification scheme' is an attempt to push the temporal resolution to 0.1 second, as shown in Fig. 1.7, so that GPS can be used as a seismometer. This scheme is based on using the standard GPS Real-Time Kinematic (RTK) technique.

In order to test such serial densification, an experiment using two Leica CRS1000 GPS receivers operating in the fast GPS-RTK mode was conducted in order to study the feasibility of using GPS as a broadband and highly dynamic seismometer. The sampling rates of both receivers were 10Hz. The 'mobile' antenna was mounted on a mechanical shaker, which generated vibrations to simulate displacements due to seismic waves.

Fast Fourier Transform analysis of the fast GPS-RTK results indicate that vibrations of 2.3Hz and 4.3Hz, with an amplitude of 12.7mmm, applied to the mobile antenna to simulate displacement due to seismic waves, can be recognized in both the time and frequency domain. This displacement signature was not only identified in the latitude and longitude components, but also in the height component.

An adaptive filter based on the Least-Mean-Square (LMS) algorithm has been used to process the very noisy GPS-RTK data. Three novel approaches, namely the ‘GPS-only’ approach, the ‘GPS and accelerometer’ approach, and the ‘multi-template’ approach, have been developed and used to process the data from the GPS seismometer experiment. The former two have improved the signal-to-noise ratio of the GPS seismometer significantly, while the latter has been proved to be very effective in cancelling the multipath effects using data collected on a previous day.

A second experiment involved two Trimble MS750 GPS receivers, operating in the 20Hz Real-Time Kinematic mode, in an attempt to detect seismic signals generated by an earthquake simulating truck. The GPS-RTK result is in very good agreement with the

results of the accelerometer and velocimeter, indicating again that a fast sampling rate (up to 20Hz) GPS system can be used as a 'GPS seismometer' for measuring displacements directly.

Investigations were carried out concerning several *implementing* issues associated with making a 'GPS seismometer' system operational. These issues include: the layout of receiver stations, noise reduction using measurements from adjacent days, temporal correlation between measurements from successive epochs, and data communications. Discussions on the pros and cons of using GPS as a seismometer reveal that an operational system based on a high sampling rate GPS-RTK system and a LMS adaptive filter is feasible. Such a strong motion amplitude seismometer would complement current seismometers. **Hence there are no major technical obstacles in upgrading current continuous GPS arrays to implement this ‘serial temporal densification scheme'.**

The propose technique can also be used for other applications such as the monitoring of tsunamis and the deformation of large engineering structures.

9.1.2 Retro-active temporal densification – multipath mitigation

The ‘retro-active temporal densification scheme' has been proposed in order to take advantage of the fact that the GPS multipath disturbance has a periodic characteristic and is repeated between consecutive days. This densification scheme is aimed to improve precision of the CGPS results rather than pushing the temporal limits of Fig. 1.7.

Multipath models for both pseudo-range and carrier phase can be reliably derived using an adaptive filter based on the LMS algorithm, independent of the combinations of time series pairs used, as long as the antenna environment remains unchanged. However, it is found that the older the multipath reference signal, the less accurate the multipath correction. Forward filtering is better than backward filtering, and hence **the best multipath mitigation strategy is forward filtering using data on two consecutive days.** Such a

strategy reduces the standard deviations of the pseudo-range multipath time series to about one fourth the original values, and in the case of carrier phase to about a half, based on the experimental GPS data considered here.

This densification scheme provides a possible mechanism to correct multipath errors from the observation data themselves. Hence there will be no need to change the operational mode of CGPS arrays. The scheme, when implemented, can be a useful enhancement for deformation monitoring in volcanoes and opencut mines. Using the data from the immediate past**, the algorithms developed are flexible enough to enable the correction of multipath errors for CGPS stations that vary seasonally as well.**

9.1.3 All-GPS parallel temporal densification – the use of multipath effects as a signal

The 'all-GPS parallel temporal densification scheme' is proposed for the detection of multipath change as a signal at permanent GPS stations. This scheme is aimed to take advantage of the GPS noise rather than pushing the temporal limits of Fig. 1.7. The technique has been tested on experimental data, indicating that **the multipath change above the receiver noise level can be detected.** A further test was carried out with some CGPS data from the Japanese GEONET when there was a snowfall. The results indicate that if there is a change in the antenna environment the proposed technique will indeed detect it in both the pseudo-range and carrier phase data.

For pseudo-range multipath change detection, data from a single dual-frequency receiver is sufficient. In the case of carrier phase multipath change detection, data from two closely-spaced receivers have to be used. This may become a limitation in a sparse CGPS array. However, in an array such as the GEONET it is always possible to identify some reference stations free of multipath, and to **generate** the data for a Virtual Reference Station located close to the CGPS station targeted for multipath change detection. For reliable multipath change detection, the temporal resolution of this method is 24 hours.

As an application of the technique, the mathematical models for slope stability monitoring using the change of GPS multipath effects have been derived. **It is found that an "equivalent ideal slope" with planar surface can always be found for the real slopes which can reflect the GPS satellite signals to the antenna from multiple points. Moreover, ambiguity resolution has been avoided by using the change of multipath rather than the multipath itself in the monitoring of slope movement.** The change of multipath is used in a least square process to estimate the slope movement parameters by employing the mathematical models developed.

This 'all-GPS parallel temporal densification scheme' provides an easy-to-implement quality assurrance tool for CGPS antenna environment sensing after effects such as typhoons, cyclones, and earthquakes. Other possible applications include the monitoring of slope stability and ground subsidence.

9.1.4 Cross-technique parallel temporal densification – the integration of GPS with VLBI and SLR

Space geodetic techniques such as the GPS, VLBI, and SLR have been collocated at many sites to address applications in the geosciences. A common-mode signal has been found among the collocated results (coordinate time series) of GPS, VLBI and SLR, although results from all these techniques are contaminated by different biases and errors. An adaptive filter based on the LMS algorithm has been proposed in this 'cross-technique parallel temporal densification scheme' to extract this common-mode signal by inputting to the filter the GPS result as the primary sequence, and VLBI and/or SLR results as the reference sequences. Data from the Matera Station in Italy and the Wettzell Station in Germany have been used to test the algorithm. The derived common-mode signal has been shown to have better repeatability than the individual time series results of GPS, VLBI and SLR.

9.1.5 Soft spatial densification – the integration of GPS with radar interferometry (INSAR)

Inter-comparisons between CGPS and InSAR indicate that the two techniques are very complementary. Therefore, the Double Interpolation and Double Prediction (DIDP) technique for integrating InSAR and GPS results in the so-called 'soft spatial densification scheme' has been proposed. In the DIDP approach, the first step is to derive the atmospheric corrections to InSAR from the CGPS measurements. The second step is to remove or mitigate the SAR satellite orbit errors by using GPS results as constraints, thus yielding GPS-corrected InSAR results. In the third step, the CGPS observations separated by one or several SAR repeat cycles are densified in a grid by interpolation in the spatial domain, based on the GPS-corrected InSAR results. Then the densified grid observations are interpolated in the time domain, based on a dynamic model derived from the CGPS time series. CGPS data from the Southern California Integrated GPS Network (SCIGN) have been used to demonstrate that adaptive filtering can be successfully used to extract a dynamic model from the GPS time series of stations **in the same classified group**. A deformation distribution model for interpolation in the spatial domain was derived based on both InSAR and GPS results for the 1992 Landers Earthquake. In the fourth step, based on the double interpolation result of the third step, forward filtering (by a Kalman filter) is used to predict the crustal deformation at all points on the grid, which is in fact a double prediction in both the time and spatial domains. A three-step reliability test procedure for the DIDP technique has also been developed.

Since a single SAR image usually covers an area of only 50km by 50km, the reliability of spatial interpolation is guaranteed. Because GPS receivers are operating continuously, and can achieve high accuracy, the DIDP approach is a promising strategy for 'soft spatial densification' that significantly improves the spatial, temporal and magnitude resolution of ground deformation monitoring to 25m, 30 second and mm level respectively, as shown in Fig. 1.7.

9.1.6 Hard spatial densification

A so-called 'hard spatial densification scheme' has been developed and tested. Two configurations have been identified: (a) deployment of a sub-network of single-frequency GPS receivers to in-fill current CGPS arrays (‘**inward hard spatial densification’**), or (b) deployment of receivers at some geophysically strategic sites outside the existing CGPS array (referred to as ‘**outward hard spatial densification’**).

The 'inward hard spatial densification scheme', in which single-frequency data are corrected using dual-frequency data, has been demonstrated in an experiment undertaken in Japan, using some stations of the GEONET. It has been shown to be a very cost effective and accurate strategy for improving the CGPS spatial resolution, and can provide some redundancy in hazardous environments like a volcano. It has been demonstrated that the single-frequency-with-correction results have a similar quality to standard dual-frequency receiver results (especially for the horizontal components).

In the 'outward hard spatial densification scheme' GPS receivers can be used more efficiently to allow the generation of different combinations of baselines, which have been used, for example, to separate plate tectonic and seismic fault movements. Tectonic and fault movements have been derived using the adaptive filter from point positioning and baseline solutions of two stations in SCIGN, and a 5 station CGPS array consisting of four stations in Taiwan and one station in Tsukuba, respectively. The results are in good agreement with each other, and with the results of published studies.

These augmentations can be used either independently, or collectively, depending on the resources available in a CGPS array and at a specific site. For example, the 'retro-densification' and the 'all-GPS densification' schemes can be used at the same time; the 'retro-densification' result can be used as an input to the GPS-VLBI-SLR 'cross-technique densification' scheme; the 'cross-technique densification' results can be used instead of the GPS-only result in the 'soft densification' with InSAR results; the 'soft densification' and 'hard densification' schemes can verify each other; and so on.

9.2 Recommendations for Future Research

In the case of the 'serial temporal densification scheme', a GPS seismometer experiment based on a network-based RTK system (the so-called 'Virtual Reference Station' concept) simulating practical (operational) environments can be carried out in, for example, Japan using the GEONET receiver infrastructure. By taking advantage of the 25km spatial resolution of the GEONET, the achievable accuracies can be easily investigated when the 'mobile' station is 25km, 50km, 75km and 100km away from the reference stations. The influence of movements in the reference stations (as will be experienced during an earthquake) on the RTK result of the 'mobile' receiver can also be studied. These additional studies will benefit other RTK applications such as the monitoring of tsunamis, and the deformation of large engineering structures.

In a further study of the 'retro-active temporal densification scheme', GPS solutions with and without the multipath corrections can be compared to assess improvements in precision and accuracy. The identification of multipath reflectors at CGPS sites can be compared with site descriptions and changes in environmental factors. Also, where possible, multipath-corrected solutions can be compared with independent techniques such VLBI and SLR to test the effectiveness of this 'retro-active temporal densification scheme'.

In the case of the 'all-GPS parallel temporal densification scheme', the proposed methodology can be further tested using CGPS data collected in antenna environments where multipath may be changed by, for example, volcanic ash accumulation, tree growth, snowfall, and so forth. CGPS data collected in a project for slope stability monitoring can be used to test the derived models that relate the change in multipath to the change of antenna environment, by comparing with results obtained from other techniques.

The 'cross-technique parallel temporal densification scheme' can be applied to process CGPS, VLBI and SLR measurements available from various geodynamic campaigns. A further study would establish whether the movement determined by the derived common-mode signal is more realistic than the individual space geodesy results.

The so-called 'soft spatial densification scheme' can be further tested by processing CGPS and InSAR data for a test region where GPS receivers and radar corner reflectors are collocated to facilitate CGPS/InSAR integration. As a matter of fact, such a project has already been proposed by researchers at The University of New South Wales (UNSW). An underground mine near Sydney has been chosen as a candidate site to study the feasibility of using GPS/InSAR for land subsidence monitoring at fine scales. The DIDP technique developed in this research can either be implemented within the InSAR software now available at UNSW, or developed into a stand-alone software package.

The 'hard spatial densification scheme' can be employed in future joint projects for fault motion and volcano monitoring between UNSW and institutions from Japan or Taiwan.

REFERENCES

Axelrad, P., C.J. Comp and P.F. MacDoran, 1994. Use of signal-to-noise ratio for multipath error correction in GPS differential phase measurements: methodology and experimental results. *7th Int. Tech. Meeting of The Satellite Division of The U.S. Institute of Navigation,* Salt Lake City, Utah, 20-23 September, 655-666.

Båth, M., 1973. *Introduction to seismology*. New York, Wiley, 395pp.

Beutler, G, I Mueller, and R Neilan, 1994. The International GPS Service for Geodynamics (IGS): Development and start of official service on January 1, 1994, *Bulletin Geodesique*, 68(1), 39-70.

Bevis, B.G., S. Bussinger, T.A. Herring, C. Rocken, R.A. Anthes, and R.H. Ware, 1992. GPS Meteorology: Remote Sensing of Atmospheric Water Vapor Using the Global Positioning System, *J. Geophys. Res.*, 97, 15787-15801.

Bishop, G., et al., 1994. Studies and performance of a new technique for mitigation of pseudo-range multipath effects in GPS ground stations. *U.S. Institute of Navigation National Technical Meeting*, San Diego, California, January, 231-242.

Bock, Y., et al., 1993. Detection of crustal deformation from the Landers earthquake sequence using continuous geodetic measurements, *Nature*, 361, 337-340.

Bock, Y., and S. Williams, 1997. Integrated satellite interferometry in Southern California. *EOS Trans., AGU*, Vol.78, No.29, 293.

Branson, E. B. and W.A. Tarr, 1952. *Introduction to geology*. McGraw-Hill, New York, 3rd ed, 306pp.

Briole, P., D. Massonnet, and C. Delacourt, 1997, Posteruptive deformation associated with the 1986-87 and 1989 lava flows of Etna detected by radar interferometry, *Geophysical Research Letters*, vol. 24, pp. 37-40.

Bücherl, A., H. Landau, C. Pagels, U. Vollath, and B. Wagner, 2000. Long Range RTK Positioning Using Virtual Reference Stations. *The Satellite Division of the Institute of Navigation 13th International Technical Meeting (ION GPS 2000),* September 19 – 22, Salt Lake City, Utah, USA.

Caltech, 2000. http://www.gps.caltech.edu/terrascope/TerraInfo.html

Chen, H.Y., RIZOS, C., & HAN, S., 1999. Rapid static medium-range GPS positioning techniques for geodynamic applications**.** *4th International Symp. on Satellite Navigation Technology & Applications*, Brisbane, Australia, 20-23 July, paper 49, 12pp.

Clarke, P.J., D. Paradissis, P. Briole, P. C. England, B. E. Parsons, H. Billiris, G. Veis, and J. C. Ruegg, 1997, Geodetic investigation of the 13 May 1995 Kozani-Grevena (Greece) Earthquake, *Geophysical Research Letters*, vol. 24, pp. 707-710.

Cohen, C. and B. Parkinson, 1991. Mitigating multipath error in GPS based attitude determination. *Guidance and Control*, 74, Advances in the Astronautical Sciences.

Colombo, O., 1999. Sub-decimeter precision in kinematic positioning over very large areas. *International Symposium on GPS - Application to Earth Sciences and Interaction with Other Space Geodetic Techniques*, Tsukuba, Japan, 18-22 October.

COM, 1999. Galileo – Involving Europe in a New Generation of Satellite Navigation Services, European Com-mission, 54 Final, 10 Feb. 1999-06-29.

DeMets, C., R.G. Gordon, D.F. Argus & S. Stein, 1990. Current plate motions, *Geophys. J. Int.*, 101, 425-478.

Ding, X., Y. Chen, J. Zhu and D. Huang, 1999. Surface deformation detection using GPS multipath signals. *12th Int. Tech. Meeting of The Satellite Division of The U.S. Institute of Navigation*, 14-17 September, Nashville, Tennessee.

Dong, D., et al.1997, Obtaining deformation field from a combination of GPS and terrestrial survey data. *The 1997 Seismological Society of Japan Fall meeting*, 24 to 26 September Hirosaki, Japan.

ERI, 2000. http://www.eri.u-tokyo.ac.jp/topics/MIYAKE_E/GPS2/

Fenton, P.C., W.H. Falkenberg, T.J. Ford, K.K. Ng and A.J. van Dierendonck, 1991. NovAtel's GPS receiver: the high performance OEM sensor of the future. *4th Int. Tech. Meeting of the Satellite Division of The U.S. Institute of Navigation*, Albuquerque, New Mexico, 11-13 September, 49-58.

Fielding, E.J., S. Fujiwara, S. Hensley, P. A. Rosen, M. Tobita, and M. Shimada, 1996, Surface deformation due to the May 27, 1995 Sakhalin earthquake and related events

measured by JERS-1 SAR interferometry, *EOS Trans AGU*, Supplement, vol. 77, no. 46, p. F36.

Freeman, A., D. L. Evans, and J. J. van Zyl, 1996, SAR applications in the 21st century, *International Journal of Electronics and Communications*, vol. 50, pp. 79-84.

Freymueller, J. T., N. E. King and P. Segall, 1994. The co-seismic slip distribution of the Landers earthquake, *Bull. Seis. Soc. America*, 84 (3), 646-659.

Fruneau, B., J. Achache, and C. Delacourt, 1996, Observation and modeling of the Saint-Etienne-de-Tinee landslide using SAR interferometry, *Tectonophysics*, vol. 265, pp. 181-190.

Fujiwara, S., M. Tobita and M. Murakami, 1997. Detecting Crustal Deformation and Generating Digital Elevation Model Using Interferometric Synthetic Aperture Radar, Jour. Japan Soc. Photogram. Remote Sensing, vol. 36, no. 3, (in Japanese).

Fujiwara, S., P. A. Rosen, M. Tobita, and M. Murakami, 1998a, Crustal deformation measurements using repeat-pass JERS 1 synthetic aperture radar interferometry near the Izu Peninsula, Japan, J. Geophys. Res., 103 , 2411-15.

Fujiwara, S., H. Yarai, S. Ozawa, M. Tobita, M. Murakami, H. Nakagawa, K. Nitta, P. A. Rosen, and C. L. Werner, 1998b. Surface displacement of the March 26, 1997 Kagoshima-ken-hokuseibu earthquake in Japan from synthetic aperture radar interferometry, submitted to *Geopys. Res. Letter*.

Fujiwara, S., M. Tobita, and M. Murakami, 1998c. Importance of water vapor information in SAR interferometry, submitted to *'Kisho kenkyu note'* (in Japanese).

Gabriel, A.G., R.M. Goldstein, and H.A. Zebker, 1989. Mapping small elevation changes over large areas: Differential radar interferometry. *J. Geophys. Res.* 94, No. B7, 9183-91.

Gaddis, L., P. Mouginis-Mark, R. Singer and V. Kaupp, 1989, Geologic analysis of Shuttle Imaging Radar (SIR-B) data of Kilauea Volcano, Hawaii, *Geol. Soc. America Bulletin*, vol. 101, pp. 317-332.

Ge, L., Y. Ishikawa, S. Fujiwara, S. Miyazaki, X. Qiao, X. Li, X. Yuan, W. Chen, & J. Wang, 1997a. The integration of InSAR and CGPS: a solution to efficient deformation monitoring. *International Symposium on Current Crustal Movement and Hazard Reduction in East Asia and South-east Asia*, November 4 -7, Wuhan, P R. China.

Ge, L., Y. Ishikawa, X. Qiao, X. Li, X. Yuan, W. Chen, & J. Wang, 1997b. InSAR Application in China. *The Second International Workshop on SAR Interferometry*, 18-20 November, Tsukuba, Japan, 195-200.

Ge, L., Han, S., & Rizos, C., 1998a. The integration of Continuous GPS and SAR Interferometry. *Pres. at Annual Research Seminars*, School of Geomatic Engineering, The University of New South Wales, 16-17 November. Also in *Geomatics Research Australia*, 69, 73-74 (abstract).

Ge, L., Han, S., & Rizos, C., 1998b. Continuous GPS: challenges, results and applications. Pres. at Annual Research Seminars, School of Geomatic Engineering, The University of New South Wales, 16-17 November. Also in *Geomatics Research Australia*, 69, 81-82 (abstract).

GE, L. H.-Y. Chen, L. Dai, S. Han, C. Rizos, Y. Ishikawa, and Y. Hatanaka, 1999a. Comprehensive Densification of Continuous GPS Measurements. *Pres. at Annual Research Seminars*, School of Geomatic Engineering, The University of New South Wales, 16-17 November. Also in *Geomatics Research Australia*, 71, 117-118 (abstract).

Ge, L., S. Han, and C. Rizos, 1999b. Interpolation of GPS Results Incorporating Geophysical and InSAR Information. *The International Symposium on GPS - Application to Earth Sciences and Interaction with Other Space Geodetic Techniques*, October 18 - 22, Tsukuba, Japan. Also in *Earth, Planets and Space*, Vol. 52, 999-1002.

Ge, L., S. Han, C. Rizos, Y. Ishikawa, M. Hoshiba, Y. Yoshida, M. Izawa, N. Hashimoto, and S. Himori, 1999c. GPS Seismometers with up to 20Hz Sampling Rate. *The International Symposium on GPS - Application to Earth Sciences and Interaction with Other Space Geodetic Techniques*, October 18 - 22, Tsukuba, Japan. Also in *Earth, Planets and Space*, Vol. 52, 881-884.

Ge, L., S. Han, and C. Rizos, 1999d. GPS-RTK applications for assisting the engineering design of large structures. *The Metrology Society of Australia 1999 Conference*, 22-24 September, Sydney, Australia, 287-291.

Ge, L., S. Han, and C. Rizos, 1999e. Fast RTK Applications of the Leica CRS1000 GPS Receiver. *The 4th International Symposium on Satellite Navigation Technology & Applications*, 20-23 July, Brisbane, Australia.

Ge, L., 1999. GPS Seismometer and its Signal Extraction. *The Satellite Division of the Institute of Navigation 12th International Technical Meeting (ION GPS '99),* September 14-17, Nashville, Tennessee, US, 41-51.

Ge, L., C. Rizos, S. Han, Y. Ishikawa, and Y. Hatanaka, 2000a. CGPS, what more can we do? *Pres. at Annual Research Seminars,* School of Geomatic Engineering, The University of New South Wales, 20-21 November. Also in *Geomatics Research Australia*, 73, 117-118 (abstract).

Ge, L., Chen, H.Y., Han, S., Rizos, C., Vespe, F., & Schlueter, W., 2000b. The integration of collocated GPS, VLBI and SLR results. *13th Int. Tech. Meeting of the Satellite Division of the U.S. Inst. of Navigation*, Salt Lake City, Utah, 19-22 September, 1525-1535.

Ge, L., Dai, L., Han, S., Rizos, C., Ishikawa, Y. & Yoshida, Y., 2000c. GPS seismometers: The implementing issues. *13th Int. Tech. Meeting of the Satellite Division of the U.S. Inst. of Navigation*, Salt Lake City, Utah, 19-22 September, 75-83.

Ge, L., Han, S., & Rizos, C., 2000d. Multipath mitigation of continuous GPS measurements using an adaptive filter. *GPS Solutions*, 4(2), 19-30.

Ge, L., Chen, H.Y., Han, S., & Rizos, C., 2000e. Adaptive filtering of continuous GPS results. *Journal of Geodesy*, 74, 7/8, 572-580.

Ge, L., Han, S., & Rizos, C., 2000f. The Double Interpolation and Double Prediction (DIDP) Approach for InSAR and GPS Integration. *The 19th International Society of Photogrammetry and Remote Sensing (ISPRS) Congress and Exhibition*, 16 - 23 July, Amsterdam, Holland, 205-212.

Ge, L., Han, S., & Rizos, C., 2000g. Multipath stability derived from continuous GPS data using an adaptive filter. *Western Pacific Geophysics Meeting*, Tokyo, Japan, 26-30 June (abstract).

Ge, L., Han, S., & Rizos, C., 2000h. The Double Interpolation and Double Prediction (DIDP) approach for InSAR and GPS integration. *Western Pacific Geophysics Meeting*, Tokyo, Japan, 26-30 June (abstract).

Giordano, A. and F. Hsu, 1985. *Least Square Estimation with Applications to Digital Signal Processing.* New York, Wiley, 412pp.

GLONASS, 1995. Interface Control Document, International Civil Aviation Organization, (ICAO), *GNSSP/2-WP/66*, Montreal, Canada, 14 November 1995.

Goldstein, R. M., H. Engelhardt, B. Kamb, an R. M. Frolich, 1993, Satellite radar interferometry for monitoring ice-sheet motion: Application to an Antarctic ice stream. *Science*, vol. 262, p. 1525.

Graham, L.C., 1974. Synthetic interferometer radar for topographic mapping. *Proc. IEEE*, 62, 763-768.

GSI, 2000. http://vldb.gsi-mc.go.jp/cgi/gps_table.pl?93059

Gubbins, D., 1990. *Seismology and plate tectonics*. New York, Cambridge University Press, 339pp.

Guo, H., J. Liao, C. Wang, C. Wang, T. Farr, and D. Evans, 1997, Dual- frequency and multi-polarization Shuttle Imaging Radar for volcano detection in Kunlun Mountains of Western China. *Remote Sensing of Environment*, vol. 59, no. 2, pp. 364-374.

Haji, G.A., 1990. The multipath simulator: a tool toward controlling multipath. *2nd Symp. on GPS Applications in Space*, Hanscom AFB, February.

HAN, S. & RIZOS, C., 1996. GPS network design and error mitigation for real-time continuous array monitoring systems. *9th Int. Tech. Meeting of the Satellite Division of the U.S. Inst. of Navigation GPS ION '96*, Kansas City, Missouri, 17-20 September, 1827-1836.

Han, S. and C. Rizos, 1997. Multipath effects on GPS in mine environments. *Xth Int. Congress of the Int. Society for Mine Surveying*, Fremantle, Australia, 2-6 November, 447-457.

HAN, S., 1997. Carrier phase-based long-range GPS kinematic positioning. *PhD Dissertation*, UNISURV S-49, School of Geomatic Engineering, The University of New South Wales, Sydney, Australia, 185pp.

Hatanaka, Y. and J. Fujisaku, 1999. Error in baseline solutions of GEONET due to snow accumulation. *92nd Meeting of the Geodetic Society of Japan*, November 9 – 11, Neo, Gifu, Japan.

Hatanaka, Y., et al., 1994. Coseismic crustal displacements from the 1994 Hokkaido-Toho-Oki earthquake revealed by a nationwide continuous GPS array in Japan - results of GPS kinematic analysis. *Japanese Symposium on GPS (1994)*, 15-16 Dec., Tokyo, Japan, 141-147. (in Japanese)

Haykin, S., 1996. *Adaptive Filter Theory*. Prentice Hall, New Jersey, 3rd ed., 989pp.

Heki, K.; Tamura, Y. 1997. Short-term afterslip in the 1994 Sanriku-Haruka-Oki earthquake. *Geophys. Res. Lett.*, 24(24), 3285-3288.

Herring, T.A., 1999. Common mode signals in combinations of VLBI, GPS and SLR data. Pres. *International Symposium on GPS - Application to Earth Sciences and Interaction with Other Space Geodetic Techniques (Tsukuba GPS 99)*, Tsukuba, Japan, 18-22 October.

Hirahara, K., et al., 1994. An experiment for GPS strain seismometer. *Japanese Symposium on GPS (1994)*, Tokyo, Japan, 15-16 December, 67-75.

IGSCB, 2000. http://igscb.jpl.nasa.gov/pub/products/WWWW/ultra

JPL, 1999. http://www.jpl.nasa.gov/missions/ future/.

Leick, A. 1995. *GPS Satellite Surveying*, New York, Wiley, 560pp.

Lin, L.S. and C. Rizos, 1997. Use of multipath template technique for mitigating GPS pseudo-range multipath: methodology and test results. *First Trans Tasman Surveyors Conf.*, Newcastle, Australia, 12-18 April, Paper no. 22, 1-9.

Lu, Z., R. Fatland, M. Wyss, S. Li, J. Eichelberer, Dean, and J. Freymueller, 1997, Deformation of New Trident volcano measured by ERS-1 SAR interferometry, Katmai National Park, Alaska, *Geophysical Research Letters*, vol. 24, no. 6, pp. 695-698.

Ma, C. & J.W. Ryan, 1998. "NASA Space Geodesy Program -- GSFC DATA Analysis -- 1998, VLBI Geodetic Results 1979-1998".

Massonnet et al.,1996, Detection postseismic fault-zone collapse following the Landers earthquake, *Nature* 382, 612-616.

Massonnet, D., K. Feigl, M. Rossi, and F. Adragna, 1994, Radar interferometric mapping of deformation in the year after the Landers earthquake, *Nature*, vol. 369, p. 227.

Massonnet, D., M. Rossi, C. Carmona, F. Adragna, G. Peltzer, K. Feigl, and T. Rabaute, 1993a, The displacement field of the Landers earthquake mapped by radar interferometry, *Nature*, Vol. 364, no. 6433, 8, pp. 138 - 142.

Massonnet, D. and T. Rabaute, 1993b, Radar Interferometry: Limits and Potential, *IEEE Trans. Geosci. Remote Sensing.*, Vol. 31, No. 2, pp. 455 - 464.

Massonnet, D., P. Briole, and A. Arnaue, 1995. Deflation of Mount Etna Monitored by Spaceborne Radar Interferometry, *Nature*, Vol.375, 567-570.

McDonald, K., 1999. Opportunity Knocks, Will GPS Modernization Open Doors? *GPS World*, September, pp. 36 –46.

Meertens, C, 2000. The Antenna and Multipath Calibration System website: http://www.unavco.ucar.edu/projects/active_projects/amcs.

Miyazaki, S., et al., 1996. Establishment of the nationwide GPS array and its initial results on the crustal deformation of Japan, *Bull. Geog. Surv. Inst. Jpn.*, 42, 27-41.

Miyazaki, S., T. Sagiya, T. Tada, Y. Hatanaka, 1997. One Hz sampling GPS as an ultra-long-period seismograph. *1997 AGU Fall Meeting*, San Francisco, California, 8-12 December.

Moreira, J., M. Schwabisch, G. Fornaro, R. Lanari, R. Bamler, D. Just, U. Steinbrecher, H. Breit, M. Eineder, G. Franceshetti, D. Geudtner, and H. Rinkel, July 1995, "X-SAR Interferometry: First Results," *IEEE Trans. Geosci. Rem. Sens.*, vol. 33, No. 4, pp 950 - 956.

Mouginis-Mark, P. J. & H. Garbeil, 1993, Digital topography of volcanoes from radar interferometry: An example from Mt. Vesuvius, Italy, *Bull. Volcanology*, 55, pp. 566 - 570.

Mouginis-Mark, P., 2000. http://satftp.soest.hawaii.edu/space/hawaii/vfts/kilauea/radar_ex/page1.html

Murakami, M., M. Tobita, S Fujiwara, T Saito, and H. Masaharu, 1996, Coseismic crustal deformations of 1994 Northridge, California, earthquake detected by Interferometric JERS-1 synthetic aperture radar, *Journal of Geophysical research*, vol. 101, No. B4, pp. 8605 - 8614.

Murakami, M., S. Fujiwara, and T. Saito, 1995, Detection of Crustal Deformations Associated with the 1995 Hyogoken-Nanbu Earthquake by Interferometric SAR, *Journal of the Geographical Survey Institute*, 83, 24-27 (in Japanese).

Murakami, M., S. Fujiwara, M. Tobita, K. Nitta, H. Nakagawa, S. Ozawa, and H. Yarai, 1997, Progress in SAR Interferometry for the Detection of Crustal Deformation by the

Geographical Survey Institute, *Journal of the Geographical Survey Institute*, 88, 1-9 (in Japanese).

Ozawa, S., M. Murakami, M. Tobita, and S. Fujiwara, 1997, SAR interferogram of the 1995 Kobe earthquake and its geodetic inversion, *Geopys. Res. Letter*, 24, 2327-2330.

Parkinson, B. and J. Spilker, 1996. Global positioning system: theory and applications. Washington, DC: American Institute of Aeronautics and Astronautics, pp793.

Peltzer, G. and P. Rosen, 1995, Surface displacement of the 17 May 1993 Eureka Valley, California earthquake observed by SAR interferometry, *Science*, vol. 268, pp. 1333-1336.

Petrovski, I., M. Ishii, H. Torimoto, K. Sasano, H. Hada, Y. Kawakita, J. Murai, T. Imakiire, B. Townsend, M.E. Cannon, and G. Lachapelle, 2000. New Flexible Network Based RTK Service in Japan. *The Satellite Division of the Institute of Navigation 13th International Technical Meeting (ION GPS 2000)*, September 19 – 22, Salt Lake City, Utah, USA.

Prati, C., C. Prati, F. Rocca, A. M. Guarnieri, and E. Damonti, 1990, Seismic Migration For SAR Focusing: Interferometrical Applications, *IEEE Trans. Geosci. Remote Sensing.*, Vol. 28, No. 4, , pp. 627 - 640.

Proakis, J. G. and D. G. Manolakis 1996. *Digital signal processing: principles, algorithms, and applications.* Prentice Hall, New Jersey, 3rd ed, 968 pp.

Proakis, J.G., 1995. *Digital communications.* McGraw-Hill, New York, 3rd ed., 905pp.

Rizos, C., 1996. *Principles and Practice of GPS Surveying*. Monograph 17, School of Geomatic Engineering, The University of New South Wales, Sydney, Australia, 555pp.

Rizos, C., Han, S. & Chen, H.-Y., 1998. Carrier phase-based, medium-range, GPS rapid static positioning in support of geodetic applications: algorithms and experimental results. *Spatial Information Science & Technology Symp.*, Wuhan, P.R. China, 13-16 December, 7-16.

Rizos, C., S. Han, L. Ge, H.-Y. Chen, Y. Hatanaka and K. Abe, 1999. Low-Cost Densification of Permanent GPS Networks for Natural Hazard Mitigation: First Tests on GSI's GEONET Network. *The International Symposium on GPS - Application to*

Earth Sciences and Interaction with Other Space Geodetic Techniques, October 18 - 22, Tsukuba, Japan. Also in *Earth, Planets and Space*, Vol. 52, 867-871.

Rosen, P.A., et al., 1997, JERS-1 SAR interferometry applications: mapping of rain forest enviroments and crustal deformation studies, in *JERS-1 Research Invitation Interim Report*, EROC/NASDA, pp. 47-61.

Rudin, H.J., 1967. Automatic equalization using transversal filters. *IEEE Spectrum*, 2(1), 53-59.

Sandwell, D.T., Sichoix, L., Agnew, D. Bock, Y. and J.-B. Minster, 2000. Near real-time radar interferometry of the Mw 7.1 Hector Mine Earthquake. *Geophysical Research Letters*, Vol.27, No.19, 3101-3105.

Schwarz, K.P. and M. Wei, 1994. Some unsolved problems in airborne gravimetry. *IAG Symposium No. 113 "Gravity and Geoid"*, Graz, Austria, 11-17 September. Springer Verlag, 131-150.

Segall P, M Matthews, 1997. Time Dependent Inversion of Geodetic Data. *J. Geophys. Res.*, 102(22), 391-22, 409.

Solo, V. and X. Kong, 1995. *Adaptive Signal Processing Algorithms: Stability and Performance*. Prentice Hall, New Jersey, 1st ed., 377pp.

SRTM, 2000. http://www.jpl.nasa.gov/srtm/mission.html

Stallings, W., 1999. *ISDN and broadband ISDN with frame relay and ATM*. N.J., Prentice Hall, 542pp.

Stavroudis, O.N., 1972. *The optics of Rays, Wavefronts, and Acaustics*, New York, Academic Press, 313pp.

Takahashi, Y. & R. Ichikawa, 1999. Comparison between station movements measured by VLBI and those measured by GPS, *Journal of the Communications Research Laboratory*, 46 (1), 171-176.

Takashima, K., S. Kurihara, M. Ishihara, K. Nemoto, M. Iwata, K. Shiba, M. Onogaki & K. Kobayashi, 2000. Status and results of GSI domestic VLBI networks, *Bulletin of the Geographical Survey Institute*, 46, 1-9.

Terrasat, 2000. http://www.terrasat.de/applications/refvirtual.htm

Tobita, M., S. Fujiwara, S. Ozawa, P. A. Rosen, E. J. Fielding, C. L. Werner, M. Murakami, H. Nakagawa, K. Nitta, and M. Murakami, 1998. Deformation of the 1995

North Sakhalin earthquake detected by JERS-1/SAR interferometry, submitted to *Earth, Planets and Space.*

Townsend, B. & P.C. Fenton, 1994. A practical approach to the reduction of pseudo-range multipath errors in an L1 GPS receiver. *7th Int. Tech. Meeting of the Satellite Division of The U.S. Institute of Navigation,* Salt Lake City, Utah, 20-23 September, 143-148.

Trimble, 1999. MS750 Operations Manual, 200pp.

Trimble, 2000. http://www.trimble.com/products/pdf/ms750pp.pdf

Turcotte, D. L., 1982. *Geodynamics : applications of continuum physics to geological problems.* Wiley, New York, 1st ed, 450 pp.

van Dierendonck, A.J., P.C. Fenton and T.J. Ford, 1992. Theory and performance of narrow correlator spacing in a GPS receiver. *Navigation,* 39(3), 265-283.

Wanninger, L. and S. Wildt, 1997. Identifikation von Mehr-wegeeinfl•ssen in GPS-Referenzstationsbeobachtungen. *Allgemeine Vermessungs-Nachrichten (AVN)*, 104, 12-15.

Wanninger, L., and M. May, 2000. Carrier Phase Multipath Calibration of GPS Reference Stations. *The Satellite Division of the Institute of Navigation 13th International Technical Meeting (ION GPS 2000)*, September 19 – 22, Salt Lake City, Utah, USA.

Ware, R.H., et al., 1999. Real-time GPS networks: opportunities for the atmospheric sciences. *International Symposium on GPS - Application to Earth Sciences and Interaction with Other Space Geodetic Techniques,* Tsukuba, Japan, 18-22 October.

Wdowinski S, et al, 1997. Southern California Permanent GPS Geodetic Array: Spatial filtering of daily positions for estimating coseismic and post-seismic displacements induced by the 1992 Landers earthquake. *J. Geophys. Res.*, 102(18), 057-18, 070.

Wegmuller, U. and C. L. Werner, Sept. 1995, "SAR Interferometric Signatures of Forest," *IEEE Trans. Geosci. Remote Sensing*., Vol. 33, No. 5, pp. 1153 - 1161, pp. 1153 – 1161.

Widrow, B., 1971. Adaptive filters. In R. Kalman and N. DeClaris (eds), *Aspects of network and system theory*, Holt, Rinehart and Winston, New York.

WU, J.T., 1994. Weighted differential GPS method for reducing ephemeris error. *Manuscripta Geodaetica*, 20, 1-7.

Yoshida, Y., Hoshiba, M., Ishikawa, Y., Ge, L., Izawa, M., Hashimoto, N., and S. Himori, 1999. Can high-sampling GPS data be used as displacement seismometer? *the Fall meeting of the Seismological Society of Japan*, 24-26 September, Sendai, Japan.

Yu SB, HY Chen, LC Kuo, 1997. Velocity field of GPS stations in the Taiwan area. *Tectonophysics,* 274, 41-59.

Zebker, H. A., and R. M. Goldstein, 1986, Topographic mapping from interferometric synthetic aperture radar observations, *J.Geophys. Res*., vol. 91, no. B5, pp. 4993-4999.

Zhang, J, Y Bock, H Johnson, P Fang, S Williams, J Genrich, S Wdowinski, and J Behr, 1997. Southern California Permanent GPS Geodetic Array: Error analysis of daily position estimate and site velocities, *J. Geophys. Res.*, Vol. 102, 18035-18055.

Zumberge, J, M Heflin, D Jefferson, M Watkins, and F Webb, 1997. Precise point positioning for the efficient and robust analysis of GPS data from large networks, *J. Geophys. Res.*, 102, 5005-5017.